

***Ab Initio* Investigation of Phase Change Materials: Structural, Electronic and Kinetic properties**

Von der Fakultät für Mathematik, Informatik und Naturwissenschaften
der RWTH Aachen University zur Erlangung des akademischen Grades
eines Doktors der Naturwissenschaften genehmigte Dissertation

vorgelegt von

Master of Science

Wei Zhang

aus Xi'an, China

Berichter: Professor Dr.rer.nat. Riccardo Mazzarello

Professor Dr.rer.nat. Matthias Wuttig

Tag der mündlichen Prüfung: 14.05.2014

Diese Dissertation ist auf den Internetseiten der Hochschulbibliothek online verfügbar.

Abstract

Phase change materials (PCMs) possess a peculiar combination of properties. They are capable of switching rapidly and reversibly between the amorphous and the crystalline phase at high temperature. However, the two phases are thermally very stable at room temperature. The pronounced optical and electrical contrast between these phases has enabled the development of data storage and memory technology based on PCMs. The investigation of PCMs is not only driven by the demands of industry, but also by the fundamental questions underlying these fascinating materials, which have drawn the attention of scientists and engineers during the past few decades.

This thesis aims at providing an in-depth understanding of various aspects of PCMs at the atomic level by employing quantum mechanical simulations: density functional theory (DFT) and DFT based *ab initio* molecular dynamics (AIMD). The two methods are known as powerful tools in simulating real materials.

After an introduction to PCMs and a review of the methodology, I start with the discussion of crystalline PCMs, in particular crystalline GeSbTe (c-GST) systems, where a significant amount of atomic disorder is detected. Recently, compelling evidence of disorder-induced localization of the electronic states has been found in c-GST experimentally. By atomistic modeling and electronic structure calculations, we have identified the microscopic origin of localization and we have proposed a plausible scenario for a disorder-order transition, which explains the metal-insulator transition (MIT) observed experimentally. All these findings provide important insights on controlling the wavefunction localization, which could lead to the development of multi-level data storage and other conceptually new devices based on multiple resistance states.

In the second part, phase transformations between the amorphous and the crystalline state are investigated. The kinetic process of both amorphization and crystallization is modeled using AIMD. The structural properties of several amorphous PCMs are studied in detail. Chemical bonding in amorphous GeTe

(a-GeTe) is analyzed, and the importance of homopolar bonds is quantified. The crystallization of growth-dominated PCMs, Ag, In doped Sb₂Te (AIST) and clean Sb₂Te, is realized with large-scale AIMD simulations. The atomic processes at the very front of the crystalline-amorphous interface are investigated. At high temperature, the growth velocity and the dynamical properties compare well with time-resolved reflectivity measurements and the role of impurities is elucidated in this temperature regime. Besides, a remarkably strong dependence of the dynamical properties on the quenching rates is observed at low temperatures.

Recently, a variety of more sophisticated applications of PCMs have been proposed and designed, e.g. arithmetic, logical and bio-inspired (or neuromorphic) processing, phase-change control over ferromagnetism, one-dimensional phase change nanowires and so on. In the last part of the thesis, we focus on the doping of PCMs with magnetic impurities, and discuss the magnetic properties of these systems in both the crystalline and the amorphous phase. We explain the magnetic contrast in Fe-doped GST observed experimentally. Moreover, we predict different magnetic behaviors upon doping with different 3 *d* impurities. These studies may lead to new applications in data storage, multifunctional spintronic devices as well as fast magnetic switching devices.

Abstrakt

Phasenwechselmaterialien (PCM) besitzen eine sonderbare Kombination von Eigenschaften. Sie sind in der Lage, schnell und reversibel zwischen der amorphen und der kristallinen Phase bei hoher Temperatur zu schalten. Jedoch sind beide Phasen thermisch sehr stabil bei Raumtemperatur. Der ausgeprägte optische und elektrische Kontrast zwischen diesen Phasen hat die Entwicklung der auf PCM basierende Datenspeichertechnologie ermöglicht. Die Untersuchung von PCM ist nicht nur von der Nachfrage der Industrie angetrieben, sondern auch durch die grundlegenden Fragen, die diese faszinierenden Materialien aufwerfen und die Aufmerksamkeit von Wissenschaftlern und Ingenieuren in den letzten Jahrzehnten auf sich gezogen haben.

Die Dissertation zielt darauf ab, ein umfassendes Verständnis der verschiedenen Aspekte der PCM auf atomarer Ebene durch den Einsatz von quantenmechanischen Simulationen: Dichtefunktionaltheorie (DFT) und die darauf beruhende *ab-initio* Molekulardynamik (AIMD). Diese beiden Verfahren sind als wirksame Werkzeuge in Simulationen realer Materialien bekannt.

Nach einer Einführung in die PCM und einen Überblick der wissenschaftlichen Methoden, beginne ich mit der Diskussion der kristallinen PCM, insbesondere der kristallinen GeSbTe (c-GST) Systeme, bei denen eine erhebliche Menge an atomarer Unordnung festgestellt wurde. Vor kurzem wurden überzeugende, experimentelle Beweise für die durch Unordnung induzierte Lokalisation der Elektronenzustände in c-GST gefunden. Durch die atomistische Modellierung und die Elektronenstrukturberechnung haben wir den mikroskopischen Ursprung dieser Lokalisation identifiziert und ein plausibles Szenario für einen Ordnungs-Unordnungs-Übergang vorgeschlagen, das den experimentell beobachteten Metall-Isolator-Übergang (MIT) erklärt. All diese Erkenntnisse liefern wichtige Erkenntnisse zur Steuerung der Lokalisation der Wellenfunktion, die zur Entwicklung von Multi-Level-Daten-Speichern und anderen konzeptionell neuartigen Geräten führen können, die mehrere Widerstandszustände ausnutzen.

Im zweiten Teil werden die Phasenübergänge zwischen dem amorphen und dem kristallinen Zustand untersucht. Die kinetischen Prozesse der Amorphisierung und der Kristallisation werden mittels AIMD modelliert. Die strukturellen Eigenschaften von mehreren amorphen PCM werden im Detail untersucht. Die chemische Bindung in amorphem GeTe (a-GeTe) wird analysiert, und die Bedeutung von homopolaren Bindungen quantifiziert. Die Kristallisation von wachstumsdominierten PCM, mit Ag und In dotiertem Sb₂Te (AIST) und reinem Sb₂Te wurde durch umfangreiche AIMD-Simulationen realisiert. Die atomaren Prozesse, die an Grenzflächen zwischen der amorphen und der kristallinen Phase stattfinden, werden untersucht. Bei hohen Temperaturen sind die Wachstumsgeschwindigkeit und die dynamischen Eigenschaften mit Resultaten von zeitaufgelösten Reflektivitätsmessungen vergleichbar und die Rolle der Verunreinigungen in diesem Temperaturbereich wird aufgezeigt. Außerdem ist eine bemerkenswert starke Abhängigkeit der dynamischen Eigenschaften von den Abkühlraten bei niedrigen Temperaturen beobachtet.

Kürzlich wurde eine Vielzahl von ausgeklügelten Anwendungen von PCM vorgeschlagen und entwickelt, wie z.B. arithmetische, logische und bioinspirierte (oder neuromorphen) Datenverarbeitung, Kontrolle des Ferromagnetismus durch PCM, eindimensionale Phasenwechsel-Nanodrähte und so weiter. In diesem Teil konzentrieren wir uns auf die Dotierung der PCM mit magnetischen Verunreinigungen, und diskutieren die magnetischen Eigenschaften dieser Systeme sowohl in der kristallinen als auch in der amorphen Phase. Wir klären den experimentell beobachteten magnetischen Kontrast in Fe-dotierten GST. Darüber hinaus sagen wir verschiedene magnetische Verhalten bei Dotierung mit verschiedenen 3d Verunreinigungen voraus. Diese Untersuchungen können zu neuen Anwendungen in Datenspeicherung, Multifunktions-Spintronik-Geräten sowie magnetisch schnell schaltenden Geräten führen.

Dedicated to my family

Contents

1. Introduction.....	1
1.1 Phase change materials.....	2
1.2 Resonant bonding in phase-change materials.....	4
1.3 Amorphization and structure of amorphous phase.....	5
1.4 Optical property contrast.....	7
1.5 Crystallization kinetics.....	8
1.6 Advanced applications.....	10
1.7 Objectives and structure of this thesis.....	11
2. Theoretical Background.....	13
2.1 Density functional theory.....	15
2.1.1 Hohenberg-Kohn Theorems.....	15
2.1.2 Kohn-Sham scheme.....	17
2.1.3 Exchange-correlation potential.....	20
2.1.4 Plane wave approach.....	23
2.1.5 Localized basis and mixed basis.....	25
2.1.6 Pseudopotentials.....	27
2.2 <i>Ab initio</i> molecular dynamics.....	30
2.2.1 Born-Oppenheimer approximation and nuclear motions.....	30
2.2.2 Car-Parrinello Method.....	32
2.2.3 Recent developments of Car-Parrinello method.....	34
2.3 Computational details.....	36

3. Crystalline Phase Change Materials.....	39
3.1 Overview of crystalline PCMs.....	39
3.2 Charge transport and metal insulator transition.....	45
3.3 Theoretical modeling of Anderson localization.....	49
3.3.1 The origin of localization -- vacancy clustering.....	50
3.3.2 Non-stoichiometric excess vacancies.....	58
3.3.3 Hybrid functional corrections and spin-orbit coupling effects.....	59
3.4 Theoretical modeling of Anderson MIT.....	62
3.4.1 Vacancy diffusion in cubic phase.....	62
3.4.2 Modeling of MIT.....	65
3.4.3 Non-stoichiometric excess vacancies.....	72
3.5 Summary and outlook.....	73
4. Amorphous Phase Change Materials.....	75
4.1 Generating amorphous phase with AIMD.....	76
4.2 Structural properties of amorphous PCMs.....	77
4.2.1 Finite size effect.....	79
4.2.2 Group 1 PCMs GeTe-Sb ₂ Te ₃ pseudobinary line.....	80
4.2.3 Group 2 PCMs doped Sb-Te.....	90
4.2.4 Group 3 PCMs doped Sb.....	93
4.3 summary and outlook.....	95
5. Crystallization Kinetics.....	97
5.1 Recent progress on crystallization kinetics of PCMs.....	97

5.2 Interface growth in group 2 PCMs -- AIST.....	99
5.3 Structural properties of amorphous and recrystallized AIST.....	101
5.4 Growth velocity versus temperature, quenching rate effects.....	107
5.5 Crystallization kinetics at high temperature, role of impurities...	114
5.6 Summary and outlook.....	123
6. Magnetically doped Phase Change Materials.....	125
6.1 Magnetic Phase Change Materials.....	125
6.2 Exchange mechanisms in dilute magnetic semiconductors.....	126
6.3 3 <i>d</i> impurities in hexagonal GST.....	129
6.4 3 <i>d</i> impurities in phase change cycle and magnetic contrast.....	136
6.4.1 3 <i>d</i> impurities in cubic GST.....	136
6.4.2 3 <i>d</i> impurities in amorphous GST.....	140
6.4.3 Magnetic contrast and exchange mechanism.....	148
6.5 Summary and outlook.....	150
7. Summary and Outlook.....	151
Appendix	
A. Density of several PCMs.....	153
B. EXAFS measurements and simulations of AIST.....	154
C. Order parameter Q_4^{dot}	156
D. Calculations of deposition rate and sticking coefficient.....	157
E. Calculations of Hubbard U in 3 <i>d</i> impurities doped GST.....	158
Acknowledgement.....	159

Bibliography.....	162
Curriculum Vitae.....	180

Chapter 1 Introduction

Recording information has been one of the most important issues since the beginning of human civilization. The way to store information has developed from ancient cave paintings, to medieval book printing and to modern non-volatile electronic devices. In the new century, the demand for data storage is growing explosively, however, both magnetic hard drives and the silicon-based flash memories seem to have reached their limits of size and speed. Scientists and engineers spare no efforts to find new candidates that could break those limits. A particularly promising candidate is so-called Phase Change Materials (PCMs) [1,2].

The phase change recording concept dates back to 1968 when S. Ovshinsky firstly discovered the reversible electrical switching phenomena [3]. In late 1980s, fast switching (on nanosecond time scales) phase change compounds have been synthesized, which have led to successful commercial products for data storage, i.e. rewriteable CD, DVD and Blu-Ray Discs. Besides optical data storage, PCMs offer good opportunities for memory technologies as well. The PCRAM, a non-volatile random-access memory based on PCMs has been designed [4], which has the potential to become a universal memory technology [5]. In the report of International Technology Roadmap for Semiconductor (ITRS) 2011 [6], PCRAM has been evaluated to be the most promising emerging candidate for memory technology, see Figure 1.1. A comprehensive and thorough review of phase change memory technology can be found in Ref. [7].

	Prototypical			Emerging					
Parameter	FeRAM	STT-MRAM	PCRAM	Emerging Ferroelectric	Nanomechanical Memory	Redox Memory	Mott Memory	Macromolecular Memory	Molecular Memory
Scalability									
MLC									
3D integration									
Fabrication Cost									
Endurance									
	Best in class		Good/Adequate		Bad/worse in class				Unknown

1.1 Phase change materials

Phase change materials are compounds that can undergo ultra fast and reversible transitions between an amorphous and a crystalline phase upon heating or lasering [1]. Both phases are very stable at room temperature, moreover, they are characterized by very different physical properties, namely, electrical and optical properties. These differences are large enough make the two phases represent different logical states, namely, "0" (amorphous, low reflectivity / high resistivity) or "1" (crystalline, high reflectivity / low resistivity), which can be utilized for data storage and memory technology. A simplified phase change framework is sketched in Figure 1.2. Applying a short and high voltage pulse locally melts the crystalline region, and an amorphous region is obtained upon subsequent rapid quenching. Fast crystallization of the amorphous region is induced by applying a long, medium intensity voltage pulse. The amorphous and crystalline states are often referred as "RESET" and "SET" states.

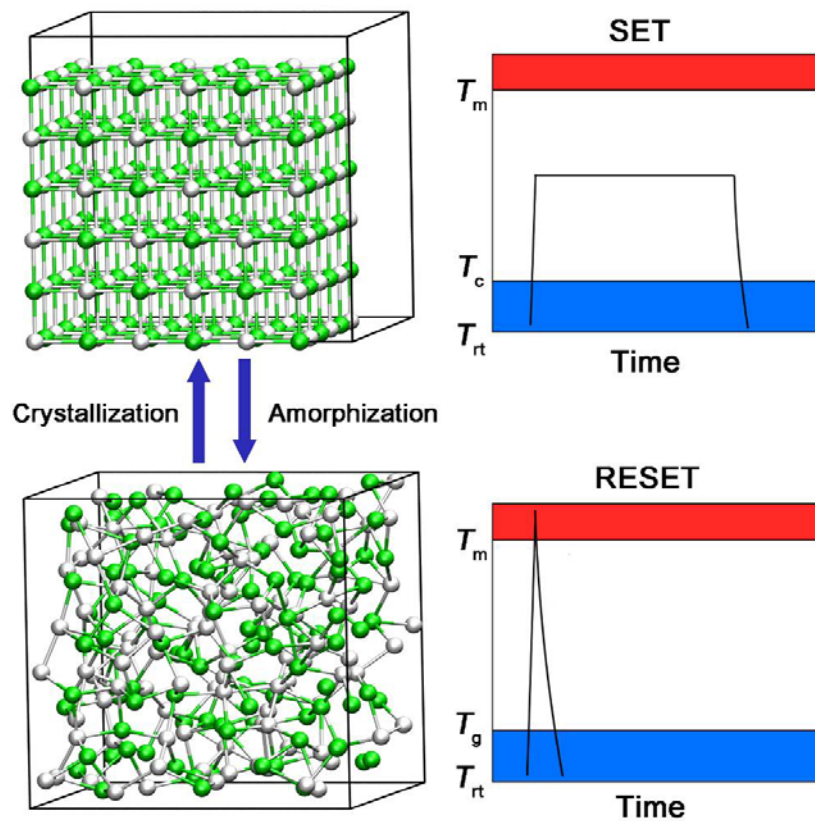


Figure 1.2 The underlying principle of phase change devices.

Several crucial criteria defining good phase-change materials are listed in Table 1.1. Besides the rapid and reversible transition between the amorphous and the crystalline phase, data retention, cyclability, storage density and property contrast are also essential in determining a good phase change material.

Crucial properties of phase change alloys	
Required property of PC materials	Specification
High-speed phase transition	Induced by nanosecond laser or voltage pulse
Long thermal stability of amorphous state	At least several decades at room temperature
Large optical change between the two states (for rewritable optical storage)	Considerable difference in refractive index or absorption coefficient
Large resistance change between the states (for non-volatile electronic storage)	Natural consequence of the transformation from amorphous to crystalline state
Large cycle number of reversible transitions	More than 100,000 cycles with stable composition
High chemical stability	High water-resistivity

Table 1.1 The crucial criteria to find good PCMs. Adapted from Ref. [1]

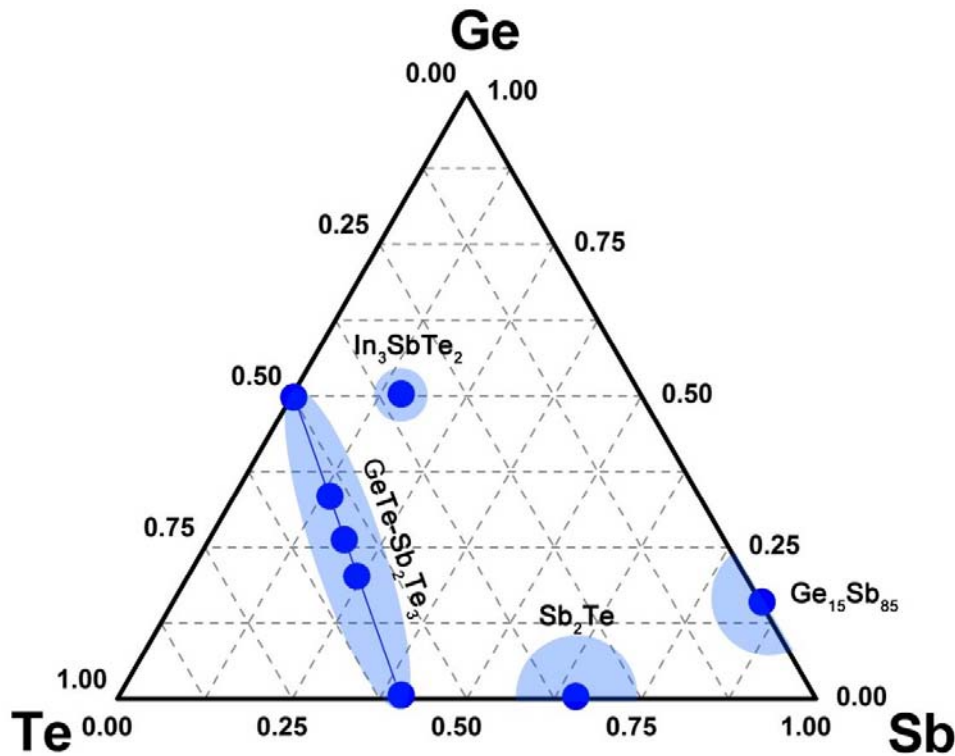


Figure 1.3 Reproduced from Ref. [8]. Overview of different families of phase change materials.

Only a few materials possess all the desired properties mentioned above. Over the past decades, three main groups of PCMs have been identified:

Group 1, GeTe and GeSbTe compounds along the GeTe-Sb₂Te₃ pseudobinary line, e.g. Ge₁Sb₂Te₄, Ge₂Sb₂Te₅, Ge₈Sb₂Te₁₁ etc. [9,10]

Group 2, Sb-Te compounds near the eutectic composition Sb₂Te, often combined with dopants like Ag, In, Ge, Ga etc. [11,12]

Group 3, doped Sb alloys, e.g. Ge₁₅Sb₈₅, Ga₁₅Sb₈₅, etc. [12, 13]

Besides these three main families, an unconventional phase change alloy In₃Sb₁Te₂ has become popular recently [14,15]. The three families are indicated in the Ge-Sb-Te ternary diagram shown in Figure 1.3.

1.2 Resonant bonding in phase-change materials

The very large optical/electrical property contrast between the amorphous and the crystalline phase indicates potentially different bonding mechanisms in the two phases. A first microscopic understanding of such phenomenon was given by Shportko and co-workers [16], who were able to demonstrate that a unique bonding scenario (resonant bonding) is present in the crystalline state, which differs significantly from the ordinary covalent bonding network in the amorphous state. Most PCMs crystallize into a cubic rock-salt like structure, where atoms possess roughly three valence *p* electrons on average, which are insufficient to form six covalent bonds with the nearest neighbors (the *s* valence electrons do not participate in chemical bonding here). The resonance between a bonding state and a non-bonding state is desirable to form, which reduces the total energy of the system. The pronounced electron delocalization in this resonantly bonded network leads to a significant increase of the electronic polarizability, as shown by the dielectric constant measurements. The increase of the dielectric constant from the amorphous to the crystalline state for non-phase change alloys (e.g. AgInTe₂) is rather small and can be explained by a density contrast via the Clausius-Mossotti model [17,18]. No resonant bonding is observed in such alloys.

Resonant bonding is considered as a fingerprint of PCMs and can be used to search for better performing PCMs: resonant bonding ensures the good reflectivity in the crystalline forms, while, in the amorphous network, only ordinary covalent bonding is

present (the resonance behavior is suppressed by the angular disorder, see section 1.4), leading to a relatively low reflectivity -- hence, the optical contrast is guaranteed. Lencer and co-workers [19,20] were able to devise a map of materials, expressed in terms of hybridization and ionicity, to locate PCMs: most of them are located in a corner, where both the hybridization and the ionicity are very low -- resonant bonding prevails. Although the optical contrast of candidate materials can be optimized with this criterion, other important criteria also need to be fulfilled, such as the thermal stability of the amorphous state, the crystallization speed at elevated temperatures and so on, which calls for investigations of the amorphous states and the transition process.

1.3 Amorphization and structure of the amorphous phase

Glasses or amorphous materials are disordered materials that lack long-range order. To obtain a glassy state, the most common way is to quench a liquid to low temperature with a very fast rate to avoid crystallization. In the diagram of time-temperature-transformation (Figure 1.4), the slope of quenching rate should be steep to avoid touching the crystalline region, where crystallization occurs very rapidly. For PCMs, typical quenching rates are 10^9 - 10^{10} K/s, due to the fact that PCMs are poor glass formers. The typical crystallization time in a phase change cell is on the order of few nanoseconds. By applying an external electrical field, the crystallization time can even be reduced to several hundreds of picoseconds [21].

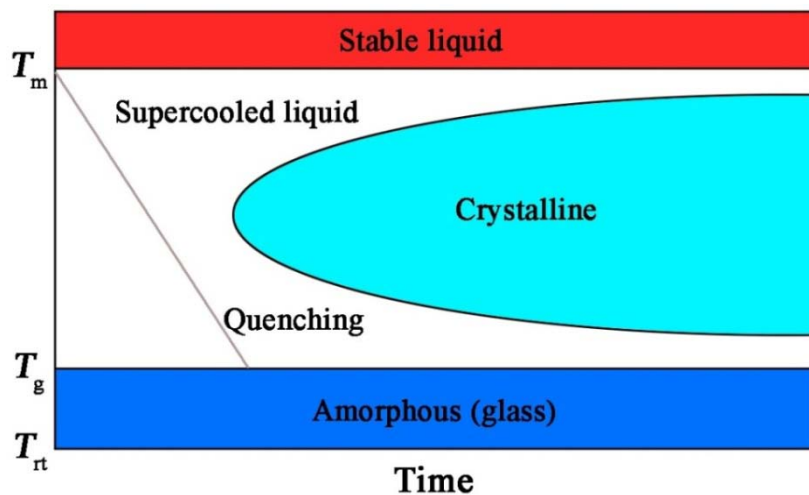


Figure 1.4 Time-temperature-transformation diagram

The study of the structural properties of the amorphous state is essential to understand the fast transition kinetics and the origin of the physical property contrast between the amorphous and crystalline state. Although glasses lack long-range order, it is often observed that the local structure of amorphous states resembles that of their crystalline counterparts, e.g. in most silicon-based glasses. In 2004, Kolobov *et al.* [22] performed extended x-ray absorption fine structure (EXAFS) and x-ray absorption near-edge structure (XANES) measurements on amorphous $\text{Ge}_2\text{Sb}_5\text{Te}_5$, and concluded that all Ge atoms are tetrahedrally coordinated with Te atoms, as opposed to their octahedral coordination in the crystalline phases. An umbrella-flip mechanism for Ge atoms was proposed for the rapid phase transformation (see Figure 1.5).

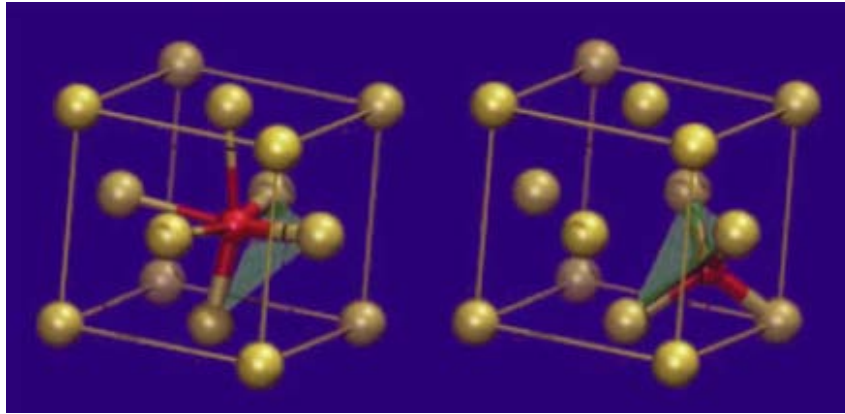


Figure 1.5 Adapted from Ref. [22]. Umbrella-flip of Ge atoms in crystalline and amorphous GeTe/GST.

However, on the one hand, it is not common to have structural motifs in the amorphous phase that do not have a stable parent crystalline phase. The crystalline form that consists of purely tetrahedral Ge and Te, -- GeTe_2 (where tetrahedral Ge atoms are bonded only with Te atoms), is highly unstable and quickly decomposes into GeTe and Te [23]. On the other hand, the umbrella-flip picture has been challenged by other EXAFS measurements [24], x-ray diffraction measurements together with reverse Monte-Carlo simulations [25] and *ab initio* molecular dynamics (AIMD) based on density functional theory (DFT) [26,27]. The AIMD simulations revealed that in the amorphous GST most of the Ge and Sb atoms are four-fold

coordinated, while Te is mostly three-fold coordinated in defective octahedral-like sites resembling the local environment of cubic crystalline GST. A fraction of Ge atoms has tetrahedral coordination ~20-30%; most of these atoms form at least one homopolar Ge-Ge or Ge-Sb bond. However, there is still a relatively big deviation (5-6%) in the Ge-Te bond lengths between AIMD and EXAFS. The structure of the amorphous phase and its evolution upon aging are still under debate.

The umbrella-flip model is intuitive in explaining the ultrafast phase transition and provides a possible scenario for the change of bonding mechanism. For these reasons, it has attracted much attention. However, it describes the transition between two crystalline states, not between an amorphous and a crystalline state. The real process of amorphization and crystallization involves more dramatic structural changes. It is noteworthy that in a recent experimental work, Simpson *et al.* [28] successfully produced a so-called interfacial phase change material, where the transition between two crystalline forms occurs by switching Ge atoms near the interface between the GeTe and the Sb₂Te₃ superlattice.

1.4 Optical property contrast

The pronounced optical contrast between the amorphous and the crystalline states should originate from different bonding mechanisms, which lead to a large difference in the optical matrix elements. By applying DFT simulations, Welnic *et al.* [29] have succeeded to reduce the optical matrix elements of the cubic GST/GeTe considerably by moving a fraction of Ge atoms to tetrahedral sites. In 2010, Huang and Robertson have shown that even in the absence of tetrahedral Ge, the medium range order loss, i.e. the misalignment of *p*-orbitals of neighboring rings, can already induce a reduction of the optical reflectivity [30]. Their DFT simulations were performed for GeTe in the crystalline form of orthorhombic GeSe, where the aligned *p*-bonds are absent. Later, Caravati *et al.* [31] considered more realistic amorphous models generated from AIMD. By comparing the amorphous models with (GeTe, GST) and without (Sb₂Te₃) tetrahedral units, the authors claimed that the change in the optical

response is mainly due to the angular disorder in p -bonding present in the amorphous phases, which supports the idea proposed by Huang and Robertson.

1.5 Crystallization kinetics

Two processes determine the crystallization kinetics of amorphous materials, namely, nucleation and growth. Nucleation refers to the formation of critical crystalline nuclei and the subsequent growth of the nuclei within an amorphous mark. Crystal growth instead describes the crystallization process occurring at the interface between the amorphous mark and the surrounding crystalline matrix. The two processes are visualized in Figure 1.6.

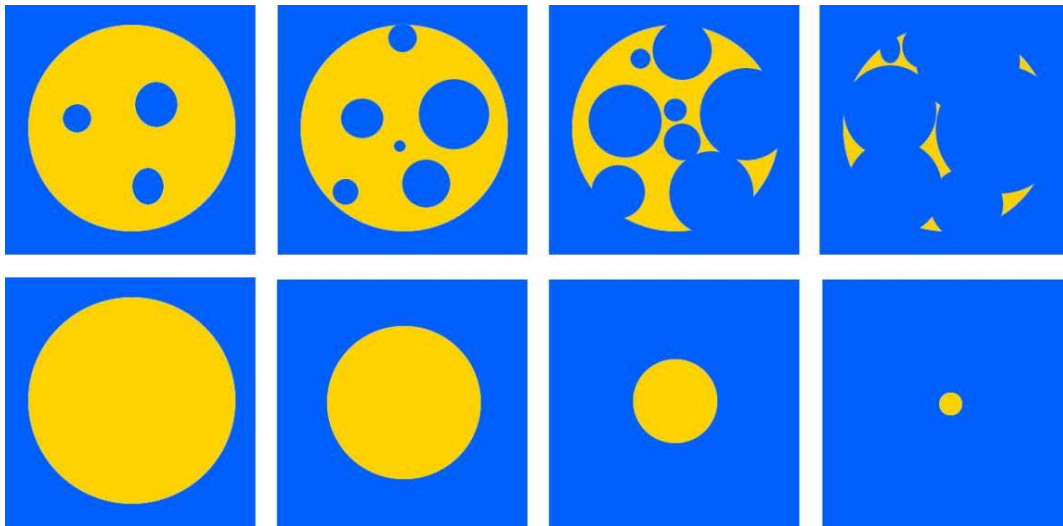


Figure 1.6 Nucleation process is described in the upper panels, while crystal growth is shown in the lower panels. Yellow and blue region refer to amorphous and crystalline phase, respectively.

As regards phase change materials, GeSbTe alloys are typically nucleation dominated, while doped Sb_2Te compounds are growth dominated. For large amorphous bits (diameter \sim hundreds of nm), the crystallization time of nucleation dominated PCMs does not depend on the volume due to the formation of multiple nuclei, while that of growth dominated PCMs does exhibit a volume dependence, i.e. the smaller amorphous bit can be fully crystallized faster. After nucleation, the PCM is in a polycrystalline state with typical grain sizes of 20 nm ($\text{Ge}_1\text{Sb}_2\text{Te}_4$ [32]). This

implies that, for smaller geometries of a few nm size, crystal growth could become dominant even for PCMs having high nucleation rates. Recently, such small phase-change memory cells have become feasible experimentally [33].

Three temperature regimes are relevant to the crystallization kinetics in PCMs, namely, a low temperature regime around the glass transition temperature T_g , a high temperature regime just below the melting temperature T_m and a middle temperature regime between T_g and T_m . In the first regime, the crystallization proceeds very slowly (on the order of minutes) due to the low diffusivities. This enables the direct experimental observation of nucleation and growth using high-resolution transmission electron microscopy (HRTEM) [34,34,35]. To measure the growth velocity or the incubation time, an alternative approach is to use atomic force microscopy (AFM) [36,37]. In the second regime, the crystallization also proceeds rather slowly due to the very small driving force, which enables the study of the undercooling of droplets [2]. By employing thermal measurements of the heat of fusion and differential thermal analysis, Kalb *et al.* [38] derived limits for the interfacial energy σ and the steady-state nucleation rate I_{ss} for different PCMs. The larger I_{ss} found for $\text{Ge}_2\text{Sb}_2\text{Te}_5/\text{Ge}_4\text{SbTe}_5$, as compared to $\text{Ag}_{5.5}\text{In}_{6.5}\text{Sb}_{59}\text{Te}_{29}/\text{Ge}_{12}\text{Sb}_{88}$, explained why nucleation is dominant for the former ones and growth is dominant for the latter ones. In the third temperature regime, the most relevant to the phase change technology, crystallization proceeds extremely fast (on the order of a few nanoseconds). This ultrafast phase transformation poses a great challenge to experimental measurements. Only very recently, two experimental groups made breakthroughs on measuring the crystallization kinetics in this middle temperature regime, i.e. the ultrafast differential scanning calorimetry (DSC) measurements by Orava *et al.* [39] and the time-resolved reflectivity measurements by Salinga *et al.* [35].

Thanks to the short time scales in this intermediate temperature regime, it becomes feasible to investigate the crystallization kinetics by (computationally heavy) AIMD simulations. A couple of computational works [40,41,42,43] have recently shed light on the nucleation and interface growth at the atomic level. Important quantities like

the growth velocity and the diffusion coefficients have been computed and compared with experimental findings.

1.6 Advanced applications

Beyond the standard optical data storage and electronic memory technologies, several sophisticated applications of PCMs have been recently proposed and designed.

Some researchers have become interested in one-dimensional systems: the so-called phase change nanowires have been synthesized and investigated during the past few years [44,45,46]. Very recently, the diameter of the phase change nanowires has even been reduced to 1.1 nm by a carbon nanotube confinement [47].

In 2008, Song *et al.* [48] doped $\text{Ge}_2\text{Sb}_2\text{Te}_5$ with Fe atoms experimentally and showed that both the crystalline and the amorphous phase are ferromagnetic and there exhibits a magnetic contrast. Later, Li and Mazzarello [49] provided a deeper understanding of the magnetic contrast in this compound. In the same year, Zhang *et al.* [50] predicted that Cr, Mn dopants could result in good, stable magnetic phase change materials, while Co, Ni dopants lead to non-magnetic states in both phases. Other than data storage, the combination of magnetic properties and phase-change properties could lead to possible spintronics applications, such as fast magnetic switching devices.

Some PCMs, such as Sb_2Te_3 [51] and GST [52,53], are also topological insulators [54,55], i.e. they are bulk insulators with conducting surface states due to time reversal symmetry. Recently, Sa *et al.* [56] predicted topological insulating behavior in $\text{GeTe}/\text{Sb}_2\text{Te}_3$ superlattices, known as interfacial PCMs [28]. Unlike Sb_2Te_3 , the topological insulating character of the superlattice can be observed under small compressive strains. By combining the phase change behavior with the topological insulating properties, novel spintronics devices, quantum computing as well as multifunctional data storage could be achieved.

Wright and coworkers extended the application of PCMs in a more advanced way. They designed arithmetic and biologically-inspired devices by utilizing the PCMs in an accumulation mode [57,58]. Suri *et al.* [59] also designed neuromorphic hardware using synapses based on Phase Change Memory (PCM) devices. All these studies paved the way for cognitive information processing [60].

1.7 Objectives and structure of this thesis

The goal of this thesis is to provide atomic level understandings of various aspects of phase change materials, including electronic properties of the crystalline phase, structural properties of the amorphous phase, crystallization kinetics as well as advanced applications based on PCMs. The thesis is divided into six chapters.

In Chapter 2, an overview of the methodologies is given, including density functional theory and *ab initio* molecular dynamics. Computational details for all the simulations performed in this thesis are provided.

In Chapter 3, first, the crystalline structures of several PCMs are introduced. Then, I provide a brief review of recent transport measurements in crystalline GeSbTe compounds (c-GST) showing an interesting metal-insulator transition, as well as a structural transition between a cubic and a hexagonal phase. These findings call for a thorough investigation of c-GST at the atomic level. By means of density functional theory calculations, we have investigated the effects of various sources of disorders and have linked them with the electronic and transport properties. We have identified the origin of electron wavefunction localization in c-GST, and we have shed light on the metal-insulator transition as well as the structural transition.

In Chapter 4, the amorphous phases of several PCMs are investigated. Models of these phases were generated by quenching from the melt. The structural properties of these phases are studied and compared to experimental measurements. Chemical bonding in amorphous GeTe is analyzed quantitatively and the importance of homopolar bonds is clarified.

In Chapter 5, the crystallization kinetics are studied for a growth dominated PCM,

AIST. The role of the Ag and In impurities is investigated at high temperature, where the dynamical properties compare well to experiments. Besides, a remarkably strong dependence of the dynamical properties on quenching rates at low temperature is found.

In Chapter 6, one possible advanced application of PCMs is discussed, namely, phase change control over ferromagnetism (inspired by the experiments on Fe doped $\text{Ge}_2\text{Sb}_2\text{Te}_5$). We add $3d$ magnetic impurities into $\text{Ge}_2\text{Sb}_2\text{Te}_5$, and study the stability of the configurations where the magnetic moments of the impurities are coupled ferromagnetically. Moreover, the observed distinct magnetic contrast between the two phases is understood at the atomic level.

In Chapter 7, the main results are summarized, and an outlook on future research is provided.

Chapter 2 Theoretical Background

Computers and supercomputers have developed explosively during the past decades. According to *top500* [61], the most powerful supercomputers are able to perform 10^{15} basic Floating-point Operations Per Second (FLOPS) -- peta-FLOPS, which is more than 12 orders of magnitude faster with respect to the first supercomputer Atlas [62] invented in 1962. Researchers and engineers are already designing next-generation exa-FLOPS supercomputers (10^{18} FLOPS). Thanks to the booming development of superclusters, computer simulations become more and more important and are regarded as the third fundamental research tool supplementing experiment and theory (see Figure 2.1).

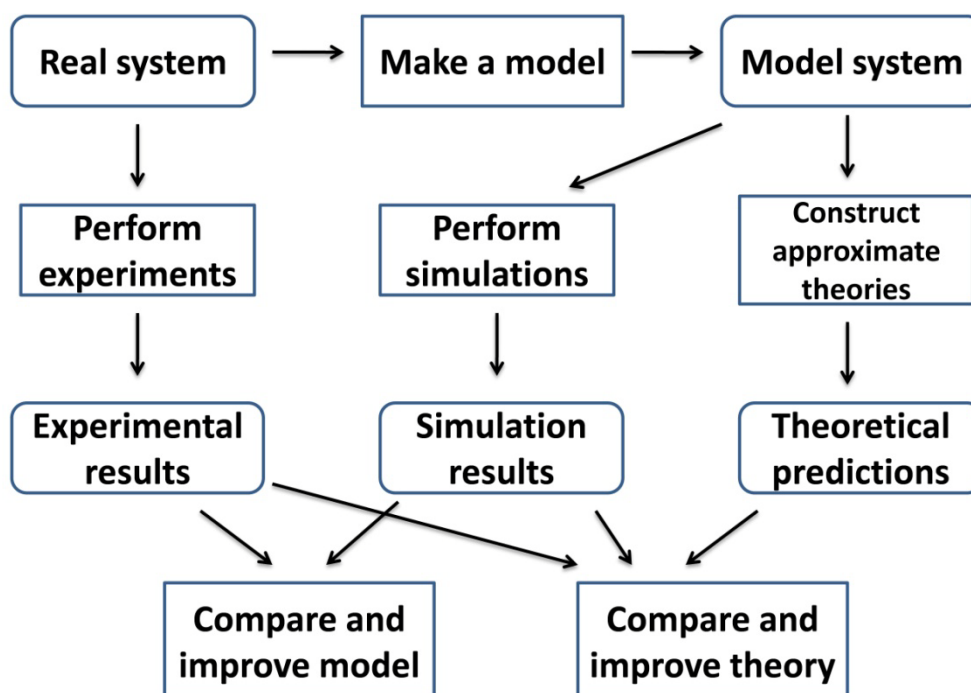


Figure 2.1 The interplay between experiment, simulation, and theory. Adapted from [63]

Nowadays, computer simulations cover a wide range of applications with very different length- and time-scales, e.g. phenomena in cosmology, weather forecasting, mechanical engineering, drugs discovery, proteins folding, crystal growth, electronic structure and many others. At the microscopic scale, two (out of many other) methods

are very important in characterizing the physical properties of real materials, namely, Density Functional Theory (DFT) [64,65] and Molecular Dynamics (MD) [66,67].

Density Functional Theory is a quantum mechanical method to investigate the electronic structure of many-body systems (principally the ground state properties). The modern formulation of DFT originated from the famous paper written by Hohenberg and Kohn [68] in 1964, where they showed the ground state electron density can be used as a basic variable, and all the ground state properties of the system can be considered to be unique functionals of such variable. Later in 1965, another classic work by Kohn and Sham [69] has converted the original interacting many-body problem to an auxiliary non-interacting particle problem, which established the framework for present-day electronic structure calculations. As an extension of DFT, Time-Dependent DFT [70] has been developed to cope with excited states and time-dependent phenomena. In 1998, W. Kohn was awarded the Nobel prize in Chemistry for his development of density-functional theory. The honor was shared by another scientist, J. Pople, who made significant contributions to computational methods in quantum chemistry [71].

Molecular dynamics describes the motions of interacting particles, which follow Newton's equations. Depending on how the interactions between particles are treated, molecular dynamics methods can be categorized into several classes. In the so called *ab initio* (or first-principles) molecular dynamics, the forces between ions are derived directly from DFT simulations without any parameter [72]. In classical molecular dynamics, the atomic interactions are modeled by classical potential functions [73], which are often fitted against experiments or *ab initio* methods. In between *ab initio* and classical methods, there are two other important schemes. The first one employs semi-empirical potentials [74], which are based on a quantum mechanical description of the electrons but with several approximations to treat the matrix elements between the Hamiltonian and the basis set. Tight-binding based molecular dynamics belongs to this scheme. The other scheme is based on QM/MM methods [75], where certain parts of the system are treated at the quantum-mechanical level (e.g. where reaction processes occur) and the rest of the system is calculated with classical potentials. Very

recently, the Nobel prize in Chemistry (2013) has been awarded to Karplus, Levitt and Warshel for their crucial contributions in bridging classical physics with quantum physics in computer simulations [76].

In this chapter, I provide a brief introduction to the framework of density functional theory and *ab initio* molecular dynamics, which are the primary tools employed in this thesis. Computational details, including software packages, functionals, pseudo-potentials, etc. are also provided.

2.1 Density functional theory

The fundamental principle of density functional theory is that all the ground state properties of an interacting many-body system are functionals of the ground state electron density. Hohenberg and Kohn proved the existence of the energy functional in their original work [68], and later Kohn and Sham provided a way to compute approximate ground state energy functional for real systems [69]. I start with the discussion of Hohenberg-Kohn theorems and the Kohn-Sham ansatz. Afterwards, some widely-used approximations for the exchange-correlation functional are introduced. Then, I focus on the approach of plane waves, localized basis sets and mixed basis sets. Furthermore, pseudopotentials are introduced. The formalism and derivations in this section mainly follow the book by R. Martin [65] and the DFT lecture slides by R. Mazzarello.

2.1.1 Hohenberg-Kohn Theorems

The Hamiltonian of an interacting electron gas in an external potential $\hat{V}(\vec{r})$ is given by,

$$\hat{H} = \hat{T} + \hat{W} + \hat{V} , \quad (2.1)$$

where $\hat{T} = -\sum_{i=1}^N \frac{\hbar^2}{2m_e} \nabla^2$ is the kinetic energy, $\hat{W} = \frac{1}{2} \sum_{i \neq j} \frac{e^2}{|\vec{r}_i - \vec{r}_j|}$ is the Coulomb interaction and $\hat{V} = \sum_{i=1}^N \hat{V}(\vec{r}_i)$ is the external potential. For the sake of simplicity, the ground state Ψ_{GS} is assumed to be non-degenerate.

The Hohenberg-Kohn theorems can be divided into two parts: 1> the external

potential and the ground state wavefunction are determined uniquely (except for a constant in the definition of the external potential) by the ground state density $\rho_{GS}(\vec{r})$; 2> a universal energy functional $E[\rho]$ can be defined in terms of density, and the ground state energy and density can be obtained by minimizing this functional.

The proof proceeds by *reductio ad absurdum*. Assume that another external potential $\hat{V}'(\vec{r})$ with ground state Ψ'_{GS} gives rise to the same ground density $\rho_{GS}(\vec{r})$. The two external potentials lead to two different Hamiltonians \hat{H} and \hat{H}' . It is rather straightforward to show the bijectivity of $\hat{V} \leftrightarrow \Psi_{GS}$, thus Ψ'_{GS} is not the ground state of \hat{H} , from which follows that

$$E_{GS} = \langle \Psi_{GS} | \hat{H} | \Psi_{GS} \rangle < \langle \Psi'_{GS} | \hat{H} | \Psi'_{GS} \rangle . \quad (2.2)$$

The last term can be written as

$$\begin{aligned} \langle \Psi'_{GS} | \hat{H} | \Psi'_{GS} \rangle &= \langle \Psi'_{GS} | \hat{H}' | \Psi'_{GS} \rangle + \langle \Psi'_{GS} | \hat{H} - \hat{H}' | \Psi'_{GS} \rangle \\ &= E'_{GS} + \int d^3r [\hat{V}(\vec{r}) - \hat{V}'(\vec{r})] \rho_{GS}(\vec{r}) \end{aligned}$$

so that

$$E_{GS} < E'_{GS} + \int d^3r [\hat{V}(\vec{r}) - \hat{V}'(\vec{r})] \rho_{GS}(\vec{r}) . \quad (2.3)$$

By considering E'_{GS} in exactly the same way, the primed and unprimed quantities interchanged,

$$E'_{GS} < E_{GS} + \int d^3r [\hat{V}'(\vec{r}) - \hat{V}(\vec{r})] \rho_{GS}(\vec{r}) . \quad (2.4)$$

If we add together (2.3) and (2.4), we obtain the contradictory inequality $E_{GS} + E'_{GS} < E_{GS} + E'_{GS}$. Thus \hat{V} is a unique functional of $\rho_{GS}(\vec{r})$ (except for a constant). As a consequence, the ground state expectation value of any observable O is a functional of the ground state density

$$O[\rho_{GS}(\vec{r})] \equiv \langle \Psi_{GS}(\rho_{GS}) | \hat{O} | \Psi_{GS}(\rho_{GS}) \rangle . \quad (2.5)$$

Since all properties are uniquely defined if $\rho(\vec{r})$ is specified, they can be viewed as a functional of $\rho(\vec{r})$, including the total energy functional,

$$\begin{aligned} E_{HK}[\rho] &= \langle \Psi(\rho) | \hat{H} | \Psi(\rho) \rangle \\ &= \langle \Psi(\rho) | \hat{T} + \hat{W} | \Psi(\rho) \rangle + \int \rho(\vec{r}) V(\vec{r}) d^3\vec{r} \\ &= F_{HK}[\rho] + \int \rho(\vec{r}) V(\vec{r}) d^3\vec{r} . \end{aligned} \quad (2.6)$$

The functional $F_{HK}[\rho] \equiv T[\rho] + W[\rho]$ is universal and includes the kinetic and Coulomb energy of the interacting electron system.

Now consider a system with ground state density $\rho_{GS}(\vec{r})$ corresponding to the external potential $\hat{V}(\vec{r})$. According to the discussion above, the Hohenberg-Kohn energy functional E_{HK} calculated at $\rho_{GS}(\vec{r})$ equals the expectation value of the Hamiltonian with respect to the unique ground state Ψ_{GS} ,

$$E_{GS} = E_{HK}[\rho_{GS}] = \langle \Psi_{GS} | \hat{H} | \Psi_{GS} \rangle \quad . \quad (2.7)$$

If one considers a different density $\rho''_{GS}(\vec{r})$, which corresponds to the ground state wavefunction Ψ''_{GS} for a different Hamiltonian \hat{H}'' , one obtains a larger energy,

$$E_{GS} = \langle \Psi_{GS} | \hat{H} | \Psi_{GS} \rangle < \langle \Psi''_{GS} | \hat{H} | \Psi''_{GS} \rangle = E'' \quad . \quad (2.8)$$

Therefore, the ground state energy and density can be obtained by minimizing the energy functional,

$$E_{GS} = \min_{\rho} E[\rho(\vec{r})] \quad . \quad (2.9)$$

The theorems can readily be extended to the degenerate case [77]. In the alternative formulation of the Hohenberg-Kohn theorems by Levy [78] and Lieb [79], the degenerate case is also included.

2.1.2 Kohn-Sham scheme

The Kohn-Sham approach boils down to replacing the interacting many-body system with a different auxiliary non-interacting particle system. The basic assumption is that there exists some non-interacting system whose ground state density equals the ground state density of the original interacting system [69]. The new non-interacting system can be exactly solved (by numerical approaches) by incorporating all the difficult many-body terms into an exchange-correlation functional of the density. With proper approximations to the exchange-correlation functional, such as the local density approximation (LDA) and the generalized-gradient approximation (GGA), the Kohn-Sham approach leads to very accurate description of the original interacting many-body system, e.g. in group IV and II-V semiconductors, metals such as Na, Al and insulators like diamond, Bi_2Se_3 , etc.

However, these approximations typically fail for strongly-correlated systems, such as Mott insulators NiO, CoO etc. Many corrective schemes have been formulated to solve these problems, e.g. DFT+U [80,81], Reduced Density Matrix Functional Theory [82], DFT+ Gutzwiller [83] and so on.

Now we consider the formulation of the Kohn-Sham scheme. For the non-interacting single particle system, the Coulomb interaction term is zero. In this case, the Hamiltonian reads,

$$\hat{H}_s = \hat{T}_s + \hat{V}_s = \hat{T}_s + \sum_{i=1}^N \hat{v}_s \quad . \quad (2.10)$$

Assuming the ground state Φ_{GS} is non-degenerate, Φ_{GS} is given by the Slater determinant of the N lowest single-particle orbitals φ_i with the eigenvalues ε_i . For each single-particle orbital,

$$-\frac{\hbar}{2m_e} \nabla^2 \varphi_i(\vec{r}) + v_s(\vec{r}) \varphi_i(\vec{r}) = \varepsilon_i \varphi_i(\vec{r}) \quad , \quad (2.11)$$

and the total density of the system is given by

$$\rho(\vec{r}) = \sum_{i=1}^N |\varphi_i(\vec{r})|^2 \quad . \quad (2.12)$$

In analogy with the interacting case, the effective potential \hat{v}_s is uniquely determined by the ground state density of this system. The energy functional E_{vs} is given by,

$$E_{vs}[\rho] = \langle \Phi_{GS}[\rho] | \hat{H} | \Phi_{GS}[\rho] \rangle + \int \rho v_s d^3\vec{r} \equiv T_s[\rho] + \int \rho v_s d^3\vec{r} \quad . \quad (2.13)$$

Clearly, for any ρ different from ρ_{GS} , $E_{vs} > E_{GS}$. The orbitals and the kinetic term T are also unique functionals of the density.

$$\varphi_i(\vec{r}) = \varphi_i([\rho], \vec{r}) \quad , \quad (2.14)$$

$$T_s[\rho] = \sum_{i=1}^N \int \varphi_i^* \left(-\frac{\hbar^2}{2m_e} \nabla^2 \right) \varphi_i d^3\vec{r} \quad . \quad (2.15)$$

As stated above the new ground state density is assumed to be equal to that of the original interacting system, so that the interacting system can be mapped onto the non-interacting system $\hat{T} + \hat{W} + \hat{V} \rightarrow \hat{T} + \hat{V}_s$. The exact density of the interacting system can then be calculated with (2.14). Now we evaluate \hat{V}_s explicitly. We rewrite the energy functional $E[\rho]$ for the interacting system in the presence of an external potential $\hat{V}(\vec{r})$ as,

$$E[\rho] = T[\rho] + W[\rho] + \int \rho V(\vec{r}) d^3\vec{r}$$

$$= T_s[\rho] + E_H[\rho] + \int \rho(\vec{r})V(\vec{r}) d^3\vec{r} + E_{xc}[\rho] , \quad (2.16)$$

where the Hartree energy E_H and the exchange-correlation energy E_{xc} are defined as

$$E_H[\rho] = \frac{1}{2} \int d^3\vec{r} d^3\vec{r}' \frac{\rho(\vec{r})\rho(\vec{r}')}{|\vec{r}-\vec{r}'|} , \quad (2.17)$$

and

$$E_{xc}[\rho] \equiv T[\rho] - T_s[\rho] + W[\rho] - E_H[\rho] . \quad (2.18)$$

The Hartree energy E_H is defined as the classical interaction energy between electrons.

The exchange-correlation energy E_{xc} includes all the many body interactions and correlations. Applying the variational principle to $E[\rho]$,

$$\begin{aligned} \delta E &= E[\rho_{GS} + \delta\rho] - E[\rho_{GS}] = 0 \\ &= \delta T_s[\rho_{GS}] + \int d^3\vec{r} \delta\rho(\vec{r})(V(\vec{r}) + \int \frac{1}{|\vec{r}-\vec{r}'|} \rho_{GS}(\vec{r}') d^3\vec{r}' + v_{xc}([\rho_{GS}], \vec{r})) \end{aligned} \quad (2.19)$$

where v_{xc} is the exchange-correlation potential defined as $v_{xc}([\rho_{GS}], \vec{r}) \equiv \frac{\delta E_{xc}}{\delta\rho(\vec{r})}|_{\rho=\rho_{GS}}$.

Similarly, one can apply the variational principle to $E_s[\rho]$,

$$\begin{aligned} \delta E_s &= E_s[\rho_{GS} + \delta\rho] - E_s[\rho_{GS}] = 0 \\ &= \delta T_s[\rho_{GS}] + \int \delta\rho(\vec{r})v_s(\vec{r})d^3\vec{r} . \end{aligned} \quad (2.20)$$

By equating the two formulas, we obtain the effective potential,

$$v_s(\vec{r}) = V(\vec{r}) + v_H[\rho_{GS}] + v_{xc}([\rho_{GS}], \vec{r}) , \quad (2.21)$$

where the Hartree potential is $v_H[\rho_{GS}] = \int \frac{1}{|\vec{r}-\vec{r}'|} \rho_{GS}(\vec{r}') d^3\vec{r}'$.

Up to now, we have shown that an interacting many-body system can be mapped onto a non-interacting system with the same ground state density. The next task is to solve the Kohn-Sham equations (2.11), (2.12) and (2.21) self-consistently. Normally, the procedure starts with a guessed electron density, then one calculates the effective potential, next solves the Kohn-Sham equations, then calculates the electron density again. After each such iteration, the obtained new density is compared to the previous one, if the difference between the two densities is sufficiently small, the self-consistency is reached and the ground state is obtained; otherwise, one needs to start another iteration. The procedure is summarized in the flow chart in Figure 2.2. The Kohn-Sham scheme can be extended to degenerate ground states and spin-polarized systems, for details, please refer to Ref. [65].

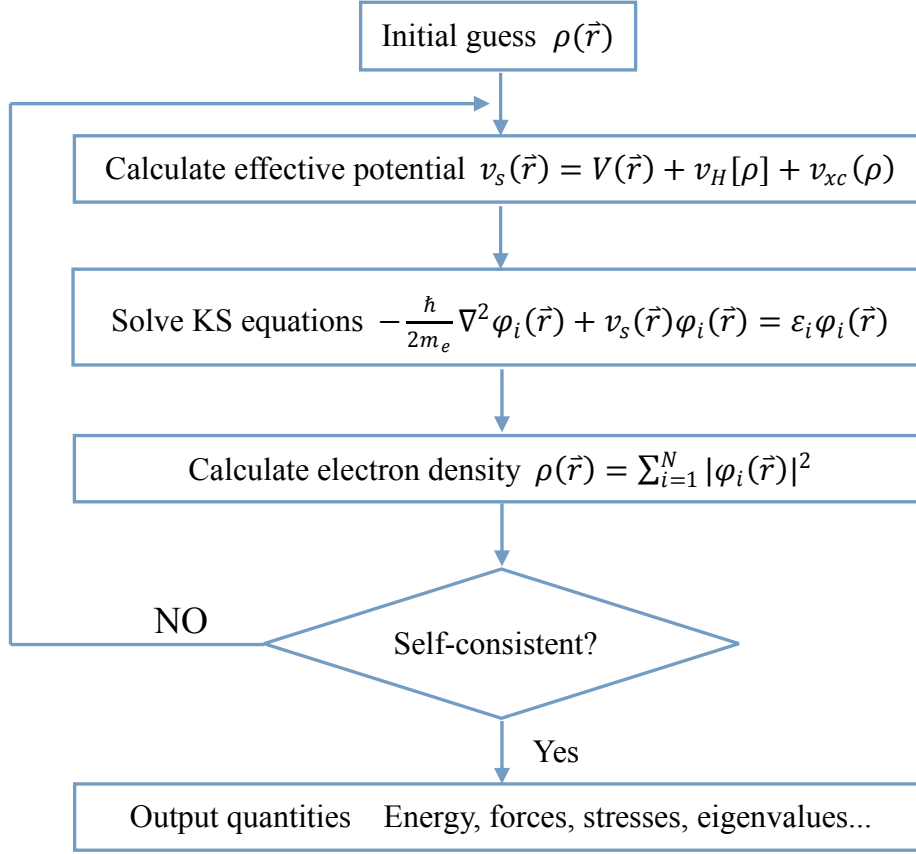


Figure 2.2 The scheme of a self-consistent loop for the solution of the Kohn-Sham equations. Reproduced from Ref. [65]

2.1.3 Exchange-correlation potential

In this section, we introduce some very useful approximations to the exchange-correlation potential, including the local density approximation (LDA), the generalized gradient approximation (GGA) and the hybrid functional approximation.

As already proposed by Kohn and Sham in their seminal paper, LDA is a very instructive and useful approximation to the exchange-correlation potential, which works remarkably well for homogeneous solids and many inhomogeneous solids. The form of the LDA exchange-correlation energy functional is simple, i.e. it is an integral over all space of the exchange-correlation energy density, which at each point, equals the energy of the homogeneous electron gas with the given local density,

$$E_{xc}^{LDA}[\rho] = \int d^3\vec{r} \varepsilon_{xc}^{hom}(\rho(\vec{r})) \quad . \quad (2.22)$$

So now we need to calculate the exchange-correlation energy of the homogeneous

electron gas. This is a well-studied problem in many-body physics. The exchange-correlation energy can be split into two parts, the exchange energy E_x and the correlation energy E_c . The exchange energy can be calculated analytically,

$$E_x^{LDA}[\rho] = \int d^3\vec{r} \varepsilon_x^{hom}(\rho(\vec{r})) = -\frac{3}{4} \left(\frac{3}{\pi}\right)^{\frac{1}{3}} \int d^3\vec{r} \rho(\vec{r})^{\frac{4}{3}}. \quad (2.23)$$

As regards the correlation energy, it has no general analytical solution. In the low density limit, Coulomb interactions dominate over the kinetic energy and electrons tend to arrange themselves into a regular lattice, which is known as "Wigner crystal" [84,85]. The correlation energy in this limit can be computed by evaluating the Coulomb energy, harmonic vibration energies and anharmonic corrections of the Wigner crystal [86]. In the high density limit, Coulomb interactions become negligible compared to the kinetic energy and the correlation energy can be calculated using perturbation theory and diagrammatic techniques [87,88]. It is more challenging to estimate the correlation energy at intermediate densities. Several approaches have been employed, such as the random phase approximation (RPA) [89], quantum Monte Carlo (QMC) calculations [90,91] and so on. The most accurate results were obtained by QMC calculations. By fitting against the QMC calculations, analytical expressions for the correlation functional can be obtained. The most popular functionals were derived by Perdew and Zunger (PZ) [92], and Vosko, Wilk and Nusair (VWN) [93].

There are a few shortcomings of LDA. The most obvious one is the unphysical self-interaction term. The electron does not interact with itself, however, in the Hartree energy term, self-interaction is included; since the exchange energy is approximated, it does not cancel out the self-interaction term exactly. To improve the LDA scheme, Perdew and Zunger [92] proposed self-interaction corrections (SIC) to the exchange-correlation energy, which make the simulations computationally more demanding. A further LDA+U scheme (DFT+U) [94,80] also leads to important improvements over the self-interaction effect. Another shortcoming of LDA is that it fails to describe accurately very inhomogeneous systems. With gradient corrections to the density, the results can be significantly improved in many cases.

Generalized gradient approximations (GGAs) are based on a perturbative expansion with respect to the density gradient,

$$E_{xc}^{GGA}[\rho] = \int d^3 \vec{r} \varepsilon_{xc}^{GGA}(\rho, \nabla \rho, \nabla^2 \rho, \dots) \quad , \quad (2.24)$$

with

$$\begin{aligned} \varepsilon_{xc}^{GGA}(\rho, \nabla \rho, \nabla^2 \rho, \dots) = & \varepsilon_{xc,00}^{GGA}(\rho(\vec{r})) + \varepsilon_{xc,22}^{GGA}(\rho(\vec{r}))(\nabla \rho(\vec{r}))^2 \\ & + \varepsilon_{xc,42}^{GGA}(\rho(\vec{r}))(\nabla^2 \rho(\vec{r}))^2 + \varepsilon_{xc,43}^{GGA}(\rho(\vec{r}))(\nabla^2 \rho(\vec{r}))(\nabla \rho(\vec{r}))^2 \\ & + \varepsilon_{xc,44}^{GGA}(\rho(\vec{r}))(\nabla \rho(\vec{r}))^4 + \dots \quad , \end{aligned} \quad (2.25)$$

where the notation $\varepsilon_{xc,ij}^{GGA}$ indicates there are i gradient operators and j functions of the density. By definition, we have $\varepsilon_{xc,00}^{GGA}(\rho(\vec{r})) = \varepsilon_{xc}^{LDA}(\rho(\vec{r}))$. The gradient corrections are calculated by assuming the system is very close to the homogeneous gas, with weak deviations from uniformity. In this limit ε_{xc}^{GGA} can be expressed in terms of linear and higher order response functions of the homogeneous electron gas. Usually, the gradient correction is considered up to the second term $\varepsilon_{xc,22}^{GGA}$ and all the high-order terms are neglected. Some widely used GGA functionals were formulated by Becke (B88) [95], Perdew and Wang (PW91) [96], and Perdew, Burke and Enzerhof (PBE) [97].

Hybrid functionals combine the exact exchange Hartree Fock term with the approximate functionals LDA and GGA. This hybrid approach, pioneered by Becke [98], provides a simple scheme to improve the descriptions of certain properties, such as atomization energies, bond lengths, vibrational frequencies, etc., which sometimes are poorly described by pure LDA and GGA functionals [99]. The hybrid exchange-correlation functional is constructed as a linear combination of the exact orbital-dependent exchange terms and the approximate LDA and GGA terms,

$$E_{xc} = E_{xc}^{LDA} + a(E_x^{exact} - E_x^{LDA}) + bE_x^{GGA} + cE_c^{GGA} \quad , \quad (2.26)$$

where the coefficients a , b and c are fitted against atomic and molecular data. The functional becomes semi-empirical. Popular hybrid functionals are HSE [100] and B3LYP [101].

2.1.4 Plane wave approach

In modern DFT calculations, the plane wave basis is the most popular approach to solve Kohn-Sham equations. Plane waves can provide an intuitive understanding for periodic solids, furthermore, their usage makes the calculation of important quantities, including the forces and the Hartree potential, simple and efficient. Many popular codes are constructed based on plane waves, such as Quantum Espresso, VASP, ABINIT, CASTEP, etc.

From the Kohn-Sham equations (2.12), (2.14) and (2.21), we have

$$\begin{aligned}\hat{H}_s(\vec{r})\varphi_i(\vec{r}) &= -\frac{\hbar}{2m_e}\nabla^2\varphi_i(\vec{r}) + v_s(\vec{r})\varphi_i(\vec{r}) = \varepsilon_i\varphi_i(\vec{r}) \\ v_s(\vec{r}) &= V(\vec{r}) + v_H[\rho] + v_{xc}([\rho], \vec{r})\end{aligned}$$

In a solid, it is convenient to consider periodic boundary conditions in a volume Ω . We can then expand the eigenfunctions in a complete discrete set of Fourier components,

$$\varphi_i(\vec{r}) = \frac{1}{\sqrt{\Omega}} \sum_{\vec{q}} c_{i,\vec{q}} e^{i\vec{q}\cdot\vec{r}} \equiv \sum_{\vec{q}} c_{i,\vec{q}} |\vec{q}\rangle \quad , \quad (2.27)$$

where $c_{i,\vec{q}}$ are the expansion coefficients of the wavefunctions in the basis of plane waves $|\vec{q}\rangle = \frac{1}{\sqrt{\Omega}} e^{i\vec{q}\cdot\vec{r}}$, and $|\vec{q}\rangle$ are orthonormal $\langle\vec{q}'|\vec{q}\rangle = \delta_{\vec{q}',\vec{q}}$. Since the effective potential $v_s(\vec{r})$ has the periodicity of the crystal, one can write

$$v_s(\vec{r}) = \sum_{\vec{G}_m} v_s(\vec{G}_m) e^{i\vec{G}_m\cdot\vec{r}} \quad , \quad (2.28)$$

where \vec{G}_m are the reciprocal lattice vectors, and

$$v_s(\vec{G}) = \frac{1}{\Omega_{\text{cell}}} \int_{\Omega_{\text{cell}}} v_s(\vec{r}) e^{-i\vec{G}\cdot\vec{r}} d^3\vec{r} \quad , \quad (2.29)$$

with Ω_{cell} the volume of the primitive cell.

If we define the vector \vec{k} as $\vec{q} = \vec{k} + \vec{G}_m$, the eigenfunction (2.27) can be written as,

$$\varphi_{i,\vec{k}}(\vec{r}) = \frac{1}{\sqrt{\Omega}} \sum_m c_{i,m}(\vec{k}) e^{i(\vec{k}+\vec{G}_m)\cdot\vec{r}} = e^{i\vec{k}\cdot\vec{r}} \frac{1}{\sqrt{N_{\text{cell}}}} u_{i,\vec{k}}(\vec{r}) \quad , \quad (2.30)$$

where $\Omega = N_{\text{cell}} \Omega_{\text{cell}}$ and

$$u_{i,\vec{k}}(\vec{r}) = \frac{1}{\sqrt{\Omega_{\text{cell}}}} \sum_m c_{i,m}(\vec{k}) e^{i\vec{G}_m\cdot\vec{r}} \quad . \quad (2.31)$$

The new functions $u_{i,\vec{k}}(\vec{r})$ have the periodicity of the crystal and are orthonormal in one primitive cell. This is the so called Bloch theorem and the solutions are called Bloch states.

If we consider the Kohn-Sham Schrödinger equations in terms of the vector \vec{k} with $\vec{q} = \vec{k} + \vec{G}_m$ and $\vec{q}' = \vec{k} + \vec{G}_{m'}$ ($\vec{G}_{m''} = \vec{G}_m - \vec{G}_{m'}$), we obtain

$$\sum_{m'} H_{m,m'}(\vec{k}) c_{i,m'}(\vec{k}) = \varepsilon_i(\vec{k}) c_{i,m'}(\vec{k}) \quad , \quad (2.32)$$

with the matrix element $H_{m,m'}$ given by

$$H_{m,m'}(\vec{k}) = \langle \vec{k} + \vec{G}_m | \hat{H}_s | \vec{k} + \vec{G}_{m'} \rangle = \frac{\hbar^2}{2m_e} |\vec{k} + \vec{G}_m|^2 \delta_{m,m'} + v_s(\vec{G}_m - \vec{G}_{m'}) \quad (2.33)$$

Equations (2.32) and (2.33) are the basic Kohn-Sham Schrödinger equations in a periodic crystal. By solving these equations, the energy eigenvalues $\varepsilon_i(\vec{k})$ and the eigenstates $\varphi_{i,\vec{k}}(\vec{r})$ at each \vec{k} can be obtained. \vec{k} is called crystal momentum and can always be confined to the first Brillouin zone.

To solve (2.32) numerically, a finite set of plane waves is used and the cutoff value is given by the inequality,

$$\frac{\hbar^2}{2m_e} |\vec{k} + \vec{G}|^2 \leq E_{cutoff} \quad (2.34)$$

This cutoff value should be large enough to calculate the eigenstates accurately, but, on the other hand, it should be as small as possible to reduce the computational efforts.

To compute certain properties, such as the number of electrons in the bands, the total energy, etc., it is essential to integrate over \vec{k} in the first Brillouin zone. For practical calculations, only a finite set of k-points can be used, which calls for the use of an accurate and efficient sampling scheme. The most widely used method was proposed by Monkhorst and Pack [102],

$$\vec{k}_{n_1,n_2,n_3} \equiv \sum_{i=1,2,3} \frac{2n_i - N_i - 1}{2N_i} \vec{G}_i, \quad n_i = 1, \dots, N_i \quad , \quad (2.35)$$

where N_i is the number of k points along each direction i . (2.35) defines a $N_1 \times N_2 \times N_3$ k-point mesh over the first Brillouin zone.

To solve the Kohn-Sham equations self-consistently, one of the most important operations is to calculate the electron density ρ . Equation (2.12) can be written as,

$$\rho(\vec{r}) = \frac{1}{N_k} \sum_{i,\vec{k}} f(\varepsilon_{i,\vec{k}}) \rho_{i,\vec{k}}(\vec{r}) \quad . \quad (2.36)$$

This is an average over \vec{k} points: i denotes the bands at each \vec{k} and $f(\varepsilon_{i,\vec{k}})$ denotes the Fermi function. The Fermi function is a step function at absolute zero temperature. To improve the convergence in metals, a smoother function is typically used. In crystals, the electron density is also periodic and by considering a plane wave basis, one obtains,

$$\rho(\vec{r}) = \frac{1}{\Omega} \sum_{i,\vec{k}} f(\varepsilon_{i,\vec{k}}) \sum_{m,m'} c_{i,m}^*(k) c_{i,m'} e^{i(\vec{G}_{m'} - \vec{G}_m) \cdot \vec{r}} \quad . \quad (2.37)$$

The Fourier transform of the density $\rho_{i,\vec{k}}(\vec{r}) \equiv |\varphi_{i,\vec{k}}|^2$ reads,

$$\rho_{i,\vec{k}}(\vec{G}) = \frac{1}{\Omega} \sum_m c_{i,m}^*(\vec{k}) c_{i,m''}(\vec{k}) \quad , \quad (2.38)$$

where m'' denotes the \vec{G} for which $\vec{G}_{m''} = \vec{G}_m + \vec{G}$. To compute the electron density in Fourier space is computationally expensive, hence it is usually transformed into real space by Fast Fourier Transform (FFT) methods and calculated in real space. Another advantage of the calculation of the electron density in real space is that it can be used to evaluate the exchange-correlation energy.

In summary, by introducing a plane wave basis set, the third diagram in the self-consistency flow chart (Figure 2.2) is changed to "Solve KS equations in G-space".

2.1.5 Localized basis and mixed basis

An alternative way of constructing the wavefunctions is to employ localized basis sets. Localized orbitals provide an intuitive description of the electronic structure and chemical bonding. They are widely used in chemistry and have become popular in recent years in physics for their efficiency in large-scale DFT simulations.

A local orbital basis is a set of orbitals $\chi_{\alpha,\kappa}(r - \vec{\tau}_{\kappa,j} - \vec{R})$ associated with atom j of atomic species κ at position $\vec{\tau}_{\kappa,j} - \vec{R}$ (\vec{R} is a Bravais lattice vector). For a given

atomic type κ , χ_α can be written as a product of radial functions and spherical harmonics,

$$\chi_{n,l,m}(r, \theta, \varphi) = \chi_{n,l} Y_{l,m}(\theta, \varphi) \quad , \quad (2.39)$$

where the quantum numbers $(n, l, m) \equiv \alpha$. Consider a state in the cell at the origin and a state in the cell at the lattice vector \vec{R} , the matrix elements of the Hamiltonian with respect to these orbitals read,

$$H_{\alpha\kappa j, \alpha' \kappa' j'}(\vec{R}) \equiv \int d^3\vec{r} \chi_{\alpha,\kappa}^*(\vec{r} - \vec{\tau}_{\kappa,j}) H \chi_{\alpha',\kappa'}(\vec{r} - \vec{\tau}_{\kappa',j'} - \vec{R}) \quad . \quad (2.40)$$

Similarly, the overlap matrix is given by

$$S_{\alpha\kappa j, \alpha' \kappa' j'}(\vec{R}) \equiv \int d^3\vec{r} \chi_{\alpha,\kappa}^*(\vec{r} - \vec{\tau}_{\kappa,j}) \chi_{\alpha',\kappa'}(\vec{r} - \vec{\tau}_{\kappa',j'} - \vec{R}) \quad . \quad (2.41)$$

The matrix elements of S and H can be divided into one-, two-, three-, four-center terms and beyond.

Two types of basis functions are widely used, namely, Slater Type Orbitals (STOs) and Gaussian Type Orbitals (GTOs). They are given in the forms,

$$\chi_{\varsigma,n,l,m}(r, \theta, \varphi) = N Y_{l,m}(\theta, \varphi) r^{n-1} e^{-\varsigma r} \quad \text{STOs} \quad , \quad (2.42)$$

and

$$\chi_{\varsigma,n,l,m}(r, \theta, \varphi) = N Y_{l,m}(\theta, \varphi) r^{2n-2-l} e^{-\varsigma r^2} \quad \text{GTOs} \quad , \quad (2.43)$$

where the ς denotes the range of the orbitals. GTOs are more desirable for calculations due to the huge advantage that all the multi-center integrals can be performed analytically, which stems from the Gaussian product theorem, stating that the product of two Gaussian orbitals centered on different atoms is also a Gaussian orbital (page 300 Ref. [65]).

Mixed basis methods utilize a combination of localized and delocalized bases, e.g. localized Gaussian orbitals and plane waves. The hybrid Gaussian and plane waves (GPW) method [103] provides an efficient way to treat the non-linearly scaling terms (with respect to the system size, e.g. the Hartree energy) at a significantly reduced cost.

In the GPW scheme, a plane wave basis set is used for the electron density, which allows to calculate the Hartree energy easily and efficiently, and the Gaussian basis

sets are used to expand the Kohn-Sham orbitals and compute the kinetic and potential energy. Due to the localized nature of the Gaussian orbitals, the representations of the overlap and density matrix become sparse with increasing system size, which, in principal, leads to a linear scaling for solving the Kohn-Sham equations. A successful GPW scheme has been implemented in the DFT code QUICKSTEP as a part of the package CP2K [104, 105].

2.1.6 Pseudopotentials

In this section we introduce *ab initio* pseudopotentials, which are crucial for practical DFT calculations. As introduced above, a plane wave basis set is very useful to describe the eigenstates of a periodic crystal system -- the Bloch states. However, when approaching the nuclei regions, the Bloch wavefunctions oscillate very rapidly and therefore a very large number of plane waves is needed to provide accurate descriptions, which makes the calculations impractical. To overcome this issue, several methods have been developed, e.g. pseudopotentials and augmented plane waves. In the pseudopotential method, only valence electrons are considered explicitly in the Hamiltonian and the original potential acting on the valence electrons is replaced with a smooth "pseudo" potential. The pseudopotential contains the average effects produced by the nucleus and the tightly bound core electrons. Augmented plane waves methods, on the other hand, constitute a new basis set that efficiently describes the rapidly varying parts of the Bloch states near the nuclei and the smoothly varying parts outside the nuclear region. Both core electrons and valence electrons are considered in this case. Compared to the pseudopotential method, the augmentation method is generally more accurate, but also computationally more demanding. Since the pseudopotential method is by far the most widely used method in DFT codes, here we mainly focus on this method. For more information about the augmentation methods, please refer to Chaps 16, 17 of Ref. [65].

Ab initio pseudopotentials are widely used because they are accurate, smooth, transferable and can be used in many different chemical environments. They are based on the frozen core approximation. A pseudopotential is generated by performing a

DFT calculation for an isolated atom, where the so called all electron (AE) solution to the Kohn-Sham equations needs to be found. From (2.12) and (2.21), we have

$$-\frac{\hbar}{2m_e}\nabla^2\varphi_i(\vec{r}) + v_s(\vec{r})\varphi_i(\vec{r}) = \varepsilon_i\varphi_i(\vec{r})$$

$$v_s(\vec{r}) = -\frac{Z}{r} + v_H[\rho] + v_{xc}([\rho], \vec{r}) \quad . \quad (2.44)$$

If we assume the effective potential v_s is rotationally invariant, the wavefunctions can be separated into radial functions and spherical harmonics,

$$\varphi(\vec{r}) = R_{n,l}(r)Y_{l,m}(\theta, \varphi) \quad . \quad (2.45)$$

By inserting (2.45) into (2.44), we obtain,

$$\left(-\frac{\hbar^2}{2m_e}\frac{d^2}{dr^2} + \frac{l(l+1)\hbar^2}{2m_er^2} + v_s(r)\right)rR_{n,l}(r) = \varepsilon_{n,l}rR_{n,l}(r) \quad , \quad (2.46)$$

where n is the principal quantum number and l is the angular momentum. For a many-electrons atom, the states with the same n and l are not degenerate due to the screening effect of the electrons. If a wavefunction reaches zero and changes its sign at some point, the point is termed as a node of the wavefunction. In general, a radial wavefunction $R_{n,l}$ has $n-l-1$ nodes and radial orbitals corresponding to 1s, 2p, 3d, 4f ... are thus nodeless.

Now we need to introduce a cutoff radius r_c and replace the original radial wavefunction of the valence electrons $R_{n,l}^{AE}$ with a smoother, pseudized and normalized radial wavefunction $R_{n,l}^{PS}$. The pseudo radial wavefunction should fulfill the following properties:

- real and pseudo eigenvalues ε_l agree;
- real and pseudo wavefunctions coincide for $r \geq r_c$;
- the pseudo wavefunction is chosen to be smooth and nodeless for $r < r_c$;

There is still considerable freedom in choosing the form of $R_{n,l}^{PS}$ within the cutoff radius, however, it is important to make $R_{n,l}^{PS}$ satisfy the norm-conserving (NC) condition,

$$Q_l \equiv \int_0^{r_c} dr r^2 R_{n,l}^{PS}(r)^2 = \int_0^{r_c} dr r^2 R_{n,l}^{AE}(r)^2 \quad . \quad (2.47)$$

which leads to transferability of the resulting pseudopotentials. The norm-conserving condition also ensures that the resulting pseudopotential is able to reproduce the scattering properties of the real potential at energies around $\varepsilon_{n,l}$. As regards the cutoff radius, a balance needs to be reached, i.e. a large r_c is desirable to keep the pseudopotential smooth, however, r_c should be small enough to describe the region near the nuclei accurately.

Now we construct the pseudopotential $v_{n,l}^{PS}$ by inverting the radial Schrödinger for each $R_{n,l}^{PS}$:

$$v_{n,l}^{PS,scr} = \varepsilon_{n,l} - \frac{l(l+1)\hbar^2}{2m_e r^2} + \frac{\hbar^2}{2m_e} \frac{1}{r R_{n,l}^{PS}(r)} \frac{d^2}{dr^2} [r R_{n,l}^{PS}(r)] \quad (2.48)$$

This pseudopotential is smooth and does not have singularities, since $R_{n,l}^{PS}$ is smooth and nodeless. Moreover, the pseudopotential is continuous if $R_{n,l}^{PS}$ is chosen to have continuous derivatives up to the second order. Since the screening effects of the valence electrons are included in $v_{n,l}^{PS,scr}$, the pseudopotential needs to be unscreened. To achieve it, one subtracts the Hartree and the exchange-correlation potentials due to the valence electrons in their pseudo radial wavefunctions $R_{n,l}^{PS}$,

$$v_{n,l}^{PS}(r) = v_{n,l}^{PS,scr}(r) - v_{H,valence}^{PS}(r) - v_{xc,valence}^{PS}(r) \quad (2.49)$$

To solve this equation is not trivial due to the non-linearity of the v_{xc} term: additional corrections and approximations are needed. Anyway, after properly treating this equation, we obtain the unscreened, ionic pseudopotentials $v_{n,l}^{PS}$ within the frozen core-electron approximation. Since the pseudopotentials depend on the angular momentum l , the total pseudopotential is a semi-local operator, i.e. local in the radial variable and non-local in the angular variables. The Schrödinger equation (2.12) can be written as,

$$\left(-\frac{\hbar}{2m_e} \nabla^2 + v_{local}^{PS} + v_{non-local}^{PS}\right) \varphi_s^{PS} = \varepsilon_s \varphi_s^{PS} \quad (2.50)$$

There are a number of popular norm-conserving pseudopotentials, e.g. Bachelet, Hamann and Schlüter (BHS) [106], Vanderbilt [107], Rappe, Rabe, Kaxiras and

Joannopoulos (RRKJ) [108], Troullier and Martins (TM) [109] and so on. Besides norm-conserving pseudopotentials, there exist two other successful schemes, namely, ultrasoft pseudopotentials [110] and the projector augmented wave method [111].

2.2 *Ab initio* molecular dynamics

So far we have assumed nuclei are fixed and focused on the ground state electronic properties in the static external potential generated by the nuclei. If one wants to consider nuclear motions, e.g. to investigate finite temperature effects, more sophisticated methods are needed. An effective approach is to combine DFT electronic structure calculations with molecular dynamics simulations -- so called *ab initio* molecular dynamics or first principles molecular dynamics.

Ab initio molecular dynamics (AIMD) simulations, pioneered by Car and Parrinello in 1985 [72], have led to a revolution in the field of computational physics. Accurate forces can be derived from electronic structure calculations and used to determine the thermal motion of real, complex molecules, solids and liquids. Dynamical properties can be derived from AIMD. The Car-Parrinello method marks the beginning of the AIMD era with a unified algorithm for electrons and ions. A conceptually simpler scheme, the Born-Oppenheimer method, became popular several years later [112].

In this section, we introduce the basic assumption behind these methods, i.e. the Born-Oppenheimer or adiabatic approximation. Together with the Hellman-Feynman theorem for the force evaluations and Newton's laws of motion, we obtain the framework of the Born-Oppenheimer method. We also discuss the Car-Parrinello method, which involves simultaneous solutions of the classical nuclear motion and a fictitious electronic dynamics. At last, we introduce some recent developments of the Car-Parrinello method.

2.2.1 Born-Oppenheimer approximation and nuclear motions

The Hamiltonian of the nuclei and electrons can be written as,

$$\hat{H} = -\sum_{i=1}^N \frac{\hbar^2}{2m_e} \nabla^2 + \frac{1}{2} \sum_{i \neq j} \frac{e^2}{|\vec{r}_i - \vec{r}_j|} - \sum_{i,l} \frac{Z_l e^2}{|\vec{r}_i - \vec{R}_l|} - \sum_l \frac{\hbar^2}{2M_l} \nabla^2 + \frac{1}{2} \sum_{l \neq j} \frac{Z_l Z_j e^2}{|\vec{R}_l - \vec{R}_j|}, \quad (2.51)$$

where the lower and upper case in the subscripts denote electrons and nuclei, respectively. Z_I and M_I denote the charge and mass of the nuclei. Since the mass of the nuclei is much larger than the mass of the electrons, the kinetic energy of the nuclei can be ignored., and the Hamiltonian for the electrons can be solved as a function of the nuclear coordinates (on which the Hamiltonian depends parametrically). This is known as the Born-Oppenheimer approximation or the adiabatic approximation. For each nuclear configuration, the interaction between the (fixed) nuclei E_{II} (the last term of (2.51)) is easy to compute. The difficulty lies in the solution of the many-body Hamiltonian for the electrons. In AIMD, this problem is solved using the Kohn-Sham scheme discussed above.

Furthermore, the nuclei are considered as classical objects, following Newton's equations. The challenge is to describe the potential energy and the forces acting on the nuclei accurately, which includes the contributions from both the interaction between nuclei and the electronic ground state energy. Hellman-Feynman theorem [113] is used to evaluate these forces from the electronic ground state energies.

$$\begin{aligned}\vec{F}_\alpha &= -\frac{\partial E}{\partial \vec{R}_\alpha} = -\frac{\partial}{\partial \vec{R}_\alpha} \langle \Phi_{GS} | \hat{H} | \Phi_{GS} \rangle - \frac{\partial E_{II}}{\partial \vec{R}_\alpha} \\ &= -\left\langle \frac{\partial \Phi_{GS}}{\partial \vec{R}_\alpha} \right| \hat{H} | \Phi_{GS} \rangle - \left\langle \Phi_{GS} \right| \hat{H} \left| \frac{\partial \Phi_{GS}}{\partial \vec{R}_\alpha} \right\rangle - \left\langle \Phi_{GS} \right| \frac{\partial \hat{H}}{\partial \vec{R}_\alpha} | \Phi_{GS} \rangle - \frac{\partial E_{II}}{\partial \vec{R}_\alpha} .\end{aligned}\quad (2.52)$$

Since in the ground state Φ_{GS} the energy is extremal with respect to all possible variations of the wavefunction, the first two terms vanish, leading to

$$\vec{F}_\alpha = -\left\langle \Phi_{GS} \right| \frac{\partial \hat{H}}{\partial \vec{R}_\alpha} | \Phi_{GS} \rangle - \frac{\partial E_{II}}{\partial \vec{R}_\alpha} .\quad (2.53)$$

With the obtained forces, the nuclei move according to Newton's law. Usually, the Verlet algorithm is used to integrate Newton's equation of motion in molecular dynamics simulations:

$$\vec{R}_I(t + \Delta t) = 2\vec{R}_I(t) - \vec{R}_I(t - \Delta t) + \frac{\vec{F}_I(t)}{M_I} \Delta t^2 ,\quad (2.54)$$

where Δt is the time step.

This *ab initio* molecular dynamics scheme is called Born-Oppenheimer molecular dynamics (BOMD). At each MD step, a full self-consistent solution of the electronic Schrödinger equation needs to be reached. BOMD was not very efficient in the past

due to the time consuming minimization of the Kohn-Sham functionals. Some advanced algorithms have been developed to overcome this issue, e.g. conjugate-gradient methods [114,115], so that the Born-Oppenheimer method has become competitive to the Car-Parrinello method discussed in the next section.

2.2.2 Car-Parrinello method

Car-Parrinello molecular dynamics (CPMD) does not require the self-consistent solution of the Kohn-Sham equations at every MD step. After reaching the true electronic ground state at the very beginning, the electronic wavefunctions will stay close to the ground state during the time evolution, if certain criteria are fulfilled. Also, there is no need to calculate forces with very high accuracy at each MD step after initialization. These advantages made CPMD the method of choice for many years.

Car-Parrinello method is achieved by introducing a fictitious dynamics for the electronic coefficients. If we expand the Kohn-Sham orbitals $\varphi_i(\vec{r})$ in a suitable basis set, e.g. a normalized plane-wave basis set,

$$\varphi_i = \sum_{\vec{G}} c_{i,\vec{G}} e^{i\vec{G} \cdot \vec{r}} , \quad (2.55)$$

the Kohn-Sham functional E_{KS} becomes a functional of the coefficients $c_{i,\vec{G}}$. The ground state energy can be obtained by minimizing E_{KS} with respect to $c_{i,\vec{G}}$. Instead of diagonalizing the Kohn-Sham Hamiltonian matrix iteratively, another optimization technique, the so called "simulated annealing" [116], can be applied, and the Kohn-Sham functional is minimized by solving a fictitious equation of motion for $c_{i,\vec{G}}$:

$$\mu \frac{d^2}{dt^2} c_{i,\vec{G}} = - \frac{\partial E_{KS}}{\partial c_{i,\vec{G}}^*} + \sum_j \lambda_{i,j} c_{j,\vec{G}} , \quad (2.56)$$

where μ is a fictitious electronic mass (mass times squared length as units) and $\lambda_{i,j}$ is Lagrange multipliers (which enforce the wavefunction orthonormality). In this way, the electronic system has an additional fictitious kinetic energy (due to the fictitious velocities $\dot{c}_{i,\vec{G}}$), which can assist the system to overcome the surrounding barriers. In

principle, by gradually reducing the fictitious temperature, the system can find its global minimum.

To unify this fictitious motion with the real motion of nuclei, we need to consider the contributions from nuclei, $E = E_{KS}(\{c_{i,\vec{G}}\}, \{\vec{R}_I\}) + E_{II}(\{\vec{R}_I\})$,

$$M_I \frac{d^2}{dt^2} \vec{R}_I = - \frac{\partial E}{\partial \vec{R}_I} , \quad (2.57)$$

$$\mu \frac{d^2}{dt^2} c_{i,\vec{G}} = - \frac{\partial E}{\partial c_{i,\vec{G}}^*} + \sum_j \lambda_{i,j} c_{j,\vec{G}} , \quad (2.58)$$

with $\frac{\partial E}{\partial c_{i,\vec{G}}^*} = \sum_{\vec{G}'} H_{\vec{G}\vec{G}'}$. Equations (2.57) and (2.58) are called Car-Parrinello equations of motion. The motions of the nuclei are generally different from BOMD, but will remain close to the BO ones by keeping the fictitious kinetic energy (or temperature) small enough during the whole simulation. Very importantly, the initial wavefunction must be fully optimized at the very first MD step. To keep the electronic subsystem close to the exact Born-Oppenheimer surface, it is very important to prevent any possible energy exchange from the "hot nuclei" to the "cold electrons" upon time evolution. This can be achieved if the system has a finite energy gap and the fictitious mass is sufficiently small. In the limit of small deviations from the ground state minimum, the electronic dynamics can be viewed as a superposition of harmonic oscillations. It has been shown by Pastore *et al.* [117] that the electronic frequencies are given by,

$$\omega_{i,j}^{(1)} \sim (f_j(\varepsilon_i^* - \varepsilon_j)/\mu)^{1/2} , \quad (2.59)$$

$$\omega_{i,j}^{(2)} \sim ((f_i - f_j)(\varepsilon_i - \varepsilon_j)/2\mu)^{1/2} , \quad (2.60)$$

where ε_i^* indicates the eigenvalue of the i -th unoccupied state and ε_j the eigenvalue of the j -th occupied state, and f_i, f_j are the occupation numbers. If the system has a finite band gap, one can tune the fictitious mass μ , so as to make the electronic frequencies sufficiently large. In fact, if the electronic frequencies are much larger than the highest vibrational frequency of the nuclei, ω_I^{max} , the electronic and ionic motions are decoupled. There is one drawback: the larger the electronic frequency, the smaller the time step size. Hence, the typical time steps of CPMD are one order of magnitude smaller than those of BOMD. The time step size of CPMD can be

significantly improved in the second generation Car-Parrinello method [118] (see next subsection). Another drawback of CPMD is the difficulty in dealing with metallic systems, where no band gap exists. By employing two different thermostats for ionic and electronic subsystems, one can overcome this issue [119].

At last, the Car-Parrinello equations of motion can be integrated with the Verlet algorithm:

$$c_{i,\vec{G}}(t + \Delta t) = 2c_{i,\vec{G}}(t) - c_{i,\vec{G}}(t - \Delta t) - \frac{\Delta t^2}{\mu} [\sum_{\vec{G}'} H_{\vec{G}\vec{G}'} c_{i,\vec{G}'}(t) - \sum_j \lambda_{ij} c_{j,\vec{G}}(t)], \quad (2.61)$$

$$\vec{R}_I(t + \Delta t) = 2\vec{R}_I(t) - \vec{R}_I(t - \Delta t) + \frac{\Delta t^2}{M_I} \vec{F}(t) . \quad (2.62)$$

2.2.3 Recent developments of Car-Parrinello method

It is very desirable to extend *ab initio* molecular dynamics simulations up to thousands of atoms (few nanometers system size) and long simulation times (few nanoseconds) to access new phenomena. BOMD provides large time step intervals but requires full minimization of the Kohn-Sham functionals at each time step. CPMD does not require such full minimization but is limited by short integration time steps. In 2007, Kühne *et al.* [118] developed a promising algorithm that combines the advantages from both BOMD and CPMD. The method is often called "Second generation Car-Parrinello method".

Similar to the Car-Parrinello scheme, a propagation of the electronic degrees of freedom is used instead of a self-consistent diagonalization of the Kohn-Sham matrix. However, the method employs a predictor-corrector scheme to propagate the electronic coefficients, instead of solving Car-Parrinello equations of motion. The authors have chosen the always stable predictor corrector (ASPC) method, firstly introduced by Kolafa [120], for the propagation, which enables long integration time steps comparable to BOMD. Up to now, Kühne's method has been successfully implemented in the Quickstep code (parts of the CP2K package), where the Kohn-Sham orbitals are expanded in a non-orthogonal Gaussian basis. Considering a $M \times N$ matrix \mathbf{C} with the expansion coefficients of the N lowest occupied orbitals with respect to the M basis functions, the projector and corrector schemes are constructed

as,

$$\mathbf{C}^p(t_n) = \sum_{m=1}^K (-1)^{m+1} m^{\binom{2K}{2K-2}} \mathbf{C}(t_{n-m}) \mathbf{C}^T(t_{n-m}) \mathbf{S}(t_{n-m}) \mathbf{C}(t_{n-1}) , \quad (2.63)$$

$$\mathbf{C}^c(t_n) = \omega \min[\mathbf{C}^p(t_n)] + (1 - \omega) \mathbf{C}^p(t_n) , \quad (2.64)$$

where \mathbf{S} is the $M \times M$ overlap matrix of the basis functions, $\omega = \frac{K}{2K-1}$ ($K \geq 2$), and $\min[\mathbf{C}^p(t_n)]$ is a single minimization step of the Kohn-Sham orbitals. The numerical coefficients of (2.63) are selected in order to ensure time reversibility up to $O(h^{K+2})$ and ω is properly chosen to ensure a stable relaxation towards the minimum. This method is used in combination with the advanced orbital transformation (OT) method developed by VandeVondele and Hutter [121].

In the Kühne's method, the energy functional is constructed as:

$$\begin{aligned} E_{PC}[\rho^p] = & \text{Tr}[\mathbf{C}^T H[\rho^p] \mathbf{C}] - \frac{1}{2} \int d^3\vec{r} \int d^3\vec{r}' \frac{\rho^p(\vec{r}) \rho^p(\vec{r}')}{|\vec{r} - \vec{r}'|} \\ & - \int d^3\vec{r} V_{xc}[\rho^p] \rho^p + E_{xc}[\rho^p] + E_{II} , \end{aligned} \quad (2.65)$$

where ρ^p is the density associated with $\mathbf{C}^p(t_n)$. E_{PC} can be considered as an approximation to the Harris-Foulkes functional [122,123].

The dynamics of the predictor-corrector scheme is dissipative and the force \vec{F}_{PC} can be written as $\vec{F}_{PC} = \vec{F}_{BO} - \gamma_D \frac{d\vec{R}_I}{dt}$, with γ_D the intrinsic friction coefficient. The intrinsic dissipative behavior of the dynamics leads to difficulties in sampling the microcanonical ensemble (NVE--constant Number of particles, Volume and Energy). By carefully tuning the parameters of the method, it is possible to keep the dissipation very small in many cases [118,124]. The method is very useful to sample to the canonical ensemble (NVT--constant Number of particles, Volume and Temperature). Using a Langevin-type equation (Langevin thermostat [66]), the canonical ensemble can be properly sampled:

$$M_I \frac{d^2 \vec{R}_I}{dt^2} = \vec{F}_{PC} - \gamma_L \frac{d\vec{R}_I}{dt} + \mathcal{E}_I = \vec{F}_{BO} - (\gamma_L + \gamma_D) \frac{d\vec{R}_I}{dt} + \mathcal{E}_I , \quad (2.66)$$

where γ_L is an imposed (i.e. non-intrinsic) friction coefficient, and $\mathcal{E}_I = \mathcal{E}_I^D + \mathcal{E}_I^L$ is the total random noise corresponding to the intrinsic and non-intrinsic friction term. The random noise has to obey $\langle \mathcal{E}_I(0) \mathcal{E}_I(t) \rangle = 6(\gamma_L + \gamma_D) M_I k_B T \delta(t)$, in order to sample the Boltzmann distribution.

In this way, the advantages of BOMD (the big integration time step) and CPMD (no self-consistent wave functions optimization at each step) are unified, leading to very high efficiency. Another big advantage of the Kühne's method is that its applicability does not depend on the energy gap of the systems. The method has been proven to be very efficient and accurate in many cases, e.g. liquid water [125], phase change materials [26], etc. Kühne's method yields a factor of 20-30 speedup over conventional BOMD for systems with 200-300 atoms. Thanks to the GPW scheme and the orbital transformation technique, the minimization procedure in the corrector scheme can be performed very efficiently for large system sizes. In fact, this method scales better than standard plane wave based BOMD and CPMD as a function of system size.

2.3 Computational details

Two DFT codes are mainly employed in this thesis, namely, CP2K [105,126] and Quantum Espresso [127,126]. As mentioned before, CP2K is constructed based on a mixed scheme of the Gaussian and plane wave basis sets. In our calculations, the Kohn-Sham orbitals are expanded in Gaussian basis sets of triple-zeta plus polarization quality, and the charge density is expanded in plane waves, with a cutoff of 300 Ry. Scalar-relativistic Goedecker-Teter-Hutter (GTH) pseudopotentials [128] and gradient-corrected functionals (GGA-PBE) [97] are used. The hybrid functional HSE03 [100] is employed for some electronic property calculations. Only Gamma point is used to sample the Brillouin zone, which is sufficient for large supercells. As regards molecular dynamics, Kühne's method is used. All of the AIMD simulations are performed at constant volume (both NVT and NVE) and a stochastic Langevin thermostat is employed for NVT simulations. The change of mass density is achieved externally.

Quantum Espresso is a standard plane wave code. For most of our simulations, scalar-relativistic ultrasoft pseudopotentials [110] are used. In some cases, the full-relativistic corrections are considered for the calculation of spin-orbit coupling

effects. The generalized gradient approximation (PBE) for exchange-correlation potential is used. Both gamma point and the Monkhorst-Pack (MP) mesh [102] are considered for samplings of the Brillouin Zone.

Chapter 3 Crystalline Phase Change Materials

To understand the properties of phase change materials, many aspects need to be considered: the various phases involved in the phase change cycle (crystalline, liquid and amorphous), the kinetic process of amorphization and crystallization, the property contrast, the stability of the solid phases at room temperature, etc. I start with the discussion of the crystalline phase of PCMs, which is an important part of the phase change cycle. Furthermore, this phase is of great interest because some crystalline PCMs possess extraordinary electronic properties, which could lead to multilevel data storage applications and conceptually new devices based on multi-level resistance states [32, 129].

3.1 Overview of crystalline PCMs

Group 1 PCMs: pseudobinary GeTe-Sb₂Te₃ line:

In Figure 3.1, GeTe is depicted. It has a rhombohedral ($R3m$) structure at low temperature, which can be viewed as a rock-salt structure with slight distortion along the $\langle 111 \rangle$ direction, see the left part Figure 3.1. Three short (2.85 Å) and three long (3.28 Å) bonds are formed due to the hybridization between p -type orbitals. This distortion reduces the total energy, opens a band gap and weakens the resonance bonding [19, 20]. It is often referred as Peierls distortion [130]. In the high temperature regime, it is believed that a phase transition to the displacive rock-salt structure ($Fm3m$) occurs (shown in the right part of Figure 3.1), however, this picture has been challenged by recent Extended X-ray Absorption Fine Structure (EXAFS) measurements [131]. The authors argued that the Peierls distortion does not disappear but only becomes invisible in the Bragg-diffraction data from 705 K (Curie temperature) [132] up to the melting temperature, due to the site averaging effects. Interestingly, the Peierls distortion could be detected again by neutron diffractions in liquid GeTe [133]. AIMD simulations should be an appropriate tool to tackle this issue.

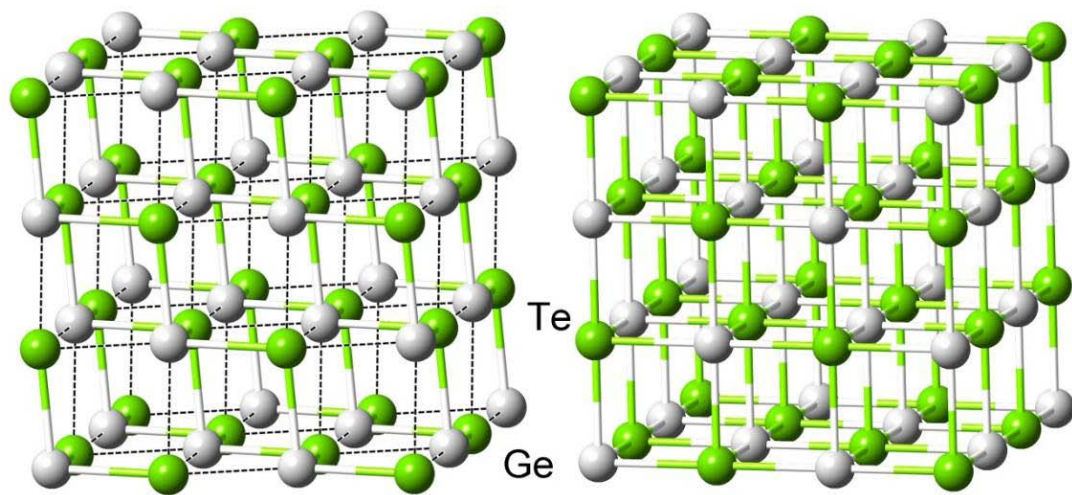


Figure 3.1 The crystal structures of GeTe, rhombohedral (left) and rocksalt (right).

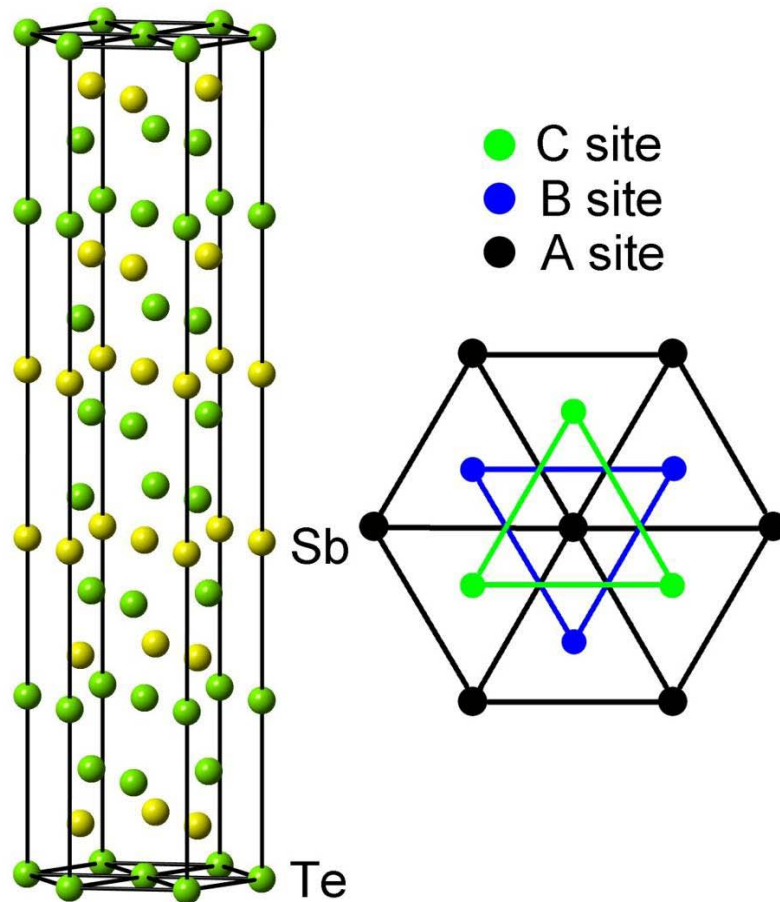


Figure 3.2 The crystal structure of Sb_2Te_3

Sb_2Te_3 has a rhombohedral geometry ($R\bar{3}m$ space group) with five atoms per unit cell [134]. It can be better visualized in the conventional hexagonal supercell with three quintuple layers (15 atoms per unit), shown in Figure 3.2. Each quintuple layer

is separated by a weakly coupled Te-Te layer, where van der Waals forces play a dominant role. The atomic arrangement within each layer is depicted in the right part of Figure 3.2, and the experimental distance a_{hex} between nearest-neighbor atoms within a layer is 4.26 Å [135], suggesting the absence of covalent bonding. The atomic positions on each layer can be categorized into three types: A (0,0,0), B (2/3,1/3,0), C (1/3,2/3,0) in hexagonal units. A, B and C sites alternate along the z-direction.

GeSbTe compounds:

Popular GeSbTe alloys (GST) are $\text{Ge}_2\text{Sb}_2\text{Te}_5$, $\text{Ge}_1\text{Sb}_2\text{Te}_4$, $\text{Ge}_8\text{Sb}_2\text{Te}_{11}$ etc., which are located in the middle part of the GeTe-Sb₂Te₃ pseudobinary line. There are two main crystal forms for GST under ambient pressure, namely, a metastable cubic phase (cub-GST) and a stable hexagonal phase (hex-GST). After rapid crystallization of amorphous samples at elevated temperatures, GST is known to form the cubic phase with Te atoms occupying one sublattice (anion) and Ge/Sb/Vacancies randomly distributing over the other sublattice (cation) (see Figure 3.3). Although cub-GST is metastable (hex-GST is lower in energy), it is thermally stable at room temperature for decades, which is crucial for data storage applications.

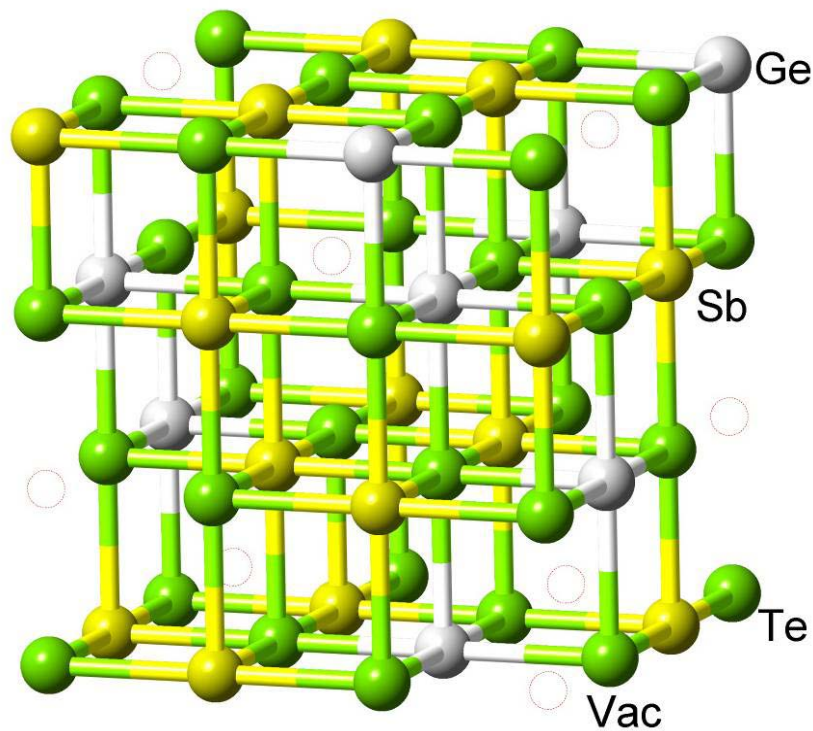


Figure 3.3 The crystal structure of cubic GST

The high amount of atomic vacancies in cub-GST is a generic feature and the underlying mechanism stabilizing these defective configurations has been elucidated by Wuttig *et al.* [10]. By performing ground state DFT calculations, large and negative vacancy formation energies were found by the removal of Ge/Sb atoms from a hypothetical $\text{Ge}_2\text{Sb}_2\text{Te}_4$ alloy. This behavior is strikingly different from that of other compounds like Si, GaAs, where large and positive vacancy formation energies are found. The removal of Te, on the other hand, is energetically very unfavorable. Further, a quantum chemistry analysis COHP (Crystal Orbital Hamilton population) [136,137] provided a good explanation for this finding: the states at and close to the Fermi energy (E_F) are energetically unfavorable antibonding states and are mainly contributed by 'cationic' Ge/Sb atoms; by creating certain amount of atomic vacancies on the cation sublattice, these antibonding states are annihilated and the whole system is therefore stabilized.

Hex-GST is lower in energy than cub-GST and can be obtained upon long thermal annealing of cub-GST at elevated temperatures (many orders of magnitude longer than crystallization times). The stacking sequence of hex-GST has been long debated, in particular for $\text{Ge}_2\text{Sb}_2\text{Te}_5$. The unit cell of $\text{Ge}_2\text{Sb}_2\text{Te}_5$ contains 9 layers and contains two weakly coupled Te layers. Three possible stacking sequences have been proposed, KH [138], Petrov [139] and mixed [140] (visualized in Figure 3.4):

- Te-Ge-Te-Sb-Te-vac-Te-Sb-Te-Ge-(KH),
- Te-Sb-Te-Ge-Te-vac-Te-Ge-Te-Sb-(Petrov),
- Te-Ge/Sb-Te-Ge/sb-Te-vac-Te-Ge/Sb-Te-Ge/Sb-(mixed).

Using the experimental lattice parameters $a_{\text{hex}} = 4.25 \text{ \AA}$, $c = 17.27 \text{ \AA}$ [140], the KH sequence is found to be the most energetically favorable sequence, although the energy difference between the three sequences is not big [141].

For hex- $\text{Ge}_1\text{Sb}_2\text{Te}_4$, the periodicity is 21:

- Te-Ge-Te-Sb-Te-vac-Te-Sb-Te-Ge-Te-Sb-Te-vac-Te-Sb-Te-Ge-Te-Sb-Te-vac-Te-Sb-.

A disordered phase with random Ge/Sb occupation is also possible; actually, it is not easy to obtain a chemically ordered phase experimentally: for this purpose, very long thermal annealing at very high annealing temperature is necessary [142].

Regarding GeTe-rich GST alloys, such as $\text{Ge}_8\text{Sb}_2\text{Te}_{11}$, it is very difficult to obtain the hexagonal phase experimentally. More information can be found in Ref [143].

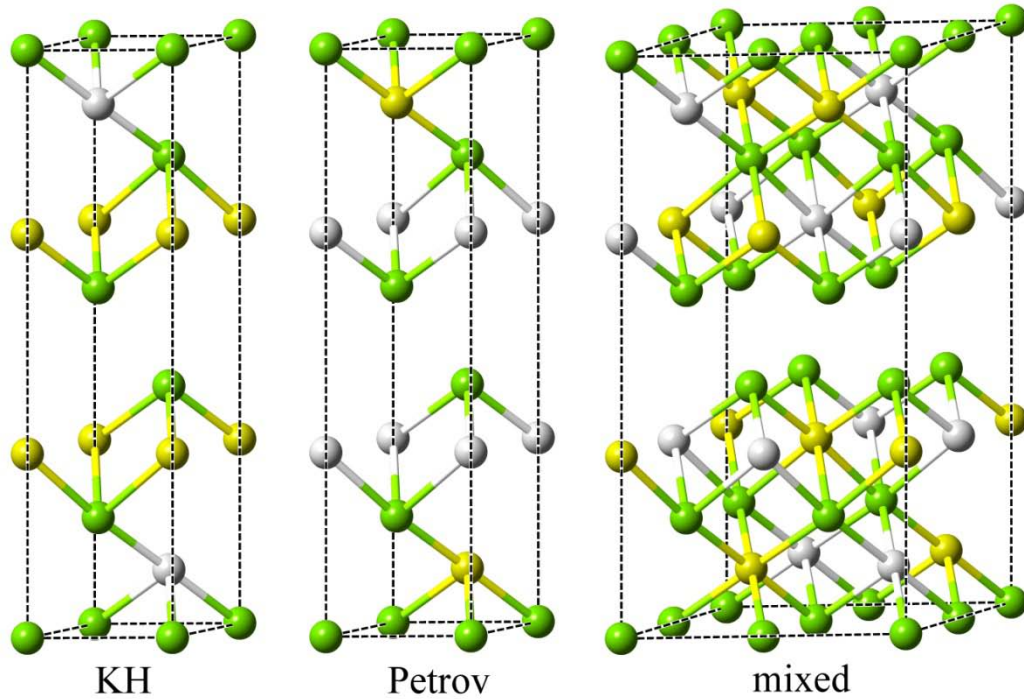


Figure 3.4 The crystal structures of hexagonal $\text{Ge}_2\text{Sb}_2\text{Te}_5$. Ge, Sb and Te atoms are rendered with grey, yellow and green spheres.

Besides these two crystalline forms, layered superlattice-like structures, such as interfacial PCMs [28], cubic superstructures [144] and other layered-like superlattices [145], have been synthesized for GST under different experimental conditions. Under very high pressure (15 Gpa), GST can transform into a bcc phase with high coordination number 8 [146,147]. A very recent theoretical work predicts another type of bcc phase under high pressure [148].

Group 2 and group 3 PCMs:

The parent phases of these two groups of PCMs are, respectively, a) Sb-Te compounds near the Sb_2Te_3 composition and b) pure Sb. Both systems have to be doped to raise their crystallization temperature (which, for Sb_2Te_3 , is 103 °C; for Sb, it is below 30 °C). Their crystalline structures are shown in the left part of Figures 3.5 and 3.6. Sb_2Te_3 has a trigonal structure with the symmetry $P-3m1$ [149]. It consists of periodically repeated nonuple layers, which can be viewed as a combination of one

Sb_2Te_3 quintuple slab and 4 layers of pure Sb. The atomic distribution on each layer is similar to that of Sb_2Te_3 with $a_{\text{hex}} = 4.272 \text{ \AA}$, however, no weakly coupled layers are found in this case. Pure Sb also has a trigonal cell with the periodicity of six, known as A7 structure, with $a_{\text{hex}} = 4.307 \text{ \AA}$.

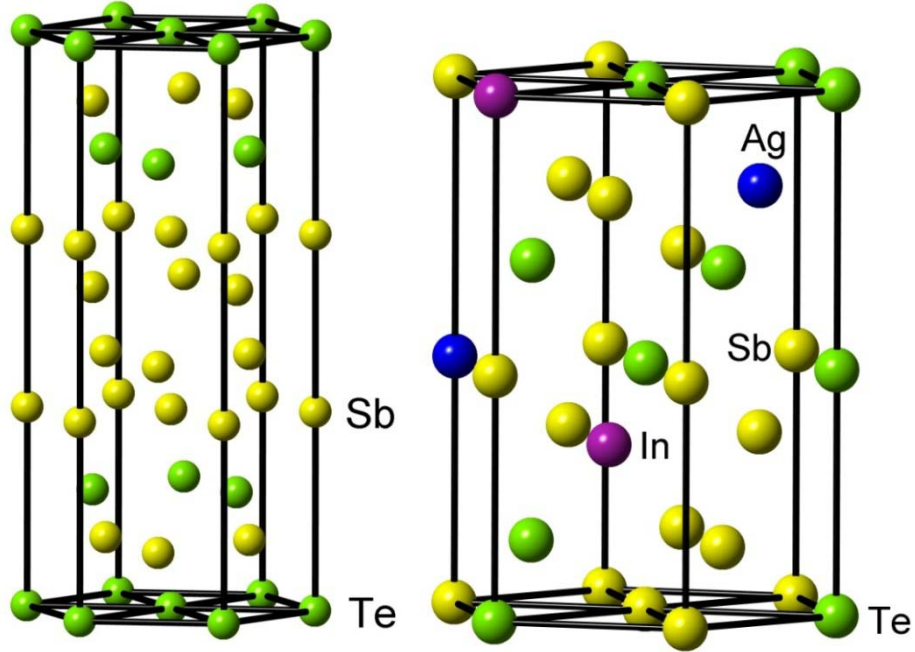


Figure 3.5 The crystal structures of Sb_2Te and AIST

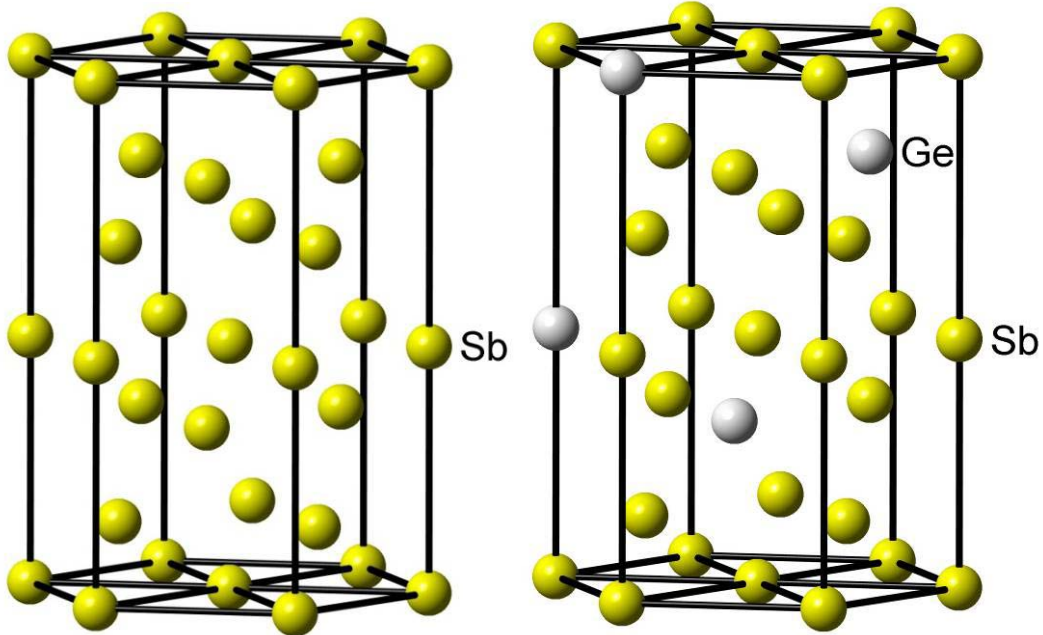


Figure 3.6 The crystal structures of pure Sb and $\text{Ge}_{15}\text{Sb}_{85}$

By introducing a few percentages of dopants like Ag, In, Ge, etc. into the system, both systems (after crystallization from the amorphous phase) form an A7 like structure, where the different types of atoms are randomly distributed over the crystalline lattice [43,150], as sketched in the right part of Figures 3.3 and 3.4. The most representative group 2 and 3 PCM are AIST and $\text{Ge}_{15}\text{Sb}_{85}$.

Unconventional PCM $\text{In}_3\text{Sb}_1\text{Te}_2$:

Compared to all the PCMs mentioned above, which roughly possess 3 valence p electrons per atom/site on average, $\text{In}_3\text{Sb}_1\text{Te}_2$ is rather unconventional, in that it has only 2.3 valence p electrons per atom. The crystalline phase is rock-salt: In atoms take one sublattice, while Sb and Te atoms randomly occupy the other sublattice in this compound. This phase is shown in Figure 3.7.

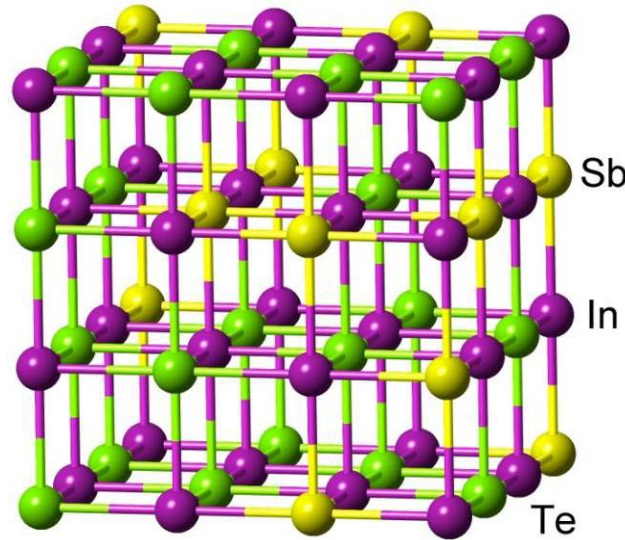


Figure 3.7 The crystal structure of $\text{In}_3\text{Sb}_1\text{Te}_2$

The density of PCMs mentioned above is summarized in appendix A.

3.2 Charge transport and metal insulator transition

To understand and tailor charge transport in crystalline solids is a very important challenge for physics, materials science and engineering. The electrical resistivity serves as a key parameter to characterize solids with different transport properties. Two different types of solids can be defined: metals and insulators. In the limit of zero

temperature, a metallic solid possesses a finite resistivity, while the resistivity of an insulating solid diverges. The temperature coefficient of the resistivity $d\rho/dT$ (TCR), is also often used to distinguish between metallic ($d\rho/dT > 0$) and insulating ($d\rho/dT < 0$) solids in experiments.

Studying solids that undergo a Metal-Insulator-Transition (MIT) is a very interesting topic. Besides MITs induced by crystallographic transformations, two well-known mechanisms can lead to such transitions, namely Anderson localization [151] and Mott transition [152]. According to Anderson, strong disorder can localize electronic states at the Fermi energy (E_F), which triggers the transition to an insulating state. Mott instead emphasized the role of electron correlations: if the correlation energy exceeds the Fermi energy, a MIT occurs.

These two concepts differ significantly from the theoretical point of view, however, in practice, it is very challenging to separate them experimentally. Doped crystalline semiconductors, in particular phosphorus doped silicon [153,154,155], have been a rich playground to study electronically driven MITs. By doping silicon with one phosphorus atom, the system gains one more p electron, which is localized around the phosphorus atom with a large localization length (~ 5 Å). If the concentration of P atoms is small, the system is an insulator due to the localization of the excess electrons. The gradual increase in the concentration of the phosphorus atoms eventually changes the behavior of the system from insulating to metallic. This MIT can partially be explained by the Mott mechanism, i.e. the increase of carrier concentration reduces the difference between electron-correlation and Fermi-energy. However, disorder effects due to the random distribution of phosphorus atoms cannot be ignored.

Many theoretical methods have been developed to gain an understanding of MITs, both Mott type [156,157,158] and Anderson type [159,160,161,162] MITs. Most of them are based on model systems, owing to the challenges in modeling real solids. Density functional theory can describe the structural and electronic properties of real solids accurately, thus it can be a very appropriate platform to study MITs. However, to model the full insulating to metallic transition in doped semiconductors like P

doped Si, several hundreds of thousands of atoms are needed, due to the relatively low critical carrier concentration, $n_c = 3.8 \times 10^{-18} \text{ cm}^3$, which is beyond the capacity of the present DFT codes. However, this situation may change in the near future, since the development of supercomputers is explosively rapid [61] and DFT codes are already being developed and optimized on peta-scale supercomputers, such as Blue Gene. DFT codes, such as cp2k [104,126] and KKR-Nano [163,164], have the potential to allow investigations of systems containing up to one million atoms.

Recently, T. Siegrist *et al.* have found strong evidence for disorder-induced localization in crystalline GeSbTe compounds by a series of transport measurement [32]. The measurements show that typical carrier concentrations are of the order of $2 \times 10^{-20} \text{ cm}^3$, which corresponds to one charge carrier per 150 atoms. It is highly desirable to study the localization and the subsequent transition to the metallic state using DFT. To capture the essence of localization, models containing several charge carriers are needed, which correspond to a few thousands of atoms. Such system sizes are now feasible for DFT methods. Moreover, unlike doped semiconductors, the MIT in crystalline GeSbTe alloys occurs at a fixed stoichiometry, so that a direct comparison of the total energies before and after the MIT can be made through DFT simulations. A set of models containing different degrees of disorder at the same stoichiometry has been generated and studied by DFT in this thesis. The origin of localization has been identified.

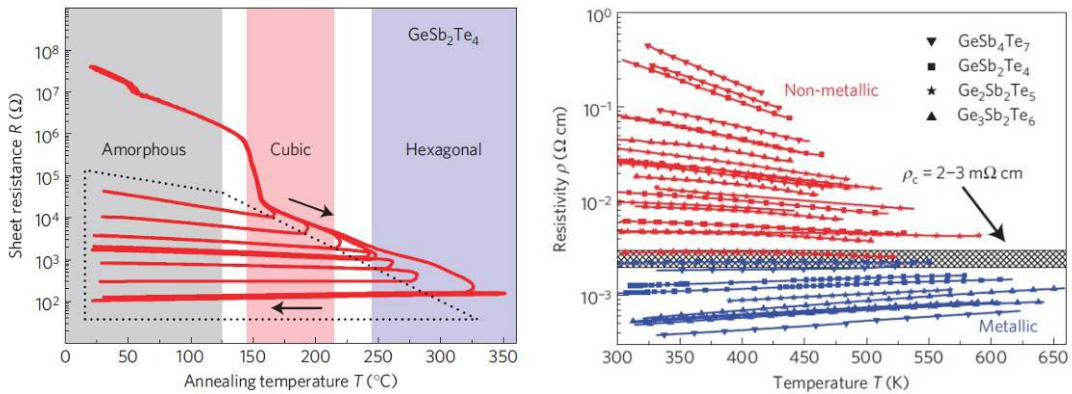


Figure 3.8 Adapted from Ref. [32]. The annealing effects on the sheet resistance of $\text{Ge}_1\text{Sb}_2\text{Te}_4$ is shown in the left figure. In the right figure, the non-metallic to metallic transition region is highlighted, and three other GeSbTe compounds are included.

Before discussing the theoretical findings, the transport experiments are briefly reviewed. In the left part of Figure 3.8, the annealing effect on the resistivity of $\text{Ge}_1\text{Sb}_2\text{Te}_4$ is shown. As-deposited thin-film amorphous $\text{Ge}_1\text{Sb}_2\text{Te}_4$ was heated up to 160 °C, at which the crystallization occurred and the resistivity dropped significantly. The crystallized phase entered the metastable cubic phase, and upon gradually annealing at higher and higher temperatures, the cubic phase was transformed into the stable hexagonal phase. The two crystalline structures have been discussed in the previous section. The resistivity measured at room temperature changed gradually as a function of the annealing temperature. The resistivity of the initial cubic state was almost 3 orders of magnitude larger than that of the final hexagonal state. The low-temperature measurements down to 5 K showed that the sign of the TCR switched from negative to positive upon increasing the annealing temperature, indicating that a MIT took place: the resistivity of insulating samples diverged at low and the resistivity difference with respect to the conducting samples increased to 6 orders of magnitude at $T = 5$ K (see Figure 3.9).

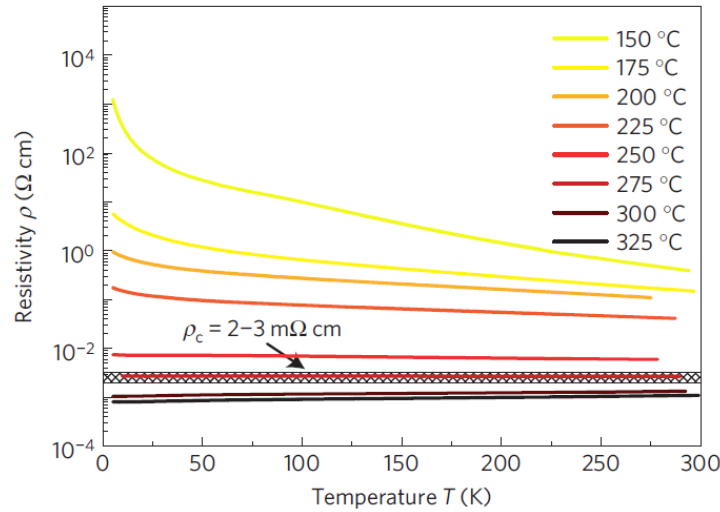


Figure 3.9 Adapted from Ref. [32]. Resistivity measurements of $\text{Ge}_1\text{Sb}_2\text{Te}_4$ films down to 5 K.

Similar transport measurements have been performed for other GeSbTe compounds, namely $\text{Ge}_3\text{Sb}_2\text{Te}_6$, $\text{Ge}_2\text{Sb}_2\text{Te}_5$, $\text{Ge}_1\text{Sb}_4\text{Te}_7$, and all of them showed a MIT upon annealing, see the right part of Figure 3.8. Therefore, such behavior is generic for the

compounds in the middle part of the GeTe-Sb₂Te₃ pseudobinary line.

It turns out that the structural transition from the cubic to the hexagonal state was not the origin for the MIT, since the MIT took place in the hexagonal phase. From Figure 3.8 left, one can observe that the TCR changed its sign at about 275 °C, whereas the crystallographic transition occurred at 225 °C. Combining Hall effect, optical spectroscopy (FTIR and ellipsometry), low-temperature van der Pauw and X-ray diffraction experiments, the charge-carrier density and mobility could be measured. Upon annealing, the carrier density changed only by a factor of 3, whereas the carrier mobility increased by more than a factor of 100. So the change of carrier mobility is expected to be responsible for the pronounced change in the electrical resistivity and for the MIT.

The mean free path λ_c has been determined from the van der Pauw and Hall measurements. At the transition point, λ_c is measured to be 8.6 Å, whereas for the sample obtained by the highest annealing temperature, λ_c is 21.3 Å. Both of them are very small compared to the typical grain size, which is 200 Å. Hence grain boundary effects can be ruled out as the main scattering mechanism here.

So now there are only two possibilities for the MIT, electron correlation (Mott transition) or disorder-induced localization effects (Anderson transition). In GST compounds, such as Ge₁Sb₂Te₄, a very high static dielectric constant ϵ_{st} 98 is found [20], which is the direct consequence of resonant bonding. The high dielectric constants screens the charge-carrier interactions efficiently, in other words, electron correlation effects are very small in crystalline GST. The only possibility left is the disorder-induced localization.

3.3 Theoretical modeling of Anderson localization

In crystalline GST, there are various sources of disorders: a high amount of randomly distributed vacancies, local atomic distortions, compositional disorders, grain boundaries, etc. In collaboration with Thiess *et al.*, we have clarified the role of

the different sources of disorders and we have identified the origin of localization by employing very large scale DFT simulations [163].

3.3.1 The origin of localization -- vacancy clustering

I start with the discussion of the cubic phase, where the model is fully disordered, despite the fact that MIT is demonstrated to occur in the hexagonal phase by experiments. Later we will prove that the underlying mechanism of localization is the same for both phases. As mentioned previously, the grain size is of the order of 200 Å for cubic $\text{Ge}_1\text{Sb}_2\text{Te}_4$, while the electron mean free path is shown to be of the order of 10 Å, indicating that the lattice disorder is much more important than grain boundaries in inducing localization.

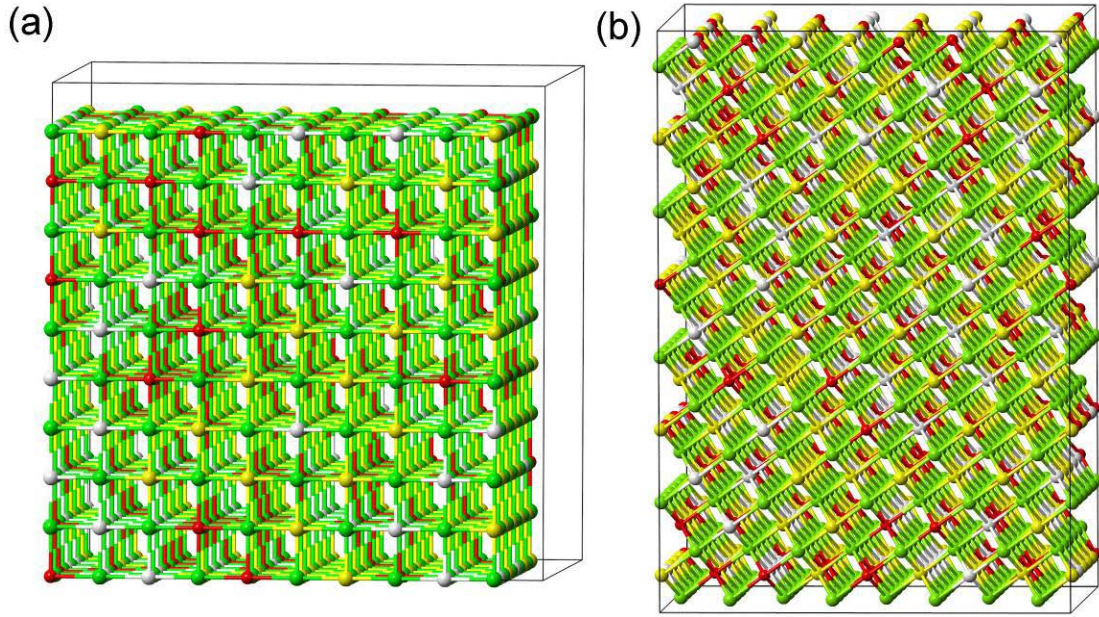


Figure 3.10 Metastable cubic $\text{Ge}_1\text{Sb}_2\text{Te}_4$ built in (a) a conventional cubic lattice and (b) an orthorhombic supercell with its z-axis parallel to the (111)-direction of (a). Ge, Sb, the atoms and Vac sites are rendered with grey, yellow, green and red spheres.

We consider models of GST containing 1000-4000 atomic sites, which are sufficiently large to observe electron localization. If smaller models were employed, with supercell parameters comparable to the typical electron localization lengths, the relevant electron wavefunctions would look extended (i.e. spreading over the whole supercell). On the other hand, the localized states can be clearly distinguished from

delocalized states in our supercells. Here we consider two kinds of supercell, namely a conventional cubic supercell, and an orthorhombic supercell with its z -axis parallel to the (111) direction of the cubic supercell. In both cases, the cation sublattice is randomly occupied by Ge/Sb/Vac. The hexagonal supercell has some advantages with respect to the cubic one when studying structural transformations and metal-insulator transitions. The two models are depicted in Figure 3.10.

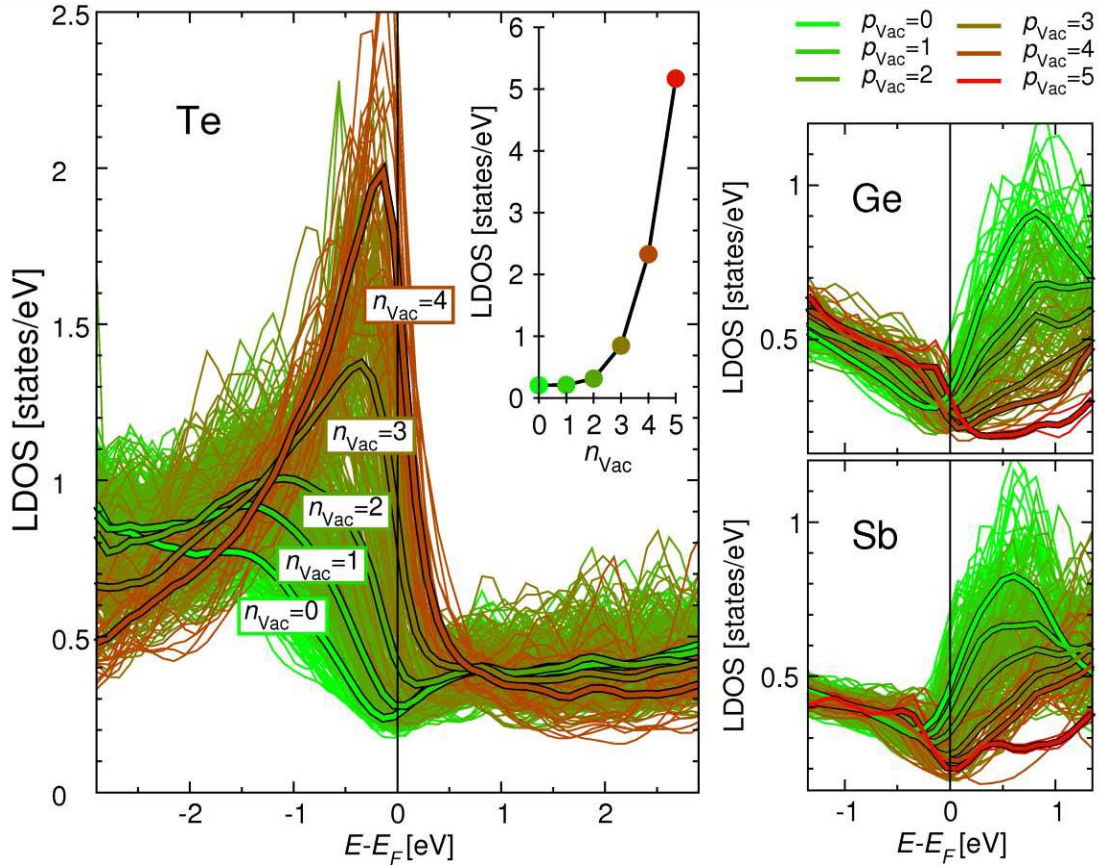


Figure 3.11 The local density of p states on the Te, Ge and Sb sites. Different colors are used to distinguish between (Ge/Sb) Te atoms with different number of (fourth) nearest-neighbor vacancies, $(p_{Vac}) n_{Vac}$. The average LDOS is shown as a thick line in the corresponding color.

In the first step, we only calculate the electronic properties of the models self-consistently, without considering atomic distortions from the ideal lattice sites. It has been shown that p orbitals govern the electronic properties of PCMs at E_F [16], so we focus on the local density of states (LDOS) of p orbitals of each atomic site. From this analysis, we find the LDOS is mostly affected by the distribution of vacancies in

the neighboring shells. The LDOS of Te atoms turns out to be more sensitive to the local vacancy distributions than the LDOS of Ge/Sb, since Te atoms have direct vacant neighbors in the first neighbor shell, whereas Ge/Sb have vacant neighbors at the second neighbor shell. An analysis of s and d states near E_F can be found in [163], where they are shown to be irrelevant for the electron localization.

We define different types of Te atoms by considering the number of vacancies in the first shell, namely, $n_{\text{Vac}}=0,1,\dots,6$. Similarly, for Ge/Sb, the second neighbor shell is considered, $p_{\text{Vac}}=0,1,\dots,6$. The LDOS of each atom and the LDOS averaged over all Te atoms of a given type (thick lines) are shown in Figure 3.11 for a 1000-site model, $\text{Ge}_{125}\text{Sb}_{250}\text{Te}_{500}\text{Vac}_{125}$. A striking dependence of the LDOS of Te atoms with respect to n_{Vac} has been found. The larger the n_{Vac} , the larger the LDOS at and below E_F . For $n_{\text{Vac}}=0$, a minimum of the LDOS around E_F is observed, due to the fact that the p orbitals of Te atoms hybridize with nearby Ge/Sb atoms. However, in the presence of vacancy neighbors, the hybridization is reduced, and the corresponding LDOS of the p orbitals of Te atoms is shifted towards higher energies. The more vacancies are present around a Te atom, the larger the energy shift is. In particular, a pronounced peak appears near E_F for Te atoms with 3 or 4 vacant neighbors. To further quantify this effect and gain better statistics, we plot the averaged LDOS at E_F as a function of n_{Vac} (shown in the inset), based on the 4000 site model $\text{Ge}_{500}\text{Sb}_{1000}\text{Te}_{2000}\text{Vac}_{500}$. The curve clearly reveals the sharp increase of LDOS as n_{Vac} increases. Since the shift in the LDOS peak depends almost exclusively on n_{Vac} , the LDOS can change dramatically from one Te to the next in the real space. In a spatial region with a high amount of vacancy (which we call vacancy cluster later on), many Te atoms have $n_{\text{Vac}}=3$ or 4, thus the LDOS near E_F will be very high inside vacancy clusters. Therefore vacancy clusters are expected to induce spatially localized electronic states near E_F .

The LDOS dependence with respect to vacant neighbors, i.e. the next-nearest neighbor sites m_{Vac} and the fourth nearest neighbor sites p_{Vac} , are much weaker for Ge and Sb atoms. Interestingly, p_{Vac} turns out to have a stronger effect than m_{Vac} due to the strong directional nature of bonding between p states. For Ge and Sb with $p_{\text{Vac}}=0$,

a large peak above E_F is present, which is reduced and shifted to higher energies when p_{Vac} increases. Overall, the effect on the LDOS of Ge and Sb is one order of magnitude smaller as compared to the LDOS of Te sites.

In summary, the shift due to the change of nearby vacancy neighbors affects the occupied peak on Te sites corresponding to bonding states, while on Ge and Sb sites the unoccupied anti-bonding states are shifted. The effect is much more pronounced on Te atoms than Ge, Sb atoms in affecting the electronic properties at E_F , which are responsible for transport properties. Note, the above LDOS analysis is done by A. Thiess using KKR Nano.

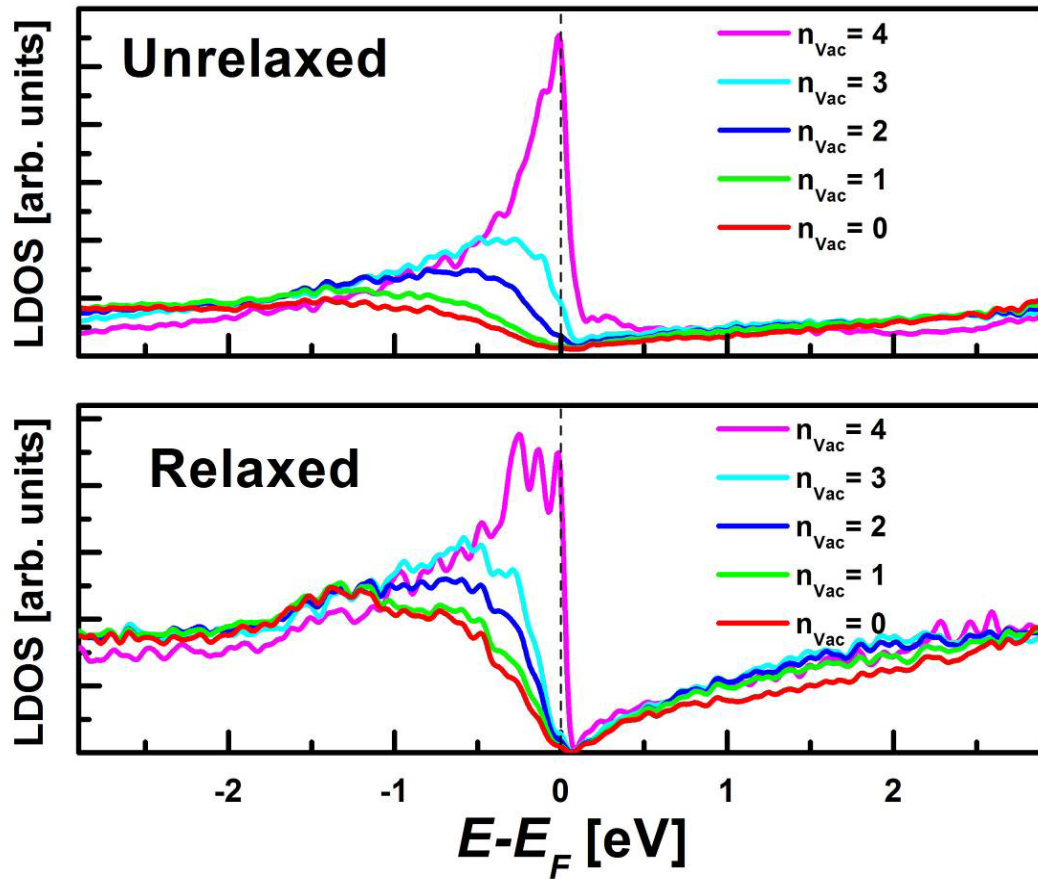


Figure 3.12 The averaged LDOS for Te sites in the disordered cubic phase (denoted Cub-25%), before and after relaxation. LDOS are averaged over all the sites having the same number of nearest neighbor vacancies, n_{Vac} .

Now we consider the effects of atomic relaxation. We switch to the supercell depicted in Figure.3.10 (b), which is more convenient to study the structural transition and the MIT. We relax the atomic positions and calculate the electronic structure of the models with GGA (PBE) functionals using cp2k. The LDOS averaged over atoms with a given n_{vac} is plotted for both the unrelaxed and the relaxed models in Figure 3.12. From (a) we can learn that this model is totally equivalent to the previous one, and also the LDOS trends do not depend on the functional. After atomic relaxations, the LDOS trends with respect to n_{vac} still hold, i.e. the occupied peak of the LDOS below E_F increases and gets closer to E_F for large n_{vac} . Moreover, the relaxation opens up a small band gap of 0.12 eV just above E_F . The band gap further increases by considering hybrid functional corrections to the GGA functionals, see the following subsection.

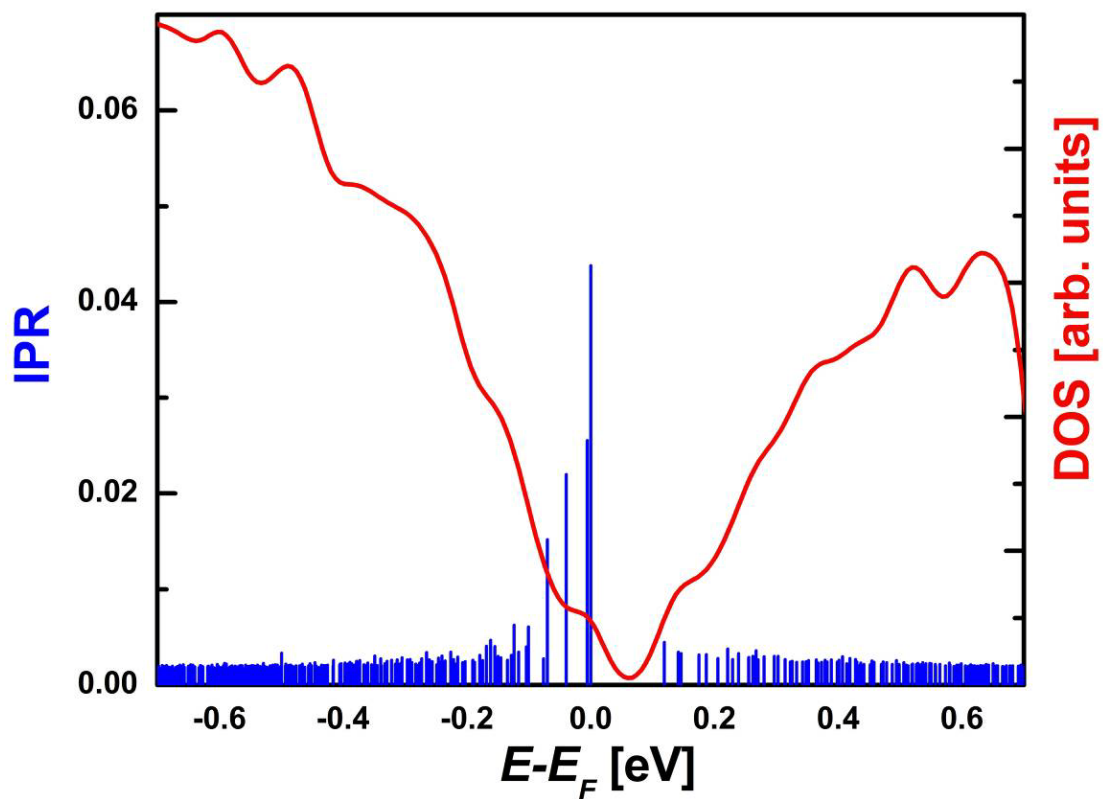


Figure 3.13 The density of state and the inverse participation ratio of Cub-25%.

We have already found convincing evidence that in the cubic phase a high density of Te p states is created at E_F due to vacancy clusters: the corresponding states are expected to be well localized. To prove it, we perform the inverse participation ratio (IPR) analysis. The IPR of a Kohn-Sham eigenstate Ψ_α is defined as

$$IPR \equiv \frac{\sum_i |\Psi_{\alpha,i}|^4}{(\sum_i |\Psi_{\alpha,i}|^2)^2} \quad (3.1)$$

where $\Psi_{\alpha,i}$ are the expansion coefficients of the state with respect to the localized Gaussian-type orbitals (GTOs) forming the basis set (see Chap. 2) and i runs over all the GTOs. For a localized state, the IPR is finite and provides an estimate for the inverse of the localization length. On the contrary, the IPR is zero (in an infinitely large system) for an extended state.

The IPR and DOS of the 1152-sites cubic model (Cub-25%) is plotted in Figure 3.13. The typical IPR values of the states around E_F are of the order of $1.5\text{--}4.4 \times 10^{-2}$. These values are an order of magnitude larger than those of the extended states located deep in the valence band. The typical IPR values of these extended states are smaller than 2×10^{-3} , which reveals that the electronic wavefunctions of these states spread over the whole supercell. These numbers also explain why very large models are necessary to distinguish between localized and extended state. The IPR value $1.5\text{--}4.4 \times 10^{-2}$ indicates that, in this fully disordered cubic $\text{Ge}_1\text{Sb}_2\text{Te}_4$ model, the typical localization region of the states around E_F covers 25-60 atoms.

To better visualize the shape of the localized states, we plot an isosurface of the Highest Occupied Molecular Orbital (HOMO) state, shown in Figure 3.14. The blue surfaces mark the localization region, and the vacancy concentration inside this region is particularly high, 200% higher than in the other region, which is in line with our previous analysis. Assuming that the distribution of vacancies is totally uncorrelated, vacancy clusters correspond to low-probability, local fluctuations, where the concentration exceeds its average value. Although vacancy clusters are energetically unfavorable, their presence cannot be avoided at low annealing temperatures.

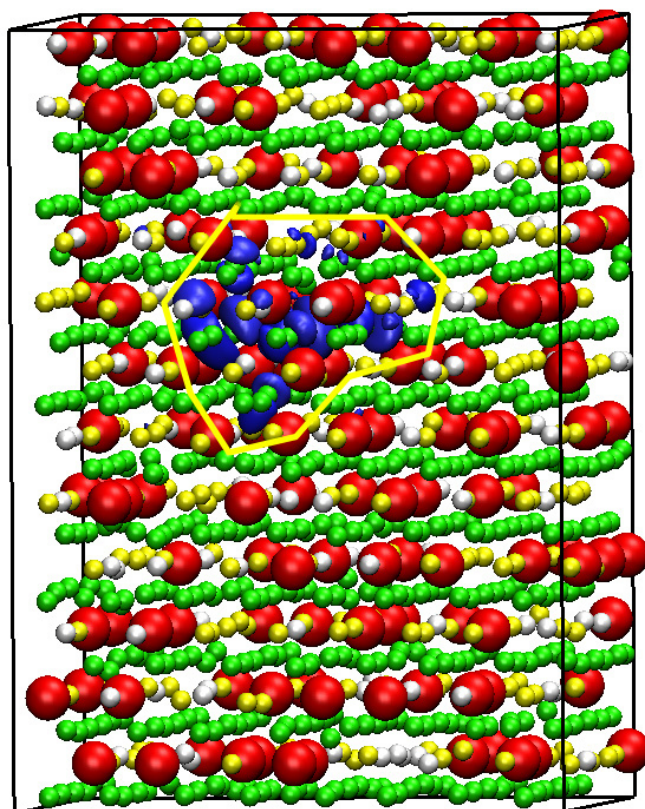


Figure 3.14 The plot of the HOMO state of the disordered cubic model of GST. Vacancy voids are rendered with big red balls. Isosurfaces render a value of 0.012 a.u.

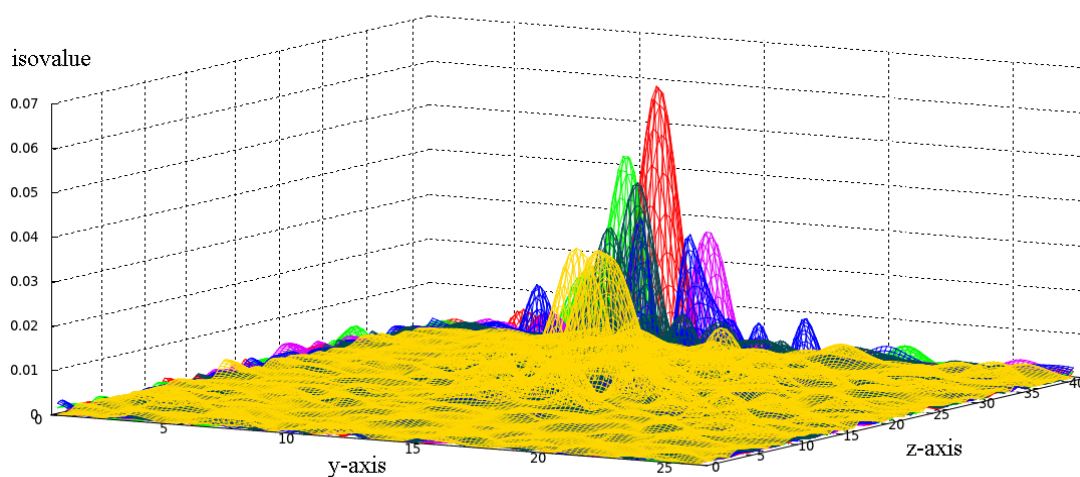


Figure 3.15 The charge density of the localized HOMO state calculated at several y-z planes corresponding to several x values (rendered with different colors).

The electronic states shown in Figure 3.14 are localized in a finite spatial region. Outside this region, the electron wavefunctions decay exponentially. We plot the charge density of the localized state calculated for several y-z planes corresponding to different values of x (see Figure 3.15). The rapid decays of the charge density are observed at 0.012 (a.u.) for all the planes. Therefore, the isovalue we used in Figure 3.14 is reasonable.

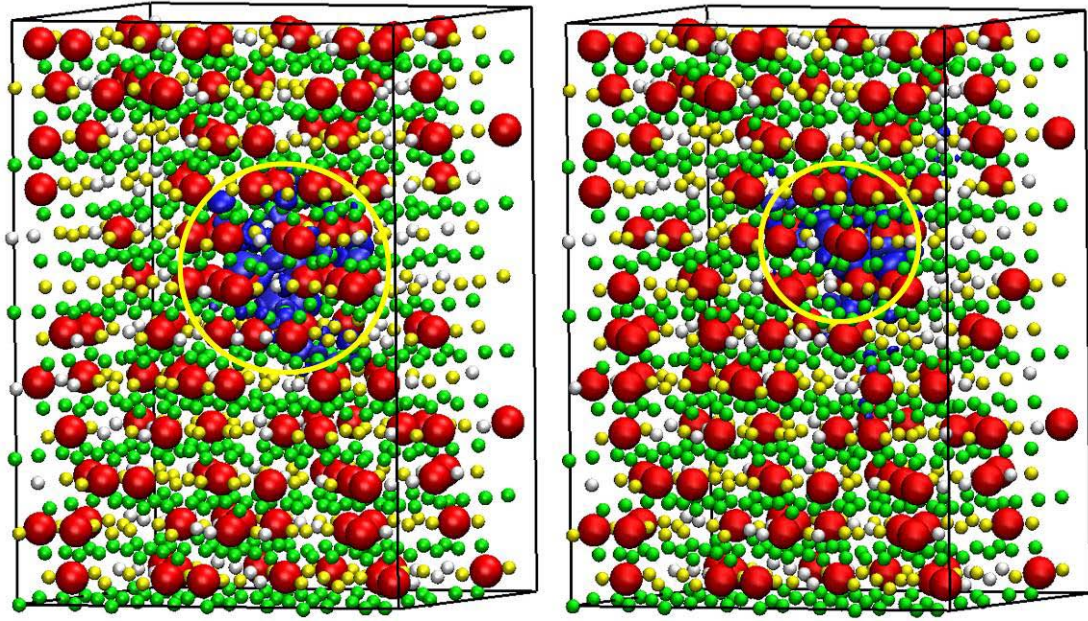


Figure 3.16 The two plots are snapshots of the HOMO state of two disordered cubic GST. Isosurfaces render a value of 0.012 a.u. Vacancy voids are rendered with big red balls.

To further study the correlation between localization and vacancy clustering, we generate two additional models with big vacancy clusters manually (see Figure 3.16). The two models contain a cluster of 30 and 15 vacancies, respectively. Certainly the vacancy concentration is at least 200% larger than in the other region. We plotted the HOMO state of the two models and found the electron wavefunctions are well localized inside these vacancy cluster regions. As expected, the larger the vacancy cluster is, the larger the localized radius of the corresponding state.

We can conclude that vacancy clusters are the origin of localization in the early annealed cubic $\text{Ge}_1\text{Sb}_2\text{Te}_4$ sample. This localization mechanism is expected to hold

for other cubic $\text{Ge}_1\text{Sb}_2\text{Te}_4$ samples upon subsequent annealing and some of hexagonal $\text{Ge}_1\text{Sb}_2\text{Te}_4$ samples. Moreover, it is expected to be universal for other GST compounds.

3.3.2 Non-stoichiometric excess vacancies

It is well known that non-stoichiometric excess vacancies are invariably present in the crystalline GST and turn it into a *p*-type degenerate semiconductor [165]. In Ref [166] it is shown that the formation energies (E_{form}) of Sb and Ge vacancies in $\text{Ge}_2\text{Sb}_2\text{Te}_5$ are relatively low (E_{form} of Sb vacancy is even lower), while that of Te vacancy is high. So it is well possible that additional vacancies form on the cation sublattice of the system. From the experimental values of the carrier concentration (typically $1-2 \times 10^{20} \text{ cm}^{-3}$), the amount of excess vacancies is of the order of 0.1-0.2%, which corresponds to 1-2 additional vacancies in our models.

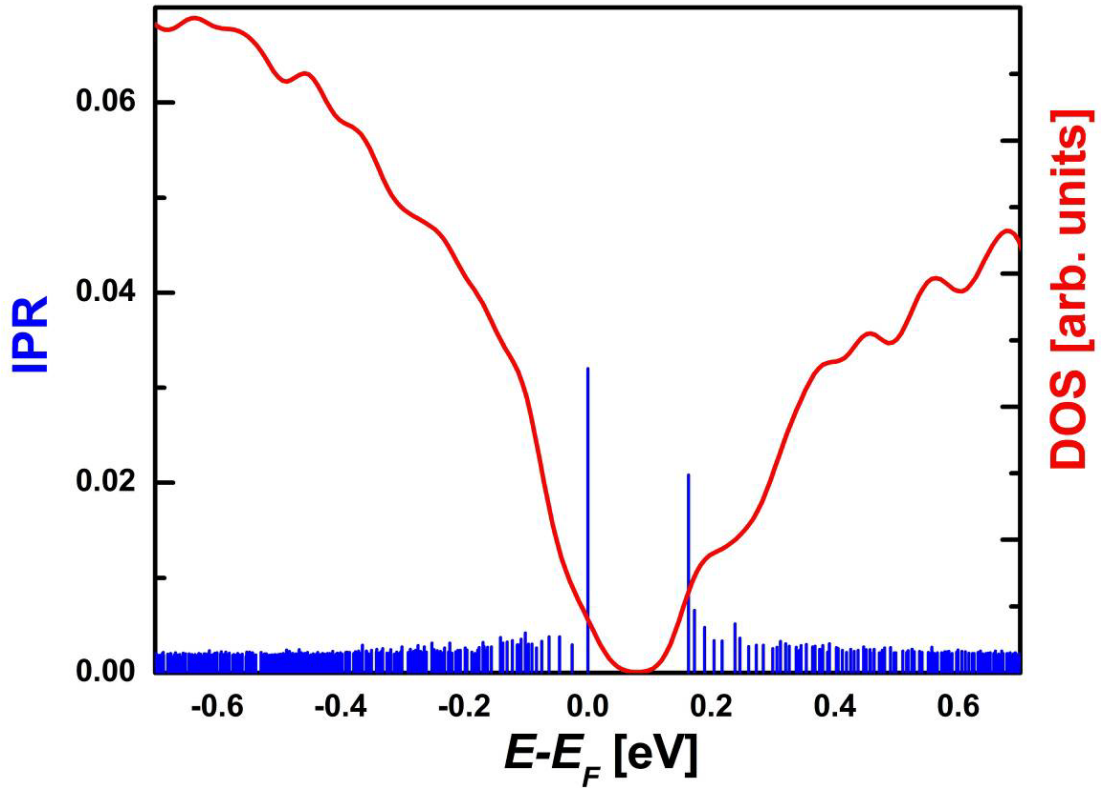


Figure 3.17 The density of state and the inverse participation ratio of disorder GST with two excess Sb vacancies.

We considered two excess Sb vacancies and studied localization properties. In Figure 3.17, the IPR and DOS are plotted. We can observe that although the Fermi level is shifted towards the valence band, it still lies in the region of localized states. Thus, we can conclude the vacancy clustering is the origin of localization in crystalline GST compounds.

3.3.3 Hybrid functional corrections and spin-orbit coupling effects

Hybrid functional corrections usually describe better the electronic properties in GST system, in particular the band gap. We employed HSE03, as used in Ref. [166], for our cubic $\text{Ge}_1\text{Sb}_2\text{Te}_4$ model. It turns out that the band gap increases to 0.23 eV, which is still smaller than the experimental value 0.5 eV. The IPR and DOS are depicted in Figure 3.18, and the localization turns out to be even stronger than the one produced by GGA functional. Moreover, the spatial shape of the localized state is very similar to that of GGA functional. The HOMO state is plotted in Figure 3.19, and compared to Figure 3.14 the changes are negligible.

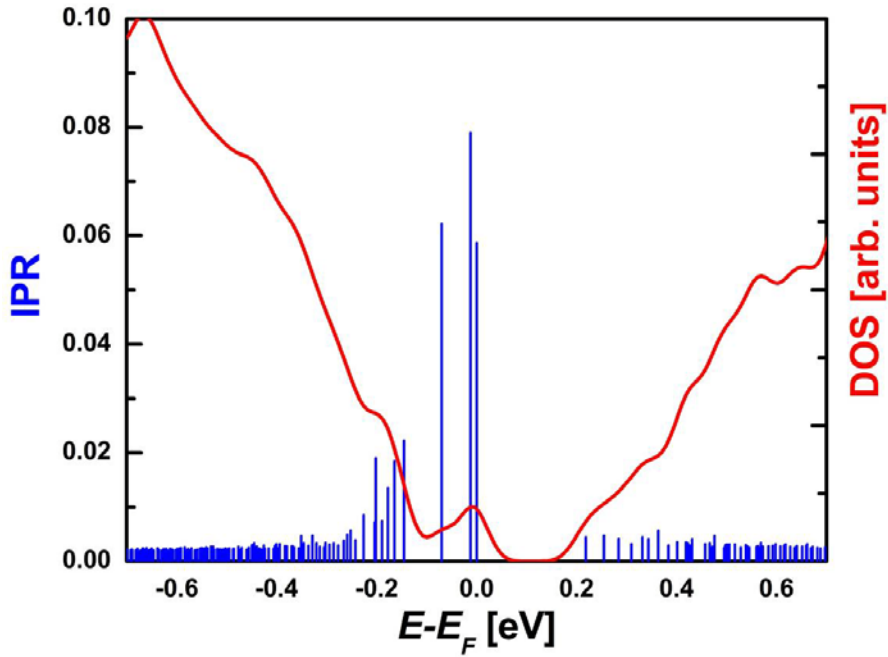


Figure 3.18 The density of state and inverse participation ratio of disorder GST calculated with hybrid functional corrections (HSE03).

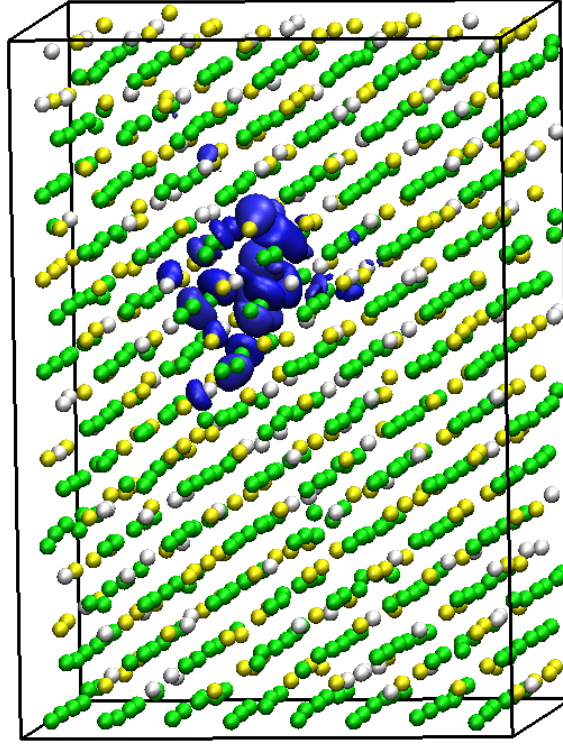


Figure 3.19 Plot of the HOMO state of the disordered cubic model of GST with hybrid functional corrections (HSE03). Isosurfaces render a value of 0.012 a.u.

The spin-orbit coupling (SOC) is known to be important for heavy elements. In some cases, SOC changes the electronic structure significantly [55,167]. Therefore, it is useful to check the SOC effects on the localization property in GST. Due to the high computational cost of the SOC effect, usually the affordable system size is around a few hundreds of atoms. However, as we wrote before large supercell is necessary to observe localization. So it is challenging to generate a GST model that fulfills both criteria. We need to minimize both the size of the model and the size of the localization region.

We consider a GeTe-rich GST model, $\text{Ge}_9\text{Sb}_2\text{Te}_{12}$, with 276 atoms and 12 vacancies in total. The vacancies are arranged to form a cluster. The model is relaxed and its electronic structure is calculated at the GGA level firstly. The IPR and DOS are shown in Figure 3.20. The states around E_F are localized and the HOMO state is plotted in Figure 3.21. Next we include the SOC effect in this relaxed model. Since the SOC is not implemented in cp2k, we use another DFT code, called Quantum

Espresso [127, 168]. The IPR and DOS with inclusion of SOC is drawn in Figure 3.20. One could see the localization near E_F is hardly changed. Besides, the spatial distribution of the electron wavefunction is also very similar to that of the GGA one for the HOMO state, Figure 3.21. Therefore spin-orbit effects do not affect the localization of wavefunctions near the Fermi level.

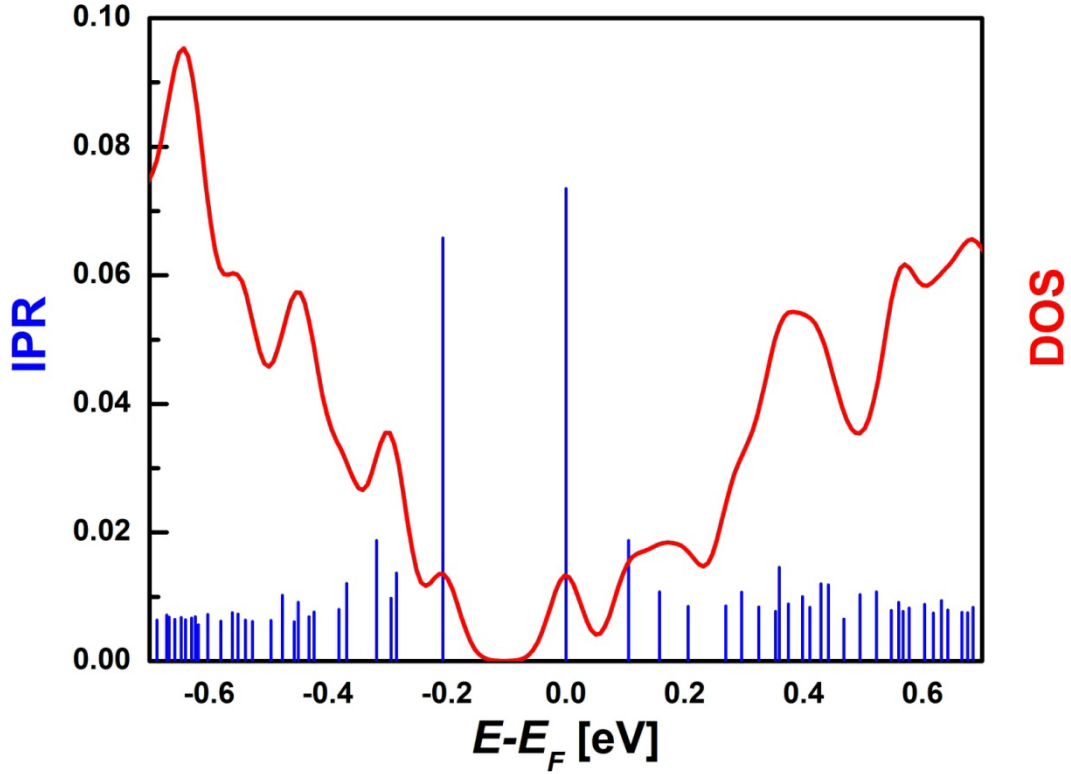


Figure 3.20 The inverse participation ratio and the density of states of $\text{Ge}_9\text{Sb}_2\text{Te}_{12}$

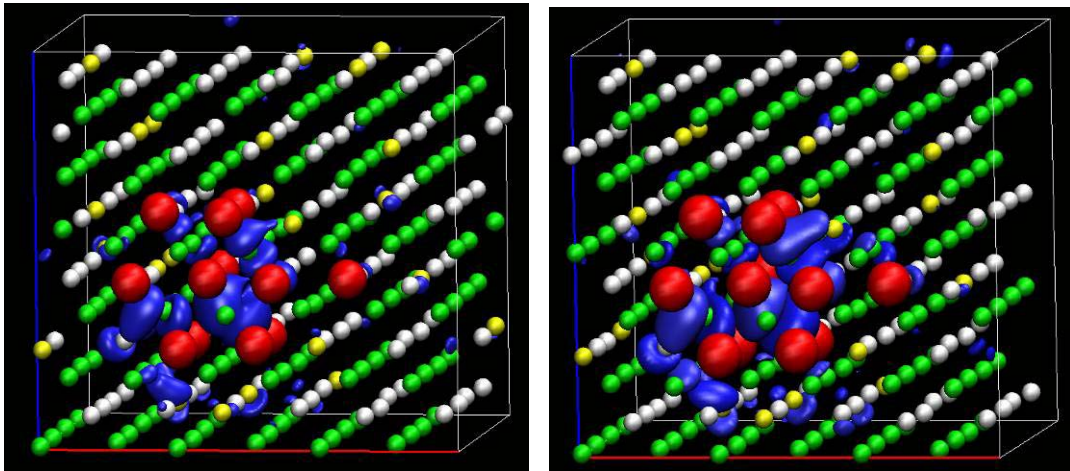


Figure 3.21 Plots of the HOMO state of the $\text{Ge}_9\text{Sb}_2\text{Te}_{12}$ with (left) and without (right) spin-orbit effects. Isosurfaces render a value of 0.012 a.u.

Up to now, we can conclude that the origin of localization in GST compounds is vacancy clustering and is independent from the functionals (LDA, GGA, hybrid HSE03) as well as SOC effects.

3.4 Theoretical modeling of Anderson MIT

The remaining crucial task is to study the transition to metallic state and the role of disorder. I start with the discussion of vacancy diffusion in the cubic phase, which triggers the construction of a set of models that could describe the insulating to metallic transition. Next by comparing the model with experiments, both the structural transformation and metal-insulator transition are identified. Finally, the effects of non-stoichiometric excess vacancies are discussed.

3.4.1 Vacancy diffusion in cubic phase

The final structure of GST upon thermal annealing is in hexagonal symmetry, which is layered-like structure. In comparison to the orthorhombic cubic model, one observes the similarity between the cubic and hexagonal phase. Exchanging the vacancy with the Ge/Sb atoms from the next nearest cation layer (fourth nearest neighbors) continuously seems to be a solution for the structural transformation. So it is useful to estimate the energy barrier for this vacancy diffusion process.

We performed NEB (nudged elastic band) [169,170] simulations to study this energy barrier. A much smaller model containing 84 atoms was constructed and further relaxed at 0 K. As shown in Figure 3.22 (a), the vacancy was exchanged with three nearby atoms, Ge, Sb and Te. The transition paths are plotted in Figure 3.22 (b). After exchanging Ge or Sb with the vacancy (Vac-Ge/Sb diffusion), the system gained energy, while after exchanging Te with the vacancy (Vac-Te diffusion) the system lost energy. In principle, this total energy variance depends on the statistical samplings, it is well possible that the system becomes slightly energetically unfavorable after Vac-Ge/Sb diffusion, but we do not expect the very large energy loss like Vac-Te diffusion in any statistical sample, since in the latter case, the system forms six energetically very unfavorable Te-Te bonds after vacancy diffusion. The

transition barriers for Ge and Sb are 0.84 and 0.74 eV respectively. Of course, the energy barriers also depend on the local chemical environment, but the general trend should be the same, i.e. Vac-Sb/Ge diffusion occurs rather than Vac-Te diffusion.

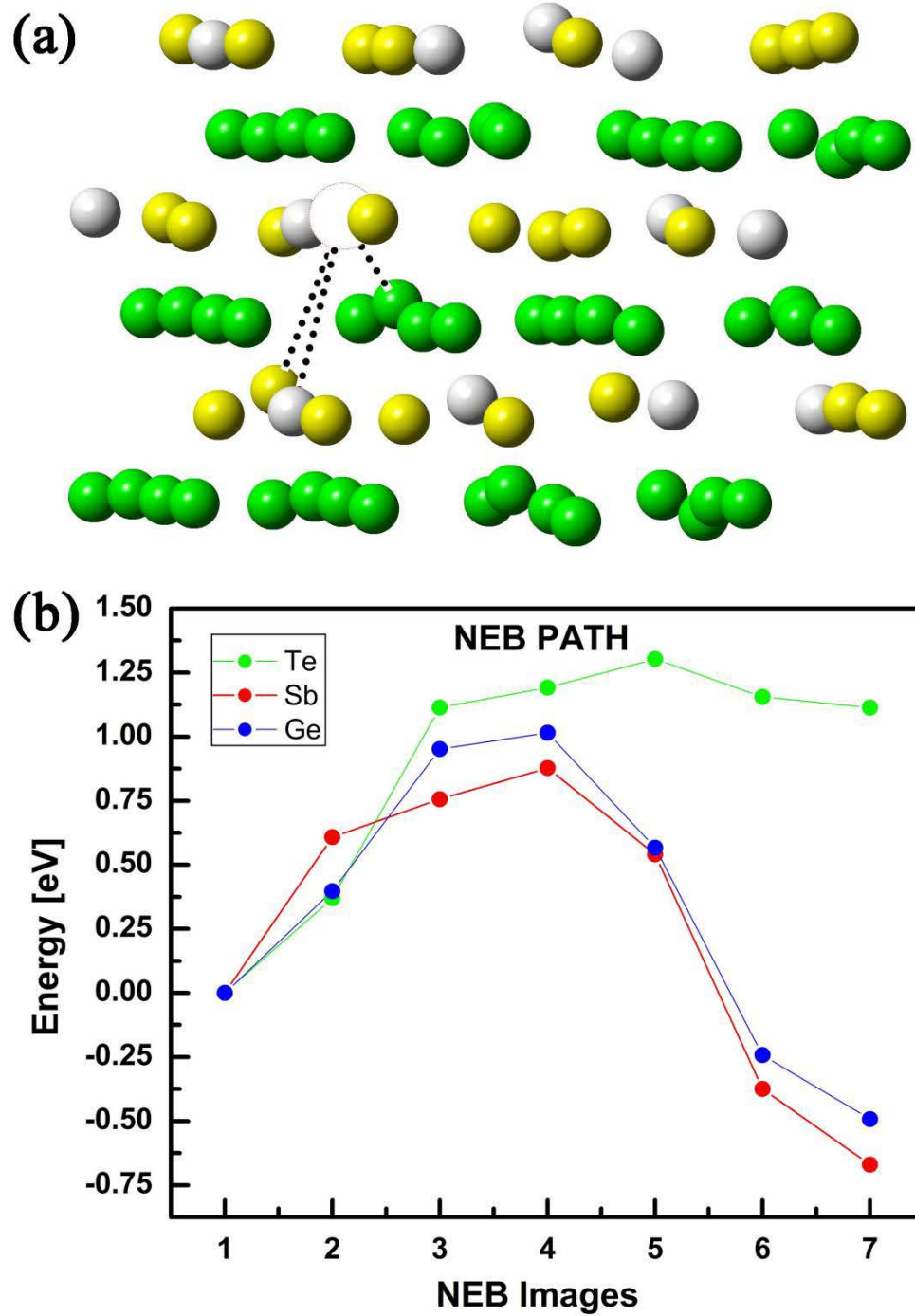


Figure 3.22 (a) fully relaxed cubic GST model and three transition paths (b) NEB calculations of the three transition paths.

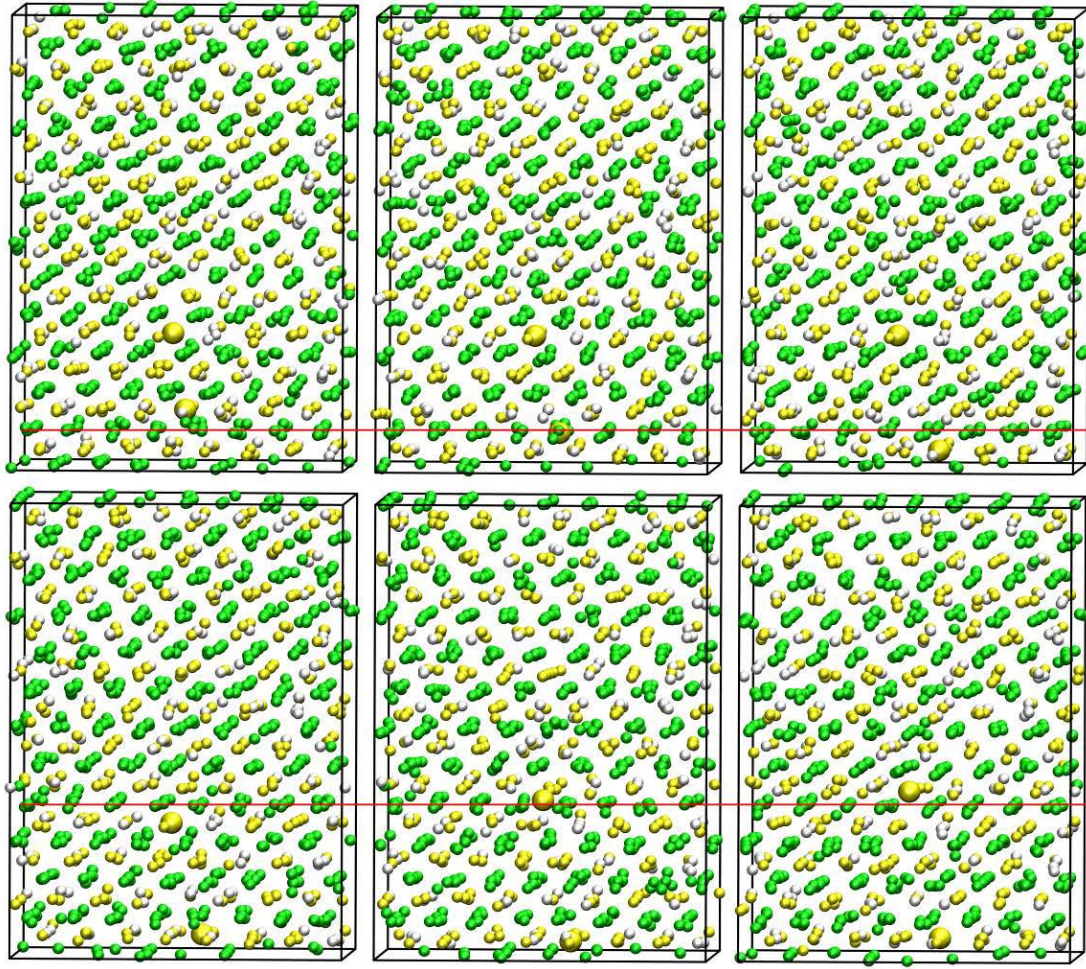


Figure 3.23 AIMD simulations of Cub-25% at 500°C. Ge, Sb and Te atoms are marked with small grey, yellow and green spheres. Two Sb atoms that undergo the Vac-Sb diffusion process are highlighted with bigger yellow spheres.

At high temperature, thermal effects can assist this diffusion process. On the one hand, the atoms become very mobile and can visit much larger spatial regions, the statistical motions can reduce the energy barrier at certain points. On the other hand, thermal effects directly provide energy for the transition. To further support the vacancy diffusion mechanism, we performed AIMD simulation at very high temperature for the cubic GST model. The typical AIMD simulation time scale is of tens to hundreds of picoseconds, therefore, to simulate the slow annealing process (hours-days) at relatively low T, e.g. 200 °C, is not possible. Therefore, we increase the annealing T to be very high (500 °C) to accelerate the annealing process. Within only 30 ps at 500 °C, we have already observed two Vac-Sb diffusion processes.

Several snapshots are given in Figure 3.23. The two Sb atoms are rendered with big spheres. The AIMD simulation is in line with the result obtained from NEB simulations, which show Vac-Sb diffusion occurs firstly, although the statistics is rather poor.

3.4.2 Modeling of MIT

Since it is not feasible to simulate the whole annealing process, we construct several models mimicking this long time process and compare them with experimental X-Ray Diffraction (XRD) patterns. As discussed before, cubic $\text{Ge}_1\text{Sb}_2\text{Te}_4$ is constructed in an orthorhombic supercell with its c-axis parallel to 111 direction of the conventional cubic supercell, each cation layer is randomly occupied by 25%Ge 50% Sb 25% Vac (Cub-25%, Figure 3.24 (a)). The number of layers is 24, a multiple number of the periodicity 6 in the cubic phase, which is intended to fit to the hexagonal case, a 21 periodic layered structure, including 6 weakly coupled Te layers (we refer to the "vacuum region" between the two weakly coupled layers as vacancy layer later on).

Using a set of 1008-atoms models we could describe the structural transition from cubic to hexagonal phase. Starting from Cub-25%, by moving Ge and Sb from every fourth cation layer to the vacant sites in other cation layers, the number of vacancies in every fourth cation layer increases. For instance, the structure Cub-50% is plotted in Figure 3.24 (b), the three target cation layers have 24 vacancy sites on each layer. Meanwhile, we consider the rest of layers as three blocks (7 layers per block, clearer in Figure 3.24 (c)), and by shifting them in the $[1,-1,0]$ direction by $\sqrt{3}/3 a_{\text{hex}}$ and $2\sqrt{3}/3 a_{\text{hex}}$ respectively, the hexagonal stacking is obtained. This shift could be performed for any percentage of the vacancy layer formation, however, only when the vacancy concentration is sufficiently high, e.g. 75%, the hexagonal stacking becomes energetically more favorable. Hex-75% is shown in Figure 3.24 (c). By moving the remaining Ge/Sb atoms from target layers to the remaining vacant sites in the three blocks, three vacancy planes are formed (Hex-100%-a-d). In Hex-100%-a, there is still

compositional disorder made by Ge and Sb atoms. Further swapping of Ge/Sb atoms reduces the compositional disorder (Hex-100%-b and Hex-100%-c) and finally a perfect hexagonal $\text{Ge}_1\text{Sb}_2\text{Te}_4$ is formed (Hex-100%-d, Figure 3.24 (d)).

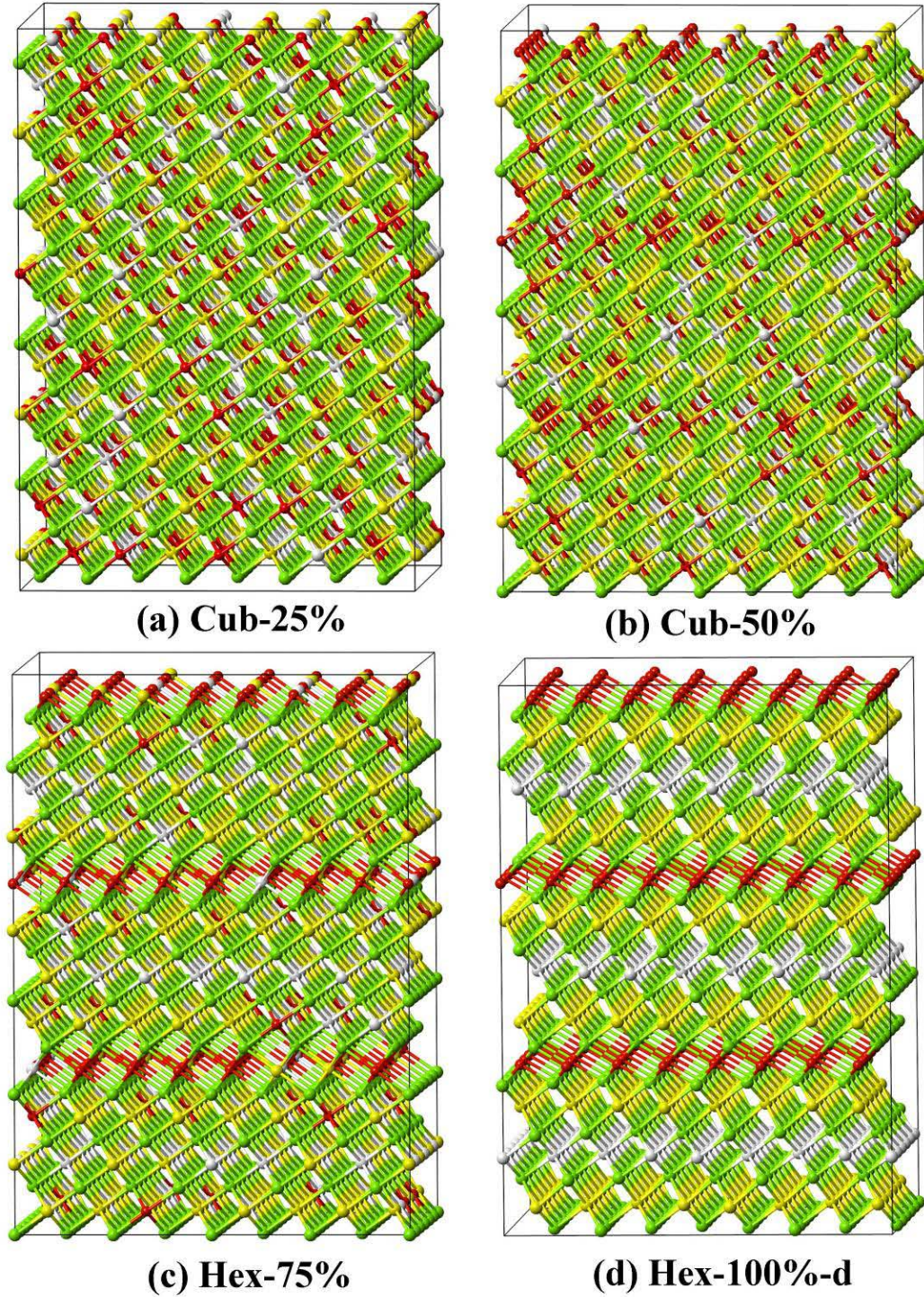


Figure 3.24 Supercells of GST (a) Cub-25%, (b) Cub-50%, (c) Hex-75% and (d) Hex-100%.

Small red spheres indicate the vacant sites.

We employ the experimental lattice parameter $a = 6.03 \text{ \AA}$ for cubic $\text{Ge}_1\text{Sb}_2\text{Te}_4$. The equivalent orthorhombic unit cell has $a_{\text{ortho}} = 7.385 \text{ \AA}$, $b_{\text{ortho}} = 4.264 \text{ \AA}$, $c_{\text{ortho}} = 13.926 \text{ \AA}$. The final cell parameters of the supercell are $A = 29.541 \text{ \AA}$, $B = 25.583 \text{ \AA}$ and $C = 41.777 \text{ \AA}$. For the hexagonal models, we use the lattice parameters $a_{\text{hex}} = 4.272 \text{ \AA}$ and $c = 41.686 \text{ \AA}$ (c is along the z -axis). The parameters of the corresponding orthorhombic supercell are $A = 29.598 \text{ \AA}$, $B = 25.633 \text{ \AA}$ and $C = 41.686 \text{ \AA}$.

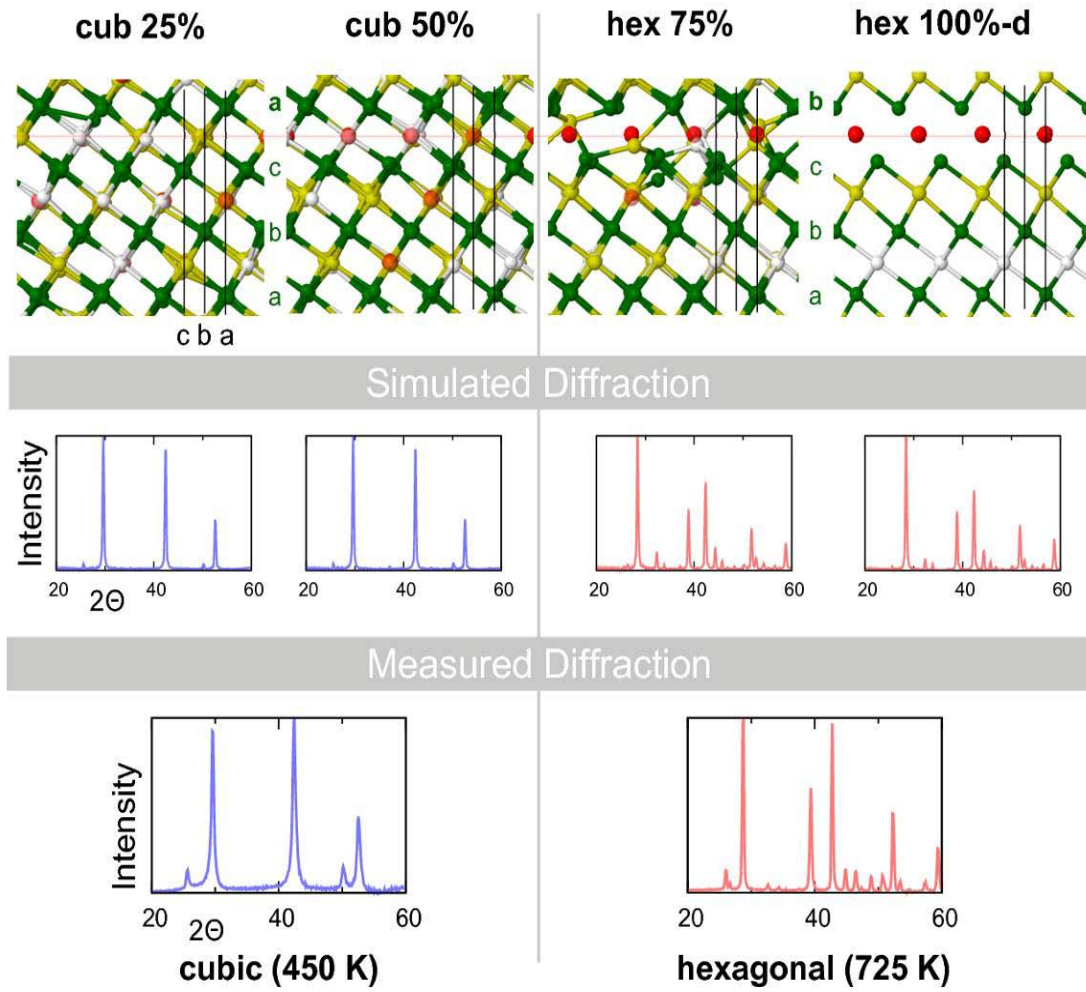


Figure 3.25 The calculated and experimental x-ray diffraction pattern of cubic and hexagonal GST. The calculated pattern were obtained from the 4 models shown in Figure 3.24.

After the full atomic relaxation of all the models mentioned above, we simulated their XRD patterns and compared to the experimental XRD patterns measured for differently annealed samples, shown in Figure 3.25. The measured XRD patterns do not change significantly over samples annealed from $150 \text{ }^{\circ}\text{C}$ to $210 \text{ }^{\circ}\text{C}$, and the one

annealed to 177 °C is shown in Figure 3.25. Similarly the XRD patterns within the hexagonal stacking (annealed above 270 °C) also do not change much, the one annealed to 452 °C is shown. Apparently, our cubic and hexagonal models compare very well with experiments. Models having the same stacking sequence but different distribution of Ge,Sb and vacancies yield very similar XRD pattern. In other words, the ordering of vacancy on the cation layers do not change the XRD pattern directly.

The experimental diffraction patterns are measured using CuK- α x rays in grazing incidence geometry on films of 750 nm thickness. For better comparisons with calculated diffraction patterns, they are divided by the Lorentz-Polarization factor. Both experimental and simulated XRD patterns are done by Zalden and co-workers [142,129].

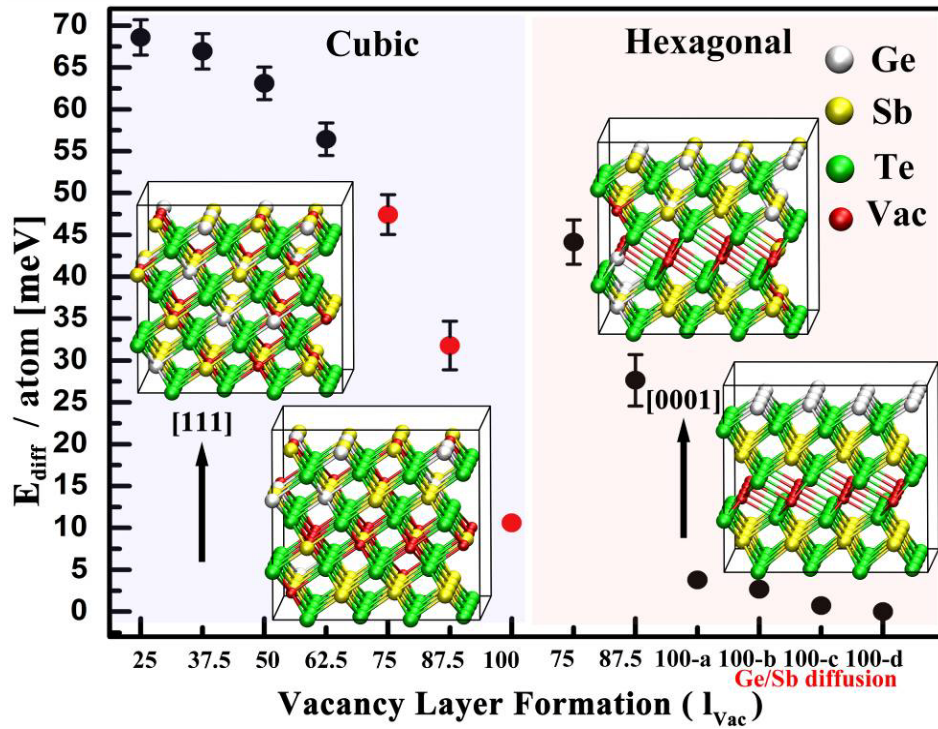


Figure 3.26 Total energy difference of GST models with respect to Hex-100%-d. The insets are 1/3 in c-axis of the models shown in Figure 3.24

In Figure 3.26, the total energy difference of the whole set of models (with respect to Hex-100%-d) is shown, which clearly shows a trend of energy gain upon the reduction of disorder. In the left part of Figure 3.26, models with cubic stacking are

shown, the atomic vacancies become gradually ordered, indicating the formation of vacancy layers in the system. The models from Cub-75% until Cub-100% probably do not exist in the annealing experiments, since the system finds lower energy configurations in the hexagonal stacking sequence. Energy differences between cubic and hexagonal arrangements are relatively small, of the order of 5-7 meV per atom. The formation of vacancy layers yields the largest energy reduction, of the order of 50 meV per atom. These findings show that the structural transition from cubic to hexagonal phase is driven by the ordering of vacancies and takes place before the full vacancy planes are formed. After the formation of vacancy layers, the system could still gain energy by further reducing the compositional disorder, shown in the right corner of Figure 3.5.5. This can be achieved by long thermal annealing at very high temperatures. Since at high temperatures, entropy effects play an important role, which can be larger than the energy difference between the (compositionally) disordered hexagonal phase and the ordered one. Therefore, the substitutional disorder on the Ge/Sb layers might not be completely removed thermal annealing [142]. Note the points in Figure 3.5.5 that contain disorder are averaged over four different samples. Further relaxations of the supercell lattice parameters do not change the energy trend qualitatively, the maximum change is 3 meV per atom.

Subsequently, we have investigated the electronic structure of these models in terms of IPR introduced before. Near the Fermi energy, Cub-25%, Cub-50%, Hex-75% and Hex-87.5% show large values that suggest localization of electron wavefunctions. The reduction of IPR values at E_F suggests the increase of localization length. The localization in the hexagonal phase is similar to that of the cubic phase: the LDOS and HOMO state of the relaxed Hex-75% is shown in Figure 3.28. When approaching the end of vacancy layers formation, the MIT occurs. The IPR values of Hex-100% a-d are below 2×10^{-3} , suggesting delocalization of the electron wavefunction, i.e. the metallic state is formed. The HOMO state of Hex-100%-d is shown in Figure 3.29. It is very delocalized along the x-y plane.

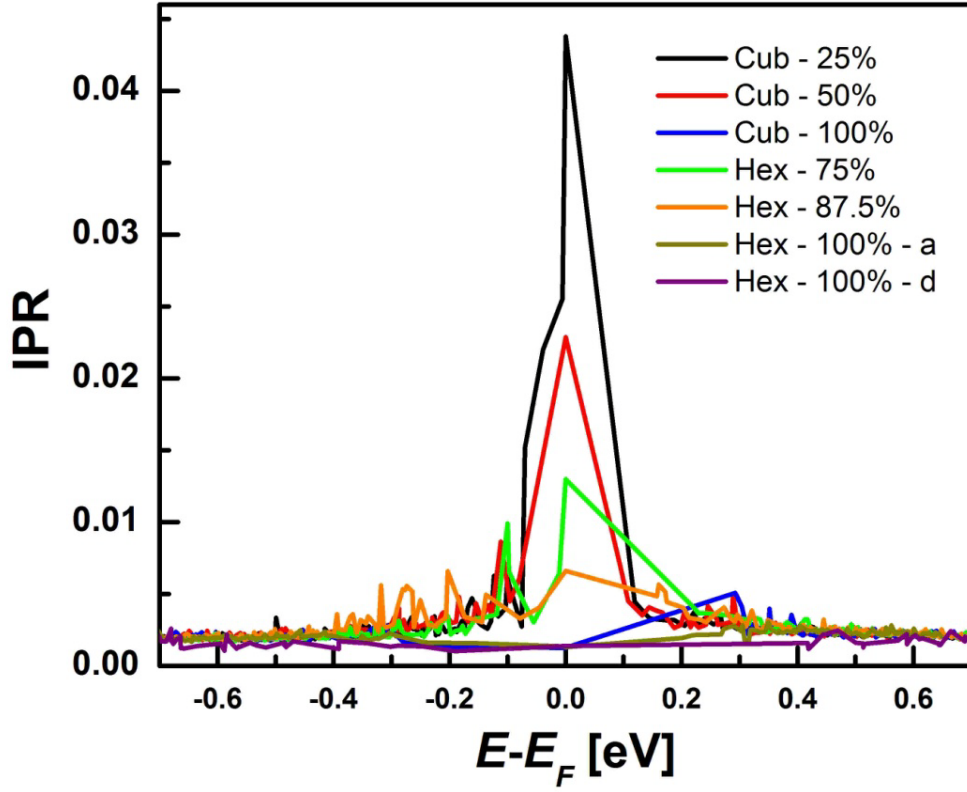


Figure 3.27 The inverse participation ratio of various models plotted in Figure 3.26

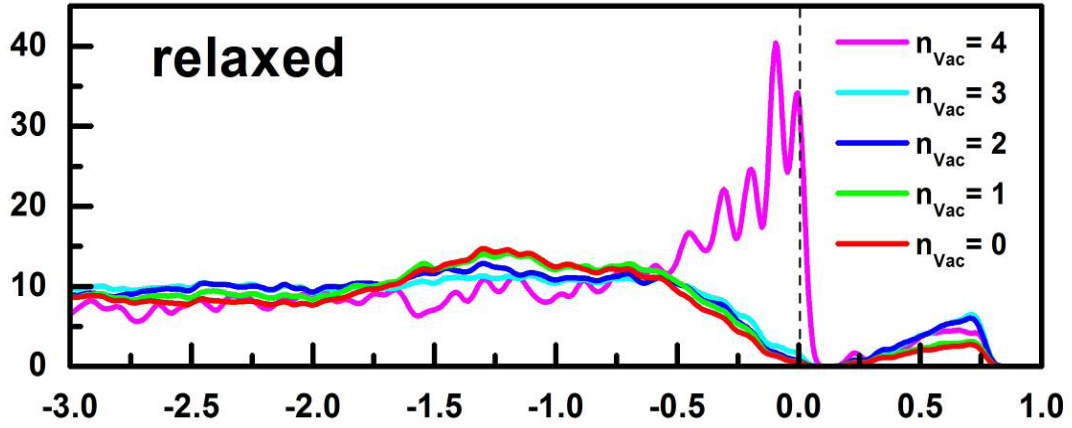


Figure 3.28 Local density of p states of Te sites as function of n_{vac} for Hex-75%.

From Figure 3.27, we observe that the localization to delocalization takes place after 87.5% vacancy layer formation in the hexagonal phase. The observation of localization becomes more and more difficult when approaches or enters this critical region, i.e. the localization length becomes comparable to or even exceeds the size of

the supercells we considered here. Much larger models are needed to describe the critical region, which might be achieved in the future with the support of much powerful supercomputing computers and DFT codes.

To assess the effect of compositional disorder on the localization properties, we plot the HOMO state of Hex-100%-a in Figure 3.30 (a): this structure has been proposed by Matsunaga *et al.* in 2004 [171]. From the shape of electron wavefunction as well as the IPR value in Figure 3.27, it is clear that the electronic states of the system near the E_F are extended. Therefore, compositional disorder alone cannot induce localization.

Interestingly, we also calculated the IPR of Cub-100% and its HOMO state (Figure 3.30 (b)): it also shows delocalization. Although this state does not exist under standard experimental conditions, it might be formed under more complicated experimental environment. For example, some recent experiments show the possibility to obtain such state by synthesizing the film by MBE on Si-111 surface [144].

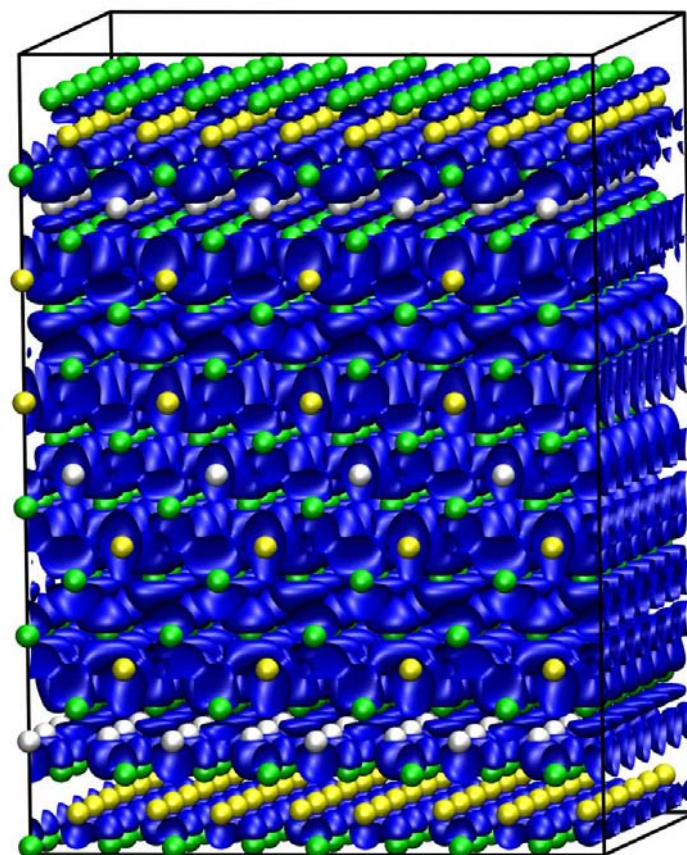


Figure 3.29 Snapshots of the HOMO state of Hex-100-d%. Isosurfaces render a value of 0.002 a.u.

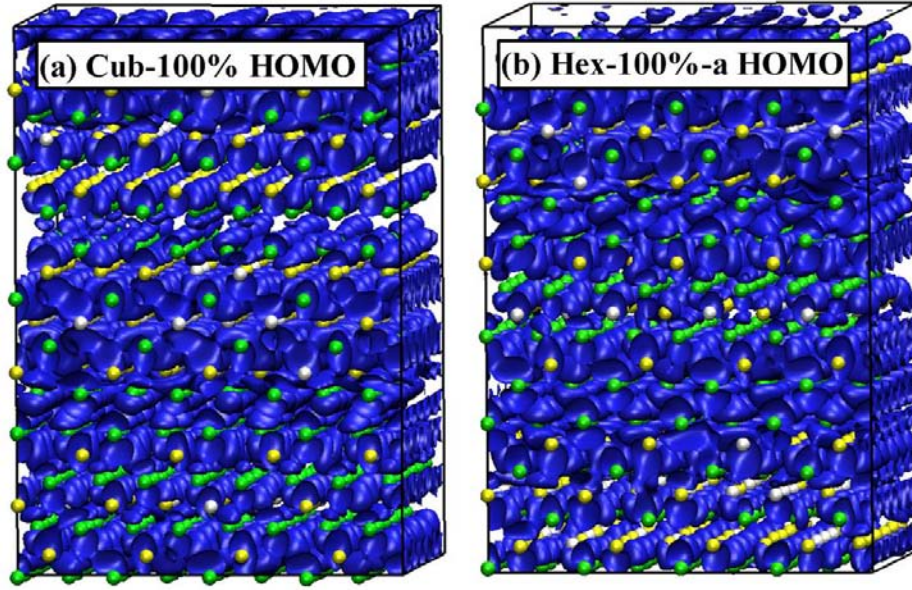


Figure 3.30 (a) and (b) are snapshots of the HOMO state of Cub-100% and Hex-100%-a containing full vacancy layers and a large amount of compositional Ge/Sb disorder. Isosurfaces render a value of 0.002 a.u.

In summary, the analysis of the set of models provides a clear picture of the structural transition and the Anderson MIT upon thermal annealing on GST compounds. Both of them are driven by vacancy ordering, and the structural transition takes place well before the MIT, in line with the experiments showing that MIT occurs in the hexagonal phase [32]. Despite the same driving mechanism, the two transitions are of different nature and independent from each other. The fully ordered vacancy planes in cubic GST further demonstrates that the structural transition is irrelevant for the occurrence of the MIT.

3.4.3 Excess vacancies

In Figure 3.31, the total DOS of several models is depicted. A finite band gap of 0.42 eV is present in the hexagonal phase, which seems to be a contrast to the observed metallic behavior of GST annealed at high temperature. Firstly, the extended nature of the HOMO state already suggests very high conducting capability of the model. Secondly, in case of the spin-orbit coupling effects, the band gap vanishes. Most importantly, the presence of excess vacancies shifts the Fermi level towards the

valence band, where all the states are delocalized. In principle, these low concentrations ($\sim 0.4\%$) excess vacancies can segregate and form vacancy clusters to localize electrons, however, it is extremely unlikely to form such clusters and they can easily dissolve at high annealing temperatures.

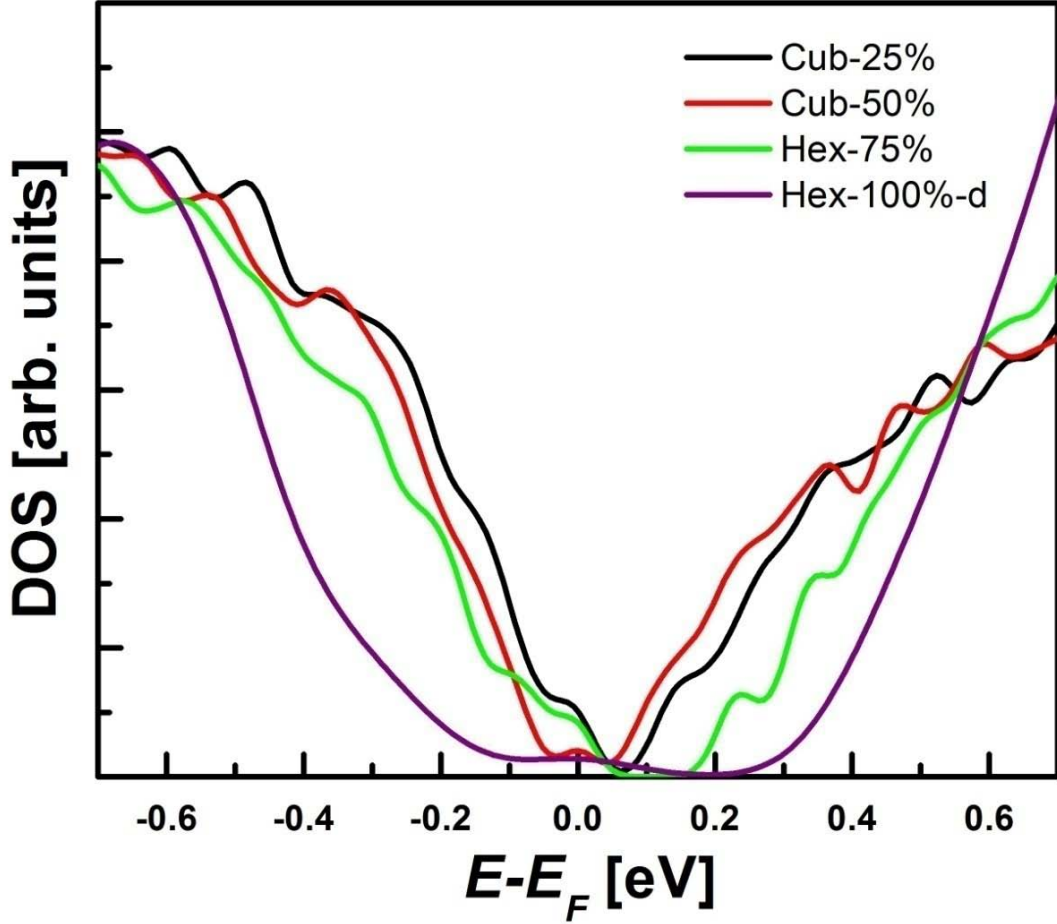


Figure 3.31 DOS of the some models of cubic and hexagonal GST.

3.5 Summary and outlook

In this chapter, I provided an overview of several crystalline PCMs. We studied the cubic to hexagonal structural transition as well as the metal insulator transition observed in GST by DFT calculations. We identified the origin of electron localization in the insulating GST, i.e. the statistically formed vacancy clusters (disorder) induced the electron localization. Upon thermal annealing the vacancy clusters dissolved and eventually formed two dimensional vacancy planes, which triggered the structural transition from cubic to hexagonal phase and the insulating to metallic transition. In

agreement with experiments, we found the structural transition occurred well before the MIT. Moreover, the delocalization of the electronic states in the hypothetical ordered cubic GST further disentangled the different roles of the two transitions. Non-stoichiometric excess vacancies, hybrid functional corrections as well as spin-orbit coupling effects do not change our picture of localization and the MIT.

As an outlook, one very challenging task is to access the mobility edge in the disordered cubic phase by generating very large models containing several tens of thousands of atoms ($\sim 10 \text{ nm}^3$), which would require a very large amount of computing powers and an appropriate simulation software. The same challenge also holds for the study of the critical region for the MIT in the hexagonal phase quantitatively.

Another interesting topic is to further control the atomic disorder in GST other than thermal annealing. The disorder-to-order transition could be accelerated by reducing the transition barrier for vacancy diffusion. Compressive stresses could be a good starting point. In a smaller volume (1-3%), the transition path is shortened for vacancy diffusion, and thereby the transition barrier might be reduced. Note, the compression cannot be too large, otherwise, the cubic GST amorphizes.

Chapter 4 Amorphous Phase Change Materials

In this chapter, I focus on the amorphous phase of PCMs, which is of even more importance than its crystalline counterpart in the studies of PCMs. Here I list a few aspects showing why it is important to study the amorphous state:

First, thermal stability. For data storage application, the amorphous phase should be very stable at room temperature for decades. Pure Sb, SnTe, etc. are not good PCMs because their amorphous states are not thermally stable at room temperature, i.e. they crystallize within a few minutes/hours. Upon doping with certain elements, the crystallization temperature can be raised considerably.

Next, physical property contrast. The amorphous state should have pronounced electrical/optical contrast with respect to its crystalline counterpart. The different atomic arrangement and/or bonding mechanism in the two states could shed light onto this question, which motivates the study of amorphous state from both theory and experiment.

Thirdly, the aging effect. It is known that in amorphous PCMs, the resistance drifts (increases) upon aging. Although this makes the electrical contrast, even more pronounced and does not affect the binary data storage, however, it hinders the development of multi-level data storage. Thus, it is very important to understand the origin of the drift phenomenon, and come up with a strategy to control it.

At last, the amorphous phase is the starting position of two important research directions in PCMs, namely, crystallization and threshold switching. Therefore, a good understanding of amorphous phase is necessary.

AIMD is a very useful tool to study the properties of amorphous phase at the atomic level and has been applied extensively to study the structural properties of amorphous PCMs in this chapter. After a short review of AIMD studies of amorphous PCMs, I discuss the structural properties of the several PCMs in detail. Besides, we performed further chemical bonding analysis for amorphous GeTe (a-GeTe), and provided a quantitative understanding of the local bonding environments. We found

that homopolar GeGe bonds are essential in stabilizing tetrahedral Ge units, while they do not play any role in stabilizing defective octahedral Ge configurations.

4.1 Generating amorphous phase with AIMD

In 2007, Cavarati *et al.* [26] firstly generated the amorphous $\text{Ge}_2\text{Sb}_2\text{Te}_5$ (a- $\text{Ge}_2\text{Sb}_2\text{Te}_5$) by means of AIMD. A melt-quench scheme was employed: starting from a metastable cubic configuration, the system was heated to a very high temperature to eliminate all possible atomic order (6 ps at 2300K), quenched (16 ps) to the melting temperature (990K) and equilibrated there for 18 ps, and finally the liquid was brought to 300K within 18 ps to generate the amorphous state. The whole simulation was performed at the amorphous atomic density, $0.030 \text{ at}/\text{\AA}^3$. In the same year, independently, Akola and Jones also generated amorphous GeTe and $\text{Ge}_2\text{Sb}_2\text{Te}_5$ using a similar melt-quench procedure [27]. Many other groups have studied melt-quenched $\text{Ge}_2\text{Sb}_2\text{Te}_5$ [172,173,174] and GeTe [175,176] using AIMD since then.

Up to now, many other melt-quenched amorphous PCMs have been generated and investigated by means of AIMD, $\text{Ge}_1\text{Sb}_2\text{Te}_4$ [177], $\text{Ge}_8\text{Sb}_2\text{Te}_{11}$ [178], Sb_2Te_3 [179], Sb_2Te [180], AgInSbTe [150], $\text{Ge}_{15}\text{Sb}_{85}$ [181], InSb [182], $\text{In}_3\text{Sb}_1\text{Te}_2$ [8] etc. These simulations provided useful insights on to the properties of the amorphous phase.

Although the melt-quench amorphous phase is relevant to real applications, experimentally, researchers also study as-deposited amorphous thin film, due to easier productions and measurements. Typically, as-deposited and melt-quench amorphous samples of the same material have different properties, e.g. As-S glasses [183] and $\text{Fe}_{80}\text{B}_{20}$ [184]. In PCMs, many melt-quench samples crystallize much faster than as-deposited ones [35, 185,186], which motivates atomically investigation from AIMD. In 2011, Akola and Jones performed the first AIMD simulation of as-deposited $\text{Ge}_2\text{Sb}_2\text{Te}_5$ [187]. The simulation was performed at 300 K. Starting with a fixed thin layer of randomly distributed GST, another 17 sparse layers were deposited step by step and all the randomly initialized Ge, Sb and Te atoms in each sparse layer were allowed for relaxation (5-10 ps). During the simulation, the vertical

box dimension was adjusted for each layer to avoid possible interactions with the replica (vacuum region 10Å). The final simulation box was reduced in the vertical dimension continuously (19 times at 300K) to obtain a cubic supercell (0.0308 at/Å³). The fixed template layer was released during this simulation and the whole process lasted 67 ps. The system was equilibrated for 34 ps before final data collection (25 ps). A similar as-deposited amorphous state has been generated for Ga_xSb_{1-x} [188].

Besides, stress/pressure-induced amorphization [147,189,190] has also been realized by means of AIMD simulations for GST and GeTe. The compressive stress is introduced by placing the amorphous model in a smaller simulation box than its equilibrium volume.

The amorphous models are usually generated using standard GGA functionals, however, more sophisticated methods employing hybrid functional corrections or vdW corrections have been considered in some recent studies [191,192].

In this thesis, I mainly focus on the melt-quenched amorphous phase. Several typical amorphous PCMs are considered, and all of them are generated following the same melt-quench procedure as discussed above, the only difference is that our quenching times are slightly longer: the liquid PCMs are brought to room temperature within 30-90 ps. The amorphous models are usually quenched to 0 K to optimize the geometry further.

4.2 Structural properties of amorphous PCMs

We characterize the structural properties of the amorphous phase. The pair correlation function $g(r)$ characterizes how the density varies as a function of distance from a reference particle. The $g(r)$ can be converted to the structure factor $S(q)$ via a Fourier transform. Experimental approaches like X-ray diffraction or neutron diffraction can determine $S(q)$, thus one can compare the amorphous phase obtained from AIMD directly with experiments. The partial $g(r)$ further distinguishes the contributions from different type of elements. By setting the decay of the first peak(s) in $g(r)$ (partial) as the cutoff(s) (assuming atoms are bonded within the cutoff(s)), one

can compute the averaged coordination number (CN) and the distribution of CNs. The angular distribution function (ADF) describes the local bond environment. In PCMs, defective octahedral and tetrahedral units are the most common structural motifs. A bond order parameter is often used to distinguish them $q = 1 - \frac{3}{8} \sum_{i>k} (\frac{1}{3} + \cos\theta_{ijk})^2$ [26]. To describe the medium range order in the amorphous network, the primitive rings statistics is often employed. The distribution of vacancy voids is also commonly investigated in amorphous PCMs. The concentration and distribution of vacancy voids can be described by different methods, e.g. tetrahedron method [27], Electron Localization Function (ELF) analysis [146] or Voronoi-Delaunay analysis [179].

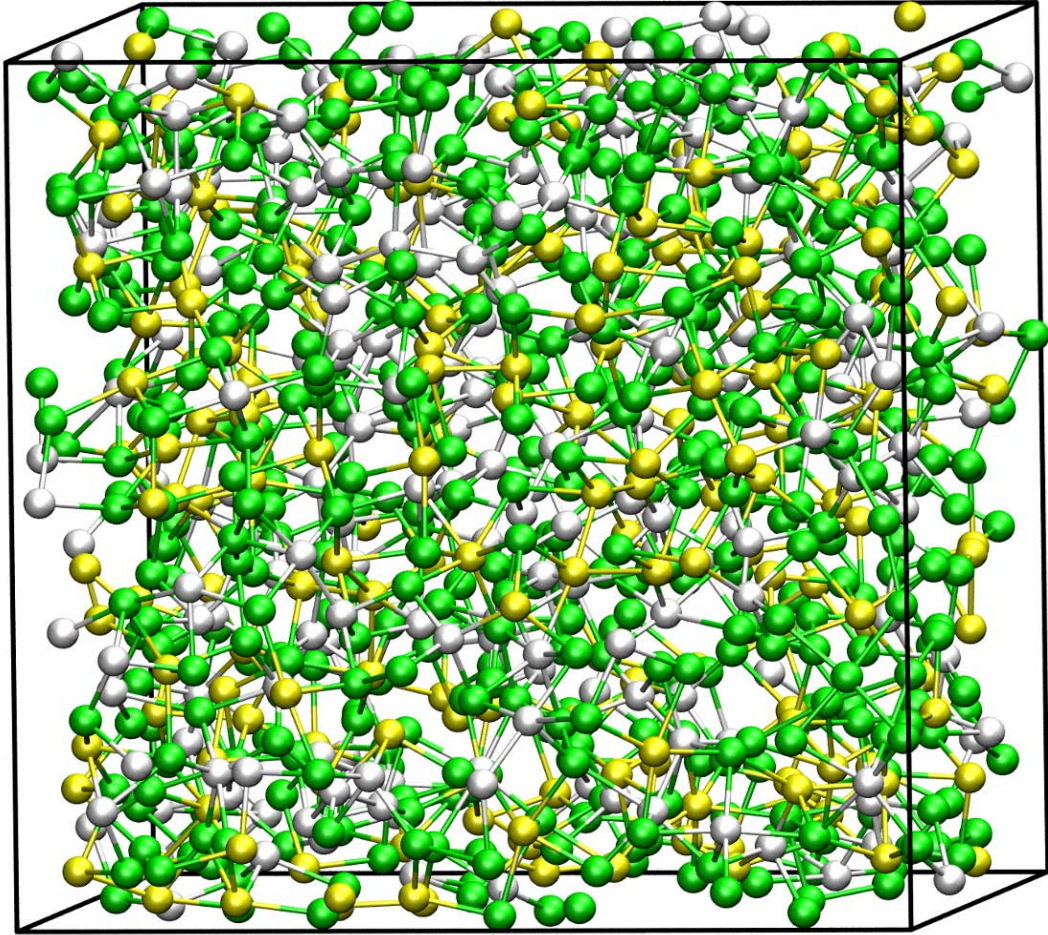


Figure 4.1 A snapshot of amorphous $\text{Ge}_2\text{Sb}_2\text{Te}_5$ at 300K (900 atoms), Ge, Sb and Te atoms are rendered with grey, yellow and green spheres.

In the following, I discuss the structural properties of various amorphous PCMs, using the quantities mentioned above. The amorphous models are generated by the melt-quenched scheme and the system size varies from a few hundreds to 1000 atoms. As mentioned in Chapter 2, computational efforts of DFT based simulations increase very rapidly with the system size: the model containing 1000 atoms is the largest model considered in this thesis. In Figure 4.1, a snapshot of amorphous $\text{Ge}_2\text{Sb}_2\text{Te}_5$ containing 900 atoms is shown.

4.2.1 Finite size effect

First, I discuss the possible finite size effects on the structural properties of the amorphous models generated by means of AIMD. We considered three amorphous GeTe models, containing 216, 512 and 1000 atoms. The pair correlation function $g(r)$ and partial pair correlation functions (PPCFs), evaluated based on AIMD trajectories at 300 K for 10 ps, are shown in Figure 4.2.

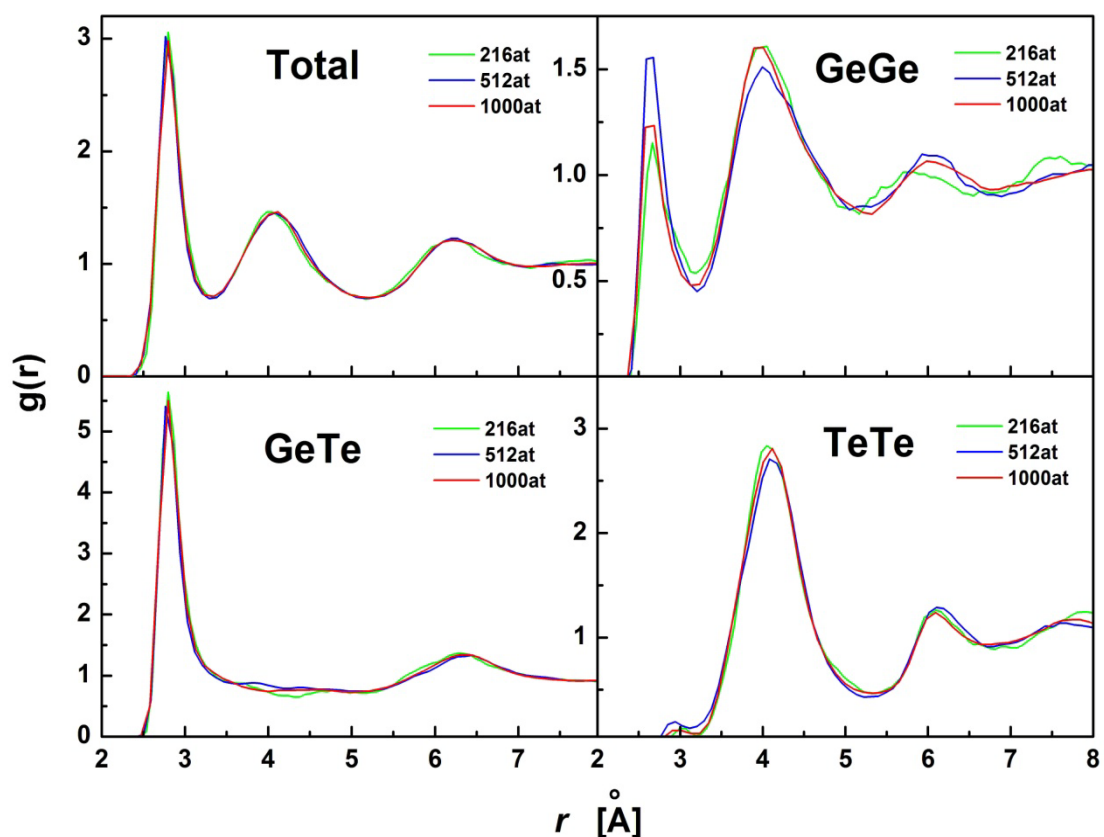


Figure 4.2 The total $g(r)$ and PPCFs of amorphous GeTe containing 216, 512 and 1000 atoms, which are rendered with green, blue and red curves. Calculated at 300K.

No sizeable difference is observed in the total $g(r)$ and the GeTe PPCF. There are certain deviations in the GeGe and TeTe PPCFs, in particular for the first peak in GeGe PPCFs, where the 512 atoms model has a slightly higher peak. However, this change is not monotonic from the 216 atoms to 1000 atoms model, therefore, the difference is rather due to statistical fluctuations. Sampling over many different amorphous models should lead to convergence. Of course, the larger the system size is, the faster the convergence is. We also checked other quantities such as bonding angles, number of tetrahedral Ge, primitive rings statistics and total energy per atom, all of them are very close for these three models. We can conclude that the periodic boundary conditions do not affect the structural properties much, and models containing a few hundreds of atoms (216 atoms) are capable of describing the structural properties of the amorphous state. It is worth mentioning that, for certain purposes, such as the study of nucleation processes or electron localizations in the amorphous phase, very large models are necessary, i.e. the size of the supercell must be much larger than the size of critical nuclei or the localization length of the system.

4.2.2 Group 1 PCMs GeTe-Sb₂Te₃ pseudobinary line

As discussed before, many successful PCMs alloys are pseudobinary alloys made of (GeTe)_{1-x}(Sb₂Te₃)_x. The study of the amorphous phase of these compounds draws great attentions from both experiments [22,25,142] and theory [26,27,173]. In this section, we considered four different amorphous materials, namely, GeTe, Ge₈Sb₂Te₁₁, Ge₂Sb₂Te₅ and Sb₂Te₃. By employing AIMD simulations, the amorphous models were generated by quenching from the melt at densities close to their experimental values (see Appendix A).

We calculated the total and partial pair correlation functions $g(r)$ based on the AIMD trajectories at 300 K for all the four amorphous models, shown in Figure 4.3. From the total $g(r)$, we can observe a gradual shift of the whole curve towards a larger distance from GeTe over GST to Sb₂Te₃, which is due to the change of bonding tendency from Ge-Te rich (shorter bonds) to Sb-Te rich (longer bonds). The most common chemical bonds in these compounds are heteropolar Ge-Te/Sb-Te bonds

(~85-90%), followed by homopolar Ge-Ge/Ge-Sb/Sb-Sb bonds (~7-9%). The least common bonds are homopolar Te-Te bonds.

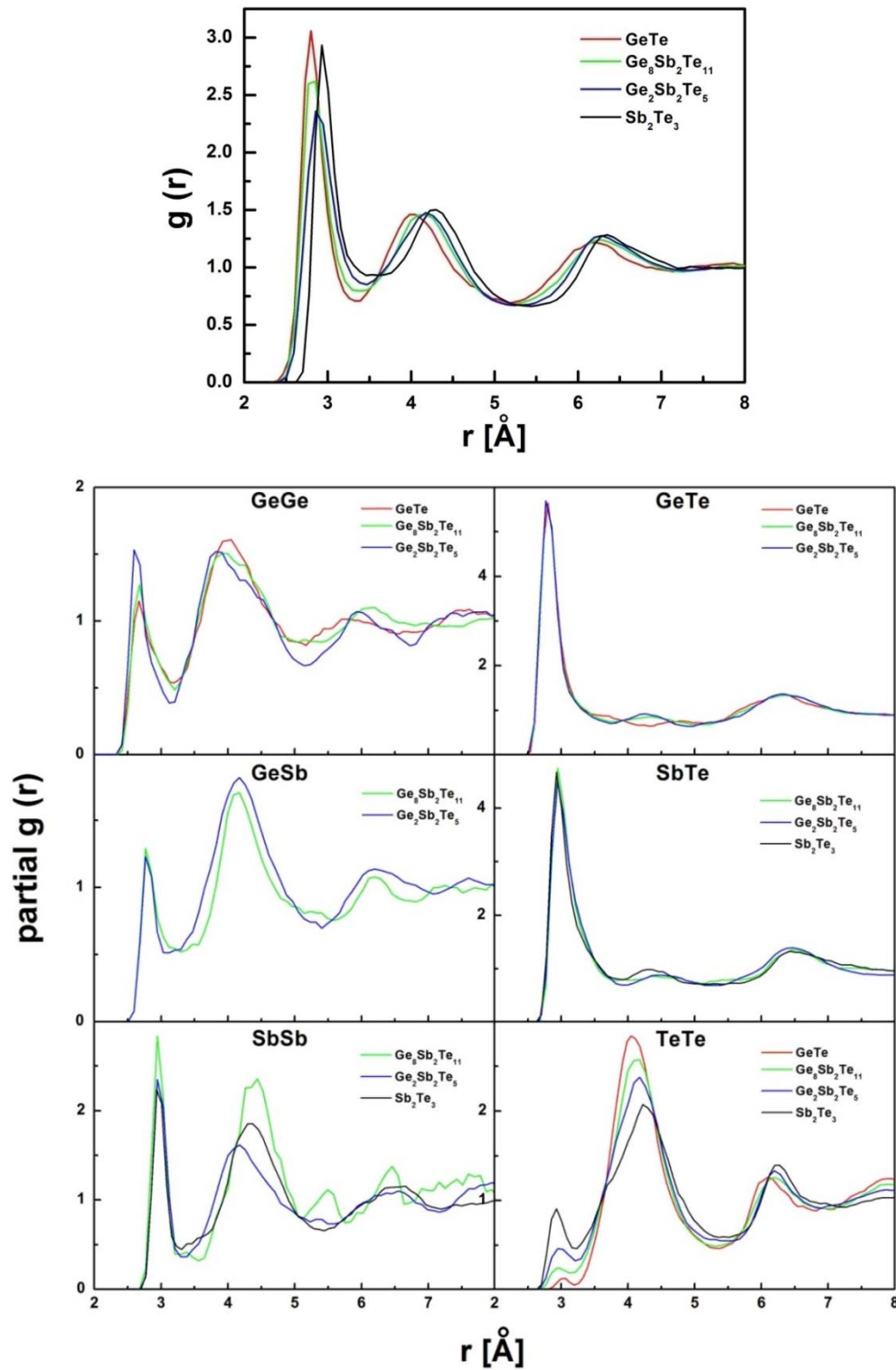


Figure 4.3 The total $g(r)$ and PPCFs of amorphous GeTe (red), $\text{Ge}_8\text{Sb}_2\text{Te}_{11}$ (green), $\text{Ge}_2\text{Sb}_2\text{Te}_5$ (blue) and Sb_2Te_3 (black) at 300K.

The calculated x-ray scattering factor $S(q)$, obtained by Fourier transform of $g(r)$ and PPCFs, enables a direct comparison to X-Ray Diffraction (XRD) experiments. Good agreement between calculated and measured $S(q)$ has been reported for a- $\text{Ge}_2\text{Sb}_2\text{Te}_5$ in ref [26].

Extended x-ray absorption fine structure (EXAFS) and x-ray absorption near-edge structure (XANES) experiments provide information about the local geometry of amorphous states. Quantities, such as the nearest neighbor bond length r and the averaged coordination numbers (CN), can be derived from these experiments. These quantities can be calculated from AIMD simulations as well: the first peak position of $g(r)$ or PPCFs indicates average or pairwise bond length(s); by integrating $g(r)$ or PPCFs up to certain cutoffs, average or pairwise coordination numbers are obtained.

GeTe			Ge ₈ Sb ₂ Te ₁₁		Ge ₂ Sb ₂ Te ₅		Sb ₂ Te ₃	
AIMD/EXP								
r_{tot} [Å]	2.78		2.82		2.86	2.73 ^a	2.94	
r_{GeTe} [Å]	2.79	2.61 ^b	2.76		2.76	2.61 ^a	/	/
r_{GeGe} [Å]	2.65	2.46 ^b	2.67		2.63		/	/
r_{GeSb} [Å]	/	/	2.76		2.76		/	/
r_{SbTe} [Å]	/	/	2.94		2.94	2.85 ^a	2.94	
r_{SbSb} [Å]	/	/					2.93	
r_{TeTe} [Å]	3.0		2.94		2.95		2.93	
CN. Ge	3.9(4)	3.7 ^b	3.8(4)		3.7(4)	3.9(8) ^c	/	/
CN. Sb	/	/	3.7(5)		3.6(5)	2.8(5) ^c	3.4(5)	
CN. Te	3.3(3)	2.5 ^b	3.1(3)		2.7(4)	2.4(8) ^c	2.3(3)	

Table 4.1 The nearest neighbor bond length r and the averaged coordination numbers (CNs) from AIMD simulations at 300K and EXAFS measurements at 10K. Numbers in the parenthesis indicate the error bars of the last digit. The error bars of AIMD simulations are calculated within certain range of cutoffs. The cutoffs of Ge, Sb and Te elements are set to be 3.0 ± 0.1 , 3.1 ± 0.1 and 3.1 ± 0.1 Å, respectively. Experimental references: a [22] b [142] c [24].

In Table 4.1, we compare the bond lengths and coordination numbers obtained from simulations and experiments. We observe that Ge-Ge and Ge-Te bond lengths from simulations are much larger than those from experiments for both a-GeTe and a-Ge₂Sb₂Te₅, while Sb-Te bonds are well matched. The mismatch of Ge-Ge and Ge-Te bond length between simulations and experiments is not fully understood yet. As regards the coordination numbers, the calculated and experimental values compare fairly well (within the error bars).

To gain more insights about the local bonding environment, we turn to the discussion of bonding angles. We computed the angular distribution function (ADF) at 300 K for all the four amorphous models and plotted them in Figure 4.4. They are averaged over all atoms (tot-ADF, black solid curve) and over each element (dash dot curves). The four tot-ADF curves are very similar: there exhibits a pronounced peak at $\sim 90^\circ$ and a smaller peak $\sim 165^\circ$, indicating most of the atoms are in a defective octahedral-like environment (d-octa) (see Figure 4.5). Sb-ADF curves are rather similar to tot-ADF, possessing an additional peak at large angles, while Te-ADF curves do not have such peak. This suggests most d-octa Sb atoms have at least 4 neighbors, while most d-octa Te atoms have 3 or 2 neighbors. The distribution of coordination numbers further confirms this point, see the insets in Figure 4.4. As regards Ge-ADF curves, the main peak $\sim 90^\circ$ is shifted towards larger angles, which is due to the formation of tetrahedral-like (tetra) units around Ge atoms. Meanwhile, a secondary peak is present at $\sim 165^\circ$, suggesting the co-existence of d-octa and tetra Ge structural motifs.

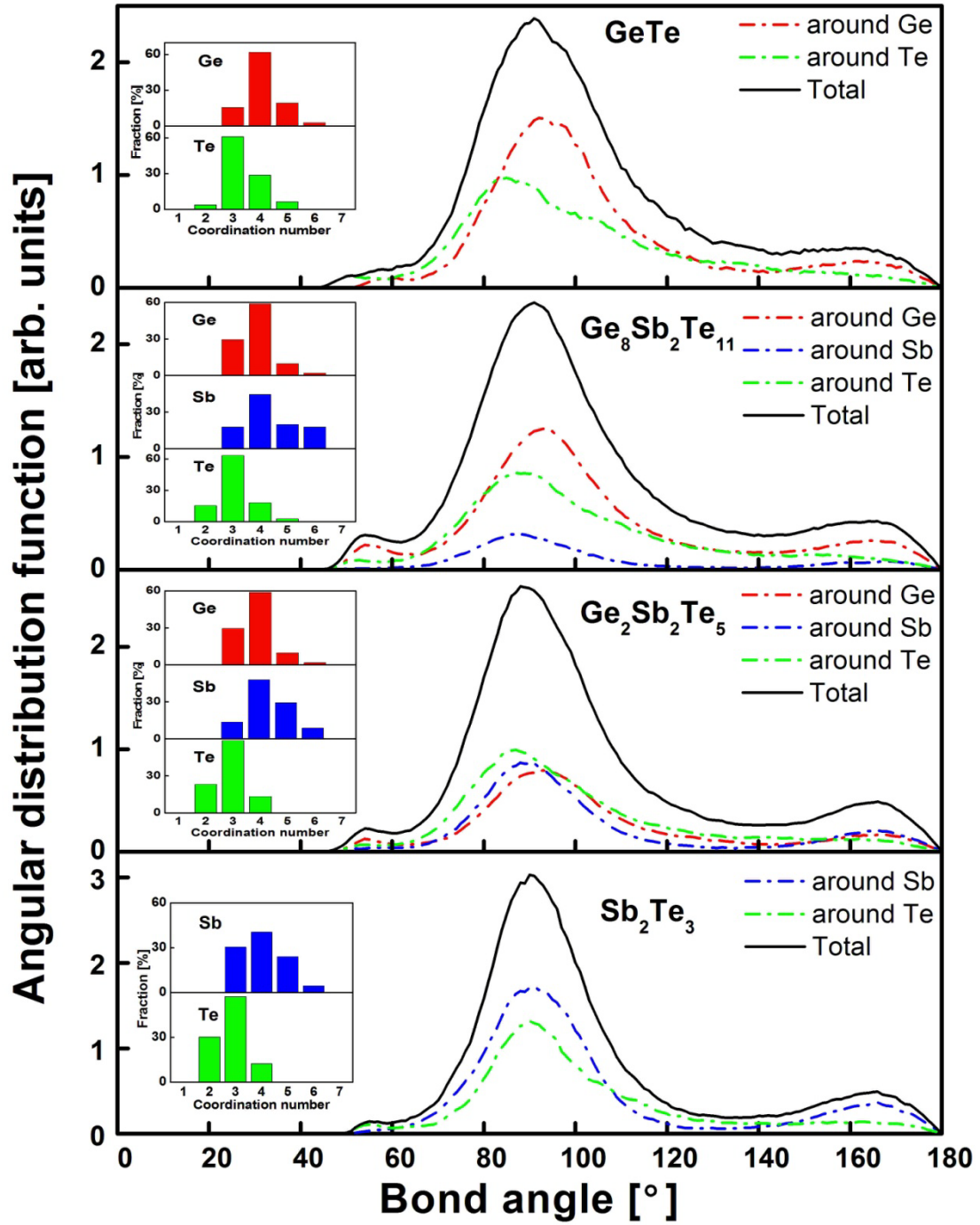


Figure 4.4 The angular distribution functions for amorphous GeTe, Ge₈Sb₂Te₁₁, Ge₂Sb₂Te₅ and Sb₂Te₃ at 300K. The tot-ADFs are marked with black solid line, while Ge-, Sb- and Te-ADFs are rendered with red, blue and green dash dot line. The insets show the distribution of coordination numbers. The cutoffs are 3.05, 3.10, 3.22, 3.25, 3.40 and 3.20 Å for Ge-Ge, Ge-Sb, Ge-Te, Sb-Sb, Sb-Te and Te-Te.

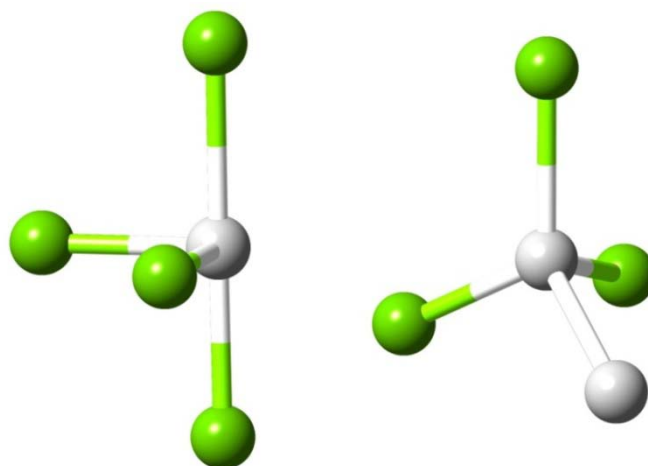


Figure 4.5 Defective octahedral and tetrahedral structural motifs, Ge and Te atoms are rendered with grey and green spheres.

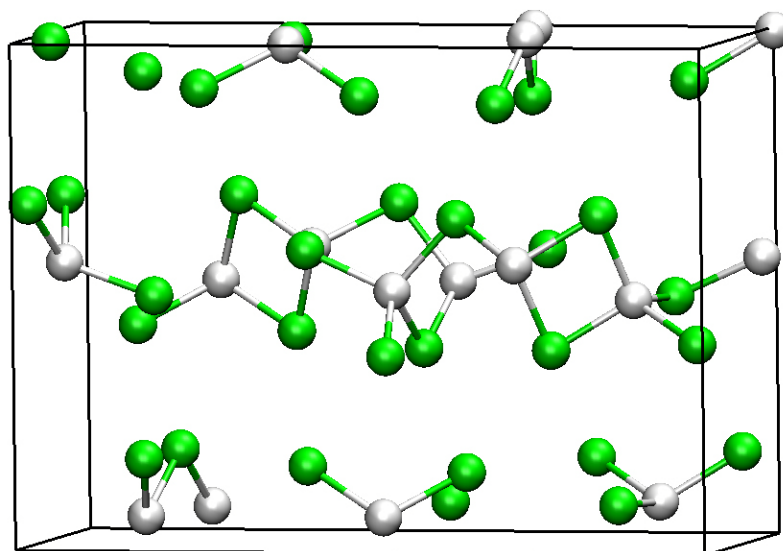


Figure 4.6 A possible crystalline form of GeTe_2 with tetrahedral Ge atoms (grey) purely bonded to Te atoms (green).

By employing the order parameter q we introduced before, we can better distinguish tetra from d-octa atoms. We found 25%, 23% and 29% tetra Ge for amorphous GeTe , $\text{Ge}_8\text{Sb}_2\text{Te}_{11}$ and $\text{Ge}_2\text{Sb}_2\text{Te}_5$, while no tetra units in amorphous Sb_2Te_3 . This observation is puzzling: why there exist certain structural motifs that cannot be found in their parent crystalline forms? In crystalline GST or GeTe , all the Ge atoms are in octahedral or slightly distorted octahedral configurations. Crystal

forms made of tetrahedral Ge and Te, such as GeTe_2 (see Figure 4.6), are highly unstable and would quickly decompose into crystalline GeTe and Te . The total energy of crystal GeTe_2 is 0.227 eV higher than rhombohedral GeTe and trigonal Te , calculated from DFT. Clearly tetra Ge made of Ge-Te_4 is not a stable configuration in the crystalline form, thus, it is important to check if amorphous tetra units are made of Ge-Te_4 or not.

In a- GeTe or a- $\text{Ge}_2\text{Sb}_2\text{Te}_5$, over 90% of the tetra Ge are found to be bonded with at least one Ge or Sb atom. Then, the story is different, since there exist stable crystalline forms, consisting of tetra Ge, for pure Ge and GeSb . Very recently, together with V. Deringer *et al.* [193], we studied chemical bonding in a- GeTe and quantified the role of homopolar Ge-Ge bonds in stabilizing tetra Ge local motifs.

Chemical bonding in a- GeTe :

To define the bonding (antibonding) character in a solid is generally challenging. Based on the electronic wavefunctions generated by DFT, the crystal orbital overlap population (COOP) [194,195] and the crystal orbital Hamilton population (COHP) [136] analysis can extract this essential chemical information. In some recent works, Deringer and co-workers have shown how to extract bonding information from numerically efficient plane-wave basis sets [196,197] that are often used for large DFT simulations (containing hundreds of atoms). The method is proved to be applicable even for very disordered systems, such as amorphous materials.

The COOP shows different bonding characters at different energies. The positive and negative COOP values stand for bonding and antibonding states, respectively. The behavior of COOP at the Fermi level E_F indicates the stability of the system. By projecting the COOP (pCOOP) onto different structural motifs in a- GeTe , we can learn the stability of local environments. In Figure 4.7, we present pCOOP data for four-coordinated Ge bonding units, namely, tetra Ge-X4 and d-octa Ge-X4.

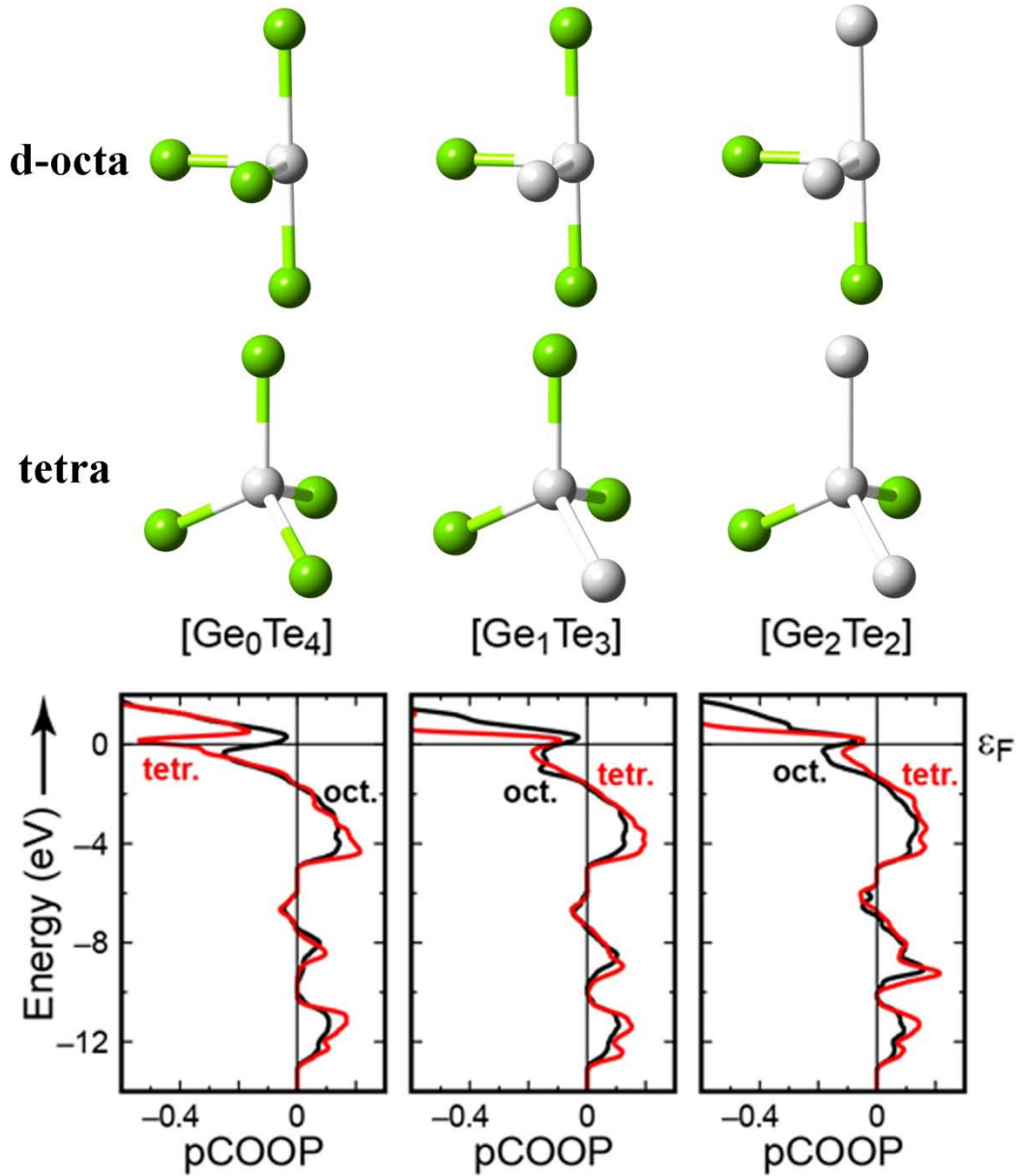


Figure 4.7 pCOOP analysis for Ge-X_4 motifs in a-GeTe. The geometry has been fully relaxed at 0 K. The tetra and d-octa units contain 0, 1 and 2 homopolar Ge-Ge bond(s). pCOOP curves are given per structural fragment (containing four bonds each) and are averaged separately over all the tetra and d-octa motifs in the amorphous model. Produced by V. Deringer.

All the pCOOP data for different tetra and d-octa-4 units have been collected and averaged. By sorting them into motifs that have 0, 1, and 2 homopolar Ge-Ge bonds, one learns the influence of homopolar bonds on the stabilization of local structures. In the left panel of Figure 4.7 (red curve), one can see a pronounced antibonding peak at

E_F for fully heteropolar tetra unit Ge-Te_4 , indicating high instability of this configuration. The antibonding character at E_F decreases drastically in the presence of homopolar Ge-Ge bonds, see middle and right panel. These data clearly show that Ge-Ge bonds are indeed stabilizing the local tetra motifs. This is in line with the observation that, in the amorphous network, over 90% tetra Ge atoms are bonded with at least one Ge-Ge bond. Interestingly, homopolar Ge-Ge bonds cannot help stabilize the d-octa-4 units. The antibonding contribution at E_F does not change much upon variation of the number of Ge-Ge bonds in the motifs (Figure 4.7 black curves), and the antibonding strength even increases slightly when a tetra Ge bonded with two Ge-Ge bonds. The majority of d-octa-4 units contain only heteropolar bonds.

The comparison of the pCOOPs between tetra and d-octa-4 units also shows that d-octa-4 units are generally more stable than tetra units: black curves at E_F give smaller values than those of red curves (see Figure 4.7). This agrees with the fact that d-octa units are the majority (~70-80%) and tetra units are the minority (~20-30%).

At melting temperatures, homopolar Ge-Ge bonds inevitably exist in liquid GeTe due to the very high kinetic energy of the atoms, and they cannot be completely removed in the subsequent fast cooling process. These "frozen" homopolar Ge-Ge bonds are essential for the formation of tetra Ge units.

It is known from experiments that the resistance of amorphous PCMs increases [198,199], the energy band gap widens [200] and the internal stress releases [201] upon time evolution, implying that there are structural relaxations in the amorphous phase. The current analysis is not yet sufficient to make any prediction about the evolution of the amorphous network upon aging, since it is an analysis of the stability of local structures. When considering the structural evolution, the global stability of the amorphous network also needs to be considered. The evolution of amorphous network and aging effects are still under investigation.

After discussing the local bonding environment, we turn to the discussion of medium range order. As mentioned before, the distribution of primitive rings (the shortest closed loops) provides important information about the medium range order of the amorphous network. In Figure 4.8, we present the analysis of rings statistics.

Obviously, the four-membered rings dominate over other primitive rings in all the four amorphous models. The majority of the four-membered rings (>80%) have ABAB alternation (A-Ge/Sb, B-Te), without homopolar bonds. This is a generic feature in group 1 PCMs.

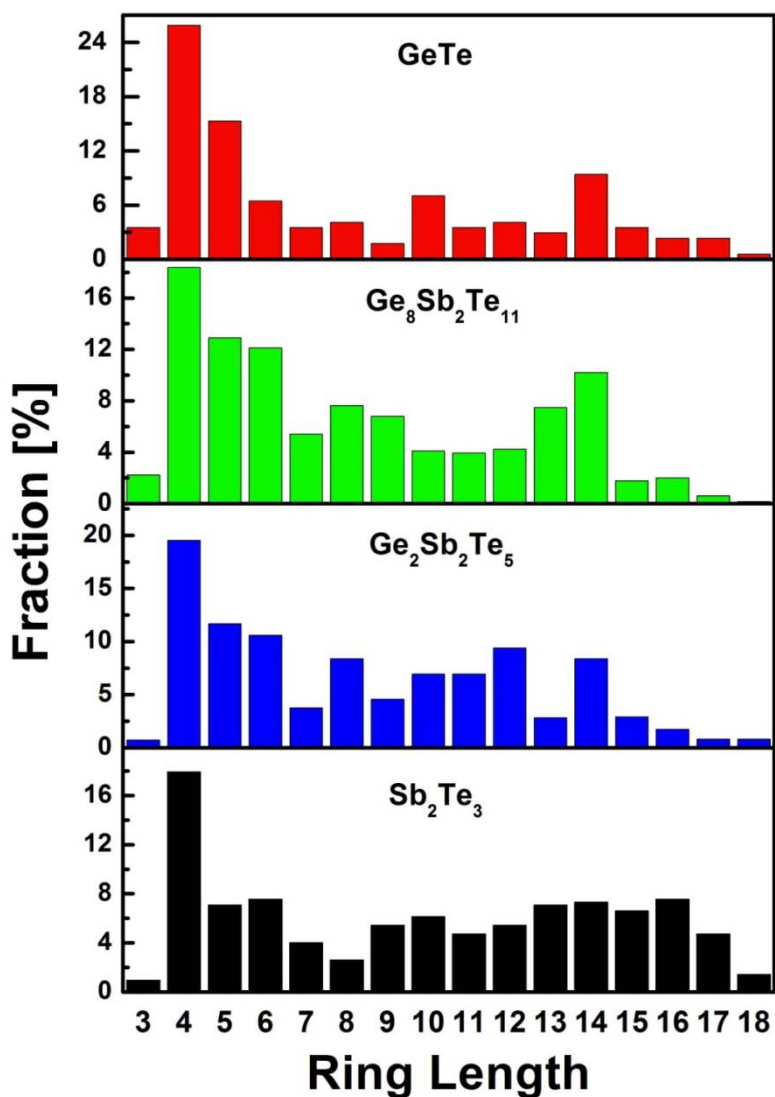


Figure 4.8 The statistics for primitive rings in GeTe, Ge₈Sb₂Te₁₁, Ge₂Sb₂Te₅ and Sb₂Te₃. The ring length is the number of atoms in the ring.

The concentration of vacancy voids is also calculated for these amorphous models. We used the method developed in Ref. [202], which is implemented in the program VNP [203]. Atomic radii are set as 50 % of the average bond length for each atom species, and the radius of the testing sphere is set to 1.3 Å. The voids concentration is

found to be 7%, 12%, 13% and 18% for amorphous GeTe, $\text{Ge}_8\text{Sb}_2\text{Te}_{11}$, $\text{Ge}_2\text{Sb}_2\text{Te}_5$ and Sb_2Te_3 , respectively. Generally, vacancy voids take a relatively large volume of the whole cell for all the four amorphous models. The large voids concentration is believed to be important for fast crystallization kinetics of these amorphous PCMs, for instance, the atomic mobility might be enhanced due to the large "free" space for atomic rearrangement [27,42]. Compared to amorphous GST and Sb_2Te_3 , a-GeTe has smaller voids volume. The large void concentration in Sb_2Te_3 may partially due to the use of theoretical equilibrium density, but it should still be large even if the volume is slightly compressed. Overall, the amorphous network of group 1 PCMs is quite open.

4.2.3 Group 2 PCMs doped Sb-Te

Sb-Te binary alloys, such as Sb_2Te , Sb_2Te_3 , are able to undergo very rapid phase transitions. However, their crystallization temperatures are quite low (80-110°C), which hinders real applications. The group 2 PCMs consists of doped Sb-Te systems (such as around Sb_2Te) with a few percent (4-8%) of dopants like Ag, In, Ga, Ge, etc. [12]. Doping effects increase the crystallization temperature of Sb-Te systems considerably. Among the doped materials, AIST (Ag, In doped Sb_2Te) has been shown to be excellent [204,205], and has been commercialized for rewritable optical discs for decades.

Here we study the structural properties of amorphous AIST ($\text{Ag}_4\text{In}_3\text{Sb}_{67}\text{Te}_{26}$) and Sb_2Te . In Figure 4.9, the total $g(r)$ and PPCFs are plotted. The total $g(r)$ is not significantly affected by the seven percent Ag/In dopants. The first peak positions of PPCFs of Ag and In atoms are slightly shifted to lower r compared to that of Sb and Te. In the partial $g(r)$ of Sb and Te, the width of the first peak decreases slightly in the presence of Ag/In dopants, i.e. certain long bonds (3.2-3.6Å) around Sb and Te atoms are shortened, indicating a slightly more compact surroundings around Sb and Te atoms. This can be better visualized by the distribution of coordination numbers at the same cutoffs, see insets of Figure 4.10. In Sb_2Te , most Sb atoms have 4 neighbors and then 3 neighbors; after doping, the number of 5 coordinated Sb atoms increases. Similar trends also hold for Te atoms. As regards Ag and In, most of the atoms are 5

fold coordinated. 6 coordination is also common for Ag. A detailed discussion of nearest neighbor bond length and averaged coordination numbers will be presented in Chap 5 together with EXAFS measurements. Here we just mention that the amorphous structures generated by AIMD compare well with experiments.

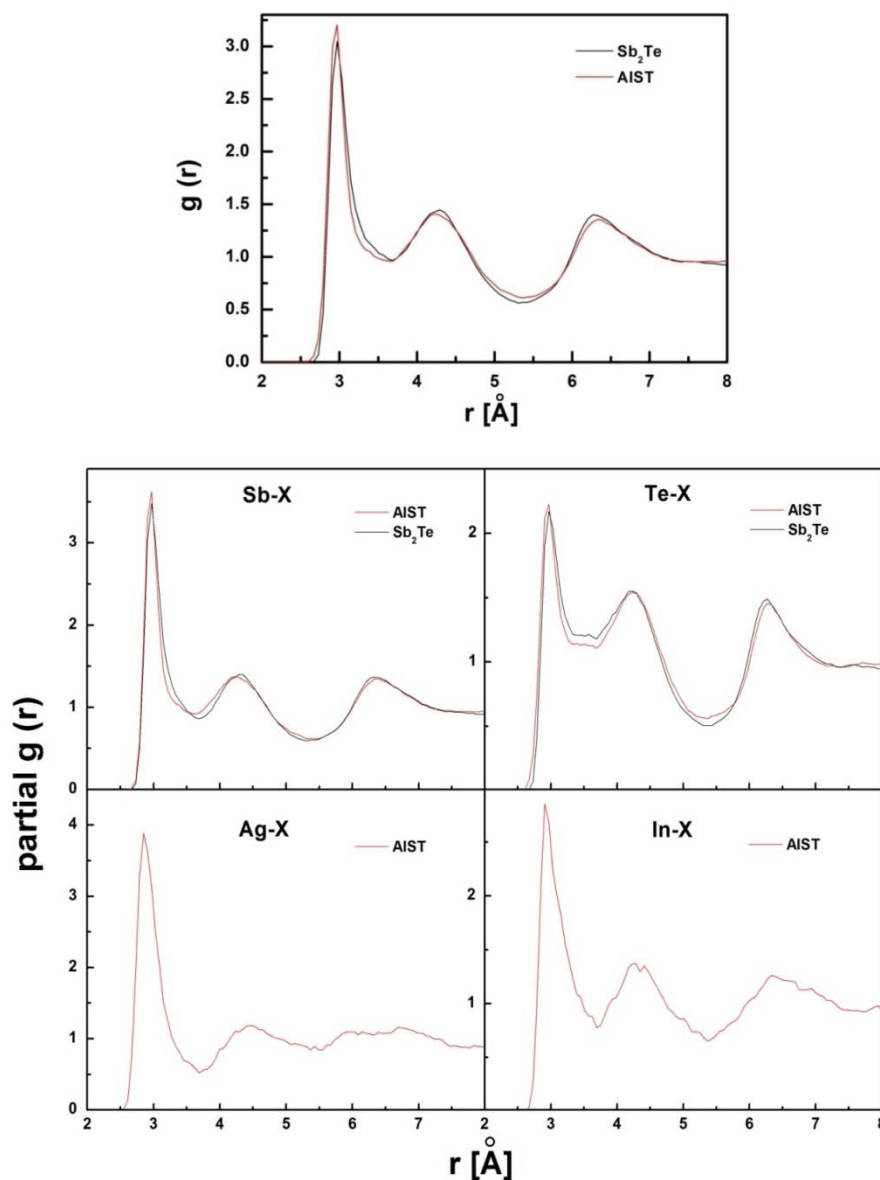


Figure 4.9 The total $g(r)$ and PPCFs of amorphous AIST (red) and Sb_2Te (black) at 300 K.

To further shed light on the local bonding environment, we calculated the angular distribution functions, shown in Figure 4.10. They exhibit a large peak at $\sim 90^\circ$ and a secondary peak at $\sim 165^\circ$. After distinguishing the contribution from different elements, it is found that the secondary peak is mainly contributed by Sb atoms,

suggesting quite some Sb atoms are in a d-octa configuration with coordination number larger than 3. The majority of Te atoms is in d-octa-3 configuration. d-octa-4 configuration for Te atoms increases slightly after doping. No tetrahedral units are found in these compounds.

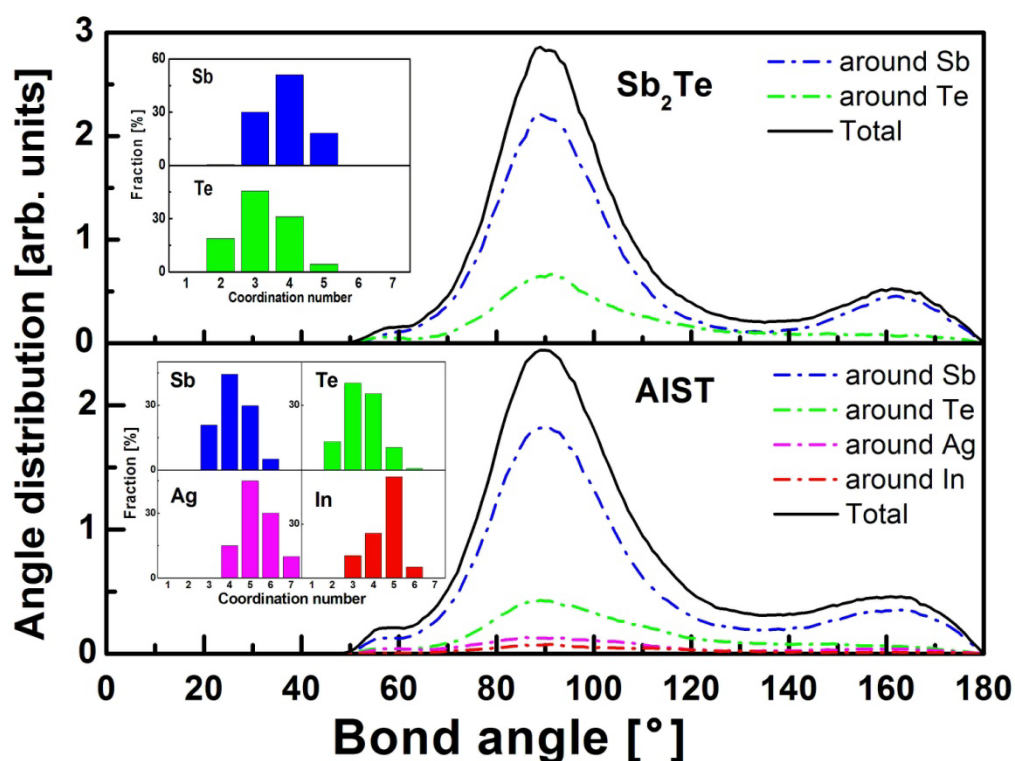


Figure 4.10 The angular distribution functions and coordination number distribution of amorphous AIST and Sb_2Te .

The medium range order of AIST and Sb_2Te is drastically different from group 1 PCMs (shown in Figure 4.11): 5-fold primitive rings dominate over 4-fold rings and other primitive rings. In AIST, the fraction of 4-fold rings further decreases. Within the four membered rings, the ABAB alternation no longer prevails (only a fraction of 20-25%). The concentration of voids is quite small in AIST and Sb_2Te (only 2-3%).

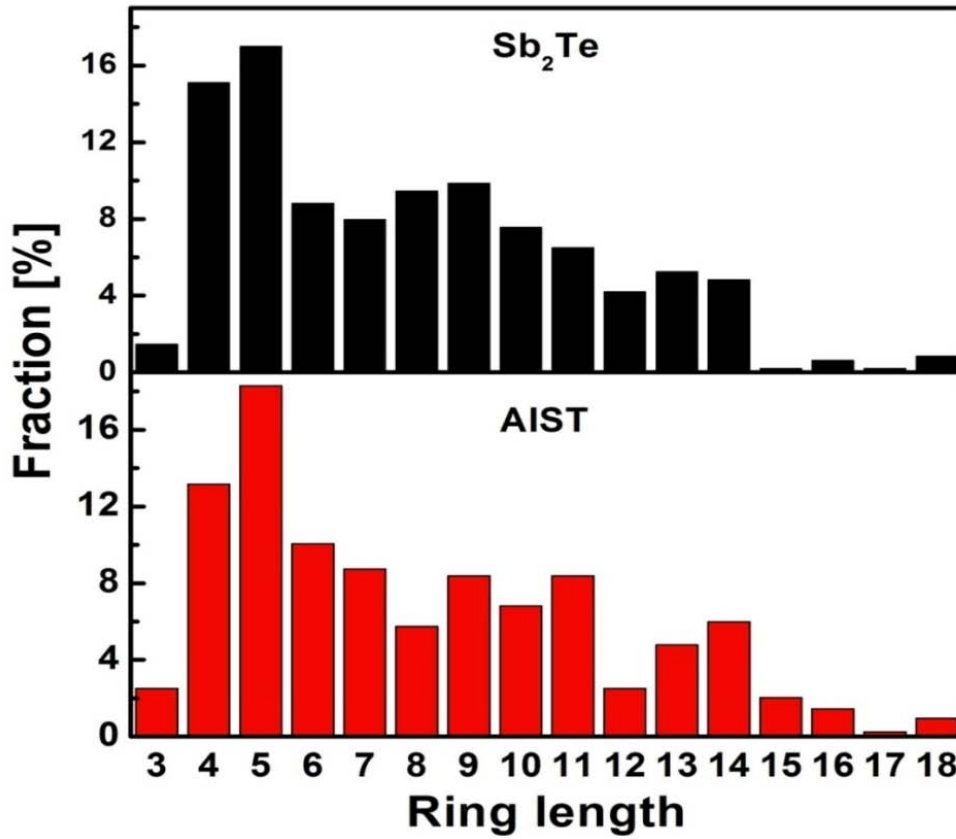


Figure 4.11 The statistics of primitive rings in amorphous AIST and Sb₂Te.

4.2.4 Group 3 PCMs doped Sb

The group 3 PCMs are located around the Sb corner in the ternary diagram. Dopants are necessary to stabilize the amorphous state at low temperatures. Note that amorphous Sb thin films crystallize in a few minutes at room temperature. Popular compounds like Ge₁₅Sb₈₅, In₁₅Sb₈₅, Ga₁₅Sb₈₅ belong to this group. Although amorphous Sb is not thermally stable at room temperature, the amorphous structural properties can still be accessed by AIMD simulations, which are performed at time scales of hundreds of picoseconds. Very recently, together with Ronneberger *et al.*, we studied the melt-quenched amorphous Sb by means of AIMD. Due to the lack of information about the experimental density of amorphous Sb, we used 6.48 g/cm³, which is close to the measured liquid density. We also tested few other densities, and found the structural properties do not depend strongly on the density (at close to ambient pressure level).

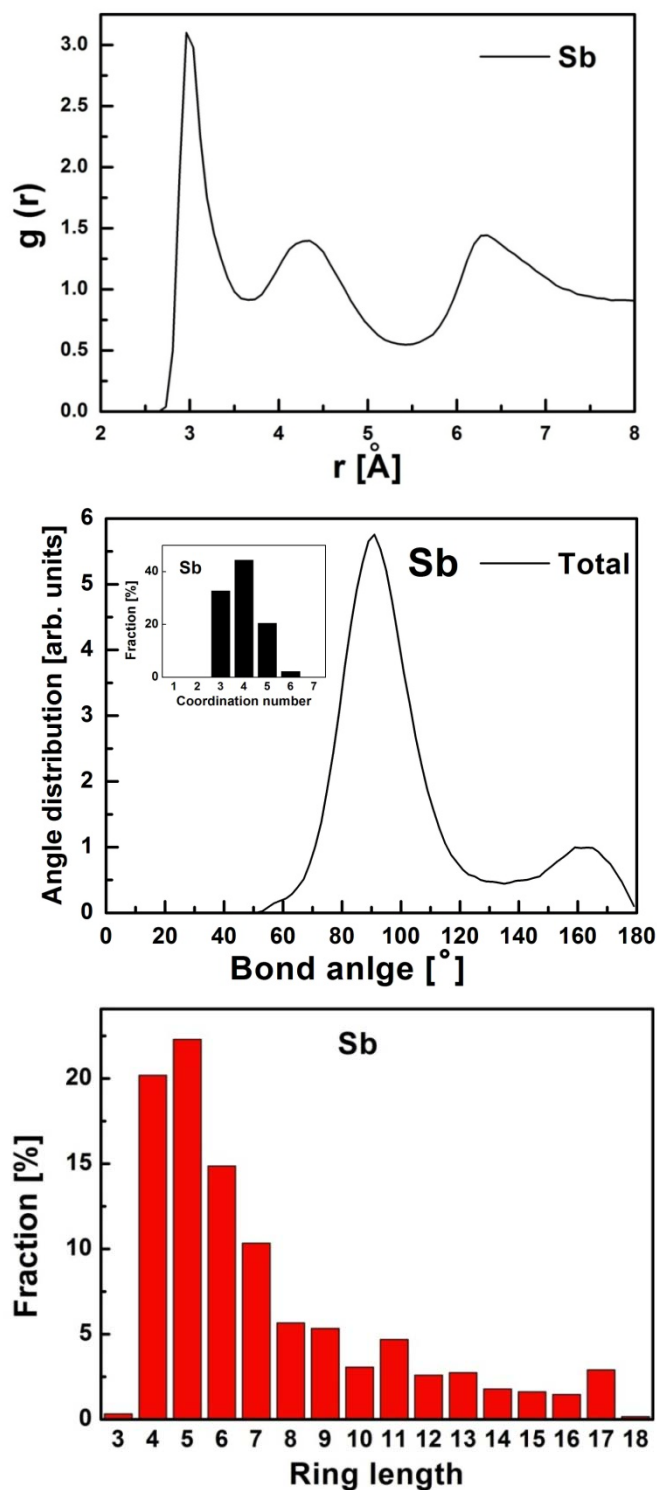


Figure 4.12 Structural properties of amorphous Sb: $g(r)$, ADF and primitive rings statistics.

The structural properties are summarized in Figure 4.12. The nearest neighbor bond length can be derived from the pair correlation function. It turns out to be 2.95 Å. The first peak of $g(r)$ decays smoothly and reaches the first minimum until 3.5 Å. A primary peak and a secondary peak are present at $\sim 90^\circ$ and $\sim 165^\circ$ in the ADF curve,

indicating most of Sb atoms are in d-octa configurations. No tetra Sb units exist in amorphous Sb. Most of the Sb atoms are 4-fold coordinated, followed by 3 and 5 coordination. The medium range order of amorphous Sb is dominated by 5-membered ring. 4- and 6- membered rings are also present in significant number. The concentration of voids is very small, only 1%.

4.3 Summary and outlook

To conclude, we studied the structural properties of several typical amorphous PCMs by means of AIMD. As regards Ge-free PCMs, the comparison of structural properties between theory and experiment is good. As regards Ge-related PCMs, such as GeTe and GST, the nearest neighbor bond lengths for Ge atoms are found to be larger than the experimental ones. We are currently working on this issue by considering more sophisticated non-local van der Waals correction. For amorphous GeTe/GST, a fraction of 20-30% Ge atoms is in a tetrahedral configuration. We performed a detailed chemical bonding analysis for a-GeTe, and found the homopolar Ge-Ge bonds stabilize the tetrahedral units significantly.

Chapter 5 Crystallization Kinetics

In this chapter, I focus on the ultrafast crystallization phenomenon, which is one of the most fascinating feature of PCMs. A PCM amorphous mark (e.g. $\text{Ge}_2\text{Sb}_2\text{Te}_5$) can remain stable at room temperature for more than 10 years, while it can crystallize very rapidly (nanoseconds level) at high temperatures (600K-700K). In other words, the crystallization kinetics changes by almost 17 orders of magnitude only by heating the samples by a few hundreds of Kelvin [206]. Very recently, sub-nanosecond crystallization has been realized by applying an external electric field to $\text{Ge}_2\text{Sb}_2\text{Te}_5$ [21]. The very rapid crystallization speed can already compete with volatile dynamic random access memories; moreover, PCMs are non-volatile materials, so that non-volatile phase change random access memories (PCRAM) are becoming feasible [207, 208].

To understand the fast crystallization phenomena, the study of the amorphous state and its comparison with the corresponding crystalline state help considerably [22, 27, 150]. However, the analysis of structural properties alone is not sufficient to clarify this strong temperature dependent behavior of crystallization speed. The crystallization process at elevated temperature involves dramatic structural changes due to the high mobility of atoms. Therefore, more direct measurements and simulations are needed to access the dynamical process at high temperatures.

I divide this chapter into two parts: 1> I review the recent theoretical and experimental progress on the crystallization kinetics of PCMs. 2> I focus on the crystallization process in growth-dominated PCMs, in particular, Ag, In doped Sb_2Te (AIST) and clean Sb_2Te . The stoichiometry of AIST considered here is $\text{Ag}_4\text{In}_3\text{Sb}_{67}\text{Te}_{26}$.

5.1 Recent progress on crystallization kinetics of PCMs

In 2008, for the first time Hegedüs and Elliott [172] succeeded in crystallizing $\text{Ge}_2\text{Sb}_2\text{Te}_5$ by slowly quenching the liquid to 600 K using AIMD. Due to the too small

system size (only 60-70 atoms), periodic boundary effects are so strong that the estimation of critical nuclei was not feasible. Later in 2011, the same group succeeded to crystallize a bigger a-Ge₂Sb₂Te₅ model (180 atoms) by heating the amorphous state to 600K, and they observed the incubation process and determined the critical nucleus to be made of 5-10 connected GST cubes (less than 50 atoms) [40]. Besides, not vacant site is present in the recrystallized part, i.e. all the vacancy voids segregate to the amorphous-crystal interface. They authors claimed that the vacancy voids would slowly diffuse into the recrystallized part and exchange with the cationic atoms Ge/Sb upon long time thermal annealing [209]. In 2012, Kalikka *et al* [41] has generated much bigger amorphous Ge₂Sb₂Te₅ models containing 460 atoms with a fixed crystalline seed (58 atoms + 6 vacancies). By reheating the model up to 500K, 600K and 700K, the authors studied the growth process from the fixed nucleus. In this work, the finite size effect is reduced to a certain extent. No cavity segregation near the amorphous-crystal interface was observed and a certain amount of "wrong" bonds (e.g. Te-Te bonds) was inevitably present in the recrystallized state. These "wrong" bonds are expected to be "healed" upon long time thermal annealing.

Besides AIMD simulations, there were also breakthroughs in experiments. In 2012, Orava and coworkers [39] were able to measure the crystallization kinetics of as-deposited a-Ge₂Sb₂Te₅ up to 650 K, and an in-depth quantification of the crystallization process was provided by taking advantage of ultrafast differential scanning calorimetry (DSC) measurements. The fast crystallization of as-deposited amorphous Ge₂Sb₂Te₅ was linked to the high fragility of the supercooled liquid phase, as well as to the breakdown in the Stokes-Einstein relation between viscosity and diffusivity near the glass transition temperature T_g . Molecular dynamics (MD) simulations of melt-quenched GeTe employing classical neural-network potentials [42,210] seem to corroborate these conclusions.

In 2013, Salinga and co-workers [35] designed a new laser based device, which allowed them to investigate of the melt-quenched amorphous phase under isothermal conditions up to 550 K (highest feasible temperature, above this temperature, the amorphous mark crystallized too rapidly). Also the new device can address a large

range of growth velocities, spanning over 8 orders of magnitude. The authors investigated a growth-dominated PCM, AIST. A smooth interface growth from the surrounding crystalline matrix has been observed and measured. It was also shown that for very fast quenching rates, on the order of 10^{10} K/s (comparable to the rates occurring in memory cells), a glassy state was already formed at temperatures above the calorimetric glass transition temperature T_g determined based on as-deposited amorphous samples. This observation challenged the view by Orava *et al.* Besides, the growth velocity of this glassy state exhibits Arrhenius behavior as a function of T down to 380 K and such behavior cannot be explained solely by a decoupling between viscosity and diffusivity. At last, it is shown that the melt-quenched amorphous state differs very significantly from the as-deposited amorphous state in terms of growth velocity at low T , i.e. the melt-quenched state is almost 1000 times faster than the as-deposited state in the range 400-450K.

5.2 Interface growth in group 2 PCMs -- AIST

The experimental works by Salinga *et al.* [35] and Orava *et al.* [39] demonstrate the very high growth speed of phase change materials at elevated temperatures. Besides, further downscaling of the cell size is an important goal driven by industrial purposes, and recently, less than 8 nanometers phase change cells have been produced experimentally [33]. All of these findings encourage further *ab initio* calculations of crystallization kinetics in phase change materials. The time- and length-scales are so small that heavy computational approaches, such as *ab initio* molecular dynamics based on density functional theory, becomes feasible.

In this chapter, I mainly focus on the crystal growth phenomena instead of nucleation, since for very small phase change cells, i.e. few nanometers in length, crystal growth at the crystalline-amorphous interface becomes more and more important, even for PCMs having high nucleation rates (e.g. GST). Note the grain size of $\text{Ge}_1\text{Sb}_2\text{Te}_4$ is 20 nm [32], and for a 8-nm phase change cell made of GST

compounds, interface growth may be dominant. Here, we focus on the well-known growth-dominated PCM, AIST.

By means of AIMD, we generate large melt-quenched amorphous models containing a fixed two dimensional crystalline matrix and study the interface growth from this matrix after reheating them to target temperatures. The models are randomized at 3000K and brought to melting temperature (850K) within 30ps. After equilibrations for 30ps at the melt and they are quenched to 300K within 30ps, and they are equilibrated at room temperature for another 30ps. The models contain 810 atoms, which corresponds to 27 atomic layers in the crystalline phase (see Chap 3). Two atomic layers are fixed at the crystalline positions along the y-z plane during randomization and melt-quench procedure, and 2-3 additional crystalline layers are formed during quenching. We set the x-axis as the growth direction. The cell size along x is more than 5 nm in total and a 4 nm thick amorphous slab remains after quenching, which is sufficiently large to study interface growth process. Snapshots of amorphous AIST (a-AIST) and Sb_2Te (a- Sb_2Te) with crystalline seeds are depicted in Figure 5.1.

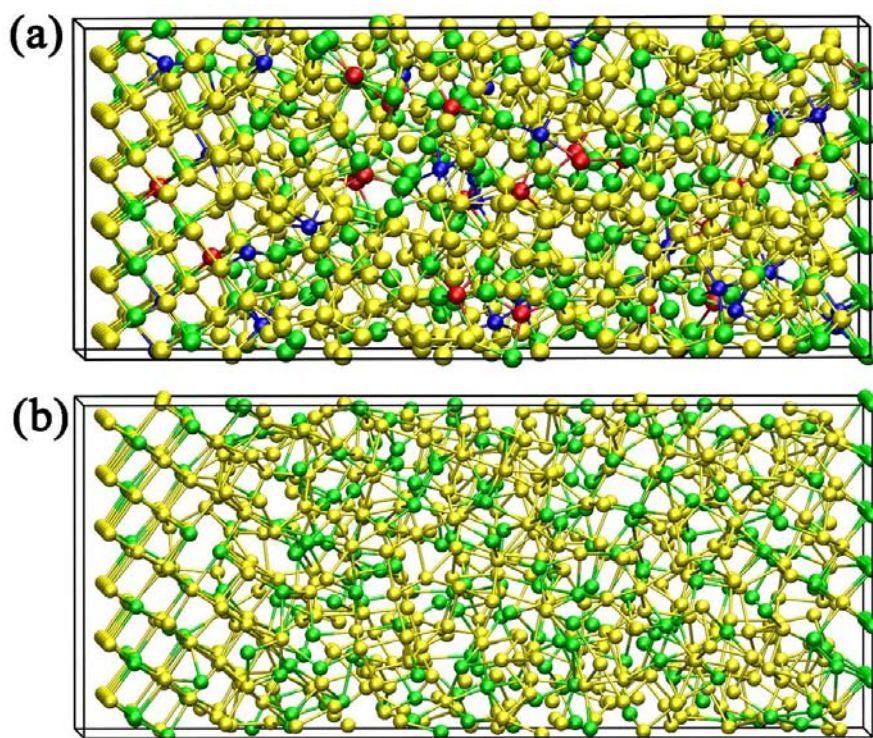


Figure 5.1 The melt-quenched amorphous (a) AIST and (b) Sb_2Te with crystalline seed. Ag, In, Sb and Te atoms are rendered with blue, red, yellow and green spheres.

In order to investigate the crystallization process, we consider different target temperatures and perform canonical (NVT) simulations there. We fix the density at the experimental value of the crystalline AIST during these crystallization simulations. Although the density contrast between amorphous and crystalline AIST is not negligible, 5 % [211], our procedure is relevant to practical experimental setups [35] and phase change memory cells [33], wherein the amorphous spots are constrained by the crystalline surroundings during the recrystallization process.

5.3 Structural properties of amorphous and recrystallized AIST

First, we investigate the structural properties of amorphous AIST by comparing the model generated by AIMD with the as-deposited sample produced experimentally. The partial pair-correlation functions (PPCFs) are computed based on the AIMD trajectory at 10 K, shown in Figure 5.2. The vertical dashed lines mark the first peak positions, indicating the nearest-neighbor bond lengths r . We present them together with the ones derived from the EXAFS measurements in Table 5.1. It is worth mentioning that the measurements of EXAFS spectra and X-ray diffraction (XRD) pattern (see below) as well as the simulations of EXAFS spectra (see below) were done by P. Zalden.

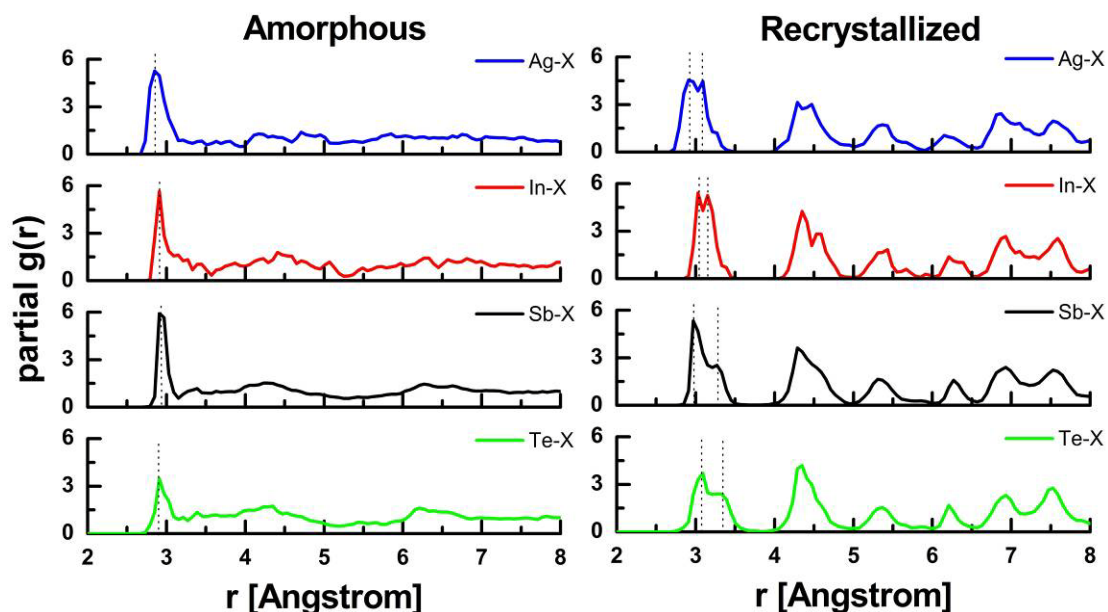


Figure 5.2 PPCFs of both amorphous and recrystallized AIST at 10 K. The vertical dashed lines indicate the primary peak positions.

Obviously, the first peak positions of both impurities (Ag-X, In-X) and Sb, Te (Sb-X, Te-X) are in good agreement with the EXAFS measurements. The bond length difference is smaller than 3%, which is within the tolerance of GGA functionals. As discussed before, the coordination numbers (CNs) are obtained by integrating the PPCFs curves up to certain cutoffs (3.1 Å is used for all four edges). The coordination numbers of Ag, In and Sb from AIMD simulations compare well with the EXAFS ones, while the coordination number of Te from AIMD simulations is slightly larger than that of EXAFS measurements.

Atom	$r_{\text{EXAFS}}(\text{\AA})$	$r_{\text{AIMD}}(\text{\AA})$	N_{EXAFS}	N_{AIMD}
Amorphous				
Ag	2.81(1)	2.85	4.0±0.7	4.5
In	2.82(1)	2.90	2.7±0.5	3.0
Sb	2.87(1)	2.92	3.4±0.6	3.2
Te	2.83(1)	2.90	1.6±0.4	2.3
Recrystallized				
Ag	2.84(3),3.02(3)	2.92,3.07	7.2±0.7	6.2
In	2.80(1),2.99(1)	3.00,3.14	6.6±0.7	6.0
Sb	2.89(1),3.32(1)	2.97,3.28	6.2±0.6	5.9
Te	2.94(1),3.39(3)	3.07,3.30	3.8±0.5	5.4

Table 5.1 The nearest neighbor bond lengths and coordination numbers for the amorphous and the recrystallized AIST, obtained from AIMD simulations and EXAFS experiments. The AIMD coordination numbers are calculated using the cutoff radius of 3.1 Å (amorphous) and 3.4 Å (recrystallized).

To gain further information about the local structure, we perform direct simulations of EXAFS spectra based on the atomic coordinates from AIMD simulations using FEFF code [212], and plot them together with measured EXAFS in Figure 5.3. More details about EXAFS experiments and simulations can be found in Appendix C.

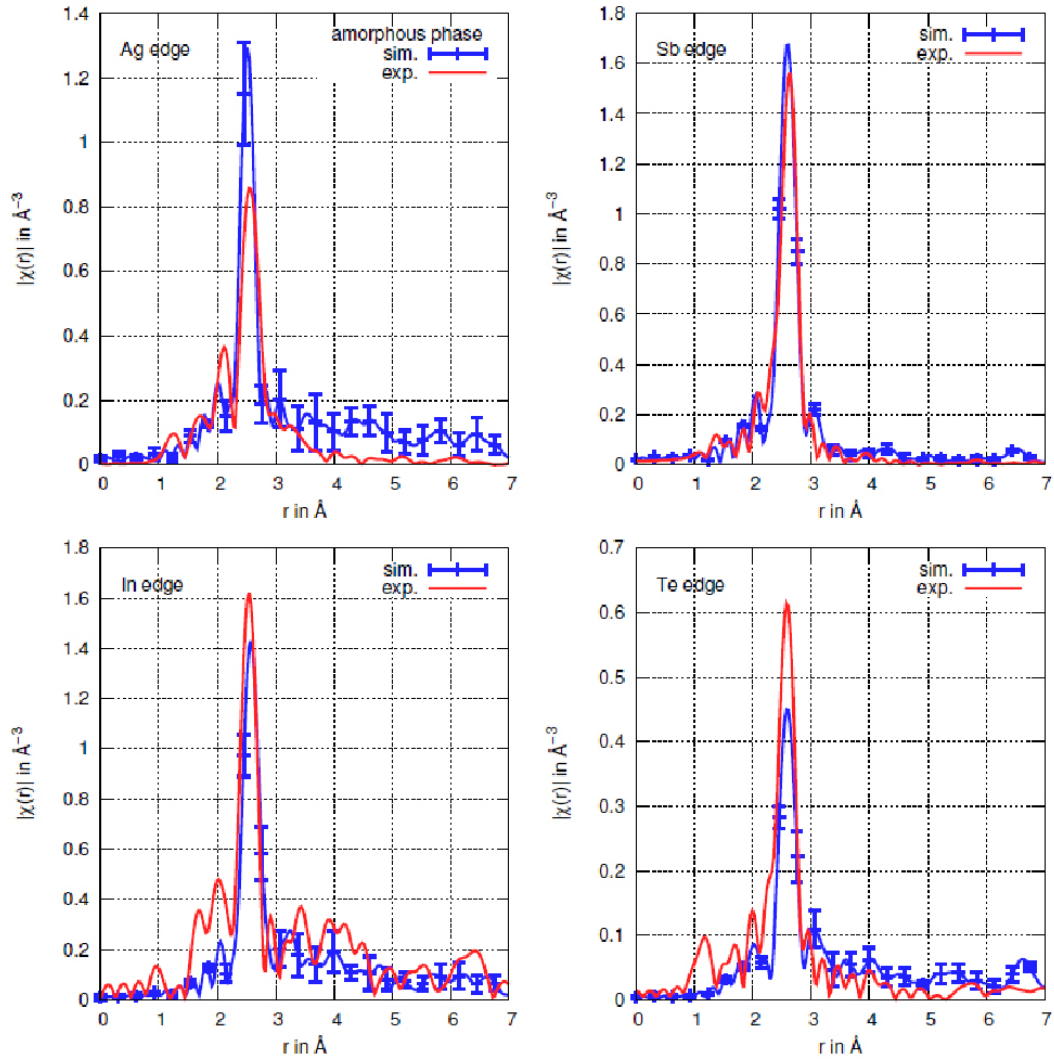


Figure 5.3 Experimental (red) and theoretical (blue) EXAFS spectra of amorphous AIST at 10 K.

Apparently, the primary peak position of the experimental and theoretical spectra overlap, suggesting very similar nearest neighbor bond lengths. The peak heights in EXAFS are dominated by the atomic disorder at the given distance and partially influenced by the CNs. One can observe that the disorder around In and Sb atoms is perfectly reproduced by AIMD, whereas discrepancies are observed at Ag and Te edges. These deviations indicate that the Te (Ag) atoms have a higher (lower) ordering tendency in the measured, as-deposited sample than in the melt-quenched simulated model.

More information about the amorphous network of AIST, including angular distribution function, primitive rings statistics, etc., can be found in Chap 4. It is worth mentioning that our results match quite well with a previous AIMD/EXAFS work on a slightly Sb-rich AIST, $\text{Ag}_{3.5}\text{In}_{3.8}\text{Sb}_{75.0}\text{Te}_{17.7}$ [150].

In the same work [150], the authors generated crystalline AIST by distributing Ag, In, Sb and Te atoms randomly onto a perfect crystalline Sb lattice (A7). After geometry optimizations, distorted octahedral local structural motifs were obtained. Since (defective) distorted octahedral units were also detected in the amorphous phase, the authors proposed a bond-interchange model based on this structural similarity for the fast crystallization mechanism at high temperatures. In the following, we directly simulate the crystallization process of AIST. We shall see that the recrystallized model contains more atomic disorder than the previous thoughts; during the crystallization process at high temperatures, atoms are mobile and diffusive, leading to more dramatic structural changes than a simple bond-interchange model.

By reheating the model shown in Figure 5.1 (a) to high temperature, 585 K, we obtain a recrystallized model within 180 ps. Similarly, the recrystallized model forms a trigonal crystal (A7) lattice with random occupation of Ag, In, Sb and Te atoms, in line with the XRD measurements. We also simulate the XRD patterns based on the atomic coordinates obtained from AIMD. The relative peak intensities as well as peak positions in the two patterns are in good agreement, as shown in Figure 5.4. The small shift of the peak positions is due to the slightly different density employed in the simulations compared to the XRD experiments.

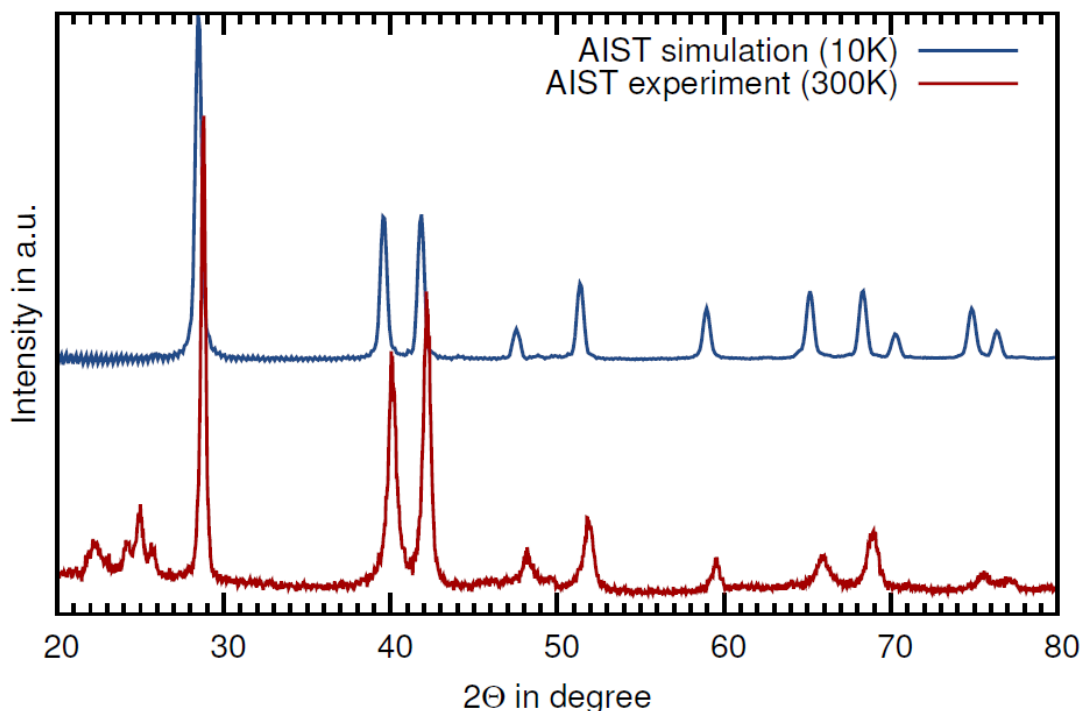


Figure 5.4 Theoretical (top) and experimental (bottom) XRD patterns of recrystallized AIST.

From the PPCFs of the recrystallized AIST (Figure 5.2 (b)), we observe double peaks for all four edges, indicating 3+3 coordination due to Peierls distortion. The EXAFS measurements also show such feature, and the nearest neighbor bond lengths as well as CNs show compatible results with our AIMD simulations for Ag, Sb and Te atoms. As regards In atoms, larger deviations 5-6% occur (summarized in Table 5.1). In a perfect A7 crystalline lattice, every atom on the lattice should have a maximum CN of 6, however, Ag and In atoms in experimental samples have higher CN of 7.2 (0.7) and 6.6 (0.7) respectively, which suggests a significant fraction of Ag and In atoms occupy interstitial sites, which yield a CN of 7 or even 8. A typical interstitial Ag is shown in Figure 5.5 together with a standard substitutional Ag. It is also obvious that interstitial sites result in shorter averaged bond lengths. In the recrystallized model we show in Table 5.1, we observe 10% interstitial Ag but no interstitial In, which is due to the poor statistics, since there are only 20 Ag and 16 In atoms in our 540 atom model. In the subsequent simulations of crystallization, we also observe interstitial In atoms.

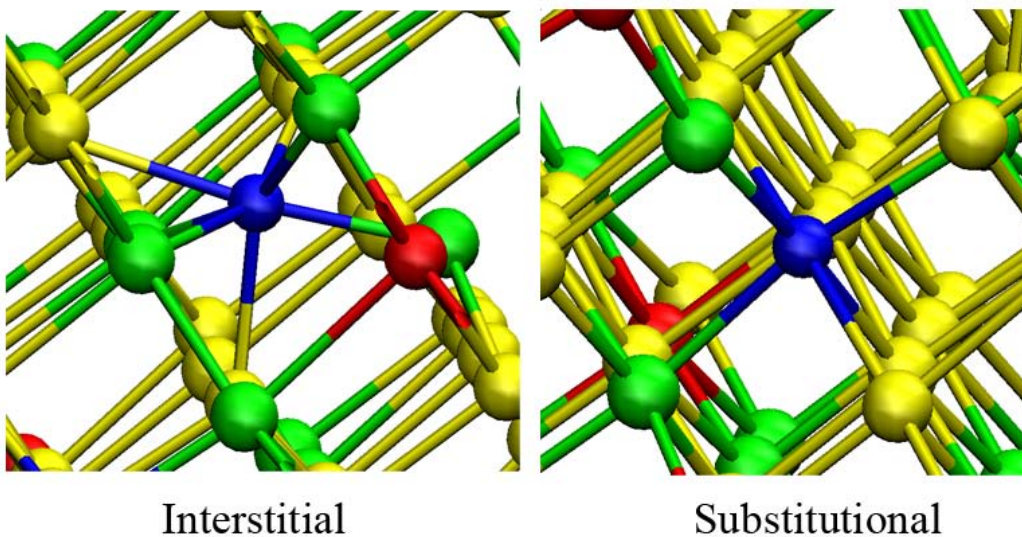


Figure 5.5 Interstitial and substitutional Ag (blue sphere) in the recrystallized AIST. CN of such interstitial Ag is 7.

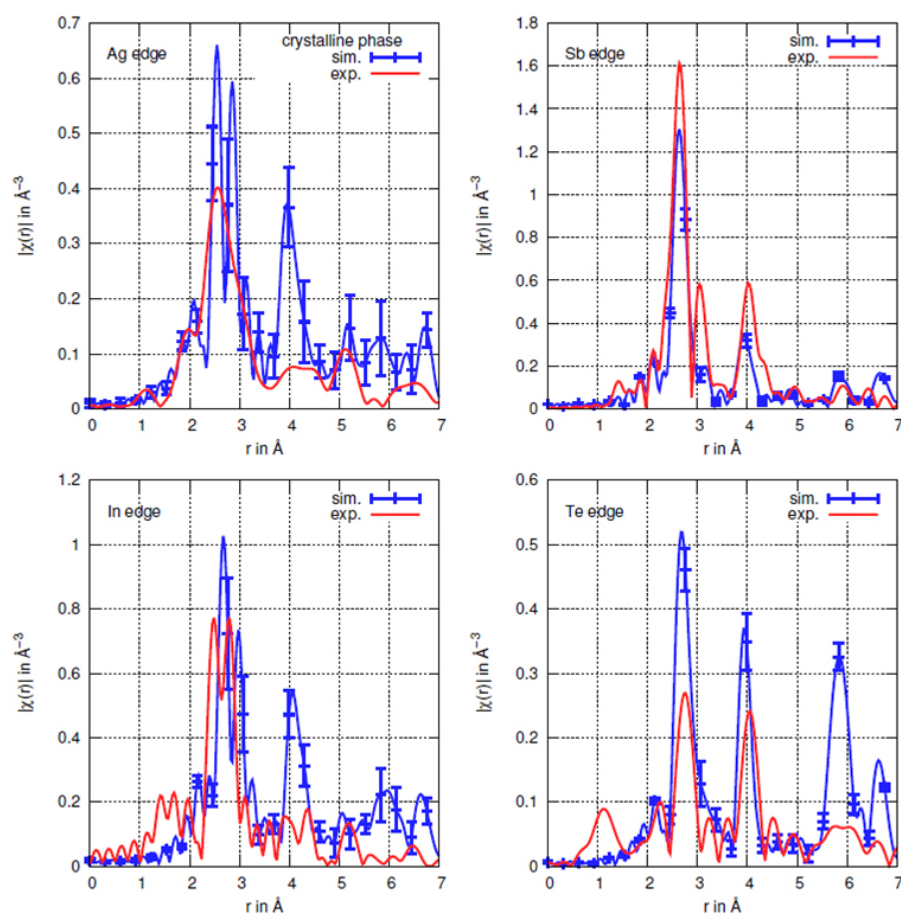


Figure 5.6 Experimental (red) and theoretical (blue) EXAFS spectra of recrystallized AIST at 10 K.

From the above analysis, we learn that many Ag and In atoms are located at interstitial sites in the oven crystallized as-deposited AIST, derived from the very high CNs. We also simulate the EXAFS spectra based on the recrystallized AIMD model, and depict them together with the experimental ones in Figure 5.6. For all edges except Sb, the atomic order resulting from the oven-heated crystallization is lower than the ordering from the simulated crystallization, in particular for the Te edge. This is also reflected in the averaged CN of Te in the recrystallized phase, which is 3.8 (0.5), significantly lower than 6. In principle, the local structure of recrystallized AIST might depend on the nature of the initial amorphous phase (as-deposited or melt-quenched), given also the very pronounced difference in crystallization speed, e.g. at 450K, AD is roughly 1000 times slower than MQ sample [35].

In summary, the recrystallized AIST has more atomic disorder than the previous thoughts, and it is difficult to predict the dynamical behaviors of the amorphous state at higher temperatures solely based on structural properties at room temperature, due to the fact that at room temperature, the structural properties of the simulated amorphous MQ model are similar to that of the experimental amorphous AD sample, while at 450 K, a factor of 1000 in growth velocity has been observed between MQ and AD sample. Thus, direct simulations of crystallization at high temperatures are desirable. In the following sections, we focus on the discussion of dynamical processes in amorphous AIST at high temperatures.

5.4 Growth velocity versus temperature, quenching rate effects

In this section, we derive the growth velocities v_g during the simulations of crystallization at different temperatures and compare them with the experimental ones. We compute the evolution of the number of crystalline-like atoms, N_c (see Figure 5.7). The ratio N_c/N (where N is the total number of atoms) marks the interface evolution along the growth direction (x-axis): by multiplying it by the x-axis cell parameter and dividing by the corresponding crystallization time Δt , one obtains v_g . To distinguish crystalline-like and amorphous-like atoms, we employ a bond order parameter

"dot-product", q_4^{dot} , which can clearly discriminate the two phases (see Figure 5.8). Details about q_4^{dot} are provided in Appendix B.

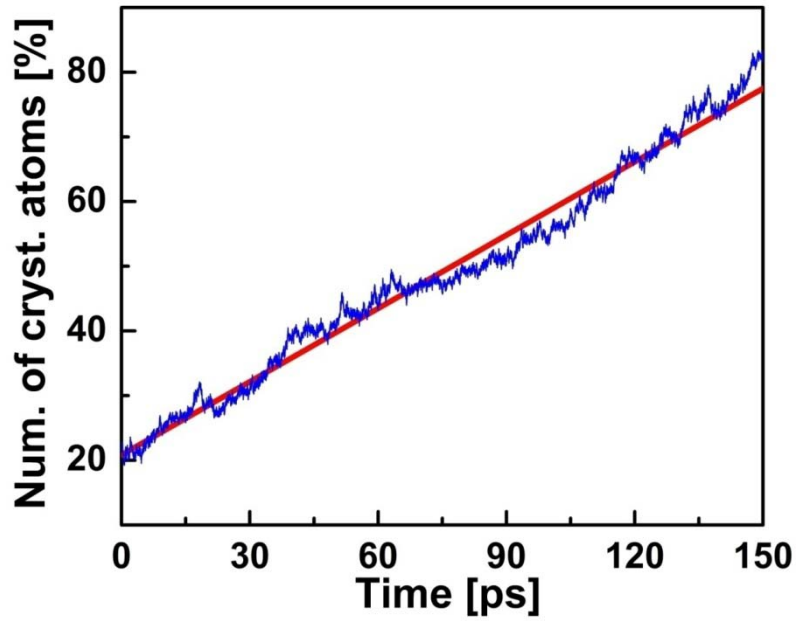


Figure 5.7 Evolution of number of crystalline-like atoms during crystallization at 585 K of AIST-810atoms model (blue line). The red straight line indicates the linear regression of the blue line. The last part of the growth (larger than 150 ps) is removed for the linear regression.

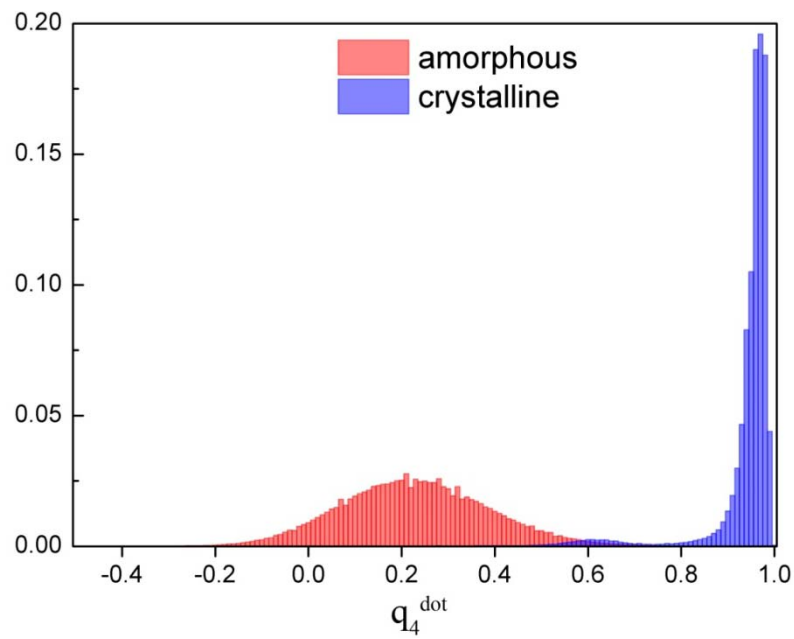


Figure 5.8 Distribution of the values of order parameter q_4^{dot} (i) for amorphous and crystalline AIST. Produced by I. Ronneberger.

Several target temperatures are considered, ranging from 585 K to 455 K. The simulated growth velocity changes from 8 m/s to 5 m/s, as shown in Figure 5.9. Above 550 K, the growth velocities are in good agreement with time-resolved reflectivity measurements [35], however, large deviations are found at lower temperatures in the range 450K-500K, the experimental growth velocities are 10^{-2} - 10^{-5} m/. This discrepancy stems from the large difference between the calculated and experimental diffusion coefficients D at these temperatures, as shown in Figure 5.10. We compute the bulk diffusion coefficients D independently based on AIMD trajectories of purely amorphous models (no crystalline seeds) at different temperatures:

$$D = \frac{\langle r^2 \rangle}{6t} \quad (5.1)$$

where $\langle r^2 \rangle$ is the mean square displacement, t is the simulation time. All these simulations are performed on a 80 ps time scale. (These calculations of diffusion coefficients were performed by I. Ronneberger.) As regards the experimental D , it is very challenging to measure it directly, instead D is obtained from the measured growth velocities by assuming the validity of Wilson-Frenkel (WF) equation [213,214],

$$v_g(T) = \frac{6D(T)}{\lambda} \left[1 - \exp\left(-\frac{\Delta\mu(T)}{k_B T}\right) \right] \quad (5.2)$$

(where $\Delta\mu(T)$ is the chemical potential difference between the supercooled liquid and the solid phase and λ is the average inter-atomic distance). Usually the chemical potential difference is estimated by employing Thompson-Spaepen formula [215],

$$\Delta\mu(T) = \Delta H_m \frac{T_m - T}{T_m} \left(\frac{2T}{T_m + T} \right) \quad (5.3)$$

where ΔH_m is the heat of fusion (173 meV/at) and T_m is the melting temperature (808 K).

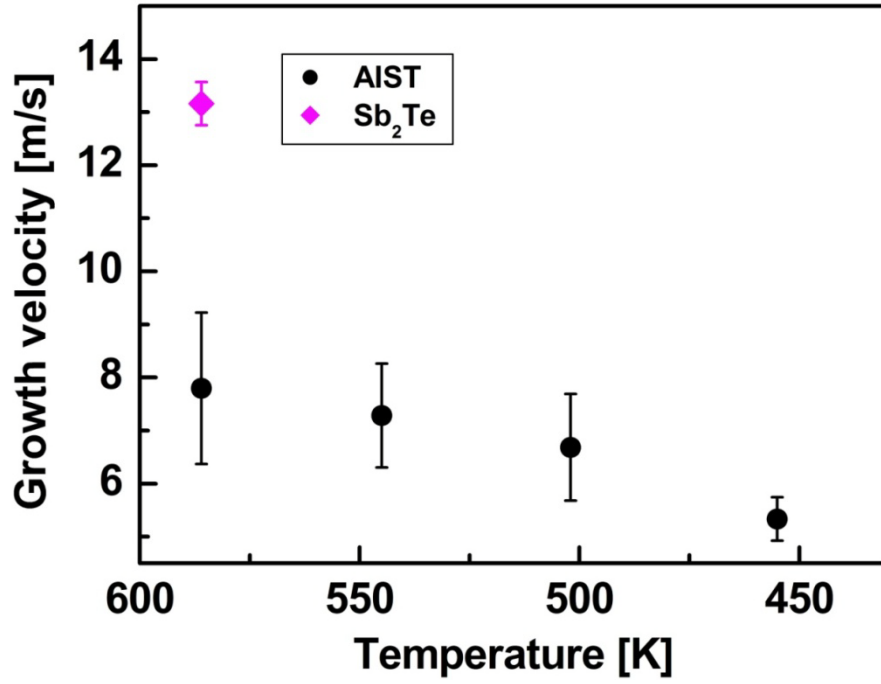


Figure 5.9 Growth velocities derived from AIMD simulation for AIST and Sb₂Te at different temperatures. Four different models containing 810 atoms and 540 atoms are considered to gain better statistics.

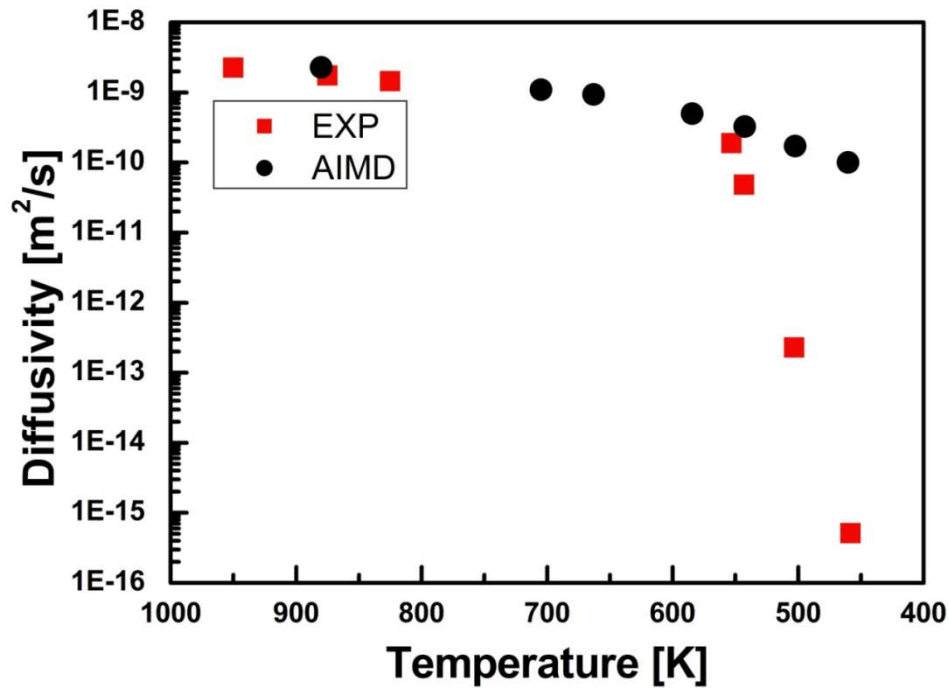


Figure 5.10 Experimental and simulated diffusion coefficients at different temperatures. The simulated diffusivity is obtained by linear fitting of mean-square displacement, see main text. The experimental values at the melting and 600K-450K are taken from ref [216] and [35].

By fitting the $D(T)$ data with formula

$$D(T) = D_0 \exp\left(-\frac{E_a}{k_B T}\right), \quad (5.4)$$

one can obtain an activation energy and a pre-factor D_0 . We fitted both the theoretical and experimental data from 450K to 550K, and obtained $E_a = 0.30$ eV, $D_0 = 2.15 \cdot 10^{-7}$ m²/s (simulations) and $E_a = 2.78$ eV, $D_0 = 2.03 \cdot 10^{15}$ m²/s (experiments). The theoretical E_a and D_0 deviate strongly from the experimental ones obtained by reflectivity measurements; instead, they are closer to the experimental data of liquid Sb₄Te at much higher temperatures (810K-950K, Figure 5.10), where $E_a = 0.24$ eV and $D_0 = 4.10 \times 10^{-8}$ m²/s. These smaller E_a and D_0 are comparable to the values observed in diffusion processes in crystals and glasses [217], where the atomic rearrangements are governed by the motion of single atoms. On the other hand, collective atomic motion has been observed in some supercooled liquid metals [218], where large E_a and D_0 were found. The experimental D_0 of AIST is even larger, suggesting a rearrangement process involving a considerable number of atoms below 550K, which eventually leads to the slowing down of the kinetics [219]. These E_a and D_0 data are summarized in Figure 5.11. Remarkably, the very large activation energies and pre-factors are crucial for PCMs to form stable amorphous states at low temperatures. From the experimental diffusivity data, a clear change of slope occurs near 550K, suggesting a change of motion mode from single-atom motion (supercooled liquid) to collective motion (glass), or vice versa. Interestingly, the small activation energies and pre-factors at high temperatures indicate the very high atomic mobility, which ensures the fast crystallization capability of PCMs.

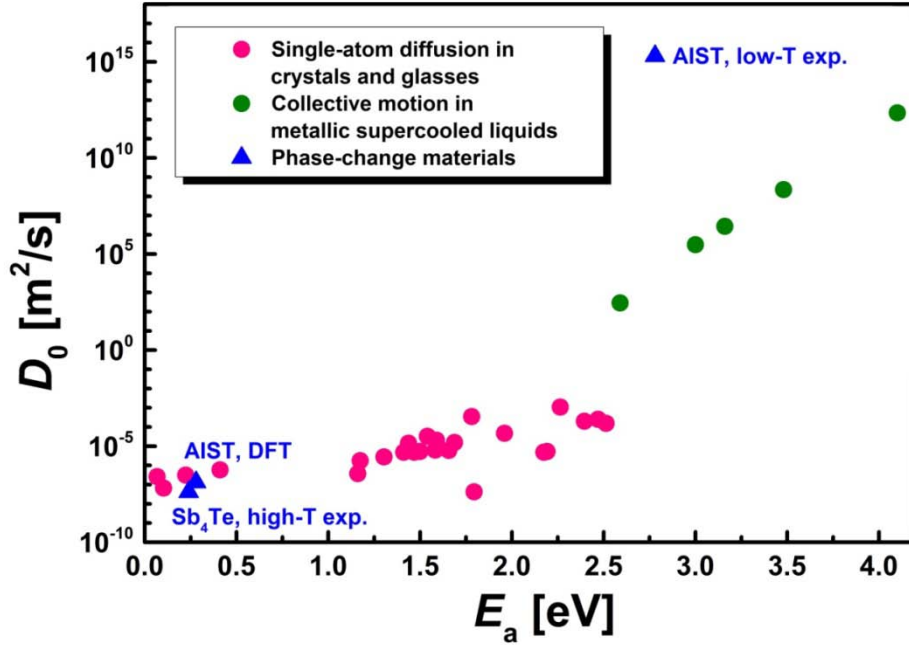


Figure 5.11 The map of E_a and D_0 for various systems. Contributed by M. Xu.

In order to make sure that the large growth velocity and diffusivity observed in our low temperature (below 550K) simulations are not due to artifacts, we discuss several spurious effects that can lead to an overestimate of v_g and D , but we argue none of them can be responsible.

1> approximated functional: we employed approximate GGA functionals in all our simulations. Although these functionals may well underestimate activation barriers, we believe that the a factor of 10 discrepancy between experiments and simulations is far too large to be attributed to them. On the other hand, the very reasonable amorphous structure as well as its dynamical properties at high temperatures support the usage of GGA functionals.

2> finite size effects: although the large system size already reduces finite size effects considerably, non-negligible errors should still exist when evaluating both the growth velocity and the diffusion coefficients. We think finite size effects cannot account for such a huge mismatch either. In fact, if one assumes that, at T above the experimental T_g , the system is in a supercooled liquid phase obeying Stokes law (this assumption may not hold for PCMs though [210]), then finite size effects would lead

to an underestimation of D [220].

3> quenching procedure: in our simulations, the systems were firstly quenched to room temperature, equilibrated there for 30 ps, and then reheated to the target temperatures (RH procedure), while experimentally the amorphous films were directly quenched to the target temperature from the melt (DQ procedure). The two procedures lead to different diffusivities, e.g. the latter D are 4 times larger than the former at 500K for GeTe (at a fixed quenching rate) [221]. This difference is much smaller than the difference between the simulated and experimental D of AIST at 500 K, a factor of 10^3 . Moreover, this difference will become even larger if DQ procedure is adopted for simulations. Since the DQ procedure is less relevant to industrial applications, we don't consider it here.

4> thermostat: we calculated the bulk diffusivity of the purely amorphous state by using a stochastic Langevin thermostat. It is well known that thermostats (in particular, stochastic thermostats) can affect the dynamical properties significantly. In general, NVE simulations are recommended for the calculation of diffusion coefficients [66]. Since we have to use stochastic thermostats for the simulations of crystallization, we use the same thermostat to calculate the bulk diffusion coefficients for the sake of consistency. In order to estimate the error due to the thermostats, we performed some crosscheck simulations within the NVE ensemble, and we found the resulting D are about 2 times larger than the D calculated using Langevin thermostats. This effect will not change the temperature dependence of D significantly.

From the above analysis, we learn that none of the effects can lead to the huge discrepancy in v_g and D below 550K between experiment and theory, hence, the most plausible explanation is the difference in quenching rates, 10^{13} K/s (simulations) versus 10^{10} K/s (experiments). It has been suggested that if the quenching rate is too large and exceeds the so called critical quenching rate, the resulting glass is less stable against crystallization [222]. This should hold in particular for fragile systems that have complex energy landscape. The higher v_g and smaller E_a observed in our simulations should be related to this property, i.e. the system stuck in some shallow minimum in the energy landscape due to fast cooling [223]. At sufficiently high

temperatures (supercooled liquid regime), atoms move very rapidly and the network develops very fast; hence, quenching rate effects are weak, while they become much stronger when approaching lower temperatures (glass regime).

Naively, one expects to see structural differences at room temperature between the samples with very different dynamical properties at elevated temperatures. However, even the structural properties between fast-quenched and as-deposited (in some sense extremely slowly quenched) amorphous samples are quite similar, despite that there exhibits a factor of 1000 difference in their dynamical behaviors at for instance 430K.

Since our model is still dominated by single-atom motion at low temperatures (mostly probably due to too large quenching rate), the simulations cannot grasp the dynamical processes that occur in experiments, therefore, we instead focus on the crystallization process in the supercooled liquid regime, where the simulated dynamical properties compare well with experimental ones. A thorough investigation of the quenching rate effects will be our future work.

5.5 Crystallization kinetics at high temperature, role of impurities

In this section, we discuss in detail the crystallization process at high temperatures, where both the growth velocity and bulk diffusion coefficients are in good agreement with experiments. We show that the transition involves very dramatic structural changes and can be categorized as diffusion-limited interface-controlled growth. Moreover, our simulation of crystal growth is able to quantify the role of small concentrations of impurities.

To gain deeper understanding of the crystallization mechanism, we focus on the amorphous-crystalline interface region. We divided the supercell into slabs along the crystal growth direction (x-axis) and calculated the profiles of the order parameter Q_4^{dot} (which denotes the average of q_4^{dot} over a set of atoms), the atomic population and the diffusion coefficients along x-axis D_x , shown in Figure 5.12. The atomic population was obtained by computing the total number of atoms in each slab averaged over 600 fs. We chose a set of very thin slabs for this calculation in order to distinguish between the crystalline region and the amorphous region, while much

thicker slabs were chosen for calculations of Q_4^{dot} and D_x to gain better statistics. Q_4^{dot} and D_x within each slab were averaged over atoms and over time (600 fs and 30 ps, respectively).

In Figure 5.12 (a), we show a snapshot of the early stage of crystallization, which contains roughly 20% crystalline-like atoms. Initially, only two layers were fixed as the crystallization seed, a few more (2-3) crystalline layers were formed during very rapid quenching from T_m to T_{room} and the subsequent re-heating to 585 K. The models must be sufficiently large along the growth direction, otherwise, they would fully crystallize during the fast quenching process, e.g. a model containing 9 crystalline layers in total is not sufficient.

By calculating the averaged order parameter within each slab, we can better characterize the local structure as crystalline ($Q_4^{\text{dot}} \sim 0.9$), amorphous ($Q_4^{\text{dot}} \sim 0.3$) or interface region (rapid reduction of Q_4^{dot}). The interface extends over 3 slabs (7-8 Å), indicating a sharp transition region, which is also reflected in the atomic population profile. The thin interface suggests the interaction between the two interfaces is negligible at the initial stages of the crystallization process.

In Figure 5.12 (d), the profile of the diffusion coefficients along x-axis is shown, which can shed light onto the applicability of the WF equation (5.2) to AIST. We calculate v_g as a function of T from WF formula, using the bulk values of D from simulations (purely amorphous, no crystalline seeds) and Thompson-Spaepen expression for $\Delta\mu(T)$, and we obtain growth velocities comparable to the directly computed values of v_g shown in Table 5.2, the biggest deviation being a factor of 2 at 450K. So we can conclude the WF formula is generally applicable for AIST.

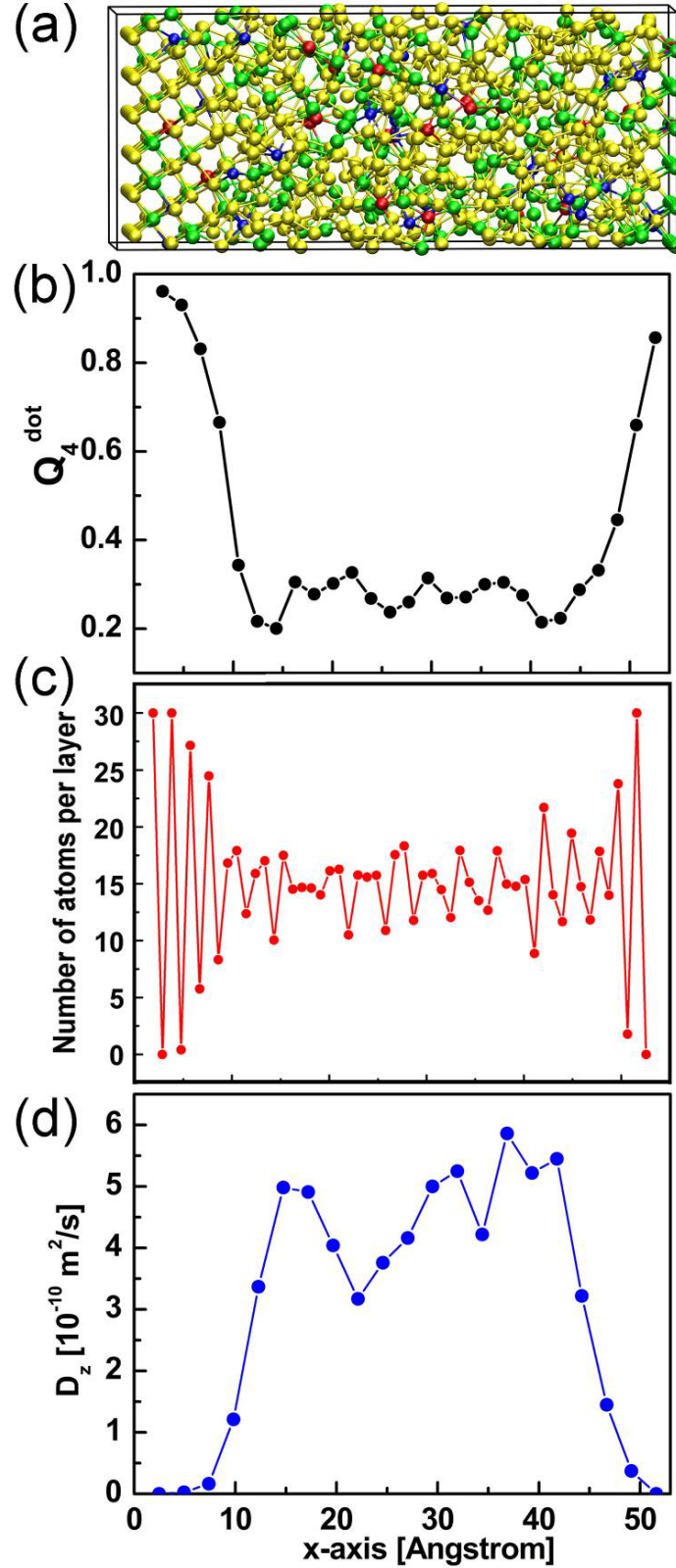


Figure 5.12 Profiles of the amorphous-crystalline interface of AIST at $T=585K$. (a) A snapshot of AIST containing 810 atoms at the initial stages of crystallization. Ag, In, Sb and Te atoms are rendered with blue, red, yellow and green spheres, respectively. Profiles of (b) the order-parameter Q_4^{dot} , (c) the atomic population and (d) the diffusion coefficients.

Temperature [K]	585	543	503	455
WF formula				
$D [\times 10^{-10} \text{ m}^2/\text{s}]$	4.97	3.27	1.72	1.00
$1-\exp[-\Delta\mu(T)/(k_B T)]$	0.54	0.62	0.68	0.75
$v_g [\text{m/s}]$	8.09	6.05	3.50	2.23
General form $v_g = \lambda k^+ S$				
$\tau [\text{ps}]$	8.30	11.27	14.37	20.15
$k^+ [\text{ps}^{-1}]$	0.1204	0.0884	0.0696	0.0496
S	0.38	0.44	0.46	0.50
$v_g [\text{m/s}]$	9.15	7.78	6.40	4.96
Simulations				
$v_g [\text{m/s}]$	7.80	7.28	6.68	5.33

Table 5.2 Comparison of the growth velocities v_g obtained from the Wilson-Frenkel (WF) formula, from the general form $\lambda k^+ S$ and directly from the simulations (see Figure 5.9 here only the averaged values are shown). λ is assumed to be equal to 2 Å.

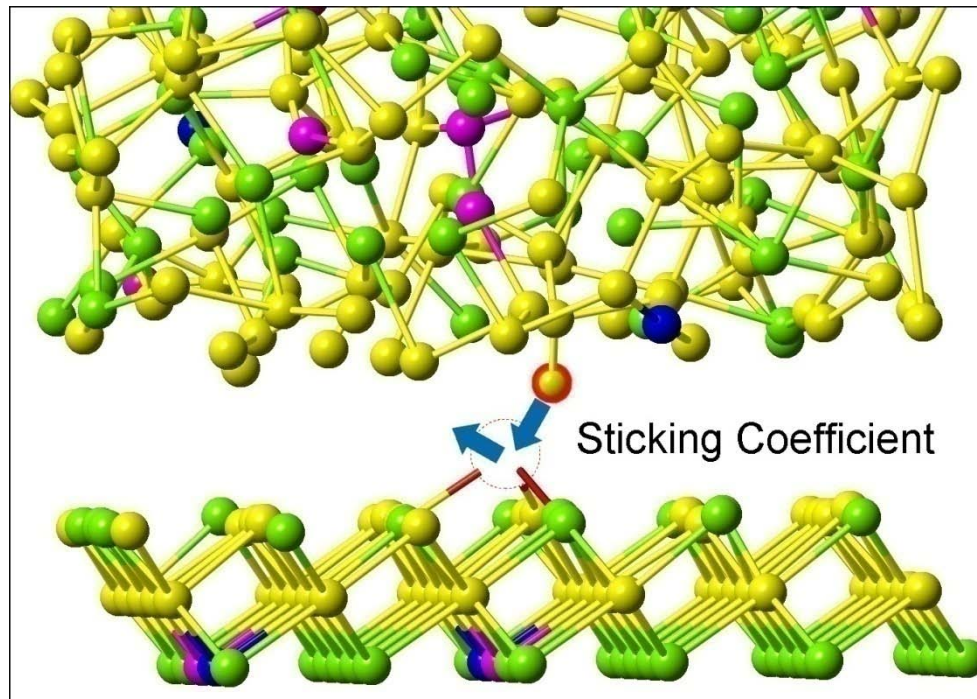


Figure 5.13 Sticking process at the crystalline-amorphous interface. An empty site is marked with dashed circle. The gap between the amorphous and the crystalline region is increased for the purpose of visualization.

During the crystallization process, atoms can jump from the amorphous phase to crystalline phase by sticking to the crystalline interface. Imagine there are certain empty sites (see Figure 5.13) formed near the crystalline interface, after occupying the site, the atom can form stable bonds with the nearest crystalline neighbors and become part of the crystal. Alternatively, the atom could jump out of the site. We name these atomic processes as "landing" and "escaping" events. Now we can better quantify the growth process by calculating the deposition rate k^+ and the sticking coefficient S . k^+ is defined as the rate of which atoms land on the crystalline part, and is given by the number of landing events per unit time. S is defined as the probability for atoms to stick to the crystalline interface and become part of the crystal after landing on it. S is computed as $(n_l - n_e)/n_l$, where n_l and n_e is the total number of landing and escaping events, respectively. Figure 5.13 is the schematic plot of the sticking process. More details about k^+ and S can be found in Appendix D.

In general, the crystal growth velocity is given by: $v_g \propto k^+ \cdot S$. In the WF limit, $k^+ \propto D$ and $S = 1 - \exp[-\Delta\mu(T)/(k_B T)]$. After calculating k^+ and S , we can evaluate the growth velocity as

$$v_g = \lambda k^+ S, \quad (5.5)$$

where λ is a constant factor having the unit of length ($\lambda=2\text{\AA}$ is used). The resulting v_g are shown in Table 5.2. Compared to the v_g from simulations, the ratio between the two sets of v_g changes about 20% in the range 585 K - 455 K. This good comparison supports our derivation of k^+ and S , despite the method we used is rather simple. By decomposing the role of k^+ and S in our simulations, we could learn that the decrease of v_g upon temperature reduction in our simulations is fully contributed by the k^+ term, since the S term increases. This is in line with WF theory, although $k^+(T)$ is not exactly proportional to $D(T)$. The ratio k^+/D changes by a factor of two from 585 K to 455 K. These deviations may be due to finite size effects.

Some snapshots during crystallization at 585 K are displayed in Figure 5.14, together with the corresponding profiles of Q_4^{dot} . The whole trajectory shows a smooth growth from the crystalline boundaries, no nucleation occurs inside the amorphous slab, which is in line with the experimental observations of Ref. [35]. In

the final stages of the crystallization process, the two interfaces interact with each other, which slightly accelerates crystallization. Therefore, the very last part of the trajectory is not included in the evaluation of the growth velocity.

Now we turn to the discussion of the impurity effects to the crystallization process. To have a direct comparison, we performed similar simulations on Sb_2Te without Ag/In dopants at 585 K. We found the crystallization is faster for Sb_2Te , i.e. v_g is 1.7 times higher than that of AIST (see Figure 5.9). Apparently, Ag/In impurities hinder the crystallization of Sb_2Te .

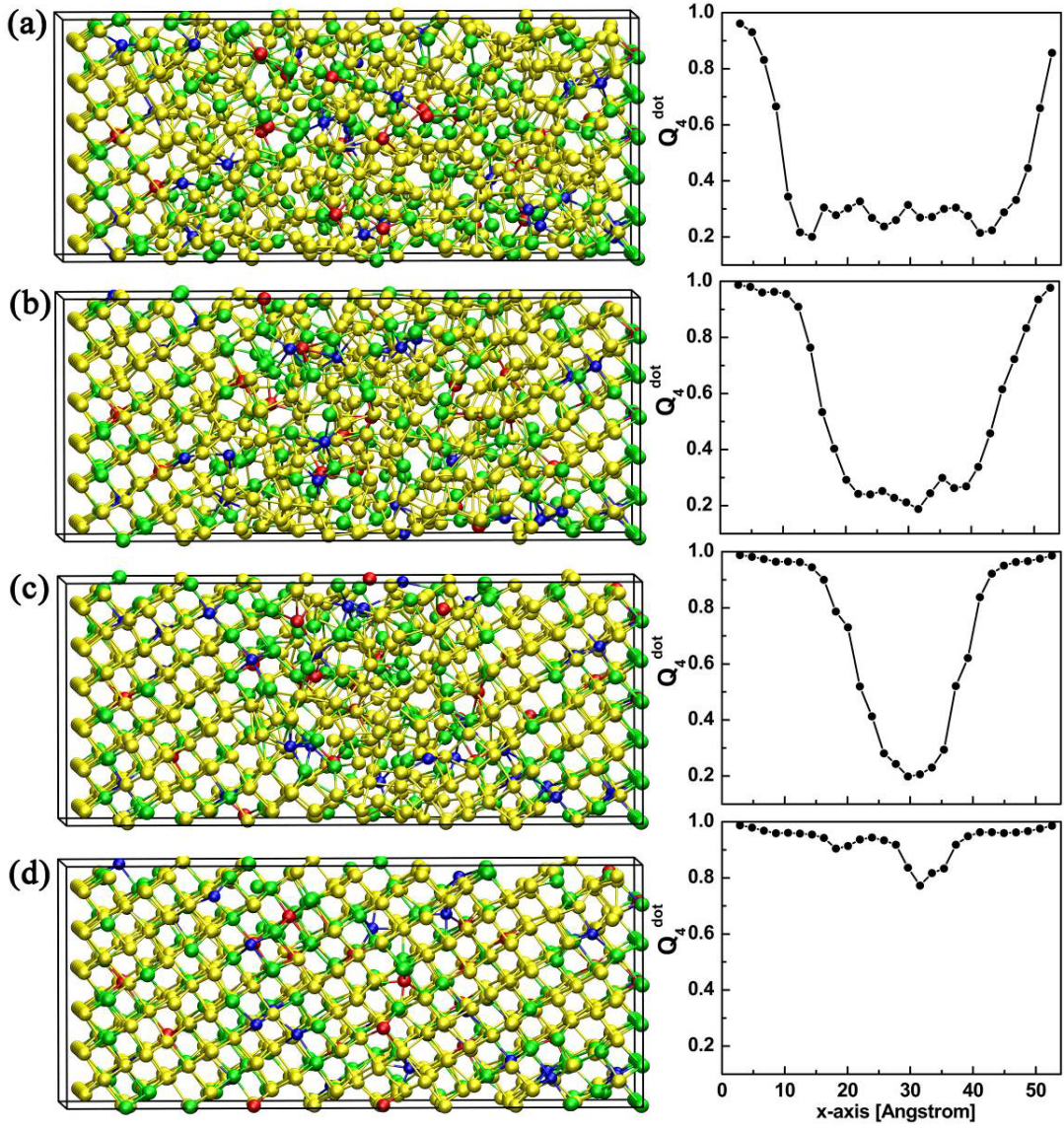


Figure 5.14 a) Snapshots of the crystallization of AIST containing 810 atoms ($T=585$ K) at 0, 60, 120 and 170 ps. b) Plots of the corresponding profiles of order parameter Q_4^{dot} .

In order to make sure this acceleration is not caused by additional nucleation effects inside the amorphous slab, several snapshots during crystallization are presented in Figure 5.15 together with the corresponding Q_4^{dot} . Clearly, no nucleation is observed and the growth process is very similar to that of AIST.

Then we check the deposition rate k^+ and the sticking coefficient S . We find the deposition rate roughly stays the same, $1/8.7 \text{ ps}^{-1}$ (Sb_2Te) and $1/8.3 \text{ ps}^{-1}$ (AIST), while the sticking coefficient differs significantly. Without Ag/In impurities, the sticking coefficient S of Sb_2Te is 0.51, however, this number decreases significantly to 0.38 upon doping. These numbers are averaged over 4 samples at 585 K.

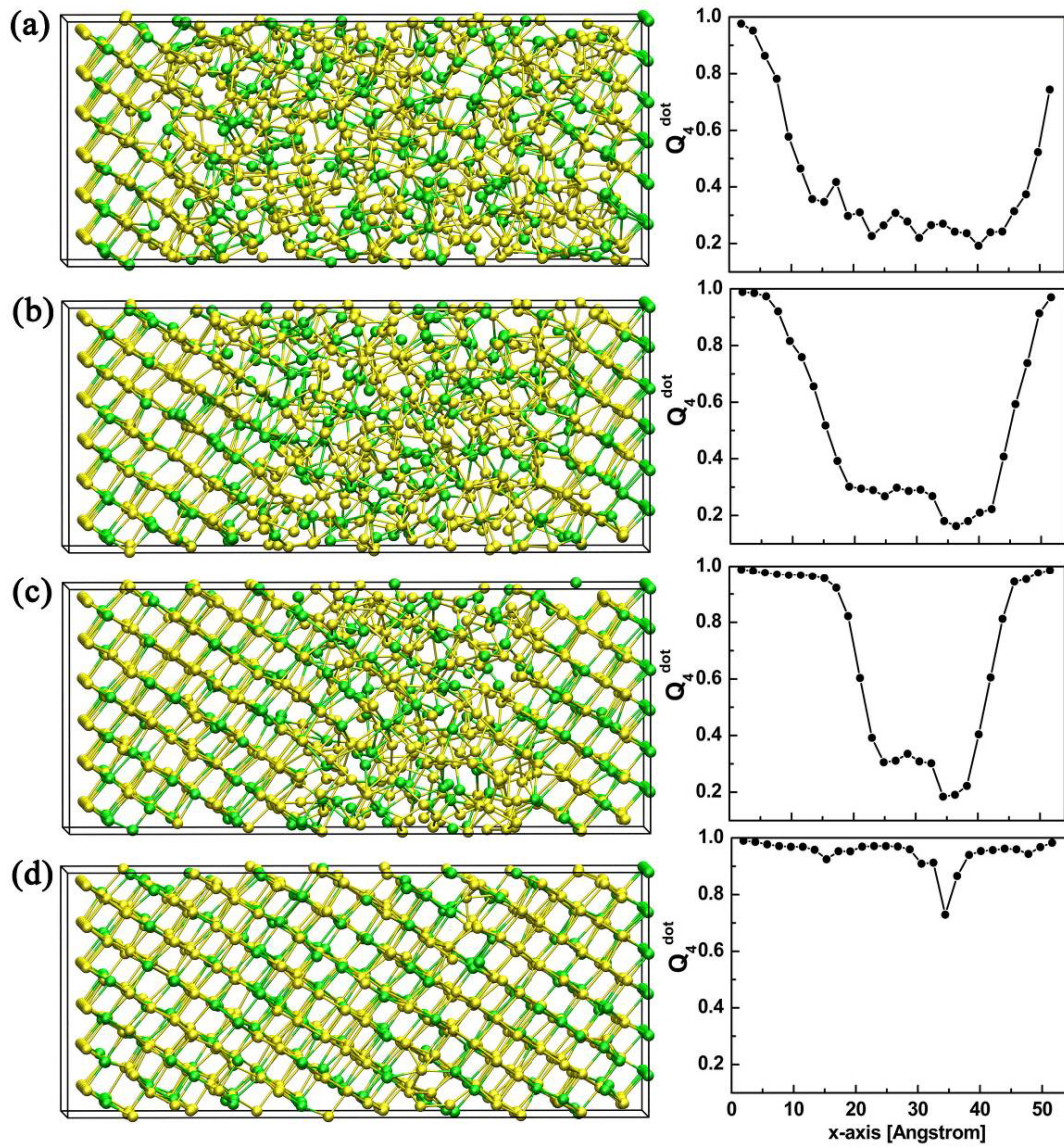


Figure 5.15 a) Snapshots of the crystallization of Sb_2Te containing 810 atoms ($T = 585 \text{ K}$) at 0, 45, 90 and 135 ps. b) Plots of the corresponding profiles of order parameter Q_4^{dot} .

To further elucidate the effects of impurities, 4 additional simulations are performed, in which the Ag and In impurities in amorphous AIST at 300 K are replaced with all Ag, In, Te or Sb atoms, respectively. The models are then heated to 585 K for crystallization. We compute the sticking coefficients for these four models, and find that three of them are very similar, 0.47, 0.51 and 0.50 (In-, Te- and Sb-"doped" Sb₂Te), while that of Ag- doped Sb₂Te has a much smaller value, 0.35. This finding suggests Ag plays a more significant role in reducing the growth velocity of Sb₂Te than In does at high temperatures (see corresponding v_g in Table 5.3). The observation of growth velocity reductions due to impurities are in line with previous experiments [12].

	v_g [m/s]	S	S_{Ag}	S_{In}	S_{Sb}	S_{Te}
AIST	7.80	0.38	0.26	0.30	0.39	0.40
Sb ₂ Te	13.16	0.51			0.51	0.50
Ag-Sb ₂ Te	5.99	0.35	0.21		0.37	0.36
In-Sb ₂ Te	11.98	0.47		0.34	0.49	0.47
Sb-Sb ₂ Te	13.22	0.50			0.50	0.49
Te-Sb ₂ Te	13.83	0.51			0.51	0.51

Table 5.3 Growth velocities and total and elemental specified sticking coefficients. For AIST and Sb₂Te, the amorphous models are generated 4 times independently (only averaged values are shown), while the other four simulations Ag-, In-, Sb- and Te- "doped" Sb₂Te are obtained by replacing one of amorphous AIST models.

By evaluating the elemental contributions to the sticking coefficients, we can understand the atomic process near the interface one step forward. From table 5.3, we observe that in AIST the sticking coefficients of impurities S_{Ag} and S_{In} are quite low 0.26 and 0.30, moreover, $S_{Sb} = 0.39$ and $S_{Te} = 0.40$ are also low, in particular lower than $S_{Sb} = 0.51$ and $S_{Te} = 0.50$ in the clean Sb₂Te system. This reveals that not only the

impurities themselves have a higher probability to escape from the interface, but also they disturb the sticking process of the major contents Sb and Te. Therefore the overall sticking coefficient of AIST reduces.

We can understand this behavior from the electronic properties. In PCMs, it is well known that p type bonding plays an important role [19], and for doped Sb_2Te alloy, there is no exception. In AIST, the crystalline interface is mainly made of Sb (3 p valence electrons) and Te (4 p valence electrons), and would preferentially form p type bonds with the atom that occupies the empty site. If the atom is Sb or Te, the bonding would be stable, leading to a high sticking coefficient. However, in the case of In, there is only 1 p valence electron, the bonding would be relatively weaker, so that In atom has a higher probability to escape from the site, which means a smaller sticking coefficient. From this point of view, the sticking coefficient should be the smallest for Ag, since it has no p valence electron at all, which is in line with our observation, shown in Table 5.3.

From the above analysis, we could also learn that only the impurities close to the interface region play a role in reducing the effectiveness of the sticking process. Impurities at other regions (amorphous or crystalline) have no contributions. Since the amount of impurity atoms is quite small in our simulations, the statistical distribution of them after melt-quench affects the growth velocity strongly, leading to a relatively large error bar ($\pm 1.43\text{m/s}$). In the case of Sb_2Te , the error bar is much smaller ($\pm 0.41\text{m/s}$), where the growth velocity does not depend on the statistical distribution of impurities.

In conclusion, impurities Ag/In near the crystalline interface affect the overall sticking process and lead to a slower growth process at high temperatures. Ag works more effectively than In in reducing the growth speed of the Sb_2Te system. At low temperatures, in particular at room temperature, Ag/In should increase the viscosity of amorphous Sb_2Te systems very significantly yielding a good thermal stability [12]. Our current simulations cannot provide useful information in such temperature range, due to the quenching rate effects.

5.6 Summary and outlook

In this chapter, I firstly reviewed the recent progress of crystallization of PCMs, then I focused on the discussions of growth dominated PCMs -- AIST and Sb_2Te . We found good comparisons of the structural properties of a-AIST between AIMD melt-quenched models and experimental as-deposited samples. The recrystallized AIST from simulations was in reasonable agreement with that from experiments. Our simulations of crystallization showed that the atomic processes near the crystalline-amorphous interface involved dramatic structural changes and could be classified as diffusion-limited interface-controlled growth.

At low temperatures (below 550 K), the dynamical properties of the amorphous models, obtained by extremely fast melt-quench simulations (with a quenching rate of 10^{13} K/s), differed very significantly from the experimental samples quenched at slower rates (10^{10} K/s), suggesting that the quenching rate plays a very important role. This property is expected to be related to the very high fragility of AIST, and it should hold for other fragile PCMs, such as GeTe and $\text{Ge}_2\text{Sb}_2\text{Te}_5$.

Good agreement between the dynamical properties of AIMD simulated AIST and experiments was found at higher temperatures. The simulations showed that AIST and Sb_2Te possessed a rather sharp crystalline-amorphous interface and the presence of Ag and In impurities led to a decrease in the crystal growth velocity of Sb_2Te , due to a reduction in the sticking coefficients. These results are in good agreement with previous experimental works.

In the future, we will continue our work on the doped Sb-Te systems to find optimal dopants for rapid crystallization at high temperatures. Also, we will consider the crystal process for other systems, even for the systems having high nucleation rate, e.g. $\text{Ge}_2\text{Sb}_2\text{Te}_5$. Besides, we anticipate a thorough understanding of quenching rate effects on dynamical properties of fragile systems. Such simulations are currently not feasible for *ab initio* simulations, since they require very long simulation time, on the order of tens to hundreds of nanoseconds. We may achieve this with the development of supercomputers and AIMD codes in the future.

Chapter 6 Magnetically doped Phase Change Materials

In this chapter, I focus on the magnetic properties in $3d$ impurities doped PCMs. Both crystalline and amorphous states are considered. The chapter is divided into five parts, 1> an introduction of magnetic phase change materials (MPCMs) is provided; 2> the exchange mechanisms in dilute magnetic semiconductors (DMSs) are briefly reviewed; 3> I focus on $3d$ impurities in stable hexagonal $\text{Ge}_2\text{Sb}_2\text{Te}_5$; 4> the phase change cycle of MPCMs is discussed; 5> a summary and outlook is provided. It is worth mentioning that Y. Li and I. Ronneberger have also contributed to this work.

6.1 Magnetic Phase Change Materials

All the known PCMs so far are nonmagnetic materials. In 2008, Song *et al.* [48] synthesized the first MPCM by doping $\text{Ge}_2\text{Sb}_2\text{Te}_5$ with Fe impurities (Fe-GST). Later in 2011, Fe doped GeTe has been synthesized and measured [224]. These new materials preserve the phase change properties, namely, reversible and rapid crystalline-amorphous phase transitions, and electrical/optical contrast between the amorphous and the crystalline states; moreover, they have been proved to be ferromagnetic in both phases and to exhibit a non-negligible magnetic contrast between the two phases. These findings open up the possibility to design new data storage, sensor and logical devices as well as multi-functional spintronic devices.

FeGST is classified as a diluted magnetic semiconductor (DMS). DMSs have drawn great attentions during the past decades [225,226,227] owing to their great technology importance (e.g. spintronic semiconducting devices) as well as fundamental research interests (e.g. spin dynamics). Curie temperature T_C is an important quantity of DMSs, which is the critical temperature at which a transition from a ferromagnetic state to a paramagnetic state occurs. For practical application of DMSs, T_C should be as high as possible, ideally above room temperature. However, usually T_C in DMSs is quite low and Fe-GST is no exception: the measured T_C for hexagonal Fe-GST (7 % Fe atoms) is 173 K. By increasing the concentration of Fe,

T_C is expected to increase, however, so far, no experimental T_C has been reported for Fe-GST close to its dilute limit -- 19% Fe atoms (above this value Fe atoms segregate and form Fe clusters inside the host [48]).

Although it has been proved by experiments that phase change control over ferromagnetism works in Fe-GST, there are a number of things that require further investigations, namely, 1> the physical mechanisms that stabilize the ferromagnetic state in both phases, 2> the microscopic origin of the magnetic contrast, 3> the effect of magnetic impurities on the phase-change properties, 4> find better performing MPCMs.

6.2 Exchange mechanisms in dilute magnetic semiconductors

Theoretical studies employing density functional theory have significantly contributed to the understanding of exchange mechanisms that stabilizing magnetism in several classes of crystalline DMSs, for instance, III-V and II-VI semiconductors with magnetic dopants [227,228]. Here I briefly review the exchange mechanisms that stabilize ferromagnetism or antiferromagnetism in DMSs [228].

It is generally accepted that Zener's double exchange mechanism [229] and Zener's p - d exchange mechanism [230] lead to ferromagnetic couplings in DMSs, while superexchange [231,232] usually results in antiferromagnetic couplings. In some cases, superexchange also favors ferromagnetism [231,232].

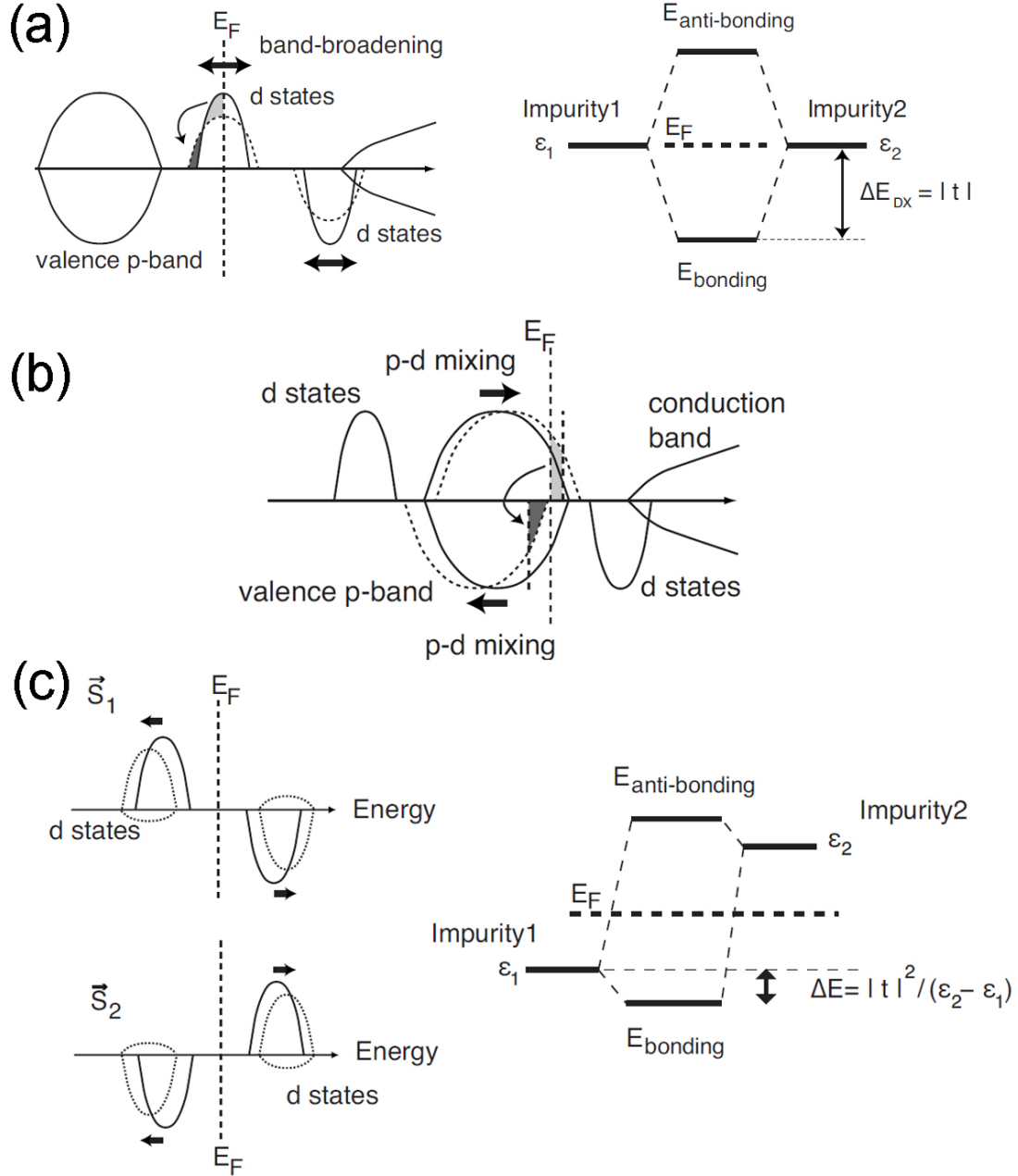


Figure 6.1 Adapted from Ref. [228]. (a) double exchange and (b) p - d exchange for ferromagnetism, and (c) superexchange for antiferromagnetism.

In transition metal impurity doped wide-band-gap semiconductors, such as Mn or Cr doped GaN, double exchange usually dominates. The stabilization of a ferromagnetic state depends on the width of the impurity band and the position of the Fermi level. In Figure 6.1 (a) a schematic spin-polarized DOS is shown. We assume the Fermi level lies in the middle of the impurity so that the bonding states are fully occupied while the antibonding states are completely empty. In this case, the system

obtains a maximum energy gain for ferromagnetically coupled impurities $\sim |t|\sqrt{c}$, where $|t|$ is the hopping matrix element between the impurity states (Figure 6.1 (a)), and c is the impurity concentration [228]. This energy gain, caused by the double-exchange mechanism, vanishes if E_F lies on either side of the band edge. In other words, the system gains no energy if either the impurity band is completely filled or completely empty.

Another exchange mechanism that stabilizes the ferromagnetic state is p - d exchange (shown in Figure 6.1 (b)), which often dominates in narrow-gap semiconductors like GeSb or InSb. In such compounds, after doping with Mn impurities, the majority d band of Mn lies below the p band of Sb, while the minority d band of Mn lies well above the Fermi level. Before interacting with the host, Mn has a well-localized local moment of $5 \mu_B$. In the neutral state Mn donates one electron per Mn atom, which is indicated in the p band at E_F (solid curve), $1/2$ for both spin-up and spin-down. After interaction between Mn and nearby Sb, the hybridization of the majority d band (Mn) and the minority p band (Sb) leads to the shift of the majority p band towards higher energy, while the minority p band is shifted towards lower energy (dashed curve). In case of strong enough hybridization, the minority p band becomes completely filled, while one electron per Mn impurity is missing in the spin-up p band, leading to a half-metallic density of state. Therefore, Sb atoms carry small antiparallel moments with respect to the local moment of Mn, resulting in an effective moment per Mn impurity of $4 \mu_B$. In short, the hybridization of occupied spin-up and unoccupied spin-down d states of Mn induces a magnetic field on the valence band states, leading to a spin-polarization of the system.

Superexchange mechanism [231,232] is also very important in DMS. Typically, it stabilizes the antiferromagnetic state. It differs from the previous two mechanisms since it does not require a finite density of states at E_F . The hybridization is actually between the state localized well below E_F and the state localized well above E_F . Usually the superexchange is explained by a magnetic coupling transferred by the ligands (the p orbitals of the anions), although these states themselves are hybrids between impurity d states and anion p states. A schematic plot is given in Fig 6.1 (c).

It shows the schematic density of states for two impurity systems, which have moments S_1 and S_2 , equal concentrations $c/2$, and are antiparallelly aligned. The electronic states with the same spin direction hybridize with each other, which shifts the lower occupied energy peaks to even lower energies and shifts the higher empty energy peaks to higher energies, indicated by the dotted bands. The downward shift of the lower occupied level yields a band energy gain, which stabilizes the antiferromagnetic couplings. In some cases, such as V doped GeAs, superexchange also stabilizes ferromagnetic couplings, a detailed discussion can be found in Ref. [228], [231] and [232].

6.3 3d impurities in hexagonal GST

We perform DFT and AIMD simulations to study the structural, electronic and zero-temperature magnetic properties of both the crystalline and the amorphous $\text{Ge}_2\text{Sb}_2\text{Te}_5$ doped with 3 d impurities, namely, Cr, Mn, Fe, Ni and Co (MI-GST). Two popular methods are currently employed in DFT to study magnetic materials, the coherent potential approximation (CPA) and the supercell method. The latter one is chosen for the current study because of the complexity of the materials, i.e. the complicated local environment of the impurities in the crystalline phases and the even more complicated amorphous network. Although it is possible that both ferromagnetic and antiferromagnetic exchange interactions play a role in MI-GST, for two reasons, we only consider ferromagnetic couplings in this study: 1> in experiments, the primary magnetic interaction has been demonstrated to be ferromagnetic for Fe-GST [48], 2> more complicated magnetic structures within the supercell method would be computationally extremely heavy, in particular for the amorphous phase.

We start with the discussion of the hexagonal $\text{Ge}_2\text{Sb}_2\text{Te}_5$ phase (hex-GST), since the first MPCM (Fe-GST) was synthesized in this phase experimentally. The subsequent amorphization and crystallization were based on it. As discussed in Chap3, the KH sequence is energetically more favorable than the Petrov sequence. Here, we

only consider KH sequence for the hexagonal phase. The experimental lattice of hexagonal $\text{Ge}_2\text{Sb}_2\text{Te}_5$ are used, $a = 4.25 \text{ \AA}$ and $c = 17.27 \text{ \AA}$.

The first step is to understand the defect formation energy of 3 d impurities in hexagonal GST. We consider several non-equivalent substitutional and interstitial sites as shown in Figure 6.2. The simulations are based on supercells contain 108 atoms and 1 impurity and on a $2 \times 2 \times 2$ Monkhorst-Pack (MP) k-point mesh [102]. GGA-PBE exchange-correlation functionals and ultrasoft pseudopotentials are employed. The plane wave code Quantum Espresso [127] are used.

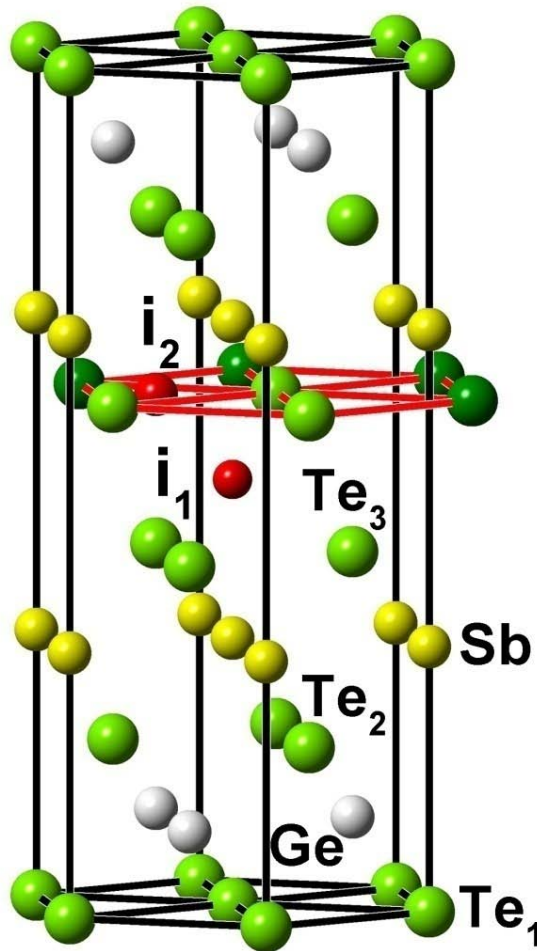


Figure 6.2 Hex-GST with several non-equivalent substitutional and interstitial sites.

The defect formation energy of the magnetic impurity (MI) is calculated with respect to the clean hex-GST and the crystalline phase of each element. The transition metals are calculated in their magnetic ground state.

$$E_{form} = E_{MI-GST} - E_{GST} + E_{Ge/Sb/Te} - E_{MI} . \quad (6.1)$$

The defect formation energies are summarized in Table 6.1. The most energetically favorable sites are substitutions Sb for Cr, Fe and Co and substitutional Ge for Mn, while for Ni, the energy of the interstitial i_2 site is comparable to that of the substitutional Ge and Sb sites. For the other impurities, interstitial sites are generally much higher in energy. For all the five 3 d impurities at substitutional Te sites, the formation energies are very high.

Site	Cr-GST	Mn-GST	Fe-GST	Co-GST	Ni-GST
E_{form} [eV]					
Ge	0.16	-0.34	0.76	0.56	0.53
Sb	-0.10	-0.18	0.71	0.16	0.62
Te ₁	2.91	2.83	3.19	1.71	1.61
Te ₂	2.67	2.42	2.89	1.48	1.39
Te ₃	1.50	1.30	2.14	1.11	1.41
i ₁	1.33	1.22	1.61	1.01	0.83
i ₂	1.62	1.23	1.60	0.82	0.62
Total Moments (Local moments) [μ_B]					
Ge	4.04 (3.71)	5.01 (4.33)	3.89 (3.19)	0.00 (0.00)	1.89 (0.93)
Sb	3.04 (3.25)	4.57 (4.29)	4.70 (3.43)	0.00 (0.00)	1.56 (0.84)
i ₁	4.66 (3.86)	4.07 (4.03)	1.93 (2.37)	0.93 (1.07)	0.00 (0.00)
i ₂	3.96 (3.43)	2.99 (3.40)	2.14 (2.57)	0.00 (0.00)	0.00 (0.00)

Table 6.1 The formation energies and magnetic moments of substitutional and interstitial impurities in hex-GST.

In Table 6.1, the total (local) magnetic moments of the MI are also shown. Some models have finite magnetic moments, while some of them are non-magnetic. Taking Cr for instance, for all considered sites, the system is magnetic and the total moment is almost an integer number, 4 and 3 μ_B at substitutional Ge and Sb sites. This can be

understood within a simple ionic model, i.e. Cr donates 2 and 3 electrons to form bonds with nearby Te atoms at the two sites. Similar behavior is observed for Mn and Fe. As regards Co and Ni, the magnetic interactions become unstable for some sites. In particular, the most energetically favorable configurations are non-magnetic, which already suggests they are not good candidates as MPCMs. More importantly, we will show that Co- and Ni- doped GST is always non-magnetic in the phase change cycle.

	Fe		Co	
	low spin	high spin	low spin	high spin
Subst. Ge				
Moments (μ_B)	0.00	3.89	0.00	2.89
MI-Te bonds	2.65-2.69	2.82-2.87	2.68-2.71	2.79-2.94
ΔE (eV)	0.69	0.00	-0.18	0.00
Subst. Sb				
Moments (μ_B)	0.87	4.70	0.00	1.94
MI-Te bonds	2.62-2.70	2.75-2.97	2.62-2.69	2.62-3.33
ΔE (eV)	0.37	0.00	-0.22	0.00

Table 6.2 Different magnetic configurations for Fe and Co dopants

As regards Fe and Co, there exists another magnetic state, which, is however, less energetically favorable, as shown in Table 6.2. The metastable states have different bond lengths (between the impurity atoms and their nearest neighbors) and different magnetic moments.

In Fe-GST, the metastable configuration has no magnetization at subst. Ge site, and a rather small magnetic moment ($0.87 \mu_B$) at subst. Sb site. These two low spin states are 0.69 and 0.37 eV higher in energy than the corresponding high spin state. The shorter bond lengths between the impurity atom and the nearby Te atoms in the low spin state reflect a stronger *p-d* hybridization. In these states, the crystal field prevails over the exchange splitting. In Ref. [233], Ding *et al.* also find this low spin state at subst. Sb site by means of DFT, which seems to fit their experiments better. However,

we argue this state is higher in energy than the high spin state, and the observed small magnetization in experiments may rather result from the interplay of both ferromagnetic and antiferromagnetic couplings between Fe impurities.

For the case of Co, the trend is opposite, i.e. the high spin state at subst. Ge ($2.89\mu_B$) and subst. Sb ($1.94\mu_B$) site is energetically less favorable than the corresponding non-magnetic states. The Co-Te bond lengths are generally bigger in the high spin states.

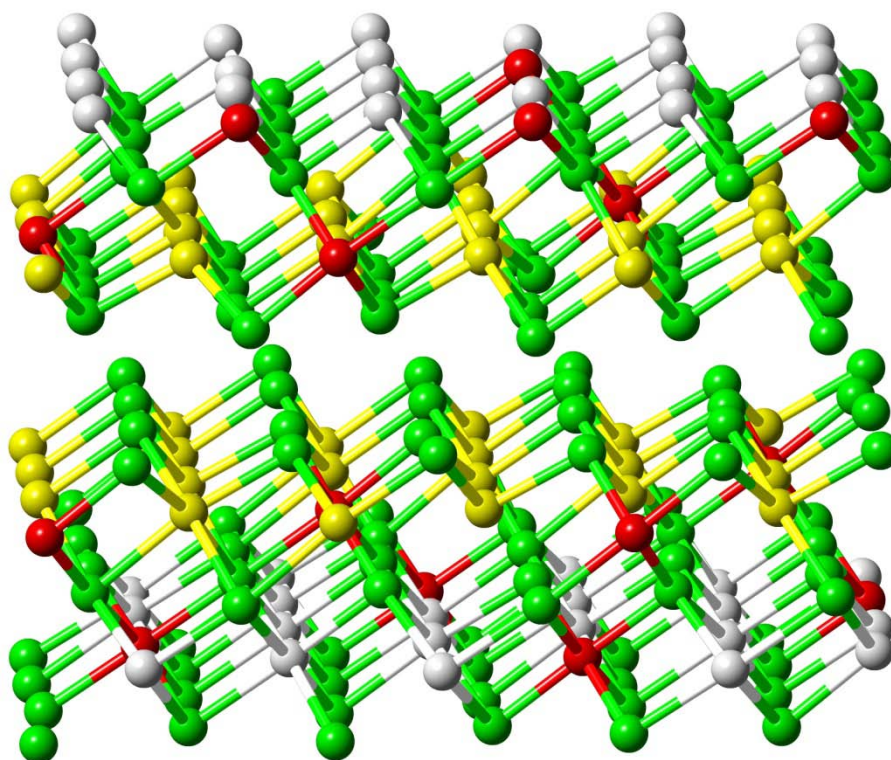


Figure 6.3 One relaxed hexagonal supercell with 7% 3d impurities.

Based on the understanding of the energetics, we construct big models containing 216 atoms with 7% substitutional 3 *d* impurities (15 atoms) at cation sites (randomly distributed). We relax these models and study their electronic and magnetic properties at 0K. A typical relaxed model is depicted in Figure 6.3. These big models are also the starting point to generate the amorphous phase, as will be discussed later.

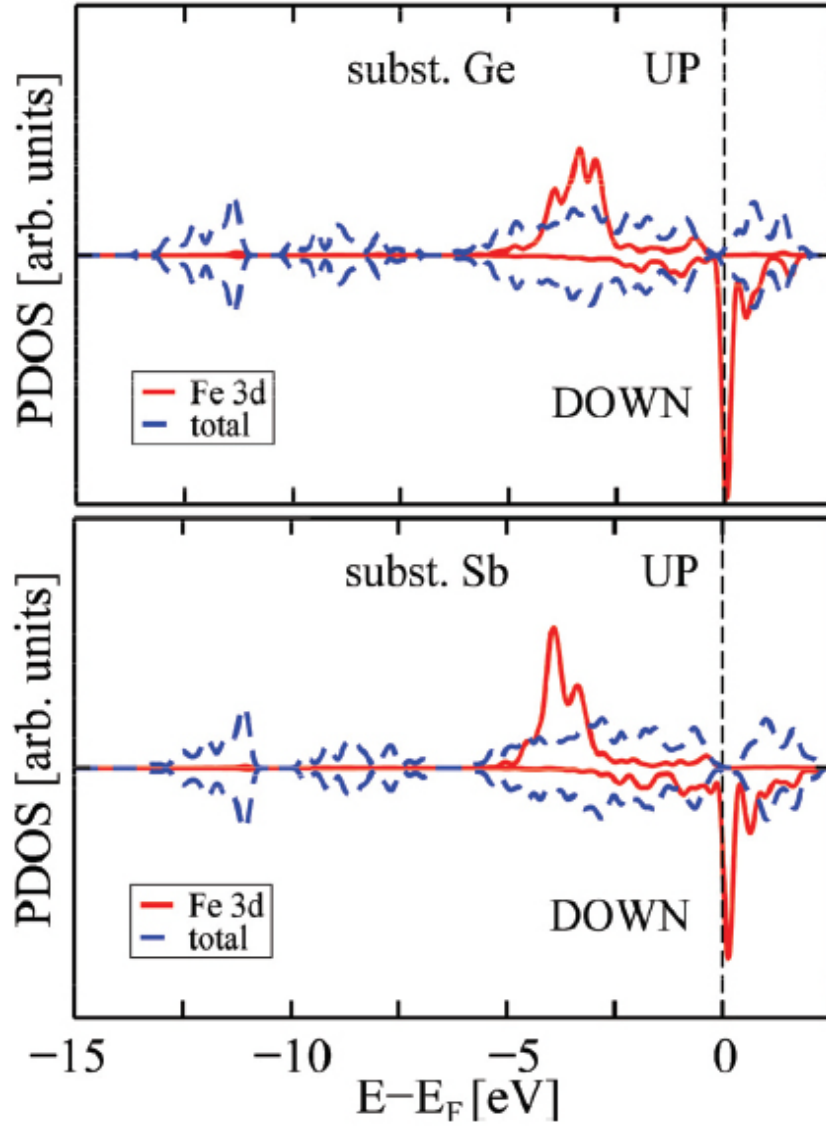


Figure 6.4 The DOS of hexagonal Fe-GST, single impurity model.

We calculate the total DOS and the projected DOS onto the 3 d orbitals of the impurities that have finite magnetic moments, e.g. Fe. In Figure 6.4, the DOS of the small models of Fe-GST at energetically favorable substitutional Ge and Sb sites are shown, which suggest that the ferromagnetic state is stabilized due to the interplay of two exchange mechanisms. On one hand, GST has a small band gap and a relatively large carrier concentration, suggesting carrier-mediated p - d exchange is important. This has been already discussed by Song *et al.* [48]. We note that the p - d exchange would be further enhanced by non-stoichiometric Ge/Sb excess vacancies (not considered in our model), which are invariably present in crystalline GST and turn it

into a *p*-type semiconductors [234]. On the other hand, the large DOS of the minority impurity band at the Fermi level suggests that double exchange could be relevant as well.

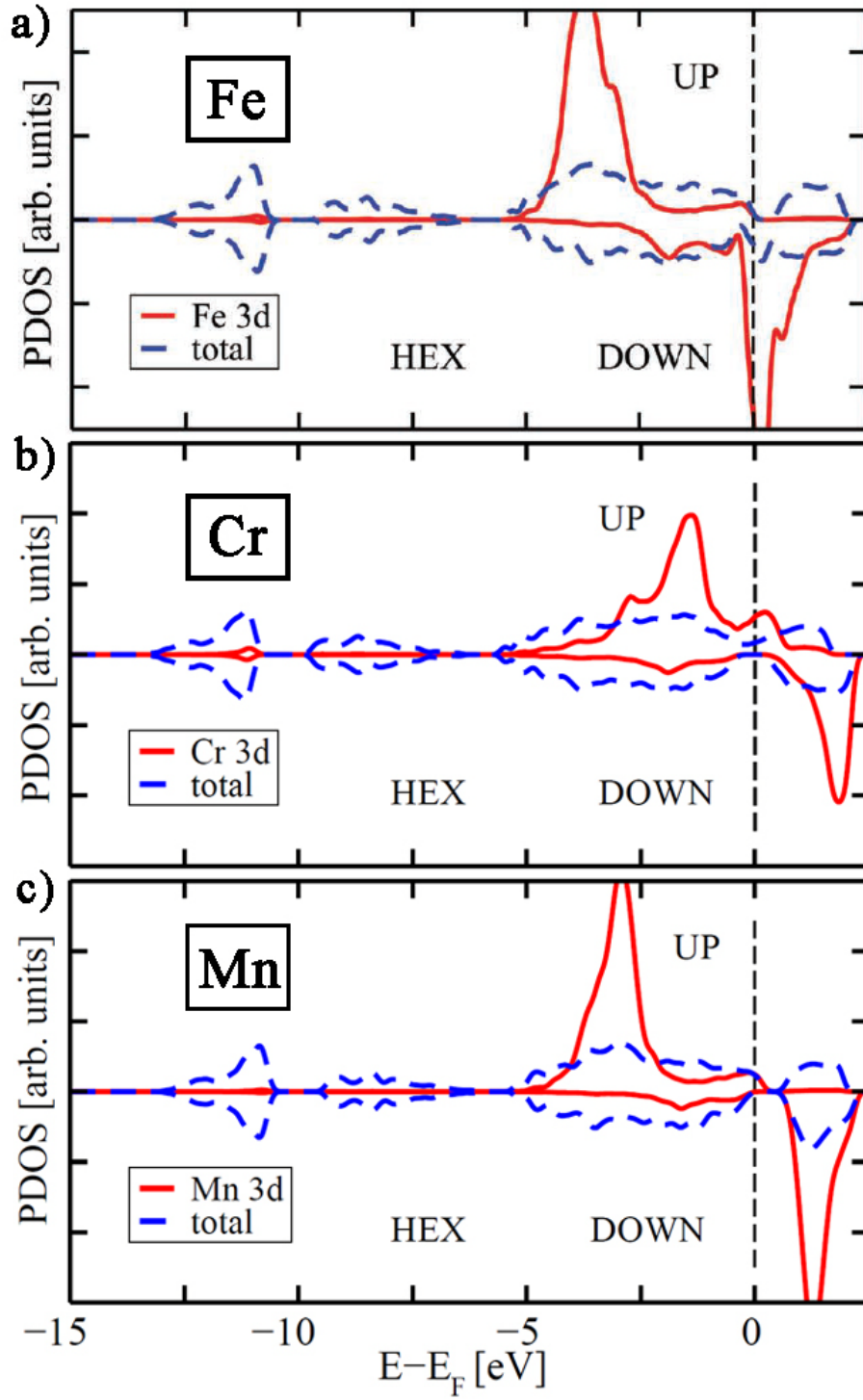


Figure 6.5 The DOS of hexagonal Fe-,Cr-, Mn-GST, multiple impurities.

The bigger model of hexagonal Fe-GST is qualitatively similar to the small model (Figure 6.5). The larger impurity concentration broadens the impurity bands. Similar spin-polarized DOS plots are also shown for hexagonal Mn-GST and Cr-GST in Figure 6.5. In these two cases, the minority bands are completely empty and well above the Fermi level and the main peaks of the majority bands are relatively deep in the valence band. This suggests that $p-d$ exchange mechanism should play an important role in hexagonal Fe-GST. However, the majority impurity bands of Mn- and Cr-GST at the Fermi level are relatively large, suggesting double exchange may be involved as well.

6.4 3d impurities in phase change cycle and magnetic contrast

Now we turn to discuss the more relevant phases in the phase change cycle of MI-GST, namely the metastable cubic phase and the melt-quenched amorphous phase. As introduced before, cubic GST is obtained after rapid crystallization, and only after sufficiently long thermal annealing at high temperature, the cubic state develops into the stable hexagonal phase (see Chap 3). A "small" concentration of impurities (e.g. 7%) is not expected to change this picture. In fact, in the experimental work by Song *et al.* [48], the recrystallized state has a smaller magnetization than the initial hexagonal state, which also suggests the two crystalline forms to be different. Very recently, Elliott *et al.* [235,236] have performed AIMD crystallization simulations of amorphous transition metal doped $\text{Ge}_2\text{Sb}_2\text{Te}_5$ and they showed that the recrystallized state was in cubic phase.

6.4.1 3d impurities in cubic GST

In Figure 6.6, we show the cubic model together with four non-equivalent substitutional sites (Te/Ge/Sb/vacancy) and one interstitial site (i_3). In this phase, disorder plays a much important role (see Chap 3), which affects the formation energy and magnetism. Therefore, we need to generate several models to gain better statistics over different local environments: for each type of defect we choose randomly four

configurations and calculate the average values of the formation energies and the magnetic moments. The cubic models contain 130 atoms (corresponding to a $3 \times 3 \times 2$ supercell of the standard standard cubic cell) and one additional impurity atom have been investigated with a MP k-point mesh $2 \times 2 \times 2$. We use the experimental lattice parameter 6.029 Å.

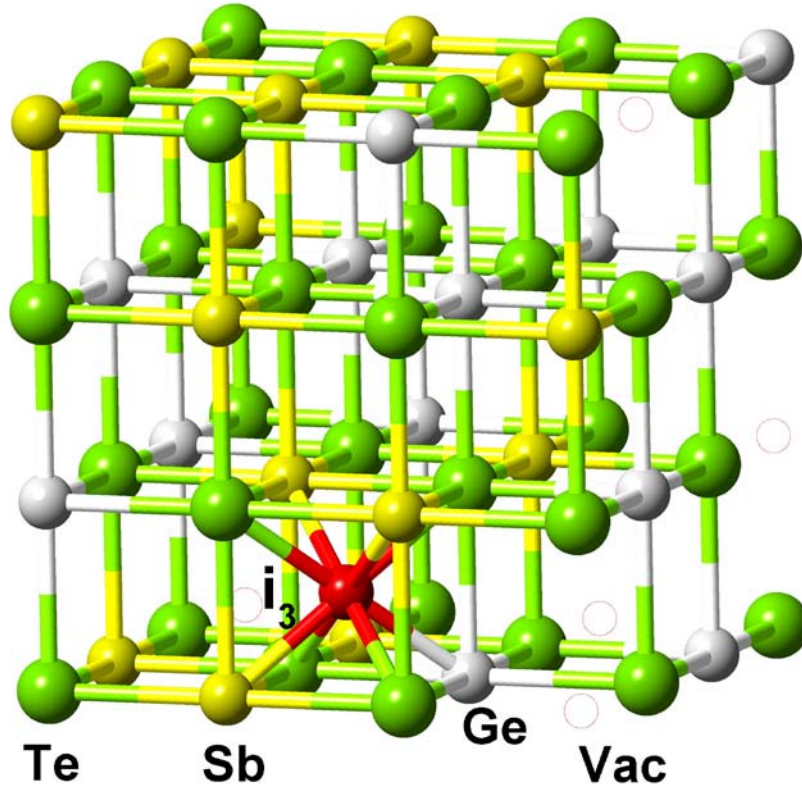


Figure 6.6 Cub-GST with substitutional and interstitial sites

From Table 6.3, we observe that Cr, Mn, Fe and Co prefer to occupy the cation sites (Ge/Sb/vacancy), while for Ni, the interstitial i_3 site is equally favorable. The formation energy for the subst. Te site is generally large for all the five impurities we consider here. As regards the i_3 site, the formation energy for Cr, Mn, Fe and Co is high.

The total and local magnetic moments of impurities in cub-GST are presented in Table 6.3. Interestingly, Cr, Mn and Fe display large magnetic moments at substitutional cation sites, which are comparable to the corresponding subst. Ge/Sb sites in hex-GST. Co and Ni are shown to be non-magnetic. Small relaxations take

place in Cr-, Mn- and Fe-GST, whereas much stronger relaxations occur in Co- and Ni-GST. At subst. Te sites, the magnetic moments of the impurities have much bigger fluctuations due to the more direct effects of the disorders. At the interstitial i_3 site, Ni and Co are non-magnetic, Cr and Mn are in a high spin state, while Fe is in a low spin state.

Site	Cr-GST	Mn-GST	Fe-GST	Co-GST	Ni-GST
E_{form} [eV]					
Ge/Sb	0.05 ± 0.19	-0.22 ± 0.11	0.51 ± 0.08	0.17 ± 0.18	0.39 ± 0.15
Te	1.38 ± 0.15	1.07 ± 0.22	1.08 ± 0.41	0.72 ± 0.05	0.72 ± 0.02
i_3	0.81 ± 0.02	0.47 ± 0.02	0.91 ± 0.03	0.38 ± 0.03	0.36 ± 0.03
Total Moments (Local moments) [μ_B]					
Ge/Sb	3.72 (3.48) ± 0.36 (0.09)	4.68 (4.13) ± 0.22 (0.08)	4.08 (3.18) ± 0.14 (0.09)	0.00 ± 0.00	0.00 ± 0.00
i_3	3.97 (3.37) ± 0.20 (0.01)	4.43 (3.88) ± 0.10 (0.00)	2.61 (2.60) ± 0.20 (0.03)	0.00 ± 0.00	0.00 ± 0.00

Table 6.3 Formation energy and magnetization of cubic GST doped with single impurity

To simulate transition metal impurities, in particular to describe the correlations of the localized d electrons, GGA often leads to spurious artifacts due to self-interaction effects. A Hubbard U parameter applied to the d states of the magnetic impurities is often considered to heal this effect [20]. We calculated the U parameter self-consistently using the linear response method introduced by Cococcioni and de Gironcoli [21]. We only consider the U for the stable subst. cation sites in c-GST. The values obtained for c-GST are 2.7, 5.1, 3.9, 7.3 and 9.3 eV for Cr, Mn, Fe, Co and Ni respectively. Further simulations have been performed with the GGA+ U approach, and the results are in agreement with pure GGA calculations. The details to obtain U parameters can be found in the appendix E.

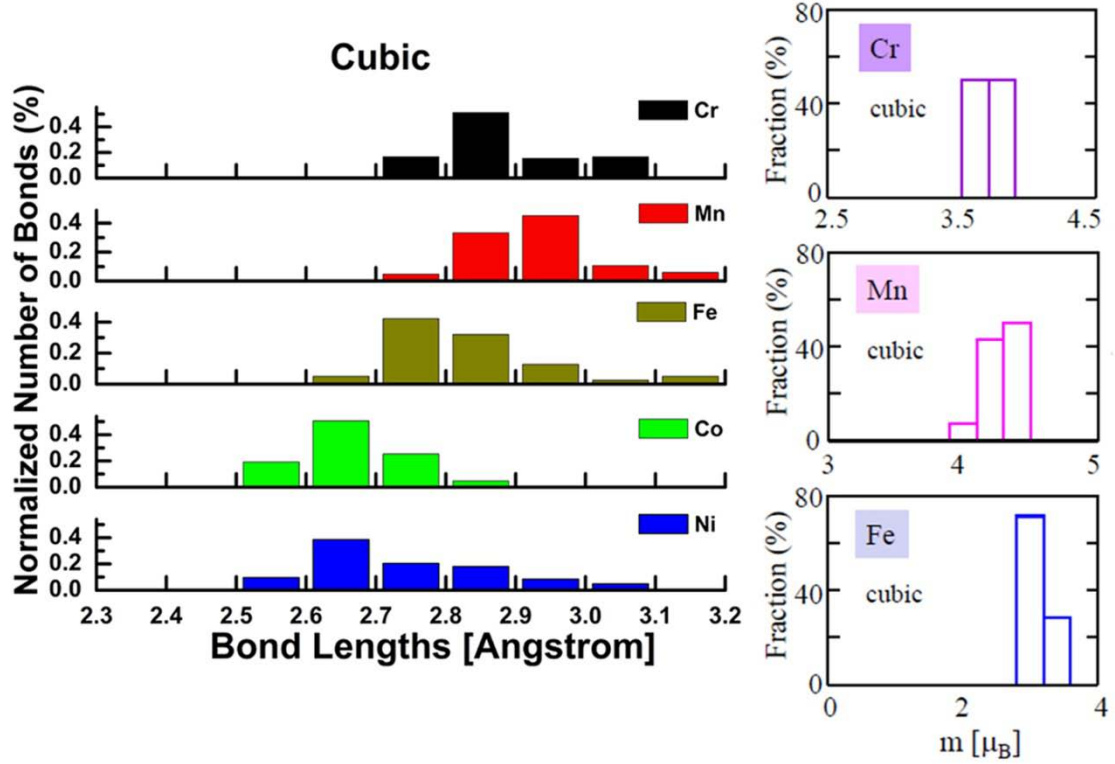


Figure 6.7 The bond length distributions and magnetic moments distributions of impurity atoms in cubic phase. Large models with multiple impurities

Larger cubic models containing 199 atoms (corresponding to a $3 \times 3 \times 3$ standard cubic cell) with 7% substitutional impurities placed at energetically favorable cation sites are constructed and relaxed (k-points $2 \times 2 \times 2$). The magnetic properties are the same of the corresponding smaller models. Since we have better statistics in the big models, we compute the distribution of the bond lengths between impurity atoms and their nearest neighbors, which is plotted in Figure 6.7 together with the magnetic moments distribution. These results confirm that relative small relaxations occur around Cr, Mn and Fe atoms, with typical bond lengths 2.8-3.0 Å, while strong relaxations take place around Co and Ni atoms, with typical bond lengths 2.6-2.7 Å. The hybridization between the d electrons of Co and Ni and the nearby p electrons of Te is strong enough to quench the magnetic moments. In other words, the crystal field produced by the host cubic GST dominates over the exchange splitting of the d states of Co and Ni. The magnetic moments of Cr, Mn and Fe do not fluctuate significantly in these cubic models. Similar trends of magnetic properties over these 3 d impurities

(except Fe) have been observed in some other doped semiconductors, like doped GaAs [237]. Fe impurities are in a low spin state in doped GaAs. We visualize one of the relaxed cubic MI-GST structures in Figure 6.8 (a).

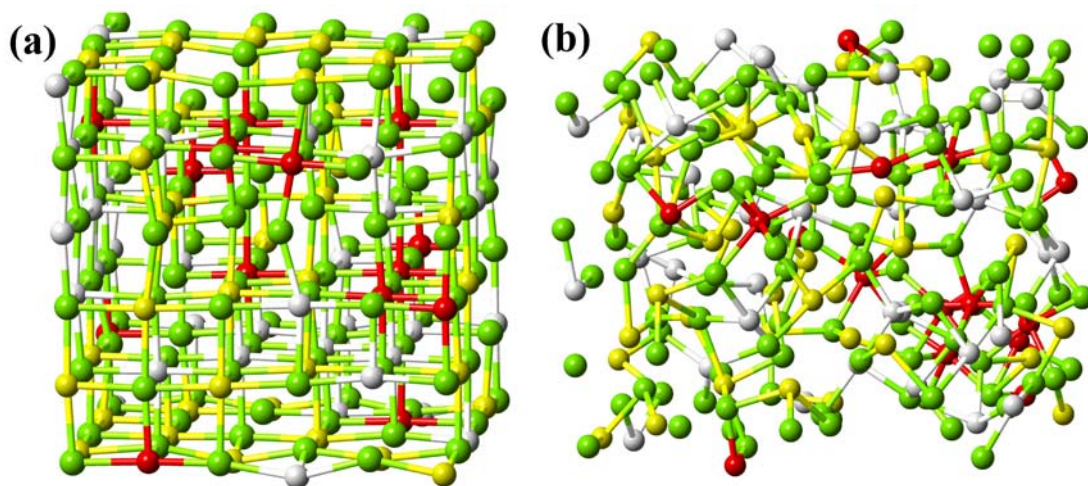


Figure 6.8 Snapshots of one relaxed cubic and one amorphous MI-GST.

6.4.2 3d impurities in amorphous GST

Now we generate amorphous MI-GST models. In the absence of experimental data of the amorphous density, we use the experimental density of clean amorphous GST 0.03 at / \AA^3 [238] and assume the relatively small concentrations of impurities do not change the atomic density significantly. To generate amorphous models, we follow the similar melt-quench scheme discussed in Chap 4 and 5, using CP2K. The computational details, including methods, functionals, basis sets, k-points, etc. are the same as before, except that we consider spin polarizations during the melt-quenched molecular dynamics simulations.

The amorphous models contain 216 atoms with 7% impurities and the different MI-GST models are produced from independent AIMD simulations. The melt-quench loop starts with randomization at 2500K for 10 ps, and then the systems are brought to 1000K in 20 ps and further equilibrated at this temperature for 50 ps. The amorphous states are obtained by subsequent quenching to 300K in 100 ps. The equilibrations at 300K last 30 ps and finally the systems are quenched to 0K and further relaxed using

Quantum Espresso with a $2 \times 2 \times 2$ k-point mesh. One of the fully relaxed amorphous MI-GST is visualized in Figure 6.8 (b).

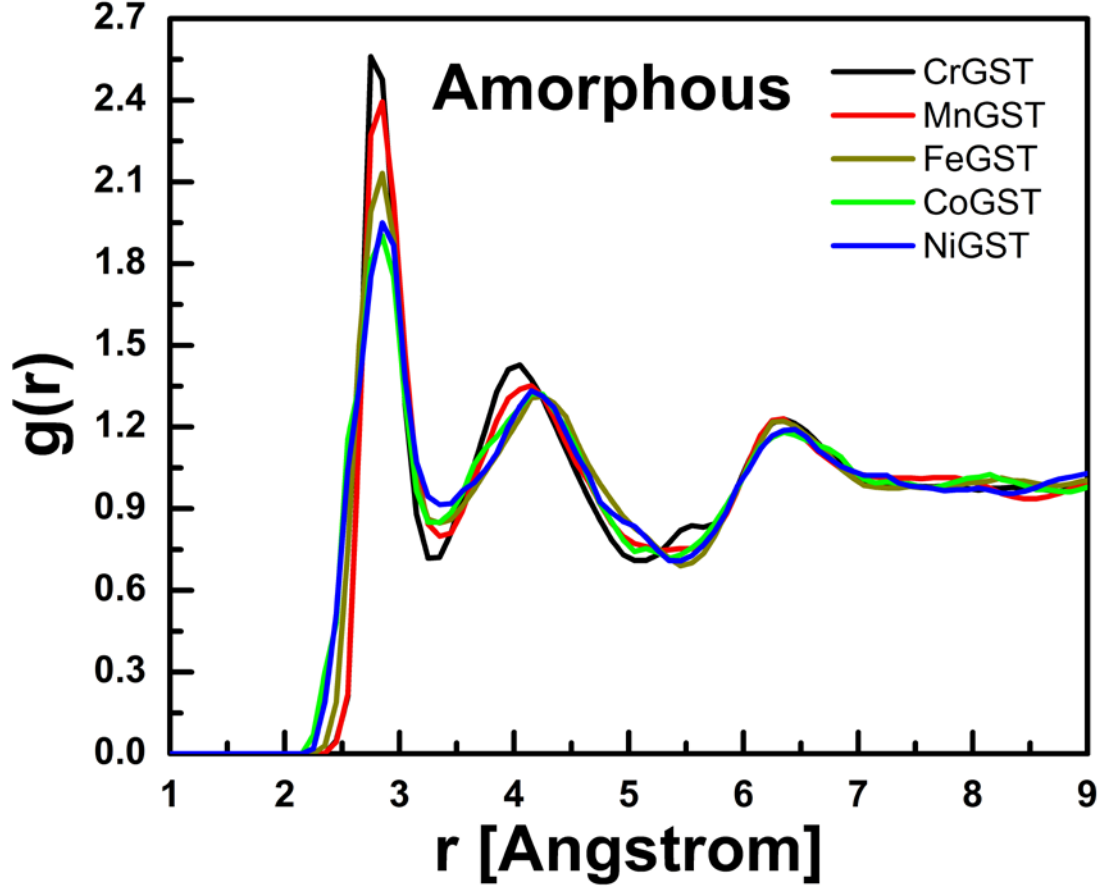


Figure 6.9 The total $g(r)$ of the five magnetically doped amorphous models.

We observe interesting differences in the magnetic properties of these amorphous MI-GST: Cr-, Mn- and Fe-GST exhibit finite magnetic moments, while Co- and Ni-GST are non-magnetic. To understand this difference, we study their structural properties first. The natural choice is to calculate the pair correlation function $g(r)$. We collect data at 300K for the five amorphous models and plot them in Figure 6.9. Apparently, the $g(r)$ of Cr- and Mn-GST are similar, and they differ from that of Co- and Ni-GST; the $g(r)$ of Fe-GST is in between. The primary peak positions of the five models are rather similar and are comparable to that of the clean GST model. The width of the first peak of Cr- and Mn-GST is comparable to the clean GST, while that of Fe-GST is slightly broader and that of Co- and Ni-GST is much broader.

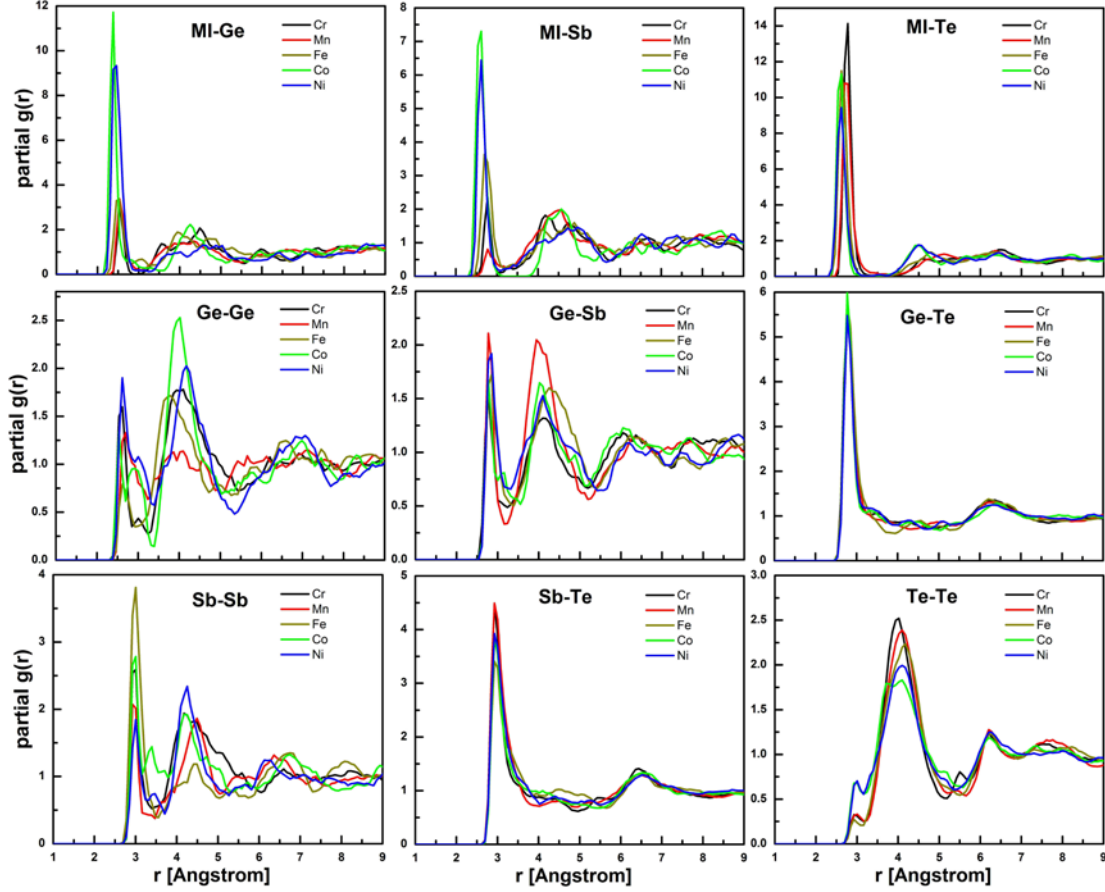


Fig 6.10 PPCFs of the five magnetically doped amorphous models.

To understand it better, we plot the partial $g(r)$ to distinguish the contributions from different pairs of elements, shown in Figure 6.10. Very big differences around impurity atoms in terms of peak positions, peak heights as well as peak widths are detected. We perform a more careful analysis around impurity atoms by counting the bond length distribution within the nearest neighbor shell, shown in Figure 6.11. The typical bond lengths are 2.7 - 2.8 Å for Cr and Mn atoms, 2.6-2.7 Å for Fe atoms, and 2.5-2.6 Å for Co and Ni atoms. The smaller bond lengths imply stronger p - d hybridizations with nearby atoms, which leads to a reduction of magnetization. In particular, the magnetic moments of Co and Ni become fully quenched. In the case of Fe, the magnetic moments of the impurities are quite sensitive to the local environment and are affected by the strength of the local p - d hybridizations. The magnetic moments of Fe range from 0 to 3 μ_B , see Figure 6.11 (g). Mn and Cr, on the

other hand, have much more robust moments, implying much weaker $p-d$ hybridizations, see Figure 6.11 (f), (g).

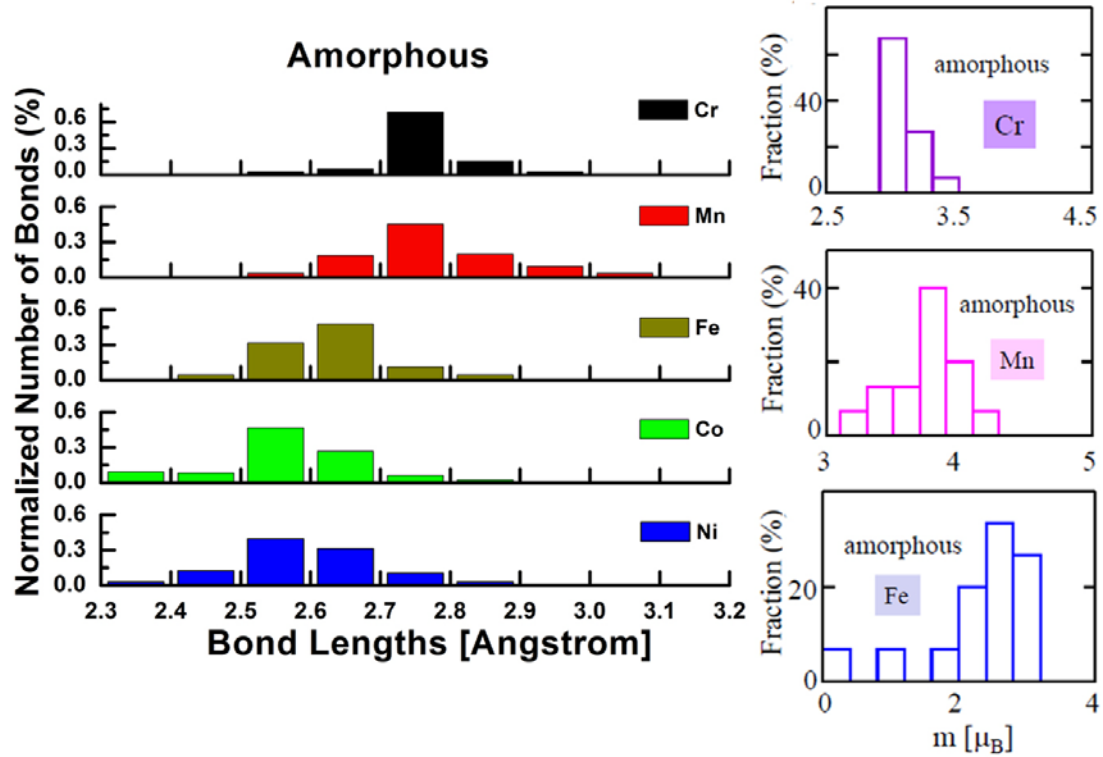


Figure 6.11 Bond lengths distribution and magnetic moments distribution of the five magnetically doped amorphous models.

To understand more about the local bonding environment, we study the angular distribution function (ADF), shown in Figure 6.12. The curves are calculated by averaging over all atoms of each type and over 30 ps at 300K. Similar to the case of clean amorphous GST phase, Sb and Te curves display a large peak at 90° , and the Sb curve also has a smaller peak at 165° , suggesting they are in a defective octahedral environment and the coordination numbers are much lower than 6. The missing peak in the Te curve at 165° suggests most Te atoms have a twofold or threefold coordination -- without neighboring atoms on the opposite sides. The distribution for Ge around 90° is broader, and extended to large angles, which also suggests a sizeable amount of tetrahedral configurations. By computing the order parameter we discussed in Chap 4 for each atom, we confirm the above findings. The majority of the Ge atoms (65-77%) are in a defective octahedral coordination, while the rest of

them are tetrahedrally coordinated. The local bonding environment of Ge, Sb and Te in amorphous MI-GST is similar to that of the pure amorphous GST [Chap4, 26,27]. Around impurities, the picture is more complicated, the distribution of angles is rather broad and the average coordination numbers of Cr, Mn, Fe are slightly smaller than 6, while that of Co and Ni are a bit larger than 6. The coordination numbers are determined by using the first minimum in the partial $g(r)$ plotted in Figure 6.10 and are summarized in Table 6.3.

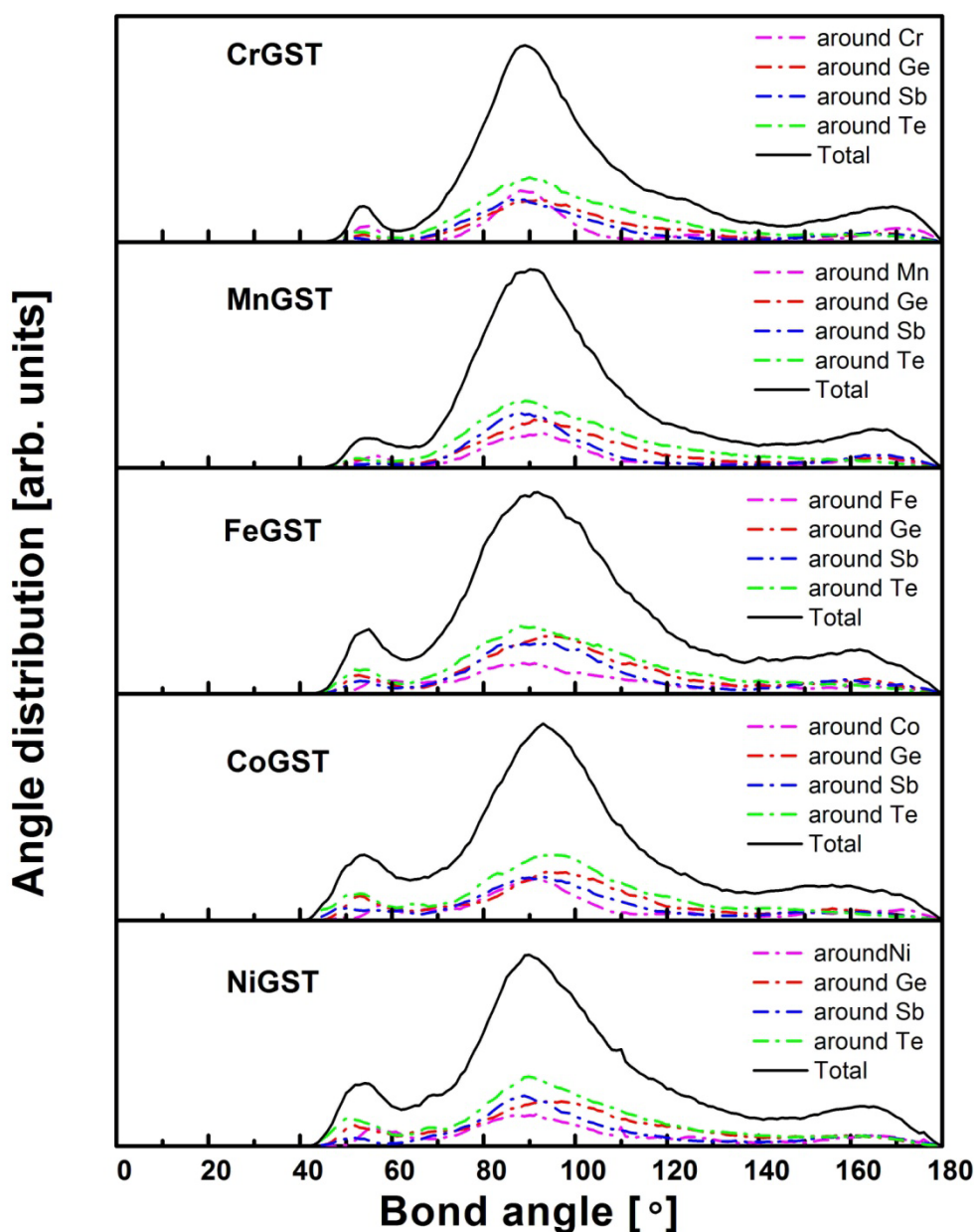


Figure 6.12 The angular distribution function of amorphous MI-GSTs.

	Cr	Mn	Fe	Co	Ni
CN. MI	5.93	5.53	5.90	6.47	6.40
CN. Ge	3.85	4.20	4.10	4.13	4.48
CN. Sb	3.49	3.56	3.50	3.37	3.68
CN. Te	2.82	2.89	2.80	2.73	2.88
tetra Ge	35%	25%	25%	25%	23%

Table 6.3 The average coordination numbers and the number of tetrahedral Ge atoms in the magnetically doped amorphous states.

Next, we focus on the medium range order of the amorphous network and try to assess the effects of magnetic impurities. The distributions of primitive rings are reported in Figure 6.13. As regards Cr- and Mn-GST, the ring statistics is very similar to that of the pure GST, namely, 4-fold rings are dominant, followed by 5- and 6-fold rings. The 3-fold rings are rather rare. In Fe-GST, the primary ring distribution is also similar, with the exception of a relatively large number of 3-fold rings. Most 3-fold rings have at least one Fe atom. Most 4-fold rings of Cr-, Mn- and Fe-GST are consisted of ABAB alternation (A=Ge,Sb; B=Te). However, for Co- and Ni-GST pronounced differences are observed: 3-, 4- and 5-fold rings are almost equivalently common in these two amorphous networks. Since the peculiar structural properties of a-GST -- large number of pre-existing ABAB rings and cavities, are believed to be essential for fast crystallizations [27], we speculate that the crystallization rate of MI-GST should not be affected significantly at moderate Cr, Mn or Fe doping, whereas Co and Ni doping might deliver bigger effects. From the experiments by Song *et al.*[48], it has been shown that moderate doping of Fe does not change the crystallization rate of a-GST much. However, the presence of impurities will affect much more significantly the structural and dynamic properties of GST when approaching the solubility limit.

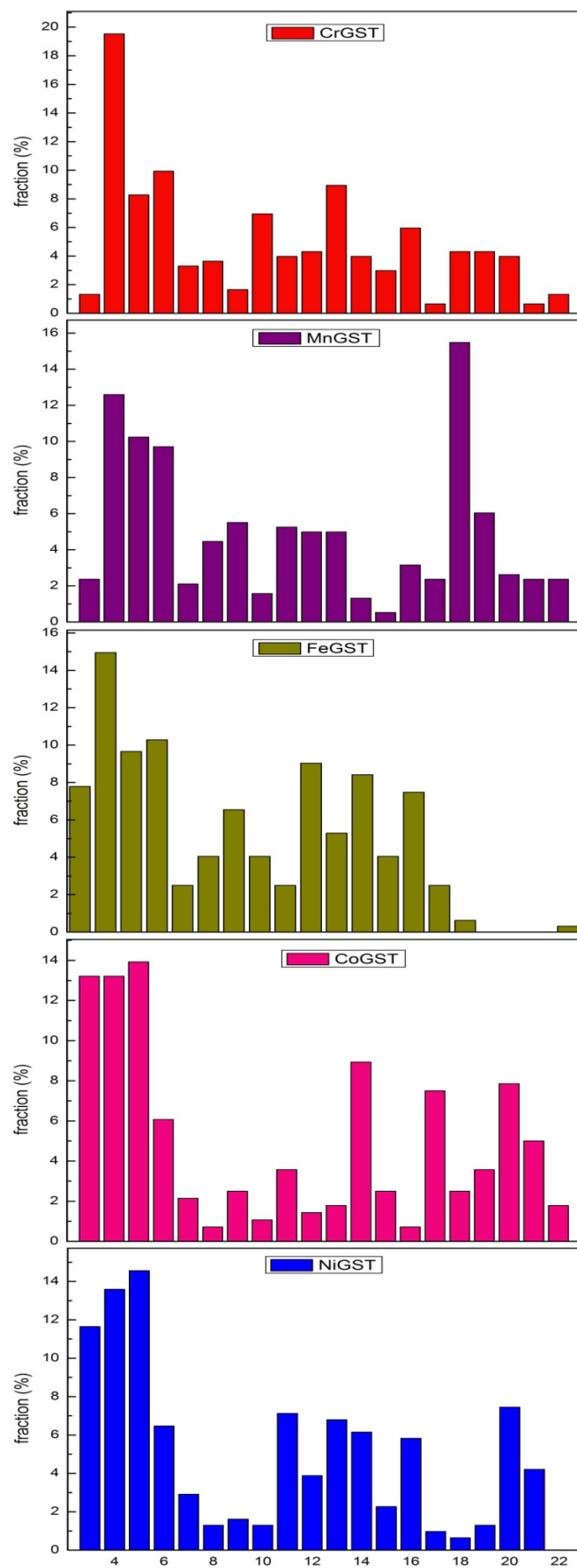


Figure 6.13 Rings statistics of amorphous MI-GSTs.

6.4.3 Magnetic contrast and exchange mechanism

In this sub-section, we focus on the magnetic contrast between crystalline and amorphous MI-GSTs as well as on the possible exchange mechanisms that stabilize ferromagnetism.

From previous discussions, we learned that Co- and Ni-GST are non-magnetic in both cubic and amorphous phases, so that they can be ruled out as magnetic phase change materials. Cr-, Mn- and Fe-GST, on the other hand, show finite magnetization in both crystalline and amorphous phases and a non-negligible contrast between the two phases (see below), suggesting they can be good magnetic phase change materials. In the following, we mainly focus on these good magnetic phase change materials.

Site	Cr-GST	Mn-GST	Fe-GST	Co-GST	Ni-GST
Total Moments (Local moments) [μ_B]					
Cubic	4.96(3.83)	4.91(4.28)	4.08 (3.18)	0.00(0.00)	0.00(0.00)
Amorphous	2.96(3.09)	3.95(3.75)	2.76 (2.33)	0.00(0.00)	0.00(0.00)

Table 6.4 The total (local) moments of impurities in cubic and amorphous MI-GSTs.

The magnetic contrast between the cubic and the amorphous Fe-GST turns out to be the largest: the magnetic moments in the amorphous Fe-GST are about 30% smaller than in the cubic Fe-GST (see Table 6.4). This large difference stems from the different local bonding environments around Fe atoms. It has been shown previously that Fe is quite sensitive to the local environment, in particular the bond length, which is a direct indication of the strength of *p-d* hybridization between the *d* orbitals of the impurities and *p* orbitals of the neighbors. In the amorphous phase, the magnetic moments vary considerably from Fe atom to Fe atom, as can be seen in Figure 6.11 In crystalline phases, high spin state should naturally exist due to the lowest formation energy, while the low spin state might also exist with a bigger penalty in the formation energy. In the perfectly cation-sites substituted cubic Fe-GST, only high spin states of Fe are detected, which leads to a big magnetic contrast. This is also

reflected in the local bond length distributions shown in Figure 6.9 (c) and 6.11 (c): the typical bond lengths around Fe in cubic phase are 2.7-2.8 Å, while those in amorphous phase are 2.6-2.7 Å.

In the experiments by Song *et al.* [48], the initial hexagonal phase and the recrystallized state (we speculate it to be the cubic phase) have different magnetic moments, i.e. the recrystallized state has smaller magnetization than the initial state. In principle, if we assume Fe atoms substitute only at Sb sites in the hexagonal phase, we would have a larger magnetic moment $5 \mu_B$ than that in the cubic phase, $4.08 \mu_B$. In a more realistic picture, the magnetization of the hexagonal state should be between 4 and $5 \mu_B$, since the formation energy of subst. Ge ($4 \mu_B$) is quite close to that of subst. Sb.

As regards Cr and Mn, the magnetic moments are more robust, even in the most complicated amorphous phase. Only high spin states have been found in both amorphous and crystalline states. The bond length distribution in Figure 6.9 and Figure 6.11 shows the different peak positions of the amorphous and the cubic Cr- and Mn-GST. In the amorphous phase, the typical bond lengths are 2.7-2.8 Å, which are smaller than those in the cubic phase, 2.8-2.9 Å, suggesting slightly stronger *p-d* hybridizations in the former state. The average magnetic moments are about 20% smaller in the amorphous than in the cubic phase for both Cr- and Mn-GST. Although the absolute magnetic contrast is not as pronounced as in Fe-GST, the magnetic properties of Cr- and Mn-GST are rather robust and should be more stable than the environment-sensitive Fe-GST in phase change cycles. In other words, we speculate Cr- and Mn-GST have better cyclicity than Fe-GST, which is very essential from the perspective of possible applications.

The remaining important task is to understand the possible exchange mechanisms that stabilize the ferromagnetic state in both cubic and amorphous phases. The spin-polarized DOS of cubic and amorphous Cr-, Mn- and Fe-GST are shown in Figure 6.13. In cubic Mn-GST, the majority *d* levels of Mn lie well below E_F , whereas the minority *d* levels of Mn are completely empty and well above E_F . Together with the fact that the cubic GST has a narrow band gap of 0.5 eV, we speculate that the

carrier-mediated p - d exchange interactions stabilize the ferromagnetic state. The unavoidable excess non-stoichiometric Ge/Sb vacancies should further enhance this mechanism. These excess vacancies are believed to be the main reason for the large concentrations of hole carriers [234]. As regards cubic Cr-GST, there are some spin-up impurity states at the E_F , whereas Fe-GST has a clear peak of the minority d levels cutting the E_F , suggesting a more complex picture of magnetic interactions, i.e. double exchange may also be involved.

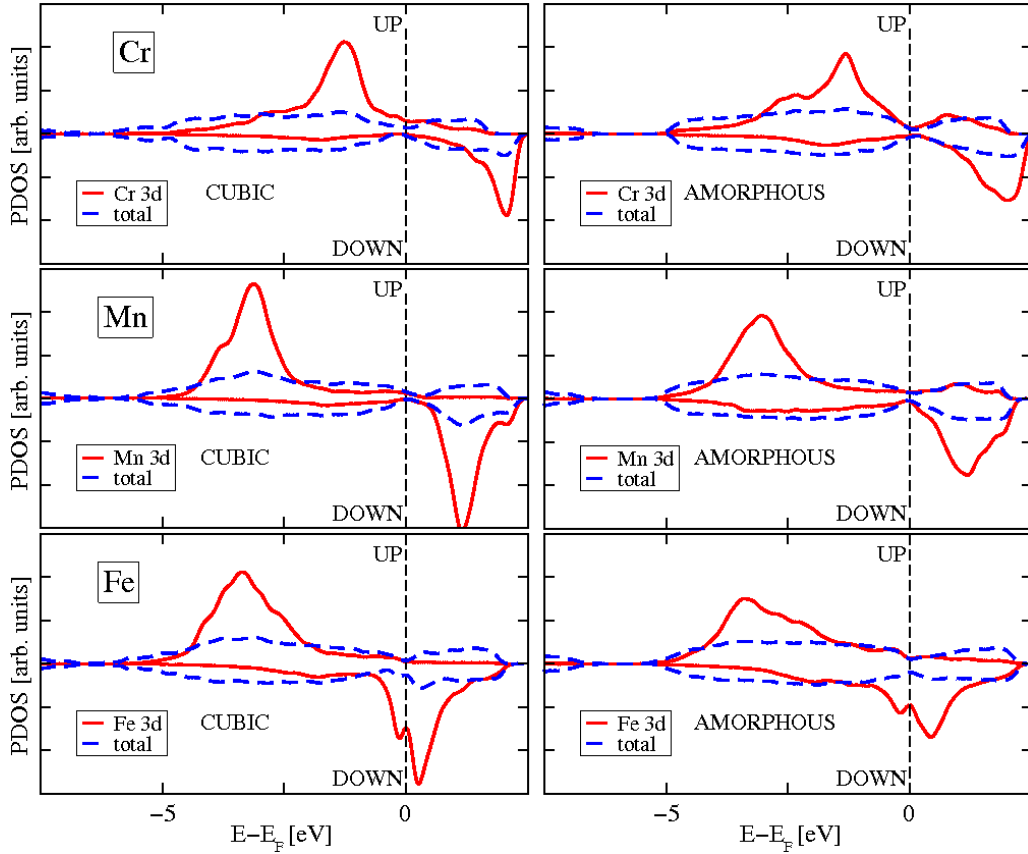


Figure 6.13 The DOS of cubic and amorphous Cr-, Mn- and Fe-GST.

In all the amorphous phases of Cr-, Mn- and Fe-GST, both the spin-up and spin-down impurity d bands are broader with respect to that of the cubic phase due to wider distributions of local moments; moreover, the pure amorphous GST has a slightly larger band gap and a lower hole concentration than those in cubic phase. All these facts suggest the p - d exchange mechanism plays a less important role in stabilizing the ferromagnetic state in amorphous MI-GST. Other exchange mechanisms can be more important.

So far we have only assumed ferromagnetic configurations for the simulations, and discussed possible exchange mechanism that can stabilize ferromagnetism. In principle, more complicated ferrimagnetic or antiferromagnetic state could exist, in particular for the systems without experimental support, namely Cr- and Mn-GST. A more thorough analysis of the magnetic states and exchange mechanisms is necessary, e.g. calculate the distance dependence of the exchange integrals J_{ij}^{QQ} between two magnetic impurities at different sites.

In recent theoretical works on Mn, Cr doped crystalline GeTe [239, 240], antiferromagnetic couplings between Mn impurities were obtained by calculating J_{ij}^{QQ} . Interestingly, the magnetic interactions changed to ferromagnetic in the presence of the non-stoichiometric excess vacancies. Since the cubic GeTe is the parent phase of cubic GST, it is well possible that Mn doped cub-GST is also in an antiferromagnetic state, however, since the excess vacancies inevitably exist in this system, we believe that ferromagnetism can be observed in Mn-GST. In the same work, ferromagnetic couplings between Cr impurities were found in Cr doped GeTe, which supports our observation of ferromagnetism in Cr-GST.

6.5 Summary and outlook

To summarize, I discussed the structural, electronic and magnetic properties of 3 *d* transition metal doped GST, and considered the stable hexagonal phase and the metastable cubic and amorphous phases. We explained the physical origin of the magnetic contrast in Fe-GST observed in experiments, moreover, we predicted Cr- and Mn-GST to be good magnetic phase materials, while Co- and Ni-GST were not. We also predicted Cr- and Mn doped GeTe to be good magnetic phase change materials, in particular with non-stoichiometric excess vacancies [241].

In the future, we will study in detail the magnetic interactions between impurities in MI-GST, and the exchange mechanisms that stabilize the interactions, with and without non-stoichiometric excess vacancies. Also, we will consider other doped PCMs with the aim of finding better performing magnetic phase change materials.

Chapter 7 Summary and Outlook

In this thesis, we provided an in-depth understanding of phase change materials by *ab initio* simulations. The study covered several important aspects of phase change materials, namely, the structural and electronic properties in both the crystalline and the amorphous phase; the kinetic properties of phase transformations between the two phases; and the magnetic properties of doped phase change materials. In this chapter, I summarize all the results and provide an outlook for future works.

In [Chapter 3](#), we studied the structural and electronic properties of the crystalline GST. We identified the origin of electron localization in the insulating GST: the statistical distribution of intrinsic atomic vacancies led to the formations of vacancy clusters (disorder), which localized the electronic wavefunctions near the Fermi level. Upon thermal annealing, these vacancy clusters dissolved and eventually formed two dimensional vacancy planes. This vacancy ordering process also triggered the structural transition from cubic to hexagonal phase and the transition from insulating to metallic behavior. As an outlook, we will investigate the atomic disorder in GST further, and consider additional approaches to control the vacancy ordering process, for instance, by compressive stresses.

In [Chapter 4](#), we studied the structural properties of several typical amorphous PCMs. We found good comparisons of structural properties between simulations and experiments for Ge-free PCMs. As regards Ge-related PCMs, such as GeTe and GST, larger discrepancy was found for Ge-Ge and Ge-Te bond lengths. We performed a detailed quantum chemistry analysis for chemical bonding in these systems, and quantified the importance of homopolar Ge-Ge bonds in stabilizing the local tetrahedral Ge units. We aim at solving the discrepancy of bond lengths in amorphous GeTe and GST in the near future.

In [Chapter 5](#), we simulated the crystallization process of AlSb and Sb₂Te in the presence of a two-dimensional crystalline seed. Smooth crystal growth process from the crystalline-amorphous interface was found, and the obtained growth velocities of

AIST at high temperatures were comparable to the experimental values. Impurities Ag/In were found to hinder the crystal growth of Sb₂Te by reducing the atomic sticking probability to the crystalline interface. At low temperatures, a large deviation of dynamical properties between theory and experiment was observed. We believed that the large deviation was due to the very high fragility of the system together with the very different quenching rate adopted in simulations 10^{13} K/s, which was three orders of magnitudes larger than that adopted in experiments. In the future, we anticipate a thorough investigation of quenching rate effects.

In [Chapter 6](#), we studied the magnetic properties of 3 *d* impurities doped PCMs. We found Cr-, Mn- and Fe-doped Ge₂Sb₂Te₅ were magnetic, while Co- and Ni-doped Ge₂Sb₂Te₅ were not. With the assumption of ferromagnetic couplings, a non-negligible contrast in the magnitude of magnetic moments between the amorphous and the crystalline state were observed for Cr-, Mn- and Fe-doped Ge₂Sb₂Te₅. The more compact surroundings (shorter bond lengths) near the impurity atoms in the amorphous state led to a stronger *p-d* hybridization (thus a smaller magnetic moment) than that in the crystalline state. Possible exchange mechanisms that could stabilize ferromagnetic couplings were discussed. In the future, we will investigate the magnetic interactions between impurities further by considering more sophisticated calculations of the exchange integrals. Non-stoichiometric excess vacancies will be considered as well.

Appendix A Density of PCMs

For *ab initio* methods, such as DFT and AIMD simulations, reasonable atomic density is important. In particular for complicated systems like amorphous states, experimental density is often used. Here I provide a list of (number) density for the PCMs that have been investigated in this thesis. Most of them are obtained experiments, and some of them are theoretical values.

atom Å ⁻³	Crystalline	Amorphous
GeTe	0.0358 [242]	0.0334 [243]
Ge ₈ Sb ₂ Te ₁₁		0.0309 [242]
Ge ₂ Sb ₂ Te ₅	0.0335 [242] a) 0.0348 [242] b)	0.0300 [238]
Ge ₁ Sb ₂ Te ₄	0.0331 [242] a) 0.0316 [242] b)	0.0304 [242]
Sb ₂ Te ₃	0.0313 [135]	0.0289 c)
Ag ₄ In ₃ Sb ₆₇ Te ₂₆	0.0324 [211]	0.0309 [211]
Sb ₂ Te		0.0309 d)
Sb		0.0321 e)
In ₃ Sb ₁ Te ₂	0.0351 [142]	

Table A1 Number density of several PCMs. a) the stable hexagonal phase; b) the metastable cubic phase; the experimental density was not known to the author, c) theoretical value was used, d) the experimental value of a-AIST was used, and e) a value close to experimental Ge₁₅Sb₈₅ was used

Appendix B

Details about EXAFS measurements and simulations of AIST

In order to obtain chemical contrast and element-specific information on the atomic structure, EXAFS measurements have been performed at beamline CEMO of the accelerator ring DORIS III, as part of Hasylab, DESY. All four K-edges of AIST were measured in trans-mission geometry on powderous samples pressed to pellets. The samples were cooled to 10K and measured at least twice to check for statistical deviations between subsequent scans. The resulting data were normalized to pre- and post-edge ranges and Fourier transformed using the computer code Athena [244]. In this way, experimental EXAFS spectra on the as-deposited amorphous and oven-crystallized phases were obtained. They are compared in Figures 5.3 and 5.6 with simulated data from the AIMD models of melt-quenched amorphous and re-crystallized phases. Since the EXAFS measurements were performed at $T = 10$ K, AIMD simulations were carried out at this temperature as well. As regards the theoretical spectra, the atomic coordinates of 36 AIMD steps were used to calculate the absorption spectra of each individual atom. All possible multiple scattering effects were taken into account, as implemented in the state-of-the-art FEFF 8.4 [212] computer code.

Thermal broadening effects were already contained in the atomic coordinates as a result of AIMD and, therefore, no further model for the vibrational states was required to match the experimental and calculated spectra. The absorption spectra of each chemical species were summed/averaged until a convergence of at least 5 % was achieved for the least abundant element. This required averaging at least 500 spectra per atomic species. The energy difference between the calculated and experimental Fermi level was corrected for, based on a refinement of the scattering paths in the experimental data (Table B1). The resulting data were Fourier transformed over the same energy range as the experimental data to allow for direct comparisons.

Atom	$r_{\text{EXAFS}} (\text{\AA})$	N_{EXAFS}	σ^2 in \AA^2	E_0 in eV
Amorphous				
Ag	2.81(1)	4.0±0.7	0.007(1)	3.0(5)
In	2.82(1)	2.7±0.5	0.002(1)	4(2)
Sb	2.87(1)	3.4±0.6	0.0025(3)	9.7(4)
Te	2.83(1)	1.6±0.4	0.0034(3)	9.4(3)
Recrystallized				
Ag	2.84(3), 3.02(3)	7.2±0.7	0.010(6), 0.011(8)	0.9(8)
In	2.80(1), 2.99(1)	6.6±0.7	0.006(1), 0.004(1)	2.3(8)
Sb	2.89(1), 3.32(1)	6.2±0.6	0.002(1), 0.006(1)	6.0(3)
Te	2.94(1), 3.39(3)	3.8±0.5	0.007(2), 0.019(6)	4.9(7)

Table B1 The nearest neighbor bond lengths (1st column) and coordination numbers (2nd column) for as-deposited amorphous and oven-crystallized AIST, obtained from EXAFS experiments. In the 3rd and 4th column, the edge shift E_0 and the Debye-Waller parameter σ^2 of each path are shown (see text). Numbers in parenthesis indicate the statistical error on the last digit.

All experimental data were also refined by the scattering path expansion method, as implemented in the computer code Artemis [244]. Due to the similar atomic numbers, the chemical contrast originates solely from the nature of the absorber atom, not from the backscattering atom. In consequence, it does not matter which atomic species of AIST is assumed to facilitate the backscattering of the photoelectrons, but for completeness we mention that we simulated Sb (the most abundant atom) at the Ag, In and Te edges and Te (the second most abundant atom) at the Sb edge. All results from a refinement of the scattering paths in the first shell are compiled in Table B1. The treatment involves the energy difference between simulations and experiments, E_0 (edge shift), the Debye-Waller parameter of each path σ^2 , a coordination number N and an interatomic distance r_i . In the absence of reference data for a well crystallized structure, the central atom loss factor S_0^2 , was set to 0.7 for all data sets to extract the

coordination numbers. The resulting systematic error of about 10% was included in the presentation of the coordination numbers (CNs). The resulting values of the nearest neighbor bond lengths and CNs are shown in Table 5.1, together with the data obtained from AIMD.

Appendix C Order parameter Q_4^{dot}

The local Steinhardt order parameter $q_l(i)$ is defined as a rotationally invariant norm of the local bond order function $q_{lm}(i)$:

$$q_l(i) = \sqrt{\frac{4\pi}{2l+1} \sum_{m=-l}^l |q_{lm}(i)|^2} \quad (1)$$

where $q_{lm}(i)$ is chosen to be the average value of the spherical harmonics in the neighborhood Ω_i of the atom i ,

$$q_{lm}(i) = \frac{1}{N_i} \sum_{j \in \Omega_i} f(r_{ij}) Y_{lm}(\hat{\mathbf{r}}_{ij}) \quad (2)$$

The spherical harmonics $Y_{lm}(\hat{\mathbf{r}}_{ij})$ depend only on the relative orientation of the vector $\mathbf{r}_{ij} = \mathbf{r}_i - \mathbf{r}_j$ connecting the atom i to its neighbor j and the average over the N_i atoms in the neighborhood i is smoothened by a radial cutoff function f :

$$f(r_{ij}) = \frac{1 - (\frac{r_{ij}}{r_c})^{p_1}}{1 - (\frac{r_{ij}}{r_c})^{p_2}} \quad (3)$$

where r_c is a cutoff radius and $p_1 < p_2$ are suitably chosen exponents yielding a sufficiently sharp cutoff function. One can simplify the notation by introducing a $(2l + 1)$ dimensional vector $\mathbf{q}_l(i)$, the components of which are the q_{lm} values:

$$\mathbf{q}_l(i) = \begin{pmatrix} q_{l,l} \\ q_{l,l-1} \\ \dots \\ q_{l,-l+1} \\ q_{l,l} \end{pmatrix} = (q_{lm}(i))_{m=-l,l} \quad (4)$$

Then $q_l(i)$ can be written as:

$$q_l(i) = \sqrt{\frac{4\pi}{2l+1}} ||\mathbf{q}_l(i)|| \quad (5)$$

The new order parameter $q_l^{\text{dot}}(i)$ is constructed from the so called bond order correlations C_{ij} between neighboring atoms, which were first introduced by Frenkel and coworkers to analyze the solid-like connections between particles. The bond order correlations C_{ij} are defined as the dot product of the vector $q_l(i)$ with the complex conjugate of $q_l(j)$, divided by the rotationally invariant norms of the two vectors:

$$C_{ij} = \frac{\mathbf{q}_l(i) \cdot \mathbf{q}_l^*(j)}{||\mathbf{q}_l(i)|| ||\mathbf{q}_l(j)||} \quad (6)$$

We define $q_l^{\text{dot}}(i)$ as the average of the C_{ij} 's taken in the neighborhood i , in a similar fashion as for $q_l(i)$,

$$q_l^{\text{dot}}(i) = \frac{1}{N_i} \sum_{j \in \Omega_i} C_{ij} \quad (7)$$

and employ it as an order parameter to characterize each atom.

For solid-like atoms, the average correlation of the bond order to its neighbors will take values close to one, whereas for particles with disordered surrounding it has values around zero. The local symmetry of the solid phase determines the value of the bond order parameter q_l . To ensure that the typical values of q_l in the two phases differ significantly, one has to select a suitable angular momentum l .

Using the parameters $l = 4$, $p_2 = 2$, $p_1 = 24$ and $r_c = 4 \text{ \AA}$, the dot product can nicely discriminate between the crystalline and amorphous phase of AIST, as shown in Figure 5.8.

Appendix D

Calculations of deposition rate and sticking coefficient

As discussed in Chap 5, we calculated the deposition rate k^+ and the sticking coefficient S near the crystalline-amorphous interface of AIST. Here we provide some technical details about the calculation. Firstly, we defined the empty crystalline sites as small spheres with a cutoff radius R , centered at the final positions of the atoms in the fully re-crystallized phase. The radius R was chosen to be equal to twice the mean squared displacement (MSD) of the atoms in the recrystallized phase at the target T ,

calculated from a MD trajectory. Although the absolute values of k^+ and S obviously depend on the value of R , the temperature dependence of the product k^+S is weakly affected by the choice of R (for reasonable values of R ranging from the MSD of the atoms to twice this quantity). Secondly, we defined the time T_{END} at which a crystalline site is no longer available for hopping, in that it is stably occupied by an atom. Thirdly, we determined the time T_{START} at which a crystalline site started to be available for an atom to hop. For a given crystalline site, T_{START} was set to be equal to the time at which at least one (out of three) nearest neighbor crystalline site (close to the crystalline part) became occupied by an atom. Hence, T_{END} and T_{START} of nearest-neighbor sites are generally correlated. In other words, T_{START} of a site always coincides with T_{END} of one of its nearest-neighbor sites. To evaluate the deposition rate k^+ , we calculated the averaged time interval between the T_{START} of a site and the first landing event. The inverse of this quantity is equal to k^+ . As regards S , we simply counted the numbers of landing and escaping events n_l and n_e for each site between its T_{START} and T_{END} , and calculated as $(n_l - n_e)/n_l$.

Appendix E

Calculations of Hubbard U in 3d impurities doped GST

In this section, I provide details about the self-consistent calculation of the Hubbard U parameter. We employed the self-consistent linear response method developed by Cococcioni and de Gironcoli [245]. Hubbard U was calculated for single impurity models in both hexagonal (108 atoms) and cubic phase (130 atoms). Only energetically favorable substitutional cation sites were considered. Two different values of $\alpha = \pm 0.15\text{eV}$ (denotes the strength of the potential shift) were used for the derivatives. The consistency was checked for several smaller values of α . The numerical accuracy with respect to the variation of α was estimated to be less than 0.1 eV. Besides, U values showed small fluctuations (~ 0.2 eV) between the relaxed and unrelaxed structures. In hexagonal phase, the calculated U values for each type of

impurities are similar at subst. Ge and subst. Sb sites. The same holds for subst. cation sites in the cubic phase. Here we summarized the U values in Table E1.

[eV]	Cr	Mn	Fe	Co	Ni
Hexagonal	2.6	5.0	4.0	6.9	4.8
Cubic	2.7	5.1	3.9	7.3	9.3

Table E1 Hubbard U values calculated self-consistently for crystalline $\text{Ge}_2\text{Sb}_2\text{Te}_5$ having one magnetic impurity. Only substitutional sites were considered.

Acknowledgement

This work would not have been possible without the support of our team. My primary supervisor Prof. Riccardo Mazzarello deserves my first and foremost thanks for his tireless support and help during my studies. Prof. Mazzarello has a great passion for science and invests most of his time on research. I share his passion for science and have benefited greatly from the extensive discussions with him. Prof. Mazzarello is always thoughtful, patient and considerate. It is really a great pleasure to work with him. I am also very grateful to my co-advisor, Prof. Matthias Wuttig, who introduces Prof. Mazzarello to me and guided me to the interesting research field of phase change materials. Prof. Wuttig always has a very tough time-schedule, but he managed to discuss with me on important issues regularly and could always provide very constructive suggestions. The most important trait I have learnt from my two advisors is to think creatively but prove rigorously, which benefits my academic career significantly.

I am indebted to my defense committee members, Prof. Riccardo Mazzarello, Prof. Matthias Wuttig, Prof. Carsten Honerkamp and Prof. Stefan Blügel. Your critical reading of the thesis and insightful comments are greatly appreciated.

I am deeply beholden to all the colleagues who worked in the group of Prof. Mazzarello and the group of Prof. Wuttig. In the past several years, I worked closely with Dr. Yan Li, Mr. Ider Ronnerberger, Dr. Pascal Rausch and Dr. Peter Zalden, who generously shared their knowledge with me and provided many valuable ideas for my work. I also appreciate the discussions with Dr. Ming Xu, Dr. Pengxiang Xu, Dr. Martin Salinga, Dr. Hanno Volker, Dr. Peter Jost, Dr. Jennifer Luckas, Mr. David Hobl, Mr. Mathias Schumacher, Mr. Peter Schmitz, Ms. Julia Benke, Mr. Tobias Schäfer and Ms. Chen Chao.

The team leads by Prof. Stefan Blügel from Research Center Jülich provided important insights on our Anderson localization work, in particular, the simulations and the analyses carried out by Dr. Alexander Thieß, Prof. Peter Dederichs, Prof. Rudolf Zeller and Prof. Stefan Blügel are essentially helpful.

I appreciate the collaborations with Mr. Volker Deringer, Dr. Marck Lumeij and Prof. Richard Dronskowski from Chemistry Department, who helped us to quantify the role of homopolar bonds in amorphous GeTe with their novel chemical bonding analysis tool, LOBSTER.

Dr. Jean-Yves Raty from University of Liège and Dr. Christophe Bichara from Aix-Marseille University are gratefully acknowledged for their help on the project of resistance drift in amorphous phase change materials.

Prof. Markus Morgenstern is acknowledged for useful discussions on graphene.

Prof. Carsten Honerkamp, Prof. Stefan Wessel and Prof. Manuel Schmidt are acknowledged for useful discussions. I find the regular seminars and group meetings organized by them particularly helpful and interesting. Besides, I would like to thank all the people from our institute, in particular, our secretaries Mrs. Gabriele Meeßen and Mrs. Helene Barton.

The High Performance Computing center of RWTH Aachen and Research Center Jülich are gratefully acknowledged. The powerful computational resources provided by them, i.e. a few tens of millions CPU hours, enabled us to explore new physics from *ab initio* theory. We owe many thanks to the HPC service team, in particular, Mr. Paul Kapinos, Mr. Tim Cramer, Dr. Hristo Iliev and Mr. Elmar Westphal.

I owe a special thank to my master supervisor, Prof. Mengbo Luo, who provided me the chance to speak with Prof. Wuttig and supported me in applying for the PhD position in RWTH Aachen.

I acknowledge German Academic Exchange Service (DAAD) and Chinese Scholarship Council (CSC) for their financial support of my PhD program.

Last but not the least, I would like to thank my parents Zhan'an Zhang, Mingfang Guo and my wife, Lei Li for their endless support, encouragement and love. I could never have reached this stage without their help and support.

Bibliography

1. Wuttig M, Yamada N. Phase-change materials for rewriteable data storage. *Nature materials* 2007, **6**: 824.
2. Lencer D, Salinga M, Wuttig M. Design rules for phase-change materials in data storage applications. *Adv Mater* 2011, **23**(18): 2030-2058.
3. Ovshinsky S. Reversible Electrical Switching Phenomena in Disordered Structures. *Physical Review Letters* 1968, **21**(20): 1450-1453.
4. Lankhorst MH, Ketelaars BW, Wolters RA. Low-cost and nanoscale non-volatile memory concept for future silicon chips. *Nature materials* 2005, **4**(4): 347-352.
5. Wuttig M. Towards a universal memory. *Nature materials* 2005, **4**: 265.
6. The International Technology Roadmap for Semiconductors (ITRS), Emerging Research Devices, 2011, <http://www.itrs.net/>.
7. Wong H-SP, Raoux S, Kim SB, Liang J, Reifenberg JP, Rajendran B, *et al.* Phase Change Memory. *Proceedings of the IEEE* 2010, **98**: 2201.
8. Rausch P. Investigations of binary and ternary phase change alloys for future memory applications. *PhD thesis, RWTH Aachen* 2012.
9. Yamada N, Ohno E, Nishiuchi K, Akahira N, Takao M. Rapid-phase transitions of GeTe-Sb₂Te₃ pseudobinary amorphous thin films for an optical disk memory. *Journal of Applied Physics* 1991, **69**(5): 2849.
10. Wuttig M, Lusebrink D, Wamwangi D, Welnic W, Gillessen M, Dronskowski R. The role of vacancies and local distortions in the design of new phase-change materials. *Nature materials* 2007, **6**(2): 122-128.
11. Iwasaki H, Ide Y, Harigaya M, Kageyama Y. Completely erasable phase change optical disk. *Japanese Journal of Appl Phys* 1992, **31**: 461.
12. van Pieterse L, Lankhorst MHR, van Schijndel M, Kuiper AET, Roosen JHJ. Phase-change recording materials with a growth-dominated crystallization mechanism: A materials overview. *Journal of Applied Physics* 2005, **97**(8): 083520.
13. Zalden P, Bichara C, van Eijk J, Braun C, Bensch W, Wuttig M. Atomic structure of amorphous and crystallized Ge₁₅Sb₈₅. *Journal of Applied Physics* 2010, **107**(10): 104312.

14. Maeda Y, Andoh H, Ikuta I, Minemura H. Reversible phase-change optical data storage in InSbTe alloy films. *Journal of Applied Physics* 1988, **64**: 1715.
15. Los JH, Kühne TD, Gabardi S, Bernasconi M. First-principles study of the amorphous In₃SbTe₂ phase change compound. *Physical Review B* 2013, **88**: 174203
16. Shportko K, Kremers S, Woda M, Lencer D, Robertson J, Wuttig M. Resonant bonding in crystalline phase-change materials. *Nature materials* 2008, **7**(8): 653-658.
17. Ibach H, Lüth H. Festkörperphysik, Einführung in die Grundlagen. *Springer* 1990.
18. Littlewood PB. Structure and bonding in narrow gap semiconductors. *Critical Reviews in Solid State and Materials Sciences* 1983, **11**(3): 229-285.
19. Lencer D, Salinga M, Grabowski B, Hickel T, Neugebauer J, Wuttig M. A map for phase-change materials. *Nature materials* 2008, **7**(12): 972-977.
20. Lencer D. Design Rules, Local Structure and Lattice-Dynamics of Phase-Change Materials for Data Storage Applications. *PhD thesis, RWTH Aachen* 2010.
21. Loke D, Lee TH, Wang WJ, Shi LP, Zhao R, Yeo YC, *et al.* Breaking the speed limits of phase-change memory. *Science* 2012, **336**(6088): 1566-1569.
22. Kolobov AV, Fons P, Frenkel AI, Ankudinov AL, Tominaga J, Uruga T. Understanding the phase-change mechanism of rewritable optical media. *Nature materials* 2004, **3**(10): 703-708.
23. Zhang W, Zalden P, Mazzarello R, Wuttig M. All the tetrahedral Ge atoms are heteropolar bonded with Te atoms in crystalline GeTe₂. The energy of crystalline GeTe₂ is 0.227 eV per unit (1 Ge 2 Te atom) higher than crystalline GeTe and Te according to density functional theory simulations. unpublished.
24. Baker D, Paesler M, Lucovsky G, Agarwal S, Taylor P. Application of Bond Constraint Theory to the Switchable Optical Memory Material Ge₂Sb₂Te₅. *Physical Review Letters* 2006, **96**(25): 255501.
25. Kohara S, Kato K, Kimura S, Tanaka H, Usuki T, Suzuya K, *et al.* Structural basis for the fast phase change of Ge₂Sb₂Te₅: Ring statistics analogy between the crystal and amorphous states. *Applied Physics Letters* 2006, **89**(20): 201910.
26. Caravati S, Bernasconi M, Kühne TD, Krack M, Parrinello M. Coexistence of tetrahedral- and octahedral-like sites in amorphous phase change materials. *Applied Physics Letters* 2007, **91**(17): 171906.
27. Akola J, Jones R. Structural phase transitions on the nanoscale: The crucial pattern in the

- phase-change materials Ge₂Sb₂Te₅ and GeTe. *Physical Review B* 2007, **76**(23): 235201.
28. Simpson RE, Fons P, Kolobov AV, Fukaya T, Krbal M, Yagi T, *et al.* Interfacial phase-change memory. *Nature nanotechnology* 2011, **6**(8): 501-505.
 29. Wehnic W, Botti S, Reining L, Wuttig M. Origin of the Optical Contrast in Phase-Change Materials. *Physical Review Letters* 2007, **98**(23): 236403.
 30. Huang B, Robertson J. Bonding origin of optical contrast in phase-change memory materials. *Physical Review B* 2010, **81**(8): 081204.
 31. Caravati S, Bernasconi M, Parrinello M. First principles study of the optical contrast in phase change materials. *Journal of physics Condensed matter : an Institute of Physics journal* 2010, **22**(31): 315801.
 32. Siegrist T, Jost P, Volker H, Woda M, Merkelbach P, Schlockermann C, *et al.* Disorder-induced localization in crystalline phase-change materials. *Nature materials* 2011, **10**(3): 202-208.
 33. D.H. Im JIL, S.L. Cho, H.G. An, D.H. Kim, I.S. Kim, H. Park, D.H. Ahn, H. Horii, S.O. Park, U-In Chung, and J.T. Moon. A Unified 7.5nm Dash-Type Confined Cell for High Performance PRAM Device. *Proc IEEE Int Electron Devices Meeting* 2008.
 34. Kooi BJ. In situ transmission electron microscopy study of the crystallization of Ge₂Sb₂Te₅. *Journal of Applied Physics* 2004, **95**(3): 924.
 35. Salinga M, Carria E, Kaldenbach A, Bornhofft M, Benke J, Mayer J, *et al.* Measurement of crystal growth velocity in a melt-quenched phase-change material. *Nature communications* 2013, **4**: 2371.
 36. Kalb J, Spaepen F, Wuttig M. Atomic force microscopy measurements of crystal nucleation and growth rates in thin films of amorphous Te alloys. *Applied Physics Letters* 2004, **84**(25): 5240.
 37. Weidenhof V, Friedrich I, Ziegler S, Wuttig M. Laser induced crystallization of amorphous Ge₂Sb₂Te₅ films. *Journal of Applied Physics* 2001, **89**(6): 3168.
 38. Kalb JA, Spaepen F, Wuttig M. Kinetics of crystal nucleation in undercooled droplets of Sb- and Te-based alloys used for phase change recording. *Journal of Applied Physics* 2005, **98**(5): 054910.
 39. Orava J, Greer AL, Gholipour B, Hewak DW, Smith CE. Characterization of supercooled liquid Ge₂Sb₂Te₅ and its crystallization by ultrafast-heating calorimetry. *Nature materials* 2012, **11**(4): 279-283.

40. Lee TH, Elliott SR. Ab Initio Computer Simulation of the Early Stages of Crystallization: Application to Ge₂Sb₂Te₅ Phase-Change Materials. *Physical Review Letters* 2011, **107**(14): 145702.
41. Kalikka J, Akola J, Larrucea J, Jones RO. Nucleus-driven crystallization of amorphous Ge₂Sb₂Te₅: A density functional study. *Physical Review B* 2012, **86**(14): 144113.
42. Sosso GC, Miceli G, Caravati S, Giberti F, Behler J, Bernasconi M. Fast Crystallization of the Phase Change Compound GeTe by Large-Scale Molecular Dynamics Simulations. *The Journal of Physical Chemistry Letters* 2013, **4**(24): 4241-4246.
43. Zhang W, Ronneberger I, Zalden P, Salinga M, Wuttig M, Mazzarello R. How fragility makes phase-change data storage robust: insights from ab initio simulations. *submitted* 2014.
44. Meister S, Peng H, McIlwrath K, Jarausch K, Zhang XF, Cui Y. Synthesis and Characterization of Phase-Change Nanowires. *Nano letters* 2006, **6**: 1514-1517.
45. Jung Y, Lee SH, Ko DK, Agarwal R. Synthesis and Characterization of Ge₂Sb₂Te₅ Nanowires with Memory Switching Effect. *JAM CHEM SOC* 2006, **128** 14026.
46. Lee SH, Jung Y, Agarwal R. Highly scalable non-volatile and ultra-low-power phase-change nanowire memory. *Nature nanotechnology* 2007, **2**(10): 626-630.
47. Giusca CE, Stolojan V, Sloan J, Bornert F, Shiozawa H, Sader K, *et al.* Confined crystals of the smallest phase-change material. *Nano letters* 2013, **13**(9): 4020-4027.
48. Song W-D, Shi L-P, Miao X-S, Chong C-T. Synthesis and Characteristics of a Phase-Change Magnetic Material. *Adv Mater* 2008, **20**(12): 2394-2397.
49. Li Y, Mazzarello R. Magnetic contrast in phase-change materials doped with Fe impurities. *Adv Mater* 2012, **24**(11): 1429-1433.
50. Zhang W, Ronneberger I, Li Y, Mazzarello R. Magnetic properties of crystalline and amorphous phase-change materials doped with 3d impurities. *Adv Mater* 2012, **24**(32): 4387-4391.
51. Zhang H, Liu C-X, Qi X-L, Dai X, Fang Z, Zhang S-C. Topological insulators in Bi₂Se₃, Bi₂Te₃ and Sb₂Te₃ with a single Dirac cone on the surface. *Nature Physics* 2009, **5**(6): 438-442.
52. Kim J, Kim J, Jhi S-H. Prediction of topological insulating behavior in crystalline Ge-Sb-Te. *Physical Review B* 2010, **82**(20).

53. Pauly C, Liebmann M, Giussani A, Kellner J, Just S, Sánchez-Barriga J, *et al.* Evidence for topological band inversion of the phase change material Ge₂Sb₂Te₅. *Applied Physics Letters* 2013, **103**(24): 243109.
54. Hasan MZ, Kane CL. Colloquium: Topological insulators. *Reviews of Modern Physics* 2010, **82**(4): 3045-3067.
55. Qi X-L, Zhang S-C. Topological insulators and superconductors. *Reviews of Modern Physics* 2011, **83**(4): 1057-1110.
56. Sa B, Zhou J, Sun Z, Tominaga J, Ahuja R. Topological Insulating in GeTe/Sb₂Te₃ Phase-Change Superlattice. *Physical Review Letters* 2012, **109**(9): 096802.
57. Wright CD, Liu Y, Kohary KI, Aziz MM, Hicken RJ. Arithmetic and biologically-inspired computing using phase-change materials. *Adv Mater* 2011, **23**(30): 3408-3413.
58. Wright CD, Wang L, Aziz MM, Diosdado JAV, Ashwin P. Phase-change processors, memristors and memflectors. *physica status solidi (b)* 2012, **249**(10): 1978-1984.
59. Suri M, Bichler O, Querlioz D, Sousa V, Perniola L, Vuillaume D. Phase Change Memory for Neuromorphic Systems and Applications. *EPCOS preceding* 2013.
60. Ovshinsky SR. Optical Cognitive Information Processing – A New Field. *Japanese Journal of Applied Physics* 2004, **43**(7B): 4695-4699.
61. Top500. <http://www.top500.org/>.
62. Atlas. http://en.wikipedia.org/wiki/Atlas_computer.
63. Computer Simulation, http://en.wikipedia.org/wiki/Computer_simulation.
64. Gross EKV, Dreizler RM. Density Functional Theory. *Springer* 1990.
65. Martin R. Electronic structure: basic theory and practical methods. *Cambridge Univ Press* 2004.
66. Frenkel D, Smit B. Understanding Molecular Simulation. *Academic Press, San Diego* 2002.
67. Landau LD, Lifshitz EM. Statistical Physics. *Oxford* 1996.
68. Hohenberg P, Kohn W. Inhomogeneous Electron Gas. *Physical Review* 1964, **136**(3B): B864-B871.
69. Kohn W, Sham LJ. Self-Consistent Equations Including Exchange and Correlation Effects.

- Physical Review* 1965, **140**(4A): A1133-A1138.
70. Runge E, Gross E.K.U. Density-Functional Theory for Time-Dependent Systems. *Physical Review Letters* 1984, **52**(12): 997-1000.
 71. Nobel prize in Chemistry 1998,
http://www.nobelprize.org/nobel_prizes/chemistry/laureates/1998/.
 72. Car R, Parrinello M. Unified Approach for Molecular Dynamics and Density-Functional Theory. *Physical Review Letters* 1985, **55**(22): 2471-2474.
 73. Jensen F. Introduction to Computational Chemistry. Wiley, 2nd edition 2007.
 74. Sadley J. Semi-Empirical Methods of Quantum Chemistry. Wiley, New York 1985.
 75. Warshel A, Levitt M. Theoretical studies of enzymic reactions: dielectric, electrostatic and steric stabilization of the carbonium ion in the reaction of lysozyme. *Journal of molecular biology* 1976, **103**: 227-249.
 76. Nobel prize in Chemistry 2013,
http://www.nobelprize.org/nobel_prizes/chemistry/laureates/2013/press.html.
 77. Kohn W. Highlights of condensed-matter theory, edited by F. Bassani, F. Fumi, and M. P. Tosi. North Holland, Amsterdam 1985.
 78. Levy M. Universal variational functionals of electron densities, first-order density matrices, and natural spin-orbitals and solution of the v-representability problem. *Proceedings of the National Academy of Sciences of the United States of America* 1979, **76**: 6062.
 79. Lieb E. Density functionals for coulomb systems. *Int J Quant Chem* 1983, **24**: 243.
 80. Anisimov VI, Gunnarsson O. Density-functional calculation of effective Coulomb interactions in metals. *Physical Review B* 1991, **43**(10): 7570-7574.
 81. Liechtenstein AI, Anisimov VI, Zaanen J. Density-functional theory and strong interactions: Orbital ordering in Mott-Hubbard insulators. *Physical Review B* 1995, **52**(8): R5467-R5470.
 82. Sharma S, Dewhurst J, Lathiotakis N, Gross E. Reduced density matrix functional for many-electron systems. *Physical Review B* 2008, **78**(20): 201103.
 83. Deng X, Wang L, Dai X, Fang Z. Local density approximation combined with Gutzwiller method for correlated electron systems: Formalism and applications. *Physical Review B* 2009, **79**(7): 075114.

84. Wigner E. On the Interaction of Electrons in Metals. *Physical Review* 1934, **46**(11): 1002-1011.
85. Wigner E. Effects of the electron interaction on the energy levels of electrons in metals. *Trans Faraday Soc* 1938, **34**: 678.
86. Carr WJ. Energy, Specific Heat, and Magnetic Properties of the Low-Density Electron Gas. *Physical Review* 1961, **122**(5): 1437-1446.
87. Gell-Mann M, Brueckner K. Correlation Energy of an Electron Gas at High Density. *Physical Review* 1957, **106**(2): 364-368.
88. Carr W, Maradudin A. Ground-State Energy of a High-Density Electron Gas. *Physical Review* 1964, **133**(2A): A371-A374.
89. Hedin L, Lundquist S. Solid State Physics, edited by Ehenreich. H et al. *Academic Press, New York* 1969, **23**.
90. Ceperley D. Ground state of the fermion one-component plasma: A Monte Carlo study in two and three dimensions. *Physical Review B* 1978, **18**(7): 3126-3138.
91. Ceperley DM. Ground State of the Electron Gas by a Stochastic Method. *Physical Review Letters* 1980, **45**(7): 566-569.
92. Perdew JP. Self-interaction correction to density-functional approximations for many-electron systems. *Physical Review B* 1981, **23**(10): 5048-5079.
93. Vosko SH, Wilk L, Nusair M. Accurate spin-dependent electron liquid correlation energies for local spin density calculations: a critical analysis. *Canadian Journal of Physics* 1980, **58**: 1200-1211.
94. Anisimov VI, Zaanen J, Andersen OK. Band theory and Mott insulators: Hubbard U instead of Stoner I. *Physical Review B* 1991, **44**(3): 943-954.
95. Becke AD. Density-functional exchange-energy approximation with correct asymptotic behavior. *Physical Review A* 1988, **38**(6): 3098-3100.
96. Perdew JP, Wang Y. Accurate and simple analytic representation of the electron-gas correlation energy. *Physical Review B* 1992, **45**(23): 13244-13249.
97. Perdew JP, Burke K, Ernzerhof M. Generalized Gradient Approximation Made Simple. *Phys Rev Lett* 1996, **77**: 3865-3868.
98. Becke AD. A new mixing of Hartree-Fock and local density-functional theories. *The Journal*

of chemical physics 1993, **98**(2): 1372.

99. Perdew JP, Ernzerhof M, Burke K. Rationale for mixing exact exchange with density functional approximations. *The Journal of chemical physics* 1996, **105**(22): 9982.
100. Heyd J, Scuseria GE, Ernzerhof M. Hybrid functionals based on a screened Coulomb potential. *The Journal of chemical physics* 2003, **118**(18): 8207.
101. Stephens PJ, Devlin FJ, Chabalowski CF, J. Frisch M. Ab Initio Calculation of Vibrational Absorption and Circular Dichroism Spectra Using Density Functional Force Fields. *J Phys Chem* 1994, **98** 11623-11627.
102. Monkhorst HJ, Pack JD. Special points for Brillouin-zone integrations. *Physical Review B* 1976, **13**(12): 5188-5192.
103. Lippert G, Hutter J, Parrinello M. A hybrid Gaussian and plane wave density functional scheme. *Molecular Physics* 1997, **92**: 477-488.
104. VandeVondele J, Krack M, Mohamed F, Parrinello M, Chassaing T, Hutter J. Quickstep: Fast and accurate density functional calculations using a mixed Gaussian and plane waves approach. *Computer Physics Communications* 2005, **167**(2): 103-128.
105. Hutter J, Iannuzzi M, Schiffmann F, VandeVondele J. cp2k:atomistic simulations of condensed matter systems. *Wiley Interdisciplinary Reviews: Computational Molecular Science* 2014, **4**(1): 15-25.
106. Bachelet G, Hamann D, Schlüter M. Pseudopotentials that work: From H to Pu. *Physical Review B* 1982, **26**(8): 4199-4228.
107. Vanderbilt D. Optimally smooth norm-conserving pseudopotentials. *Physical Review B* 1985, **32**(12): 8412-8415.
108. Rappe A, Rabe K, Kaxiras E, Joannopoulos J. Optimized pseudopotentials. *Physical Review B* 1990, **41**(2): 1227-1230.
109. Troullier N, Martins JL. Efficient pseudopotentials for plane-wave calculations. *Physical Review B* 1991, **43**(3): 1993-2006.
110. Vanderbilt D. Soft self-consistent pseudopotentials in a generalized eigenvalue formalism. *Physical Review B* 1990, **41**(11): 7892-7895.
111. Blöchl PE. Projector augmented-wave method. *Physical Review B* 1994, **50**(24): 17953-17979.

112. Kresse G, Hafner J. Ab initio molecular dynamics for liquid metals. *Physical Review B* 1993, **47**(1): 558-561.
113. Feynman R. Forces in Molecules. *Physical Review* 1939, **56**(4): 340-343.
114. Teter M, Payne M, Allan D. Solution of Schrödinger's equation for large systems. *Physical Review B* 1989, **40**(18): 12255-12263.
115. King-Smith R, Payne M, Lin J. Real-space implementation of nonlocal pseudopotentials for first-principles total-energy calculations. *Physical Review B* 1991, **44**(23): 13063-13066.
116. Kirkpatrick S, Gelatt Jr. CD, Vecchi MP. Optimization by Simulated Annealing. *Science* 1983, **220** 671-680.
117. Pastore G, Smargiassi E, Buda F. Theory of ab initio molecular-dynamics calculations. *Physical Review A* 1991, **44**(10): 6334-6347.
118. Kühne T, Krack M, Mohamed F, Parrinello M. Efficient and Accurate Car-Parrinello-like Approach to Born-Oppenheimer Molecular Dynamics. *Phys Rev Lett* 2007, **98**: 066401.
119. Blöchl P, Parrinello M. Adiabaticity in first-principles molecular dynamics. *Physical Review B* 1992, **45**(16): 9413-9416.
120. Kolafa J. Time-Reversible Always Stable Predictor-Corrector Method for Molecular Dynamics of Polarizable Molecules. *J Comput Chem* 2004, **25**: 335.
121. VandeVondele J, Hutter Jr. An efficient orbital transformation method for electronic structure calculations. *The Journal of chemical physics* 2003, **118**(10): 4365.
122. Harris J. Simplified method for calculating the energy of weakly interacting fragments. *Physical Review B* 1985, **31**(4): 1770-1779.
123. Foulkes W, Haydock R. Tight-binding models and density-functional theory. *Physical Review B* 1989, **39**(17): 12520-12536.
124. Kühne T, Krack M, Parrinello M. Static and Dynamical Properties of Liquid Water from First Principles by a Novel Car-Parrinello like Approach. *J Chem Theory Comp* 2009, **5**: 235-241.
125. Kuehne T. Second Generation Car-Parrinello Theory and Application to Liquid Water and Phase Change Materials. *PhD thesis, ETH Zurich* 2009.
126. www.cp2k.org.
127. Giannozzi P, Baroni S, Bonini N, Calandra M, Car R, Cavazzoni C, et al. QUANTUM

- ESPRESSO: a modular and open-source software project for quantum simulations of materials. *Journal of physics Condensed matter : an Institute of Physics journal* 2009, **21**(39): 395502.
128. Goedecker S, Teter M, Hutter J. Separable dual-space Gaussian pseudopotentials. *Physical Review B* 1996, **54**: 1703.
 129. Zhang W, Thiess A, Zalden P, Zeller R, Dederichs PH, Raty JY, *et al.* Role of vacancies in metal-insulator transitions of crystalline phase-change materials. *Nature materials* 2012, **11**(11): 952-956.
 130. Gaspard JP, Pellegatti A, Marinelli F, Bichara C. Peierls instabilities in covalent structures I. Electronic structure, cohesion and the $Z=8$ -Nrule. *Philosophical Magazine Part B* 1998, **77**(3): 727-744.
 131. Fons P, Kolobov AV, Krbal M, Tominaga J, Andrikopoulos KS, Yannopoulos SN, *et al.* Phase transition in crystalline GeTe: Pitfalls of averaging effects. *Physical Review B* 2010, **82**(15): 155209.
 132. Chattopadhyay T, Boucherle J, Von Schnering H. *J Phys C* 1987, **20**: 1431.
 133. Raty J, Godlevsky V, Gaspard J, Bichara C, Bionducci M, Bellissent R, *et al.* Local structure of liquid GeTe via neutron scattering and ab initio simulations. *Physical Review B* 2002, **65**(11): 115205.
 134. Sosso GC, Caravati S, Bernasconi M. Vibrational properties of crystalline Sb₂Te₃ from first principles. *Journal of physics Condensed matter : an Institute of Physics journal* 2009, **21**(9): 095410.
 135. Anderson TL, Krause HB. Refinement of the Sb₂Te₃ and Sb₂Te₂Se structures and their relationship to nonstoichiometric Sb₂Te₃-ySey compounds. *Acta Crystallogr B* 1974 **30** 1307.
 136. Dronskowski R, Blöchl PE. Crystal orbital Hamilton populations (COHP): energy-resolved visualization of chemical bonding in solids based on density-functional calculations. *J Phys Chem* 1993, **97**: 8617-8624
 137. Glassey W, Papoian G, Hoffmann R. Total energy partitioning within a one-electron formalism: A Hamilton population study of surface-co interaction in the c(2×2)-CO/Ni (100) chemisorption system. *J Chem Phys* 1999, **111**: 893-910.
 138. Kooi BJ, De Hosson JTM. Electron diffraction and high-resolution transmission electron microscopy of the high temperature crystal structures of GexSb₂Te₃+x (x=1,2,3) phase change material. *Journal of Applied Physics* 2002, **92**(7): 3584.

139. Petrov II, Imamov RM, Pinsker ZG. *Sov Phys Crystallogr* 1968, **13**: 339.
140. Matsunaga T, Kubota Y, Yamada N. Structures of stable and metastable Ge₂Sb₂Te₅, an intermetallic compound in the GeTe-Sb₂Te₃ pseudobinary systems. *Acta Crystallogr B* 2004, **60**: 685
141. Sosso GC, Caravati S, Gatti C, Assoni S, Bernasconi M. Vibrational properties of hexagonal Ge₂Sb₂Te₅ from first principles. *Journal of physics Condensed matter : an Institute of Physics journal* 2009, **21**(24): 245401.
142. Zalden P. Phase-Change Materials Structure, vibrational states and thermodynamics of crystallization. *PhD thesis, RWTH Aachen* 2012.
143. Volker H. Disorder and electrical transport in phase-change materials. *PhD thesis, RWTH Aachen* 2013.
144. Calarco R, et al. Epitaxial GeSbTe grown on Si(111). *unpublished*.
145. Tong H, Miao XS, Yang Z, Cheng XM. Insulator-metal transition in GeTe/Sb₂Te₃ multilayer induced by grain growth and interface barrier. *Applied Physics Letters* 2011, **99**(21): 212105.
146. Xu M, Cheng YQ, Wang L, Sheng HW, Meng Y, Yang WG, *et al*. Pressure tunes electrical resistivity by four orders of magnitude in amorphous Ge₂Sb₂Te₅ phase-change memory alloy. *Proceedings of the National Academy of Sciences of the United States of America* 2012, **109**(18): E1055-1062.
147. Xu M. Atomic Structure and Pressure-Induced Phase Transformations in Phase-Change Alloy Ge₂Sb₂Te₅. *PhD thesis, Johns Hopkins University* 2013.
148. Caravati S, Sosso GC, Bernasconi M, Parrinello M. Density functional simulations of hexagonal GeSb₂Te₅ at high pressure. *Physical Review B* 2013, **87**(9): 094117.
149. Agafonov V, Rodier N. Structure of Sb₂Te. *Acta Cryst* 1991, **C47** 1141-1143.
150. Matsunaga T, Akola J, Kohara S, Honma T, Kobayashi K, Ikenaga E, *et al*. From local structure to nanosecond recrystallization dynamics in AgInSbTe phase-change materials. *Nature materials* 2011, **10**(2): 129-134.
151. Anderson PW. Absence of diffusion in certain random lattices. *Phys Rev* 1958, **109**: 1492
152. Mott NF. Conduction in glasses containing transition metal ions. *J Non-Cryst Solids* 1968, **1**: 117
153. Alexander MN, Holcomb DF. Semiconductor-to-metal transition in n-type group IV

- semiconductors. *Rev Mod Phys* 1968, **40**: 815-829.
154. Rosenbaum TF, Andres K, Thomas GA, Bhatt RN. Sharp insulator transition in a random solid. *Phys Rev Lett* 1980, **45**: 1723-1726.
 155. Gaymann A, Geserich HP, Löhneysen HV. Temperature dependence of the far-infrared reflectance spectra of Si:P near the metal-insulator transition. *Physical Review B* 1995, **52**: 16486-16493
 156. Hubbard J. Electron correlations in narrow energy bands. *Proc R Soc Lond A* 1963, **276**: 238-257
 157. Georges A, Kotliar G. Hubbard model in infinite dimensions. *Phys Rev B* 1992, **45**: 6479-6483.
 158. Kotliar G. Electronic structure calculations with dynamical mean-field theory. *Rev Mod Phys* 2006, **78**: 865-951
 159. Kramer B, MacKinnon A. Localization: Theory and experiment. *Rep Prog Phys* 1993, **56**: 1469-1564.
 160. Abrahams E, Anderson PW, Licciardello DC, Ramakrishnan TV. Scaling theory of localization: Absence of quantum diffusion in two dimensions. *Phys Rev Lett* 1979, **42**: 673-676.
 161. Wegner F. The mobility edge problem: Continuous symmetry and a conjecture. *Z Phys B* 1979, **35**: 207-210
 162. Shklovskii BI, Efros AL. Electronic Properties of Doped Semiconductors. *Springer* 1984.
 163. Thiess A. Development and application of a massively parallel KKR Green function method for large scale systems. *PhD thesis, RWTH Aachen* 2012.
 164. KKR Nano, FZ Jülich, <http://www.judft.de/pm/index.php>.
 165. Lee B-S, Abelson JR, Bishop SG, Kang D-H, Cheong B-k, Kim K-B. Investigation of the optical and electronic properties of Ge₂Sb₂Te₅ phase change material in its amorphous, cubic, and hexagonal phases. *Journal of Applied Physics* 2005, **97**(9): 093509.
 166. Caravati S, Bernasconi M, Kühne TD, Krack M, Parrinello M. First principles study of crystalline and amorphous Ge₂Sb₂Te₅ and the effects of stoichiometric defects. *Journal of Physics: Condensed Matter* 2009, **22**(39): 399801-399801.
 167. Mazzarello R, Corso AD, Tosatti E. Spin-orbit modifications and splittings of deep surface

- states on clean Au(111). *Surface Science* 2008, **602**(4): 893-905.
168. <http://www.quantum-espresso.org/>.
 169. Henkelman G, Uberuaga BP, Jonsson H. A climbing image nudged elastic band method for finding saddle points and minimum energy paths. *J Chem Phys* 2000, **113**: 9901.
 170. Henkelman G, Jonsson H. Improved tangent estimate in the nudged elastic band method for finding minimum energy paths and saddle points. *J Chem Phys* 2000, **113**: 9978.
 171. Matsunaga T, Yamada N. Structural investigation of GeSb₂Te₄: A high-speed phase-change material. *Physical Review B* 2004, **69**(10): 104111.
 172. Hegedus J, Elliott SR. Microscopic origin of the fast crystallization ability of Ge-Sb-Te phase-change memory materials. *Nature materials* 2008, **7**(5): 399-405.
 173. Xu M, Cheng Y, Sheng H, Ma E. Nature of Atomic Bonding and Atomic Structure in the Phase-Change Ge₂Sb₂Te₅ Glass. *Physical Review Letters* 2009, **103**(19): 195502.
 174. Cai B, Drabold DA, Elliott SR. Structural fingerprints of electronic change in the phase-change-material: Ge₂Sb₂Te₅. *Applied Physics Letters* 2010, **97**(19): 191908.
 175. Mazzarello R, Caravati S, Angioletti-Uberti S, Bernasconi M, Parrinello M. Signature of Tetrahedral Ge in the Raman Spectrum of Amorphous Phase-Change Materials. *Physical Review Letters* 2010, **104**(8): 085503.
 176. Ghezzi GE, Raty JY, Maitrejean S, Roule A, Elkaim E, Hippert F. Effect of carbon doping on the structure of amorphous GeTe phase change material. *Applied Physics Letters* 2011, **99**(15): 151906.
 177. Raty J-Y, Otjacques C, Gaspard J-P, Bichara C. Amorphous structure and electronic properties of the Ge₁Sb₂Te₄ phase change material. *Solid State Sciences* 2010, **12**(2): 193-198.
 178. Akola J, Jones R. Structure of amorphous Ge₈Sb₂Te₁₁: GeTe-Sb₂Te₃ alloys and optical storage. *Physical Review B* 2009, **79**(13): 134118.
 179. Caravati S, Bernasconi M, Parrinello M. First-principles study of liquid and amorphous Sb₂Te₃. *Physical Review B* 2010, **81**(1): 014201.
 180. Zhang W, Ronneberger I, Li Y, Mazzarello R. Ab initio investigation of amorphous Sb₂Te. *Chemical Monthly* 2014, **145**: 97
 181. Micoulaut M, Raty JY, Otjacques C, Bichara C. Understanding amorphous phase-change materials from the viewpoint of Maxwell rigidity. *Physical Review B* 2010, **81**(17): 174206.

182. Los JH, Kühne TD, Gabardi S, Bernasconi M. First principles simulation of amorphous InSb. *Physical Review B* 2013, **87**(18): 184201.
183. Dale G, Ewen PJS, Owen AE. Thermally induced changes in refractive index of As-S and Ag-As-S thin films. *Journal of Non-Crystalline Solids* 1999, **256**: 348-352.
184. Tsunashima S, Mitsuya S, Uchiyama S. Properties of Amorphous Iron-Metalloid Thin Films. *Jpn J Appl Phys* 1981, **20**: 727-731.
185. Khulbe PK, Wright EM, Mansuripur M. Crystallization behavior of as-deposited, melt quenched, and primed amorphous states of Ge₂Sb₂Te₅ films. *Journal of Applied Physics* 2000, **88**(7): 3926.
186. Raoux S, Cheng HY, Caldwell MA, Wong HSP. Crystallization times of Ge-Te phase change materials as a function of composition. *Applied Physics Letters* 2009, **95**(7): 071910.
187. Akola J, Larrucea J, Jones RO. Polymorphism in phase-change materials: melt-quenched and as-deposited amorphous structures in Ge₂Sb₂Te₅ from density functional calculations. *Physical Review B* 2011, **83**(9): 094113.
188. Kalikka J, Akola J, Jones RO. Density functional simulations of structure and polymorphism in Ga/Sb films. *Journal of physics Condensed matter : an Institute of Physics journal* 2013, **25**(11): 115801.
189. Caravati S, Bernasconi M, Kühne T, Krack M, Parrinello M. Unravelling the Mechanism of Pressure Induced Amorphization of Phase Change Materials. *Physical Review Letters* 2009, **102**(20): 205502.
190. Sun Z, Zhou J, Pan Y, Song Z, Mao HK, Ahuja R. Pressure-induced reversible amorphization and an amorphous-amorphous transition in Ge₂Sb₂Te₅ phase-change memory material. *Proceedings of the National Academy of Sciences of the United States of America* 2011, **108**(26): 10410-10414.
191. Yeop Kim K, Cho D-Y, Cheong B-k, Kim D, Horii H, Han S. Competing local orders in liquid and amorphous structures of Ge₂Sb₂Te₅: Influence of exchange-correlation functional. *Journal of Applied Physics* 2013, **113**(13): 134302.
192. Micoulaut M. Communication: Van der Waals corrections for an improved structural description of telluride based materials. *The Journal of chemical physics* 2013, **138**(6): 061103.
193. Deringer V, Zhang W, Lumeij M, Maintz S, Wuttig M, Mazzarello R, *et al.* Bonding nature of local structural motifs in amorphous GeTe. *Angew Chem Int Ed (in press)* 2014.

194. Hughbanks T, Hoffmann R. Chains of Trans-Edge-Sharing Molybdenum Octahedra: Metal-Metal Bonding in Extended Systems. *J Am Chem SOC* 1983, **105**: 3528-3537.
195. Hoffmann R. How Chemistry and Physics Meet in the Solid State. *Angew Chem Int Ed* 1987, **26** 846-878.
196. Deringer VL, Tchougreeff AL, Dronskowski R. Crystal orbital Hamilton population (COHP) analysis as projected from plane-wave basis sets. *The journal of physical chemistry A* 2011, **115**(21): 5461-5466.
197. Maintz S, Deringer VL, Tchougréeff AL, Dronskowski R. Analytic projection from plane-wave and PAW wavefunctions and application to chemical-bonding analysis in solids. *Journal of Computational Chemistry* 2013, **34**: 2557-2567.
198. Pirovano A, Lacaita AL, Pellizzer F, Kostylev SA, Benvenuti A, Bez R. Electronic switching in phase-change memories *IEEE Trans Electron Devices* 2004.
199. Ielmini D, Lacaita AL, Mantegazza D. Recovery and Drift Dynamics of Resistance and Threshold Voltages in Phase-Change Memories. *IEEE Trans Electron Devices* 2007, **54**: 308
200. Fantini P, Brazzelli S, Cazzini E, Mani A. Band gap widening with time induced by structural relaxation in amorphous Ge₂Sb₂Te₅ films. *Applied Physics Letters* 2012, **100**(1): 013505.
201. Rizzi M, Spessot A, Fantini P, Ielmini D. Role of mechanical stress in the resistance drift of Ge₂Sb₂Te₅ films and phase change memories. *Applied Physics Letters* 2011, **99**(22): 223513.
202. Medvedev NN, Voloshin VP, Luchnikov VA, Gavrilova ML. An algorithm for three-dimensional Voronoi S-network. *J Comput Chem* 2006, **27**(14): 1676-1692.
203. SMS Group at the Institute of Chemical Kinetics and Combustion SR. Calculation of the Voronoi S-network (additively weighted Voronoi diagram) 2006:
<http://www.kinetics.nsc.ru/sms/?Software:VNP>.
204. Njoroge WK, Wuttig M. Crystallization kinetics of sputter-deposited amorphous AgInSbTe films. *Journal of Applied Physics* 2001, **90**(8): 3816.
205. Tominaga J, Kikukawa T, Takahashi M, Phillips RT. Structure of the optical phase change memory alloy, Ag–V–In–Sb–Te, determined by optical spectroscopy and electron diffraction. *Journal of Applied Physics* 1997, **82**(7): 3214.
206. Wuttig M, Salanga M. Phase-change materials: Fast transformers. *Nature materials* 2012, **11**(4): 270-271.

207. Wang WJ, Shi LP, Zhao R, Lim KG, Lee HK, Chong TC, *et al.* Fast phase transitions induced by picosecond electrical pulses on phase change memory cells. *Applied Physics Letters* 2008, **93**(4): 043121.
208. Bruns G, Merkelbach P, Schlockermann C, Salinga M, Wuttig M, Happ TD, *et al.* Nanosecond switching in GeTe phase change memory cells. *Applied Physics Letters* 2009, **95**(4): 043108.
209. Lee TH, Elliott SR. Structural role of vacancies in the phase transition of Ge₂Sb₂Te₅ memory materials. *Physical Review B* 2011, **84**(9): 094124.
210. Sosso GC, Behler J, Bernasconi M. Breakdown of Stokes-Einstein relation in the supercooled liquid state of phase change materials. *physica status solidi (b)* 2012, **249**(10): 1880-1885.
211. Njoroge W. Phase Change Optical Recording - Preparation and X-ray Characterization of GeSbTe and AgInSbTe film. *PhD thesis, RWTH Aachen* 2001.
212. Ankudinov AL, Ravel B, Rehr JJ, Conradson SD. Real-space multiple-scattering calculation and interpretation of x-ray-absorption near-edge structure. *Physical Review B* 1998, **58**: 7565-7576.
213. Wilson HA. *Phil Mag* 1900, **50**: 238.
214. Frenkel Y. The Kinetic Theory of Liquids, . *Oxford University Press* 1946.
215. Thompson CV, Spaepen F. *Acta Metall Mater* 1979, **27**: 1855.
216. Herwig FW. Measurements of viscosity in the systems antimony tellurium and tin tellurium. *Z Metallkd* 1992, **83**: 35–39.
217. Naundorf V, Macht M-P, Bakai AS, Lazarev N. The pre-factor D₀ of the diffusion coefficient in amorphous alloys and grain boundaries. *J Non-Cryst Solids* 1999, **250**: 679.
218. Fielitz P, Macht M-P, Naundorf V, Froberg G. Diffusion in ZrTiCuNiBe bulk glasses at temperatures around the glass transition. *J Non-Cryst Solids* 1999, **250**: 674.
219. Bauer T, Lunkenheimer P, Loidl A. Cooperativity and the Freezing of Molecular Motion at the Glass Transition. *Physical Review Letters* 2013, **111**(22).
220. Duenweg B, Kremer K. Molecular dynamics simulation of a polymer chain in solution. *J Chem Phys* 1993, **99**: 6983.
221. G. C. Sosso JB, M. Bernasconi. Atomic mobility and fast crystallization of the phase change compound GeTe. *E\PCOS preceding* 2013.

222. Jund P, Caprion D, Jullien R. Is There an Ideal Quenching Rate for an Ideal Glass. *Phys Rev Lett* 1997, **79**: 91.
223. Parisi G, Sciortino F. Structural Glass: Flying to the bottom. *Nature materials* 2013, **12**: 94.
224. Tong F, Hao JH, Chen ZP, Gao GY, Miao XS. Phase-change control of ferromagnetism in GeTe-based phase change magnetic thin-films by pulsed laser deposition. *Applied Physics Letters* 2011, **99**(8): 081908.
225. Ohno H. Making Nonmagnetic Semiconductors Ferromagnetic. *Science* 1998, **281**(5379): 951-956.
226. Dietl T. Zener Model Description of Ferromagnetism in Zinc-Blende Magnetic Semiconductors. *Science* 2000, **287**(5455): 1019-1022.
227. Jungwirth T, Mašek J, Kučera J, MacDonald AH. Theory of ferromagnetic (III,Mn)V semiconductors. *Reviews of Modern Physics* 2006, **78**(3): 809-864.
228. Sato K, Bergqvist L, Kudrnovský J, Dederichs PH, Eriksson O, Turek I, *et al.* First-principles theory of dilute magnetic semiconductors. *Reviews of Modern Physics* 2010, **82**(2): 1633-1690.
229. Zener C. Interaction between the d-Shells in the Transition Metals. II. Ferromagnetic Compounds of Manganese with Perovskite Structure. *Physical Review* 1951, **82**(3): 403-405.
230. Zener C. Interaction Between the d Shells in the Transition Metals. *Physical Review* 1951, **81**(3): 440-444.
231. Goodenough JB. Theory of the Role of Covalence in the Perovskite-Type Manganites [La, M(II)]MnO₃. *Physical Review* 1955, **100**(2): 564-573.
232. Kanamori J. Superexchange interaction and symmetry properties of electron orbitals. *J Phys Chem Solids* 1959, **10**: 87-98.
233. Ding D, Bai K, Song WD, Shi LP, Zhao R, Ji R, *et al.* Origin of ferromagnetism and the design principle in phase-change magnetic materials. *Physical Review B* 2011, **84**(21).
234. Raoux S, Wuttig M, edit. Phase Change Materials: Science and Applications. *Springer, Berlin* 2008.
235. Skelton JM, Lee TH, Elliott SR. Structural, dynamical, and electronic properties of transition metal-doped Ge₂Sb₂Te₅ phase-change materials simulated by ab initio molecular dynamics. *Applied Physics Letters* 2012, **101**(2): 024106.

236. Skelton JM, Elliott SR. In silico optimization of phase-change materials for digital memories: a survey of first-row transition-metal dopants for Ge₂Sb₂Te₅. *Journal of physics Condensed matter : an Institute of Physics journal* 2013, **25**(20): 205801.
237. Mirbt S, Sanyal B, Mohn P. Magnetic properties of 3d impurities substituted in GaAs. *Journal of physics Condensed matter : an Institute of Physics journal* 2002, **14**: 3295.
238. Njoroge WK , Wölftgens H -W, Wuttig M. Density changes upon crystallization of Ge₂Sb_{2.04}Te_{4.74} films. *Journal of Vacuum Science & Technology A: Vacuum, Surfaces, and Films* 2002, **20**(1): 230.
239. Liu Y, Bose SK, Kudrnovský J. Half-metallicity and magnetism of GeTe doped with transition metals V, Cr, and Mn: A theoretical study from the viewpoint of application in spintronics. *Journal of Applied Physics* 2012, **112**(5): 053902.
240. Sato K, Katayama-Yoshida H. Electronic structure and magnetism of IV–VI compound based magnetic semiconductors. *Journal of Non-Crystalline Solids* 2012, **358**(17): 2377-2380.
241. Zhang W, Ronneberger I, Li Y, Mazzarello R. Ab initio investigation of crystalline and amorphous GeTe doped with magnetic impurities. *Sci Adv Mater* 2014, **6**: 1655
242. Boyn S. Elektrische und optische Eigenschaften von kristallinen pseudo-binaeren GeSbTe Phasenwechselmaterialien. *Bachelor thesis, RWTH Aachen* 2009.
243. Dove DB. Short-range order in amorphous GeTe films. *Applied Physics Letters* 1970, **16**(3): 138.
244. Ravel B, Newville M. ATHENA, ARTEMIS, HEPHAESTUS: data analysis for X-ray absorption spectroscopy using IFEFFIT. *J Synchrotron Rad* 2005, **12**: 537-541.
245. Cococcioni M, de Gironcoli S. Linear response approach to the calculation of the effective interaction parameters in the LDA+U method. *Physical Review B* 2005, **71**(3): 035105.

Curriculum Vitae

Family name: Zhang (张)

Given name: Wei (伟)

Nationality: China

Date of Birth: 28/09/1985

City of Birth: Xi'an

Gender: Male

Education:

- 2011-2014 Ph.D, RWTH Aachen University, Germany
Institute for Theoretical Solid State Physics, Department of Physics
- 2008-2010 Master of Science, Zhejiang University, China
Institute of condensed matter physics, Department of Physics
- 2004-2008 Bachelor of Science, Zhejiang University, China
Department of Physics

Honors and Awards:

- 2010 DAAD-CSC PhD Scholarship
- 2010 Excellent postgraduate students' award
- 2009 First-Class Award of Honor for Graduate
- 2009 Graduate of Merit/Triple A graduate
- 2009 ASML Scholarship (2009)

List of Publications:

1. V. Deringer, **W. Zhang**, M. Lumeij, S. Maintz, M. Wuttig, R. Mazzarello,* R. Dronskowski*, "Bonding Nature of Local Structural Motifs in Amorphous GeTe", *Angew. Chem. Int. Ed.* in press (2014)
2. **W. Zhang**, I. Ronneberger, Y. Li, R. Mazzarello*, "Ab initio investigation of crystalline and amorphous GeTe doped with magnetic impurities", *Sci. Adv. Mater.*

- 6, 1655 (2014) (invited paper)
3. **W. Zhang**, I. Ronneberger, Y. Li, and R. Mazzarello*, "*Ab initio* investigation of amorphous Sb₂Te ", *Chem. Month.* **145**, 97 (2014) (invited paper)
 4. Y. Li, **W. Zhang**, M. Morgenstern, and R. Mazzarello*, "Electronic and magnetic properties of zigzag graphene nanoribbons on the (111) surface of Cu, Ag and Au", *Phys. Rev. Lett.* **110**, 216804 (2013)
 5. **W. Zhang**, A. Thiess, P. Zalden, R. Zeller, P. H. Dederichs, J.-Y. Raty, M. Wuttig*, S. Blügel, and R. Mazzarello*, "Role of vacancies in metal-insulator transitions of crystalline phase-change materials", *Nat. Mater.* **11**, 952 (2012)
 6. **W. Zhang**, I. Ronneberger, Y. Li, and R. Mazzarello*, "Magnetic properties of crystalline and amorphous phase-change materials doped with 3d impurities", *Adv. Mater.* **24**, 4387 (2012)
 7. **W. Zhang**, Wei Zhou, Meng-Bo Luo*, "Irreversibility of two-dimensional vortex systems with random pinning", *Phys. Lett. A* **374** 3666 (2010)
 8. **W. Zhang**, Li-Zhen Sun, Meng-Bo Luo*, "Simulation of Dynamics in Two-Dimensional Vortex Systems in Random Media", *Chin. Phys. Lett.* **26** 027402 (2009),
 9. **W. Zhang**, Meng-Bo Luo*, "Dynamic critical phenomena in two-dimensional fully frustrated Coulomb gas model with disorder", *Phys. Lett. A* **372** 4726 (2008)
 10. **W. Zhang**, I. Ronneberger, P. Zalden, M. Xu, M. Salinga, M. Wuttig, R. Mazzarello*, "How fragility makes phase-change data storage robust: insights from *ab initio* simulations ", submitted
 11. J.-Y. Raty, **W. Zhang**, J. Luckas, R. Mazzarello, C. Bichara, and M. Wuttig, "Aging mechanisms in amorphous phase-change materials", submitted